Spin control and coherence in scalable phosphorus donor qubits

Author:
Hile, Samuel

Publication Date:
2017

DOI:
https://doi.org/10.26190/unsworks/3342

Spin Control and Coherence in Scalable Phosphorus Donor Qubits

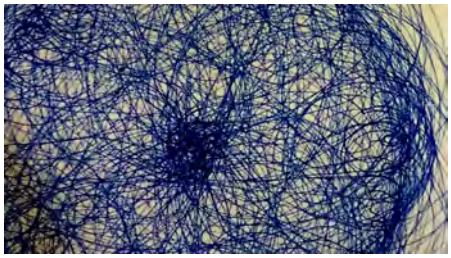

A THESIS PRESENTED

BY

SAMUEL JAMES HILE

IN FULFILMENT OF THE REQUIREMENTS FOR THE DEGREE OF

DOCTOR OF PHILOSOPHY

UNSW AUSTRALIA

SCHOOL OF PHYSICS – FACULTY OF SCIENCE

&

THE CENTRE FOR QUANTUM COMPUTATION AND COMMUNICATION TECHNOLOGY

NOVEMBER 2017

samhile@gmail.com

Supervisor: Professor Michelle Yvonne Simmons
Co-Supervisor: Professor Sven Rogge

Accepted on the recommendation of:
Professor Amir Yacoby, Harvard University, USA
Professor Rainer Blatt, Universität Innsbruck, Austria

Cover art: "The Atom" Steven Durbach

Copyright Statement

Authenticity Statement

Originality Statement

I hereby declare that this submission is my own work and to the best of my knowledge it contains no materials previously published or written by another person, or substantial proportions of material which have been accepted for the award of any other degree or diploma at UNSW or any other educational institution, except where due acknowledgement is made in the thesis. Any contribution made to the research by others, with whom I have worked at UNSW or elsewhere, is explicitly acknowledged in the thesis. I also declare that the intellectual content of this thesis is the product of my own work, except to the extent that assistance from others in the project's design and conception or in style, presentation and linguistic expression is acknowledged.

Signed:

Date:

Spin Control and Coherence in Scalable Phosphorus Donor Qubits

Abstract

Phosphorus donor impurities in a silicon substrate are a promising platform for the development of a quantum computer. Utilising a scanning tunnelling microscope as an atomic scale lithography tool, we pattern precision nanoelectronic devices and explore the use of localised electron or nuclear spin states of phosphorus atoms as quantum bits (qubits). Throughout this thesis we present four key developments in atomic-scale devices, focused on addressability and scalability.

We extend the measurement capabilities in precision donor devices, showing that a radio frequency reflectometry technique allows us to reduce the overall gate density by using a single terminal charge sensor with stronger electrostatic coupling for addressable qubit readout.

We demonstrate controllable exchange coupling between two individual electron states of a single phosphorus donor and a two-donor molecule. By detuning the donor potentials we take two initially independent spin states and induce an exchange interaction where the spins become anti-correlated, demonstrating the first step toward controlled interactions between pairs of donor qubits as required for a scalable quantum computer.

We then perform electron spin resonance on the electron states of the single donor and the two-donor molecule, observing distinct resonance spectra. The large separation in resonance frequency of $\sim$260MHz between these electron spin states allows inherent addressability between the two qubits. In a separate device we observe coherent electron spin rotation, about an arbitrary axis, achieving full qubit control in a scalable precision donor device architecture. We demonstrate a dephasing time T_2^* of $\sim$280ns and find this to be limited by magnetic field noise from the interacting ^{29}Si nuclear spins in the silicon substrate. The coherence can be recovered with a Hahn spin echo sequence to realise a T_2 coherence time of $\sim 300\mu$s.

Finally we outline a full scale architecture for a scalable quantum computer, describing all the core operations required to implement the 'surface code' error correction protocol. We present detailed models of our architecture to show that the rate of occurrence of errors can be brought below the surface code error threshold.

For Cora

Acknowledgments

I've had a great time working at C_QC^2T , and I've learned a great deal. I've voiced the body of this thesis as "we this... we did that..." and that reflects the collaborative nature of all the work. I could never have done this without the assistance and involvement of many people. So thankyou, to loads of people, and for loads of reasons:

Michelle, you are an inspiring supervisor. The attention to detail you insist upon is no doubt a key reason behind the success of the group. You've taught me a lot about managing priorities whilst juggling multiple projects, and I admire your enthusiasm in our research and your passion for communicating it.

Matt, Sam, Joris, Matt, and Will, the indefatigable team Viper, who have been amazing people to work with, and more than half-decent friends as well.

Lukas, whose patience and sense of humour I have very much appreciated. I think I owe you a muffin.

Suddho, Martin, Holger, Bent, and Tom, a great bunch of guys who taught me all manner of tips and tricks in the beginning.

Eldad, Matthias, Yu, Prasanna, Anubhav, Charley, Stuart and Matt, for all your help and friendship in the lab and around the office.

Daniel, Ludwik, Mark, Felix, Michael, and Misha, who have picked up everything so well, and who I am sure will see so many exciting new results over the next few years.

Otte, Rod, Dave, Sheree, Savita, and Tony, the miracle workers making sure everything runs smoothly.

Sven, Giuseppe, Arjan, Joost, Takashi, Joe, Gabe, Andrea, Arne, Juan, Raj, Juha, and the others down the hall, its great to have had such a healthy collaboration, from technical minutiae right up to nutting out high level experiment design.

Lloyd and Charles in Melbourne and Rajib, Yu, Yuling, and Chinyi at Purdue, who have been great collaborators over the phone.

And many others within the centre and within the school, who have shared with me me their cool results, or helped me crack a problem, or just for being lovely people to work around.

My family and friends far and near, for their love and support and sometimes (when needed) distraction.

And Chloe, for everything.

Contents

Publications

The results presented in Chapter 4 include work from the following publications:

- **S. J. Hile**, M. G. House, E. Peretz, J. Verduijn, D. Widmann, T. Kobayashi, S. Rogge, and M. Y. Simmons, "Radio frequency reflectometry and charge sensing of a precision placed donor in silicon," Applied Physics Letters 107, 093504 (2015).[1]
- M. G. House, T. Kobayashi, B. Weber, **S. J. Hile**, T. Watson, J. van der Heijden, S. Rogge, and M. Y. Simmons, "Radio frequency measurements of tunnel couplings and singlet-triplet spin states in Si:P quantum dots," Nature Communications 6, 8848 (2015).[2]

The results presented in Chapter 5 include work from the following publications:

- M. A. Broome, S. K. Gorman, M. G. House, **S. J. Hile**, J. G. Keizer, D. Keith, C. D. Hill, T. F. Watson, W. J. Baker, L. C. L. Hollenberg, and M. Y. Simmons, "Two-electron spin correlations in precision placed donors in silicon," Submitted (2017).[3]
- **S. J. Hile**, L. Fricke, M. G. House, E. Peretz, Y. Wang, C. Y. Chen, M. A. Broome, S. K. Gorman, J. G. Keizer, R. Rahman, and M. Y. Simmons, "Electron spin resonance spectra of precision donor qubits," in Preparation (2017).[4]
- **S. J. Hile**, L. Fricke, M. G. House, P. Pakkaim, S. K. Gorman, J. G. Keizer, and M. Y. Simmons, "Coherent oscillations and electron spin decoherence in precision donor qubits," in Preparation (2017).[5]

The results presented in Chapter 6 include work from the following publications:

- C. D. Hill, E. Peretz, **S. J. Hile**, M. G. House, M. Fuechsle, S. Rogge, M. Y. Simmons, and L. C. Hollenberg, "A surface code quantum computer in silicon," Science advances 1, e1500707 (2015).[6]

- L. C. L. Hollenberg, C. D. Hill, M. Y. Simmons, E. Peretz, S. Rogge, M. Fuechsle, and **S. J. Hile**, "Apparatus and method for quantum processing [i]," (2016), US Patent 20,160,125,310.[7]

- M. Fuechsle, **S. J. Hile**, C. D. Hill, L. C. L. Hollenberg, M. G. House, E. Peretz, S. Rogge, and M. Y. Simmons, "Apparatus and method for quantum processing [ii]," (2016), US Patent 20,160,125,311.[8]

Additional publications contributed to in the course of this PhD but not directly included in this thesis:

- M. G. House, E. Peretz, J. G. Keizer, **S. J. Hile**, and M. Y. Simmons, "Single-charge detection by an atomic precision tunnel junction," Applied Physics Letters 104, 113111 (2014).[9]

- T. Kobayashi, J. van der Heijden, M. G. House, **S. J. Hile**, P. Asshoff, M. Gonzalez- Zalba, M. Vinet, M. Y. Simmons, and S. Rogge, "Resonant tunneling spectroscopy of valley eigenstates on a donor-quantum dot coupled system," Applied Physics Letters 108, 152102 (2016).[10]

- S. K. Gorman, M. A. Broome, J. G. Keizer, T. F. Watson, **S. J. Hile**, W. J. Baker, and M. Y. Simmons, "Extracting inter-dot tunnel couplings between few donor quantum dots in silicon," New Journal of Physics 18, 053041 (2016).[11]

- M. Broome, S. K. Gorman, J. G. Keizer, T. F. Watson, **S. J. Hile**, W. Baker, and M. Y. Simmons, "Mapping the chemical potential landscape of a triple quantum dot," Physical Review B 94, 054314 (2016).[12]

- G. C. Tettamanzi, **S. J. Hile**, M. G. House, M. Fuechsle, S. Rogge, and M. Y. Simmons, "Probing the quantum states of a single atom transistor at microwave frequencies," ACS Nano (2016).[13]

- M. A. Broome, T. F. Watson, D. Keith, S. K. Gorman, M. G. House, **S. J. Hile**, J. G. Keizer, W. J. Baker, and M. Y. Simmons, "High fidelity single-shot singlet-triplet readout of precision placed donors in silicon," Submitted (2017).[14]

Figures

Tables

Nature isn't classical, dammit, and if you want to make a simulation of nature, you'd better make it quantum mechanical, and by golly it's a wonderful problem, because it doesn't look so easy.

Richard Feynmann

1

Introduction & Context

One of the grand technological challenges of the present is to build a quantum computer. That is – a general computing device where the behaviour of its constituent parts is determined by quantum mechanics. Of course our universe is demonstrably quantum mechanical in nature, so the operation of any computer is inherently determined by quantum mechanics, but the uniquely quantum effects of superposition and entanglement are not often observable at the macroscopic level. Random interactions with the environment around and within any device often lead to a return to classically predictable behaviour. So what is meant by the term 'quantum computer' is something where the non-classical quantum behaviour dominates, and can be preserved and harnessed to provide improved computational performance.

The nature of the expected enhancement is subtle. By analogy with the way that the light generated by a laser is fundamentally different from that emitted by even the brightest lightbulb, a quantum computer will not be simply 'faster' or 'more powerful' than a modern supercomputer. Laser light is *coherent* – the electromagnetic waves produced in a laser are synchronised: all at a single frequency, and all with matching phase offsets. A lightbulb (or a candle flame, or the sun) on the other hand produces incoherent light, where although each individual photon of light can be described by a

particular frequency and phase, all the photons have different and randomly distributed wave properties, washing out certain behaviours, for example the interference effects that can be produced with a laser. A quantum computer will store and manipulate information in a coherent way, permitting certain types of operations that are simply not possible with classical, or incoherent, processors.

The concept of quantum computing arose in the 1980s, with Feynman[15] who discussed the difficulty of simulating some physical process which is determined by quantum physics using a computing machine which is not. He suggested the notion of a quantum simulator, which would use a specific array of well understood quantum mechanical particles to model the action of some other quantum mechanical system of interest. Deutsch[16] generalised the concept of a specific-use simulator to the paradigm of universal quantum computing, proposing a computer based on quantum mechanics which is capable of solving any generic problem. Deutsch[16] noticed that the so-called 'Church-Turing Principle':

> *Every finitely realisable physical system can be perfectly simulated by a universal computing machine operating by finite means*

is not satisfied by classical computers simulating classical physics – because the computer is discrete, and classical mechanics allows for a continuum of states. Remarkably, the same principle applied to a quantum computer simulating quantum physics *is* satisfied – by virtue of the quantised states of quantum particles and fields. It is thus expected that quantum computers will have far reaching applications in molecular simulations for chemistry, medicine and materials science[17,18].

Broader applications were realised in the 1990s, with Shor[19] describing a quantum algorithm for computing the prime factors of a number, which is exponentially faster (in essence – can be completed in $\sim \log(N)$ steps compared to N) than the best known classical factoring algorithm, and Grover[20] providing a quantum search algorithm that is quadratically faster ($\sqrt{N}$ rather than N) than what is possible classically. The fact that there are a large class of economically important problems related to either search or factorisation has amplified interest in the development of quantum computer technology over the last 20 years.

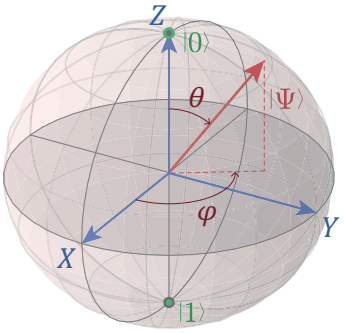

Figure 1.1: Bloch sphere representation of a single qubit state. The sphere is a convenient representation of the two-dimensional Hilbert space in which a qubit exits. Opposite points correspond to orthogonal states, for instance $|0\rangle$ and $|1\rangle$ (marked in green), which are traditionally placed on the Z-axis. Other points on the surface indicate pure superposition states, parametrised by a probability angle θ and phase angle φ.

Quantifying qubits

The fundamental unit within a quantum computer is called a qubit, a quantum bit[21]. Whilst a single classical bit can take one of two values '0' or '1', the state of a qubit is allowed to be in a complex superposition of two states $|0\rangle$ and $|1\rangle$, in general:

$$|\Psi\rangle = \alpha\,|0\rangle + \beta\,|1\rangle \tag{1.1}$$

where α, β are complex numbers with the restriction that $|\alpha|^2 + |\beta|^2 = 1$. It is illustrative to then re-parameterise the superposition in a form which permits a geometric representation known as the Bloch sphere, shown in Figure 1.1. It illustrates the nature of a single qubit as having two degrees of freedom, corresponding to the spherical angles:

$$|\Psi\rangle = \cos\left(\frac{\theta}{2}\right)|0\rangle + e^{i\varphi}\sin\left(\frac{\theta}{2}\right)|1\rangle \tag{1.2}$$

The θ angle relates to the weighting of the two basis states ($|0\rangle$ and $|1\rangle$); if the state of the qubit is measured, the probability to measure $|0\rangle$ is $\cos\theta/2$ (and $\sin\theta/2$ for $|1\rangle$). Such a measurement destroys the value of the phase angle φ, and 'projects' the qubit into one of the basis states. Although it is the multi-dimensional nature of the so-called

Hilbert space which a qubit occupies that is the fundamental distinction from a classical system, the final measurement of a qubit abruptly removes this freedom, collapsing back into a classical-like outcome. Thus, the cleverness in the quantum algorithms mentioned above is in utilising the extra dimensions during the computation in such a way that at the end of the process, the answer to the problem is represented only by θ, and not φ, so that it can be recovered. It is worth noting that the number of extra dimensions available in the Hilbert space grows exponentially with the number of qubits, so that for example, adding five more qubits brings the total number of dimensions not to $6 \times 2 = 12$, but in fact to $2^6 = 64$, so the additional capacity for information content during a computation grows remarkably fast.

DiVincenzo[22] was one of the first to describe the physical requirements that need to be satisfied to effectively combine a set of physical qubits together to form a quantum computer. There are many different physical implementations that meet the requirements to some extent, most of which are not discussed at all in this thesis, an extensive survey can be found in a general review by Ladd *et al.*[23]. Here we are concerned with semiconductor spin qubits, and in particular, donor spin qubits in silicon. We shall describe the state of the art in this one technology following a general discussion of the most important requirements for a good qubit.

Most critically, the qubits must not be accidentally measured by interactions with their environment, an effect termed decoherence, and there are two distinct ways in which things can go wrong. The first is characterised by a relaxation time T_1, which describes the timescale of inelastic interactions which cause the qubit to relax to its lower energy ground state ($|0\rangle$). In the Bloch sphere picture this is a random and uncontrolled change in θ. The second is described by a characteristic time T_2, which represents uncontrolled interactions which only impact the phase of a qubit. Since there is no energy loss, dephasing can often be unwound, recovering a well defined phase angle. For instance, slow variations in a qubit's environment may cause the qubit state to accumulate phase at a different rate for a number of different repetitions of an experiment, or quantum computation. This is sketched in Figure 1.2(a), where sine waves of differing frequencies represent the phase decoherence across three trials. Although the average response quickly decays with a characteristic timescale T_2^*, the qubit has a well defined phase throught each individual trial. Hence the time T_2^* describes the pure dephasing time, which is the decoherence time if nothing is done to try to recover lost

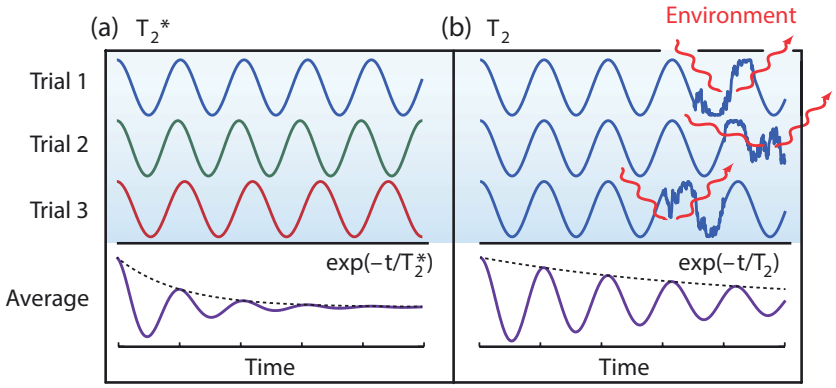

Figure 1.2: Dephasing and decoherence of qubits due to environmental interactions. (a) Inconsistent phase relationships due to a slowly varying environment across different trials of a quantum computation lead to decay of the average system response on a timescale T_2^*, although for each single trial the phase remains well defined, and so the set of trials can be refocused. (b) Sudden random shifts of the phase within each single trial due to environmental fluctuations determines the limiting dehoherence time T_2. Adapted from Ladd *et al.* [23].

phase information. Quite often the qubit state can be effectively prolonged beyond T_2^* by so-called 'dynamical decoupling' strategies which refocus the decaying average response. There are environmental interactions that abruptly alter the phase, as expressed in Figure 1.2(b), such that even in an individual trial the phase becomes randomised. These processes determine the limiting decoherence time T_2.

Any qubit implementation must support a means to both initialise and measure the qubit state as well as a universal set of quantum gates, allowing the quantum computer's programmer to access any point within the many-dimensional Hilbert space. Single qubit gates rotate the vector defining the qubit state by a certain angle about a certain axis on the Bloch sphere. An additional key component is the ability to perform an entangling gate between two qubits. Entanglement is a uniquely quantum property of a set of qubits, which after having interacted may exist in a state which cannot be described separately. For instance, in the two qubit Bell state $\Phi^+ = 1/\sqrt{2}(|0\rangle_A |0\rangle_B + |1\rangle_A |1\rangle_B)$, each qubit (A and B) has equal probability of being measured in either basis state, so the outcome of the measurement of qubit A alone is completely random, as is that of B, yet in every case the two will be found to 'project' into the same state. In essence, entanglement is yet another manifestation of the large Hilbert space of multiple qubit states.

Another vital quality is that a chosen physical implementation must be extensible to an arbitrarily large system of interacting qubits, without an exponential increase in required resources (run-time, or cost to operate). We refer to this requirement as scalability, and related to it is another – that each individual qubit may be operated on independently, or in other words the system of qubits needs to be addressable.

If a system is scalable and addressable, and the full set of universal gates are accurate (and do not introduce too much decoherence themselves), then it is possible through quantum error correction[24,25] to indefinitely extend the overall coherence time of a full quantum computer, which is the ultimate long-term goal for the field.

The state of the art in silicon

Loss and DiVincenzo[26] initially proposed the spin 1/2 states of a single isolated electron within a semiconductor quantum dot as a qubit platform in the late 1990s. The first successful experiments implementing the concept of an electron spin qubit were achieved in modulation doped gallium arsenide (GaAs/AlGaAs) heterostructures[27,28], demonstrating measurement of individual electron spin states[29], coherent manipulation[30], and controlled interactions between pairs of electrons[31,32]. An unfortunate limitation in GaAs is that both gallium and arsenic atomic nuclei are spin 1/2 particles, and the random evolution of the many nuclei strongly interacting with the electron cause rapid decoherence. Techniques have been proposed to combat the decohering effect of this nuclear spin bath[33], but an alternative is to select a material with fewer nuclear spins present.

Silicon is an attractive host material in which to host spin qubits for several reasons[34]. The natural abundance of the only spin 1/2 isotope – ^{29}Si is less than 5%. This concentration can be further reduced to nearly zero by gas centrifugation of silicon tetrafluoride SiF_4 or silane SiH_4 to produce high purity ^{28}Si[35,36] which has no nuclear spin bath at all. Recent results have shown that this can significantly extend the achievable coherence time[37,38]. Additionally, silicon qubit technologies are expected to be able to benefit in terms of eventual large-scale fabrication from the tremendous engineering effort behind the modern silicon microelectronics industry.

Single electron states have been isolated in Si/SiGe heterostructure quantum dots[39], and in metal-oxide-semiconductor field effect transistor (MOSFET) quantum dots[40]. Both of these systems have recently demonstrated single qubits with highly accurate single qubit gates[41–43], and MOSFET qubits have recently demonstrated a two qubit entangling gate[44].

As an alternative to electrons in electrostatically confined quantum dots, Kane[45] proposed a qubit based on the nuclear spin of an intentionally placed phosphorus dopant atom within a silicon substrate. Related ideas using other donor species[46], and in particular using the spin of an electron bound to the donor[47,48] followed. There are natural benefits to both donor qubit flavours: the nuclear spin state is strongly isolated from the environment and provides an excellent 'quantum memory' at the cost of being relatively slow to operate; the electron spin on the other hand permits much more rapid logical operations, both single qubit gates and entangling gates between two electrons, at the cost of a somewhat shorter coherence time.

Both the donor electron[49] and donor nuclear spin[50] qubits have been achieved by implanting phosphorus atoms into a region near to a MOSFET type spin measurement device, using a high energy ion beam. Within isotopically purified silicon, these implanted donor qubits have exhibited remarkably long coherence times[38] and high single qubit gate accuracy[51]. The limitation of the implant strategy is that its positional accuracy is to date not high enough to facilitate a reliable two qubit entangling gate, and so without advances in the implantation technology is incompatible with the scalability requirement.

An alternate strategy for the placement of donors is to *"really arrange the atoms the way we want them"**, which has become possible to a large extent using scanning tunnelling microscope lithography[52]. And thus we arrive at the subject of this thesis, which is to explore atomic precision phosphorus donor devices to create a scalable spin qubit implementation in silicon. The isolation of an electron to a single donor[53], and high fidelity($> 99\%$) single shot measurement of a single electron spin state[54,55] has already been achieved with this fabrication strategy. In addition, the recent demonstration of devices containing coupled phosphorus donor quantum dots, able to host multiple interacting electrons[56,57] represents a promising first step toward scalable qubit systems based on donors in silicon.

* another Richard Feynman quote

The results expressed in this thesis advance the state of the art in a number of directions, which we outline in the following pages.

1.2 Thesis outline

The aim of this introductory chapter has been to give some context and to introduce some of the terminology and associated concepts in quantum computation generally, and the field of silicon quantum computing in particular.

In Chapter 2 we will provide a brief overview of the physics at play within a silicon nanoelectronic device and describe the behaviour of confined electrons. We also outline the behaviour of donor electron and nuclear spins within a magnetic field, and the various interactions that may be engineered between spins.

In Chapter 3, the fabrication methodology for our devices is laid out. We describe the use of a scanning tunnelling microscope (STM) under ultra high vacuum (UHV) conditions to perform atomic scale lithography, focussing on the chemical process by which phosphorus donors are incorporated into the silicon lattice before being encapsulated in a protective silicon layer. We then explain the microfabrication process by which electrical contact is made to the buried donor structures.

Chapter 4 contains the first set of significant results of this thesis. Here we introduce methods to reduce the gate density in donor based qubit devices by replacing the ubiquitous three-terminal single electron transistor charge sensor with a single-terminal tunnel-coupled reservoir using radio frequency (RF) detection techniques. We show that additional information is available in the phase and amplitude of a reflected RF signal, relative to the DC conductance signal historically used to monitor electron tunnelling events. In addition we examine the other benefits of a tunnel coupled reservoir, in terms of the strength of coupling to a bound electron, and in terms of the potential bandwidth of the sensor. Using a double quantum dot device, we find that a tunnel-coupled reservoir sensor can provide a measure of electron tunnel rates, and we demonstrate Pauli spin blockade and use the sensor to accurately measure the tunnel coupling between two donor quantum dots, and the related exchange interaction energy.

In Chapter 5 we introduce a two qubit device consisting of a single P donor and a 2P molecule. In this system we show effective spin initialisation and measurement, and explore the exchange interaction between the two qubits, observing the onset of anticorrelated spin states with increasing inter-qubit coupling. Following theoretical analysis, we demonstrate the successful integration of a microwave transmission antenna onto this device. We outline the development of an automated alignment scheme to stabilise against electrical noise, and demonstrate the use of an adiabatic passage technique to overcome magnetic noise, and thus perform the first spin resonance experiments comparing 1P and 2P qubits. We analyse the measured spin resonance spectra, extracting information about the nuclear spin dynamics in our device. Using a second two qubit device, we perform additional coherent spin resonance experiments, demonstrating universal single qubit logic in the ability to rotate the spin state about an arbitrary axis on the Bloch sphere. Additionally we asses the coherence properties of our qubit, finding that the limiting decoherence mechanism is a fluctuating effective magnetic field due to ^{29}Si nuclear spins within our substrate. We extract a dephasing time $T_2^* > 280$ns, and with a Hahn spin echo sequence extend the coherence time to $T_2 = 300\mu$s.

Chapter 6 looks to the future, and sets out the concept for a large-scale array of donor qubits capable of overcoming decoherence and relaxation through error correction using a scheme known as the 'surface code'. We specify the geometry of our architecture: a 2D lattice of single P donors and readout sensors in a central layer, with parallel sets of control wires above and below, all within a solid crystal of isotopically purified ^{28}Si. We describe the means of executing a universal set of quantum gates in the proposed quantum processor, in particular focussing on a two qubit entangling gate which is achieved through the dipole-dipole interaction between two neighbouring donor-bound electrons. We produce detailed simulations of several aspects of the design, including electrostatic gate voltage control requirements, and the error rate associated with the fundamental physical operations, showing that the scheme does allow for effective error corrected operation.

Finally, in Chapter 7 we summarise the major results and discuss future objectives and potential short term outcomes.

2

Phosphorus donors in silicon

We define a number of key concepts and much of the terminology used throughout the thesis in the course of a brief overview in this chapter, of the physics relevant to donor nanostructures. We discuss the quantisation of energy levels through confinement, then introduce the bandstructure of silicon, and examine the impact of dopants. We next review single electron transport mechanics within the so-called constant interaction model. The chapter concludes with a description of the various spin interactions present for donors under the influence of electric and magnetic fields.

2.1 Confined electrons

We begin by looking at the behaviour of electrons in the absence of an atomic crystal lattice. The behaviour of free electrons in three dimensions can be described* by a

* Full derivations are not provided here, refer to one of many textbooks on the subject e.g. Kittel [58], Ashcroft and Mermin [59]

vacuum Hamiltonian consisting of simply the kinetic energy:

$$H_0 = -\frac{\hbar^2}{2m_0}\left(\frac{\partial^2}{\partial x^2} + \frac{\partial^2}{\partial x^2} + \frac{\partial^2}{\partial x^2}\right) \tag{2.1}$$

where m_0 is the electron mass. We will show later that the behaviour of electrons within a semiconductor lattice is approximately the same as for free electrons, after substituting the electron mass with an effective mass determined by the material $m_0 \rightarrow m^*$. The dynamics are described by the Schrödinger equation:

$$H_0\Psi_k = E_k\Psi_k \tag{2.2}$$

Where the states Ψ and energies E are labelled by a wavevector $\vec{k} = (k_x, k_y, k_z)$ satisfying the condition:

$$k_x, k_y, k_z = \frac{2n\pi}{L} \tag{2.3}$$

when the electrons are confined to a cube of volume $V = L^3$. The k are quantised, but for a large volume, the allowed values form a quasi continuum of wavevectors. Assuming periodic boundary conditions, the solutions are plane wave states with energy proportional to the square of the wavevector:

$$\Psi_k(\vec{r}) = e^{i\vec{k}\cdot\vec{r}} \qquad\qquad E_k = \frac{\hbar^2}{2m_0}\left(k_x^2 + k_y^2 + k_z^2\right) \tag{2.4}$$

At some temperature T, the occupation of states is described by the Fermi-Dirac distribution:

$$f(E) = \frac{1}{e^{\frac{(E-\mu)}{k_bT}} + 1} \tag{2.5}$$

where the electrochemical potential μ depends in general on the specific potential energy of electrons in an external field. The Fermi energy E_F describes the highest energy occupied orbital in the ground state, and in the free electron case equal to μ.

Thus $2N$ free electrons (accounting for spin degeneracy) will fill N states as per

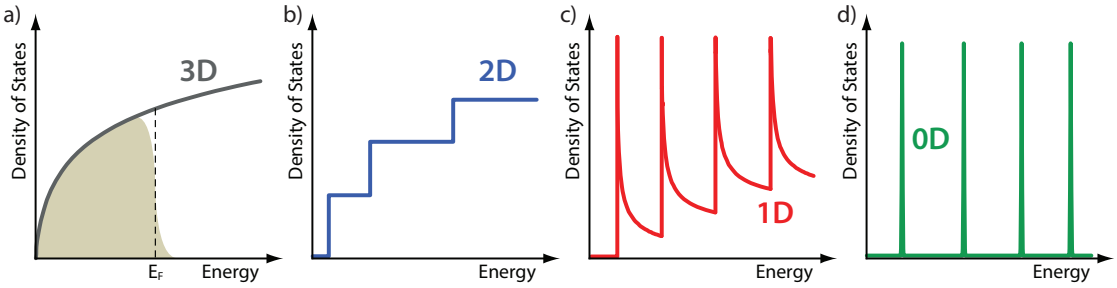

Figure 2.1: Density of states for low dimensional systems. (a) Schematic of the 3D density of states, which approaches zero at small energies. Occupied states upto the Fermi energy at a finite temperature are indicated by the shaded area. (b) 2D density of states, constant above the minimum energy for each sub-band. (c) 1D density of states, which diverge at the sub-band minima. (d) 0D density of states, representing discrete energy levels.

Equation (2.3) in the three dimensional reciprocal space of $\vec{k}$ out to a sphere of radius:

$$k_F = \sqrt{\frac{2m_0 E_F}{h^2}} \tag{2.6}$$

As the energy increases, the number of available k states also increases. Enumerating occupied states as a function of energy produces the electron density of states $d(E)$ in three dimensions:

$$d_{3D}(E) = \frac{\partial N}{\partial E} = \frac{L^3}{2\pi^2}\left(\frac{2m_0}{h^2}\right)^{3/2}\sqrt{E} \tag{2.7}$$

This relationship is shown in Figure 2.1(a), with the shaded area indicating filled states up to the Fermi energy at a finite temperature ($k_B T < E_F$), given by the product $f(E)d(E)$. Thermal excitation results in a number of states above E_F being occupied, in lieu of some states directly below E_F, according to Equation (2.5).

2.1.1 2D CONFINEMENT

A one-dimensional potential well can be applied to confine electrons to a 2D plane. This is often achieved in a heterostructure where the conduction band energy in two materials is different, allowing electrons to be tightly confined at the material interface, forming a

2DEG (two dimensional electron gas). Common heterostructures used in nanoelectronics include GaAs/AlGaAs and Si/SiGe. Alternatively a semiconductor/insulator interface can be combined with an applied electric field to produce similar confinement in devices based on the principle of a MOSFET (metal oxide semiconductor field effect transistor). In this thesis we employ an atomically abrupt doping profile to achieve 2D confinement.

The additional confinement in the z direction reduces the number of allowed $\vec{k}$ vectors. Repeating the arguments above, the density of states in two dimensions can be found to be:

$$d_{2D}(E) = \frac{\partial N}{\partial E} = \frac{L^2}{2\pi^2}\left(\frac{2m_0}{h^2}\right)\Theta(E - E_s) \tag{2.8}$$

where Θ is the Heaviside step function and E_s the minimum energy for conduction in one so-called sub-band. The key characteristic here is that the density of states is independent of the energy, attaining a constant value above E_s. Equation (2.8) describes the availability of states within one sub-band, but additionally, with increasing energy additional sub-bands become accessible associated with excited states of the sharp potential well in the z direction. The cumulative d_{2D} for a number of sub-bands is shown in Figure 2.1(b).

The conduction electron density, or sheet carrier density n_s, in electrons per unit area, is therefore (by integrating the energy up to E_F and assuming only one band is relevant):

$$n_s = \frac{m_0}{\pi\hbar^2}E_F \tag{2.9}$$

2.1.2 1D CONFINEMENT

Further confining electrons to a single spatial degree of freedom again modifies their dynamics. 1D confinement is often achieved by restricting the 2DEG formed at an interface with positively charged depletion gates at the device surface. Other methods include physically etching away parts of the 2D plane leaving a narrow 'mesa', or forming a nano-wire by catalysed growth of a semiconductor material into a long narrow cylinder.

We achieve crystalline 1D nanowires in the precision donor devices studied in this work by selective doping of narrow regions.

Predictably, the density of states is again different for 1D electrons, given by:

$$d_{1D}(E) = \frac{\partial N}{\partial E} = \frac{L}{2\pi^2}\left(\frac{2m_0}{\hbar^2}\right)^{1/2}\frac{1}{\sqrt{E-E_s}} \tag{2.10}$$

Again there are a number of sub-bands associated with quantised values of the z and y momenta due to the sharp confinement in those directions. The form is plotted in Figure 2.1(c), which indicates that the number of available states diverges at the onset of each sub-band. Nevertheless, as for the 3D and 2D cases, there are states available at all energies.

2.1.3 0D CONFINEMENT

Making the potential well three-dimensional confines an electron in all directions. The associated density of states is described by a delta function, one discrete spin degenerate state at each allowed eigenenergy:

$$d_{0D}(E) = \frac{\partial N}{\partial E} = 2\delta(E-E_s) \tag{2.11}$$

which is sketched in Figure 2.1(d). The spacing between states, and the spacing between sub-bands s in the 1D and 2D cases above, depends on the length scale of the confinement R:

$$\Delta E = E_j - E_{(j-1)} \sim \frac{\hbar^2}{2m_0}\left(\frac{C\pi}{R}\right)^2 \tag{2.12}$$

where we use s to label the states/sub-bands.

This is a truly discrete spectrum and the regime of most interest in implementing donor qubits, although the 1D and 2D behaviours are important also in understanding the flow of current in our devices.

2.2 Silicon bandstructure

Silicon, the element at the centre of the modern electronics industry, is a covalently bonded crystal in which the four outer shell electrons of each atom are shared with neighbouring atoms positioned tetrahedrally around it. This arrangement is the diamond cubic crystal form, displayed in Figure 2.2(a). The distance between bonded atoms is $\sqrt{(a/4)^2 + (a/4)^2 + (a/4)^2} = 0.235\text{nm}$ given the lattice constant $a = 0.543\text{nm}$. The face-centred-cubic basis of the diamond lattice results in a Brillouin zone in the form of a truncated octahedron as shown in Figure 2.2(b). Lines and points of high symmetry are marked with standard labels.

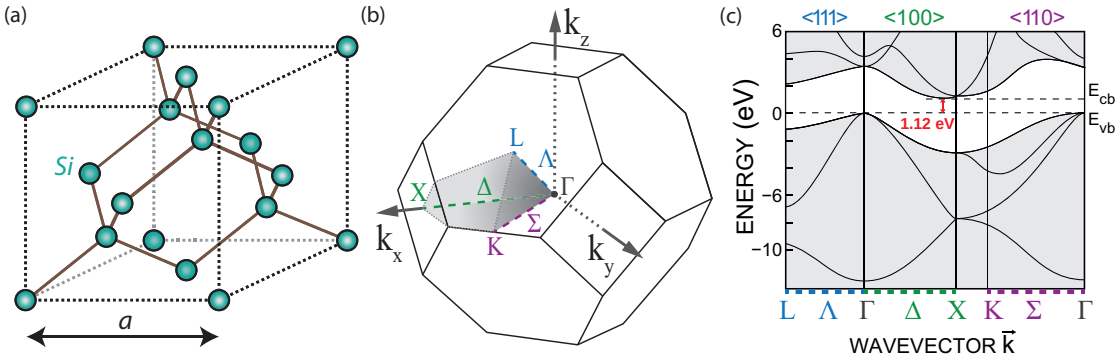

Figure 2.2: Bandstructure of intrinsic silicon. (a) Silicon crystal unit cell, an example of the face-centred-cubic diamond lattice, containing 8 atoms per unit volume a^3. (b) The Brillouin zone of silicon, showing the fundamental unit cell of reciprocal space. High symmetry lines and points are marked with canonical labels. (c) Bandstructure of silicon, displaying the energy as a function of wavevector k. The x-axis represents a range of directions within the Brillouin zone, marked in correspondence with (b). The conduction band minimum occurs near the X point, where the band-gap is $\sim 1.12\text{eV}$ relative to the valence band maximum at Γ. Reproduced from Chelikowsky and Cohen [60].

Silicon is an indirect band-gap semiconductor, with a bandgap of $\sim 1.12\text{eV}$. The bandstructure is displayed in Figure 2.2(c), reproduced from Chelikowsky and Cohen [60]. The conduction band minimum is located along the Δ axis (green dashed line) at $k_0 \approx 0.85k_a = 0.85(2\pi/a)$. There are six such minima, or valleys, located along the 6 $\langle 100 \rangle$ equivalent crystal directions.

2.2.1 Effective mass approximation

Electron motion within the silicon lattice is affected by the presence of the atomic cores. The nuclei contribute a periodic potential $V_p(\vec{r})$ to the electron Hamiltonian. The Bloch theorem allows us to express the wavefunctions $\Psi_k(\vec{r})$ of an unconstrained electron within a periodic crystal as a simple product of a plane wave and a Bloch function $u_k(\vec{r})$, which shares the periodicity of the potential V_p.

$$\Psi_k(\vec{r}) = U_k(\vec{r}) = u_k(\vec{r})e^{i\vec{k}\cdot\vec{r}} \tag{2.13}$$

In the effective mass approximation, which considers only the contribution of states near k_0, the electron mass is replaced with the effective mass m^*, which in the most general case is a rank 2 tensor describing the curvature of the dispersion relation $E(\vec{k})$ near the conduction band minima.

$$\left(\frac{1}{m^*}\right)_{ij} = \frac{1}{\hbar^2}\frac{\partial^2 E(\vec{k})}{\partial k_i \partial k_j} \tag{2.14}$$

The tensor nature of m^* is important in calculating the energies, and the model has been used to great success, but for simplicity of notation we shall express it simply as a scalar.

Thus, in the effective mass approximation, solutions to the Schrödinger equation, for a general confining potential $V(r)$ in addition to the periodic nuclear Coulomb potential V_p, and the vacuum Hamiltonian H_0 (Equation (2.1)):

$$[H_0 + V_p + V(r)]\Psi_k = E_k\Psi_k \tag{2.15}$$

can be expressed as a product:

$$\Psi_k(\vec{r}) = U_k(\vec{r})\Phi_k(\vec{r}) \tag{2.16}$$

where Φ_k is a slowly varying envelope function, and U_k is a Bloch plane wave state as per

Equation (2.13). The effective mass Schrödinger equation is thus separable, and yields:

$$[H^* + V(r)]\Phi_k = (E_k - E_{k_0})\Phi_k \tag{2.17}$$

$$H^* = -\frac{\hbar^2}{2m^*}\left(\frac{\partial^2}{\partial x^2} + \frac{\partial^2}{\partial x^2} + \frac{\partial^2}{\partial x^2}\right) \tag{2.18}$$

which is the Schrödinger equation for a free electron in a confining potential $V(r)$, where the periodic lattice potential V_p has been removed, the electron mass is rescaled to m^*, and the energy origin is offset by E_{k_0}, the energy at the conduction bamd minimum.

Solutions to the above (Φ_k) are conduction band electron states with energies above the band-gap, and hence are not occupied at equilibrium. The Fermi energy can be raised out of the band-gap and above E_{k_0} by doping the semiconductor, which occupies these effectively free electronic states and activating conduction through the semiconductor.

2.2.2 The effect of delta-doping

By introducing dopants to a semiconductor, we provide a source of electrons and also modify the confining potential $V(r)$ within the effective mass approximation, changing the bandstructure. Typical dopants in silicon are group III elements (B, Ga) which act as acceptors, producing free holes as charge carriers; and group V elements (P, As, Bi) which act as donors, and produce free electrons. We dope our devices with phosphorus (P), with each P atom providing an electron to fill a state in the conduction band. The electron density we achieve in the devices presented in this thesis is on the order of $n_s = 10^{14}\text{cm}^{-2}$, well above the so-called metal-insulator transition[61,62] at around $2 \times 10^{12}\text{cm}^{-2}$.

This high density is achieved by δ-doping, where 1 in 4 Si atoms in a single mono-layer along a [001] crystal plane is substituted by a phosphorus, as illustrated in Figure 2.3(a). The fabrication method is described in the following chapter.

The potential in the z-direction due to the sheet of Coulomb potential wells is approximated by a delta function (hence the name δ-doping), which confines the crystal momentum of the electrons, represented by the wavevector k to a 2D plane. The six valley minima are projected onto the [001] crystal plane in Figure 2.3(b), resulting in

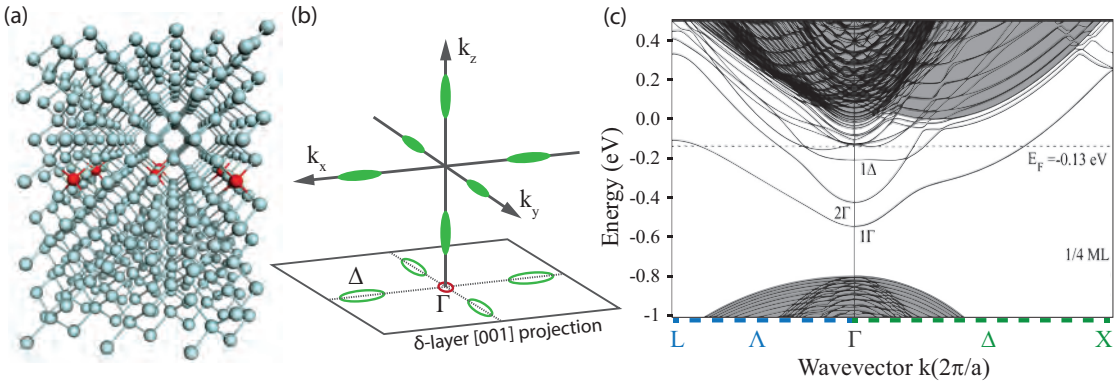

Figure 2.3: Density of states for low dimensional systems. (a) Representation of a region of the silicon lattice above and below a δ-doped layer of 1/4 mono-layer density. Phosphorus donors are shown in red. (b) Band minima, or valleys, shown in reciprocal space. Green ellipsoids represent constant energy surfaces near the k_0 points. Projecting the Brillouin zone onto the [001] plane leaves 5 valley minima, 4 marked Δ, and a doubly degenerate band at the Γ point (where $k = 0$). (c) Calculated bandstructure of a delta-doped layer, showing . Reproduced from Carter *et al.* [63].

a double sub-band at the Γ point (red) at the centre of the Brillouin zone where the out-of-plane valleys have collapsed, and four degenerate Δ sub-bands (green) due to the in-plane valleys. Figure 2.3(c) shows a simulation by Carter *et al.* [63] of the confined 2D bandstructure resulting from a δ-doped plane similar to that shown in (a). The two lowest bands have their minima at $k = 0$ as expected, and the third line, labelled '1Δ' has a minimum at a finite k_Δ (the exact value of which varies with the exact layout of donors within the δ-doped layer). All six bands are occupied, with the Fermi energy 0.13eV below the bulk undoped conduction band minimum (shaded in grey).

Within the nanostructured devices presented in this thesis, the δ-layer is lithographically patterned, producing additional lateral confinement. The transition from 2D conduction to 1D conduction is primarily determined by the Fermi wavelength (defined in Equation (2.6)):

$$\lambda_F = \frac{2\pi}{k_F} = \frac{2\pi\hbar}{\sqrt{2m^* E_F}} = \frac{2\pi^{3/2}}{\sqrt{n_s}} \tag{2.19}$$

which, substituting the measured n_s for a P donor δ-layer[64] of $\sim 2 \times 10^{14}\text{cm}^{-2}$ is on the order of 5-10nm.

Thus, we expect the constant 2D electron density of states for patterned features wider than 10nm. Nanowires narrower than this show evidence of 1D behaviour, with

discontinuities in the conductance observed in electron transport measurements involving transport along such narrow wires[65]. Nevertheless, for the most part, any continuous area doped with phosphorus effectively behaves like a metallic conductor[66].

2.3 Single electron transport

The dynamics of electron motion in the devices we investigate can be modelled quite effectively with a principally classical theory known as the constant interaction model[27,67]. The core concept is that fixed capacitances between all metallic elements of a given circuit determine the charge state of each isolated zero-dimensional quantum dot element given the applied voltages on all other (1D/2D) elements.

Consider the simple arrangement of conductive elements shown in Figure 2.4(a). Here a single 0D structure, a quantum dot (green) is tunnel-coupled to source and drain reservoirs on the left and right, and capacitively coupled to a gate. The coupling is parameterised by resistances R and capacitances C as labelled. The isolated quantum dot has an intrinsic charge $-q_e N$ given by the number of conduction electrons N (and $-q_e$ is the electron charge) localised at the site. The non-isolated elements may have a voltage V applied to them, which has the effect of modifying the energy levels of the quantum dot by inducing an additional charge CV on the quantum dot. The total charge is then:

$$Q = C_G V_G + C_L V_S + C_R V_D - q_e(N - N_0) \tag{2.20}$$

where N_0 is the number of electrons localised at the quantum dot at equilibrium, with all voltages zero. The electrostatic energy associated with the total charge Q is given by:

$$E_Q = \frac{Q^2}{2C_\Sigma} \qquad C_\Sigma = C_G + C_L + C_R \tag{2.21}$$

The total energy $U(N)$ of the N electron configuration is the sum of all single particle

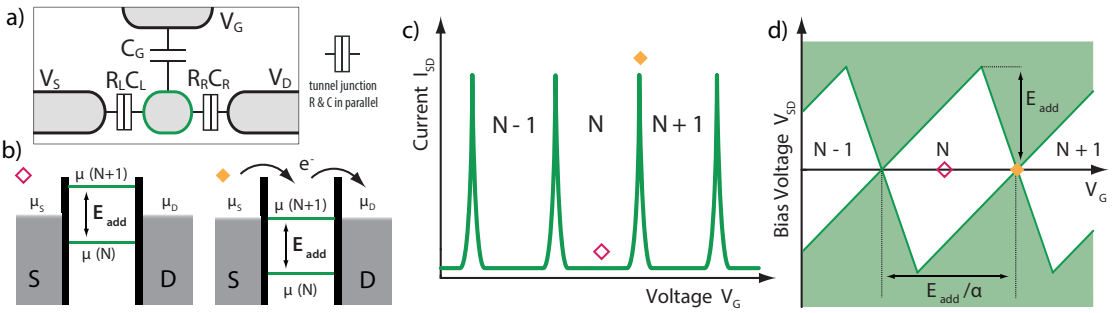

Figure 2.4: Coulomb blockade in a quantum dot. (a) Schematic circuit diagram of a single quantum dot (green), tunnel-coupled to source and drain reservoirs, and capacitively coupled to a gate. (b) Electrochemical potential representation of two configurations. On the left Coulomb blockade where electron transport is not possible; on the right showing sequential electron transport through the quantum dot, permitted by the transition potential μ being aligned to both $\mu_S \approx \mu_D$. Together these two behaviours define a single electron transistor. (c) Coulomb peaks in the current through an SET occurring regularly as a function of gate voltage. Configurations shown in (b) are marked with corresponding diamond markers. (d) High bias transport through an SET. The recognisable Coulomb diamond regions of blockaded current define the addition energy E_{add} and the gate lever arm α.

orbital energies E_i plus the electrostatic energy:

$$U(N) = \sum_{i=1}^{N} E_i + \frac{[C_G V_G + C_L V_S + C_R V_D - q_e(N - N_0)]^2}{2C_\Sigma} \tag{2.22}$$

More often, we are interested in the electrostatic potential for a particular charge state transition, which will occur when the applied gate voltages cause μ to cross the Fermi energy of one of the metallic tunnel-coupled reservoirs (source or drain, which are typically at approximately the same energy):

$$\mu(N) = U(N) - U(N-1) \tag{2.23}$$

$$= E_N + \frac{-2(C_G V_G + C_L V_S + C_R V_D) q_e[(N - N_0) - (N - 1 - N_0)]}{2C_\Sigma} + \frac{q_e^2[(N - N_0)^2 - (N - 1 - N_0)^2]}{2C_\Sigma} \tag{2.24}$$

$$= E_N + \frac{-(C_G V_G + C_L V_S + C_R V_D) q_e}{C_\Sigma} + \frac{q_e^2[1 - 2N - 2N_0]}{2C_\Sigma} \tag{2.25}$$

The energy associated with a particular charge state, representing the maximum

amount of energy that can be added or removed without changing the charge state is termed the addition energy:

$$E_{\text{add}}(N) = \mu(N) - \mu(N-1) = \Delta E(N) + \frac{q_e^2}{C_\Sigma} \tag{2.26}$$

consisting of the orbital energy spacing ΔE and the electrostatic charging energy $E_c = \frac{q_e^2}{C_\Sigma}$. The energy spacing is proportional to the length scale of confinement, as per Equation (2.12). For a quantum dot that is simply a single P donor, or a small number of donors clustered together the orbital energy difference is significant[53,56,65], while for dots larger than $\sim 50\text{nm}^2$, the orbital spacing becomes negligible with reference to the thermal energy at millikelvin temperatures, and the charging energy alone is a good approximation of the total addition energy*.

2.3.1 Coulomb blockade

We confine our discussion for now to a regime where electron transport occurs sequentially only through single orbital ground states of the quantum dot. The conditions required are:

$$h\Gamma \ll k_B T \qquad\qquad q_e V_{SD} \ll \Delta E \tag{2.27}$$

where the tunnel rates Γ, depend on the resistances R_L, R_R. T is the temperature, and $V_{SD} = V_D - V_S$. Thus there are two distinct configurations, shown in Figure 2.4(b). In the left panel, there is no quantum dot transition potential μ at the effective Fermi level, which is given by the source potential $\mu_S = -q_e V_S$, or drain potential $\mu_D = -q_e V_D$. This configuration is known as Coulomb blockade – electrons cannot flow from source to drain, and the quantum dot remains in a fixed charge state.

Alternatively, as shown in the right panel of Figure 2.4(b), when a transition potential, in this case $\mu(N+1)$, aligns with μ_S and μ_D, the quantum dot charge state may

* terminology in the literature varies, with some authors using the term charging energy to refer to the full addition energy even in the case of significant orbital energy variation

continuously switch between $N \leftrightarrow N+1$, and a small bias voltage V_{SD} will drive a DC current of electrons sequentially from source to drain as indicated by the arrows. This condition is met periodically as a function of the gate voltage V_G, as sketched in Figure 2.4(c), which shows the current flow through the quantum dot. Because electrons pass through the system one by one, and a change in voltage can switch the current flow on and off, this configuration is known as a single electron transistor (SET). Positions corresponding to (b) are tagged with diamond markers.

Relaxing the $q_e V_{SD} \ll \Delta E$ condition and increasing the source-drain bias produces characteristic Coulomb blockade diamonds, which are schematically sketched in Figure 2.4(d). Green shading represents a non-zero current flow from source to drain. A horizontal cut at $V_{SD} = 0$ reproduces (c), but as the bias V_{SD} increases, the range of voltage settings that place a transition potential within the window:

$$\mu_S > \mu > \mu_D \tag{2.28}$$

also becomes greater. Once a point is reached where $q_e V_{SD} > E_{\text{add}}$, then there is always at least one transition potential within the large bias window and the Coulomb blockade is unconditionally overcome. The scale of the Coulomb diamonds on the gate voltage axis is given by $\Delta V_G = E_{\text{add}}/\alpha$, as indicated. The lever arm

$$\alpha = \frac{\partial \mu}{\partial V_G} = q_e \frac{C_G}{C_\Sigma} \tag{2.29}$$

relates the voltage to the quantum dot energy.

2.3.2 Double quantum dots

We now introduce the circuit shown in Figure 2.5(a) – a double quantum dot, serially coupled to source and drain reservoirs. Each dot D_1 and D_2 is additionally coupled capacitively to a gate, G_1 or G_2. There is some cross-coupling of G_1 to D_2 and vice versa, not shown. With this circuit, current may only flow between source and drain at

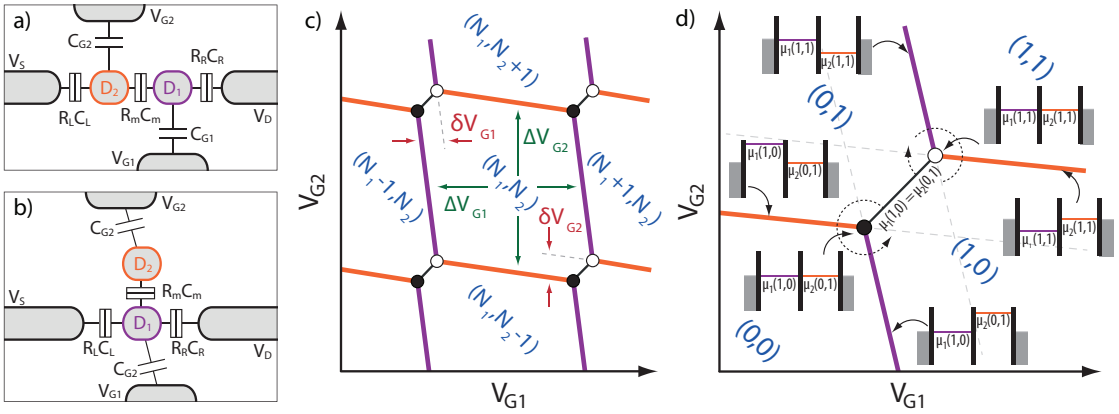

Figure 2.5: Stability diagram of a double quantum dot. (a) Schematic circuit diagram of two serially coupled quantum dots (purple and orange), tunnel-coupled to source and drain reservoirs and to each other, and capacitively coupled to two gates, as indicated. (b) Schematic circuit diagram of a double quantum dot with alternate coupling. Here D_1 is tunnel-coupled to both source and drain, and D_2 is only tunnel-coupled to D_1. (c) The charge stability diagram is effectively equivalent for both cases (a) and (b), the difference being in which features appear in the measured source-drain current. in the serially coupled case, transport is only possible at the triple points (black and white dots). In the alternate case, the charge transitions of D_1 (purple lines) produce a finite DC current flow under a small applied V_{SD}. Voltage spans ΔV correspond to the addition energy of each dot; and δV the mutual energy between the two dots. (d) Electrochemical potential configurations around a pair of triple-points. Charge states are marked in blue. Figures reproduced from Van der Wiel *et al.* [67].

low bias if both dot potentials are aligned within the bias window:

$$\mu_S > \mu_1(N_1, N-2) = \mu_2(N_1, N_2) > \mu_D \tag{2.30}$$

for some pair of integers N_1 and N_2, the electron occupation numbers for the two dots.

Figure 2.5(b) shows a slightly different circuit arrangement, where the second dot is only tunnel-coupled to the first, which in turn is tunnel-coupled to both source and drain. This configuration is employed throughout the thesis as a charge sensing technique. Current may flow from source to drain through D_1 under the same condition as we saw in the single quantum dot case ($\mu_S > \mu_1 > \mu_D$), except that an additional term appears in the electrochemical potential expression due to the presence of D_2.

As a result of the capacitive interaction between the two quantum dots (parameterised by the mutual capacitance C_m), the potential of one shifts by a discrete amount when the charge state of the other changes. The magnitude of the shift is termed the mutual

charging energy:

$$E_m = \frac{q_e^2 C_m}{C_{\Sigma 1} C_{\Sigma 2} - C_m^2} \tag{2.31}$$

where $C_{\Sigma 1}$ and $C_{\Sigma 2}$ are the total capacitances of dot D_1 and D_2 respectively. This mutual interaction also modifies the single quantum dot charging energies:

$$E_{C1} = \frac{q_e^2 C_{\Sigma 1}}{C_{\Sigma 1} C_{\Sigma 2} - C_m^2} \qquad E_{C2} = \frac{q_e^2 C_{\Sigma 2}}{C_{\Sigma 1} C_{\Sigma 2} - C_m^2} \tag{2.32}$$

a full derivation of these relations can be found in Van der Wiel *et al.*[67].

The charge stability diagram (applicable to both double quantum dot configurations), indicating the ground state charge configuration (in blue) across a range of gate voltage coordinates (V_{G1}, V_{G2}) is sketched in Figure 2.5(c). Gate voltage spans ΔV and δV are marked in green and red, corresponding to the addition and mutual energies as follows:

$$E_{C1} = \alpha_{G1}^{D1} \Delta G_1 \qquad E_m = \alpha_{G1}^{D1} \delta G_1 \tag{2.33}$$

$$E_{C2} = \alpha_{G2}^{D2} \Delta G_2 \qquad E_m = \alpha_{G2}^{D2} \delta G_2 \tag{2.34}$$

with α_B^A being the lever arm of gate B for dot A. Purple lines represent charge degeneracy conditions for D_1, orange lines charge degeneracy conditions for D_2, and the black lines denote inter-dot charge transitions where the total number of isolated electrons $N_1 + N_2$ remains fixed. At the intersection of the lines are triple points, marked by black and white dots.

The detail around a pair of triple points is displayed in Figure 2.5(d). The key difference between the two configurations in Figure 2.5(a) and (b) is that in the first case, electron transport occurs only at the triple points. This involves sequential electron tunnelling at the black dot – cycling through the charge states $(0,0) \rightarrow (1,0) \rightarrow (0,1)$ as indicated by the dashed arrow encircling the triple point. At the white dot, the transport can be viewed as sequential hole transport, cycling $(1,1) \rightarrow (1,0) \rightarrow (0,1)$. In the second case, dot D_1 sustains a transport current at all points along the purple lines, where the insets show that $\mu_1 = \mu_S \approx \mu_D$. The orange lines do not correspond to any transport current in either case, they only denote the gate coordinates where the charge ground state shifts – a charge reconfiguration may or may not occur depending on the tunnel gap resistances R_m, R_L, R_R.

2.4 Donor spin dynamics

We have considered quantum dots in general in the previous section. Next we look at the specific wavefunction of an electron (with charge q_e) bound to a single P donor. The confining potential is a Coulomb potential well $V_C(r)$, centred at the donor site r_0:

$$V_C(r) = -\frac{q_e^2}{4\pi\epsilon_0|\vec{r} - \vec{r_0}|} \tag{2.35}$$

Thus the solutions to the effective mass Schrödinger equation (Equation (2.17)):

$$[H^* + V_C(r)]\Phi_n = (E_n - E_{k_0})\Phi_n \tag{2.36}$$

are simply scaled versions of the Hydrogen atom wavefunctions, and we restrict our analysis to the 1s orbital state which is the only relevant orbital at low energy. The interplay of the tetrahedral symmetry of the single donor atom, and the cubic symmetry of the silicon lattice results in a breaking of valley degeneracy into a singlet groundstate (A), a doublet (E), and a triplet (T). The total donor wavefunctions can be written as a sum over valleys ν:

$$\Psi(\vec{r}) = \sum_\nu c_\nu \Phi_\nu(\vec{r}) U_\nu(\vec{r}) \tag{2.37}$$

$$\Phi_\nu(r) = \frac{1}{\sqrt{\pi} a_B^{3/2}} e^{-r/2a_0} \tag{2.38}$$

$$\tag{2.39}$$

where a_B is the scaled Bohr radius $\sim$ 2.5nm for P donors in Si. Here we label a discrete basis of k-vectors along the positive and negative x-, y-, and z-directions collectively as ν for the Bloch functions U_ν and envelope functions Φ_ν (Equation (2.16)). The coefficients c_ν are the weighting of the six valley basis states. Kohn and Luttinger[68] give the coefficients for the six eigenstates $(c_x, c_{-x}, c_y, c_{-y}, c_z, c_{-z})$, by considering the symmetry group, and the energies have been measured by Ramdas and Rodriguez[69].

State	Valley weighting	Binding energy (meV)
A	$\frac{1}{\sqrt{6}}(1,1,1,1,1,1)$	45.6
E	$\frac{1}{\sqrt{4}}(1,1,-1,-1,0,0)$	32.6
	$\frac{1}{\sqrt{4}}(1,1,0,0,-1,-1)$	
T	$\frac{1}{\sqrt{2}}(1,-1,0,0,0,0)$	33.9
	$\frac{1}{\sqrt{2}}(0,0,1,-1,0,0)$	
	$\frac{1}{\sqrt{2}}(0,0,0,0,1,-1)$	

Table 2.1: Valley content of the donor electron states in silicon. Valley weightings are specified in the basis $(c_x, c_{-x}, c_y, c_{-y}, c_z, c_{-z})$ as determined by Kohn and Luttinger [68]. Measured binding energies of each set of degenerate states taken from Ramdas and Rodriguez [69].

Both are reproduced in Table 2.1.

Importantly, for a single donor, the valley degeneracy is broken, leaving a non-degenerate valley groundstate, with the first valley excited state, the triply degenerate T, located $\sim$ 12meV higher in energy. Thus the only remaining degeneracy is due to spin.

2.4.1 Donor in a magnetic field

The spin Hamiltonian for an electron bound to a donor, within an external magnetic field B_0 oriented along the z-axis is analogous to a hydrogen atom in a magnetic field:

$$H = H_{\text{electron Zeeman}} + H_{\text{nuclear Zeeman}} + H_{\text{hyperfine}} \tag{2.40}$$

$$H = \gamma_e B_0 S_Z - \gamma_n B_0 I_Z + \vec{S} \cdot \hat{A} \cdot \vec{I} \tag{2.41}$$

Here the electron $\gamma_e = g_e \mu_B / h = 27.97$GHz/T (and nuclear $\gamma_n = g_n \mu_n / h = 17.25$MHz/T) gyromagnetic ratios [70,71] are determined by the electron g-factor and Bohr magneton (nuclear g-factor, and nuclear magneton), along with Planck's constant. $\hat{A}$ is the hyperfine interaction tensor describing the electron-nuclear interaction. $S = (S_X, S_Y, S_Z)$ is the electron spin operator and $I = (I_X, I_Y, I_Z)$ the P nuclear spin

operator, with components given by the Pauli matrices:

$$S_X = I_X = \frac{1}{2}\begin{pmatrix} 0 & 1 \\ 1 & 0 \end{pmatrix}; \quad S_Y = I_Y = \frac{1}{2}\begin{pmatrix} 0 & i \\ -i & 0 \end{pmatrix}; \quad S_Z = I_Z = \frac{1}{2}\begin{pmatrix} 1 & 0 \\ 0 & -1 \end{pmatrix} \tag{2.42}$$

Zeeman energy and Larmor precession

The z-spin operator in the electron (and nuclear) Zeeman term establishes an energy difference $E_{Z_e} = \gamma_e B_0$ ($E_{Z_n}\gamma_n B_0$) between the quantised electron spin (nuclear spin) up and down states: $|\uparrow\rangle$ and $|\downarrow\rangle$ ($|\Uparrow\rangle$ and $|\Downarrow\rangle$).

Considering $H_{\text{electron Zeeman}}$ in isolation (an equivalent consideration holds for the nuclear term), its action on the spin vector $\vec{S}$ is to drive a continuous precession about the z-axis, with a Larmor frequency proportional to the field, $\omega_{L_e} = \gamma_e B_0$.

Hyperfine interaction

The hyperfine tensor $\hat{A} = A\hat{I} + \hat{D}$ consists of a scalar contact term[71]:

$$A = \frac{8\pi}{3}\frac{\mu_0}{4\pi}h^2\gamma_e\gamma_n|\Psi(r{=}0)|^2 = 117.5\text{MHz} \tag{2.43}$$

proportional to the electron wavefunction density $|\Psi(r{=}0)|^2$ at the nuclear core of the P atom; and a dipolar tensor component $\hat{D}$, negligible in the case of the spherically symmetric s-like orbital of a single donor-bound electron in the groundstate. In assuming $\hat{D} \approx 0$, the hyperfine Hamiltonian term simplifies to:

$$H_{\text{hyperfine}} = A\vec{S}\cdot\vec{I} \tag{2.44}$$

2.4.2 Solution for arbitrary magnetic field

The solution to Equation (2.40) for a single phosphorus donor in silicon has eigenstates[72] analogous to the hydrogen atom[73]. In general for a magnetic field B_0 they can be written:

$$|\uparrow\Uparrow\rangle \tag{2.45}$$

$$\left|\widetilde{\uparrow\Downarrow}\right\rangle = \cos(\eta/2)\,|\uparrow\Downarrow\rangle + \sin(\eta/2)\,|\downarrow\Uparrow\rangle \tag{2.46}$$

$$|\downarrow\Downarrow\rangle \tag{2.47}$$

$$\left|\widetilde{\downarrow\Uparrow}\right\rangle = \cos(\eta/2)\,|\downarrow\Uparrow\rangle - \sin(\eta/2)\,|\uparrow\Downarrow\rangle \tag{2.48}$$

$$\tan(\eta) = \frac{A}{(\gamma_e + \gamma_n)B_0} \tag{2.49}$$

Where η is a small parameter in our experimental regime with $B_0 \sim 1.5\text{T}$. The form of the non-product states $\left|\widetilde{\uparrow\Downarrow}\right\rangle, \left|\widetilde{\downarrow\Uparrow}\right\rangle$ can be understood by considering that they evolve from the singlet and triplet T^0 states at zero field, as shown in Figure 2.6(a). The evolution is sketched in Figure 2.6(b) as a function of magnetic field. The four eigenstates have corresponding energies:

$$E(|\uparrow\Uparrow\rangle) = \frac{\gamma_e B_0 - \gamma_n B_0 + A}{2} \tag{2.50}$$

$$E(\left|\widetilde{\uparrow\Downarrow}\right\rangle) = \frac{\sqrt{(\gamma_e B_0)^2 + (\gamma_n B_0)^2 + 4A^2} - A}{2} \tag{2.51}$$

$$E(|\downarrow\Downarrow\rangle) = \frac{\gamma_n B_0 - \gamma_e B_0 + A}{2} \tag{2.52}$$

$$E(\left|\widetilde{\downarrow\Uparrow}\right\rangle) = \frac{-\sqrt{(\gamma_e B_0)^2 + (\gamma_n B_0)^2 + 4A^2} - A}{2} \tag{2.53}$$

2.4.3 High magnetic field approximation

The experiments presented in this thesis all use a magnetic field $B_0 > 1\text{T}$, which permits a simplification. With $\gamma_e B_0 \gg A$, the parameter $\eta \approx 0$. In Figure 2.6(b) we note that

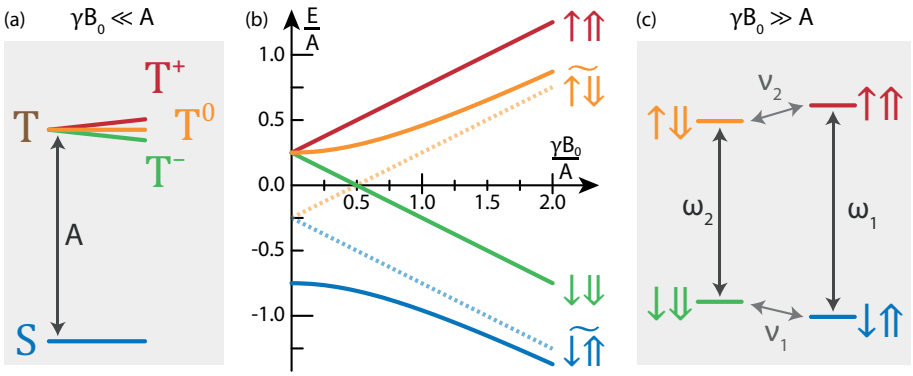

Figure 2.6: Energy spectrum of a donor in a magnetic field. (a) Low magnetic field regime, where the hyperfine coupling, A, produces singlet and triplet eigenstates. Here $\gamma = \gamma_e + \gamma_n$. (b) Evolution of the eigenstates with increasing magnetic field B_0. Here the two antiparallel spin product states are shown as blue and yellow dotted lines. (c) High magnetic field regime, where the Zeeman energy dominates and the product states are a good approximation of the eigenstates. The four resonant transition energies ($\omega_1, \omega_2, \nu_1, \nu_2$) are shown.

the blue and yellow lines approach the linear approximations (dotted lines). Here the eigenstates are well approximated by the product states:

$$|\uparrow\Uparrow\rangle \qquad |\uparrow\Downarrow\rangle \tag{2.54}$$

$$|\downarrow\Downarrow\rangle \qquad |\downarrow\Uparrow\rangle \tag{2.55}$$

With energies:

$$E(|\uparrow\Uparrow\rangle) = \frac{\gamma_e B_0 - \gamma_n B_0 + A}{2} \tag{2.56}$$

$$E(|\uparrow\Downarrow\rangle) = \frac{\gamma_e B_0 + \gamma_n B_0 - A}{2} \tag{2.57}$$

$$E(|\downarrow\Downarrow\rangle) = \frac{-\gamma_e B_0 + \gamma_n B_0 + A}{2} \tag{2.58}$$

$$E(|\downarrow\Uparrow\rangle) = \frac{-\gamma_e B_0 - \gamma_n B_0 - A}{2} \tag{2.59}$$

This high field basis is shown schematically in Figure 2.6(c). The transition frequencies between these four states that conserve one spin while inverting the other are the modified Larmor frequencies for the electron and nuclear spins, which vary by A,

depending on the state of the other spin:

$$\omega_1 = \gamma_e B_0 + \tfrac{A}{2} \qquad \omega_2 = \gamma_e B_0 - \tfrac{A}{2} \tag{2.60}$$

$$\nu_1 = \tfrac{A}{2} + \gamma_n B_0 \qquad \nu_2 = \tfrac{A}{2} - \gamma_n B_0 \tag{2.61}$$

This is the approximation used in the spin resonance experiments of Chapter 5, and is also used in defining the qubit basis states in Chapter 6.

2.4.4 Rabi oscillations in the rotating frame

We consider now the effect of a sinusoidally varying magnetic field of amplitude B_ω in the x-direction, with frequency ω. Such a field contributes a so-called Rabi term to the system Hamiltonian:

$$H_{\text{Rabi}}(t) = \gamma_e B_\omega cos(\omega t) S_X \tag{2.62}$$

The rotating wave approximation* provides a convenient transformation into a reference frame rotating with the spin at the Larmor frequency. For an example we consider the electron Larmor frame provided the nuclear state is $|\Uparrow\rangle$, such that $\omega_{L_e} = \omega_1$. In this frame

$$H_{\text{electron Zeeman}} \rightarrow H'_{\text{electron Zeeman}} = (\omega - \omega_1) S_Z \tag{2.63}$$

$$H_{\text{Rabi}} \rightarrow H'_{\text{Rabi}} = \frac{\gamma_e B_\omega}{2} S_X = \gamma_e B_1 S_X \tag{2.64}$$

where we define $B_1 = B_\omega/2$. The result, which can be applied in a similar fashion to the nuclear spin, is that the time-dependence in H_{Rabi} has been removed, providing a Hamiltonian that is simple to conceptualise. Any offset in frequency away from ω_1 drives z-rotations in the Larmor frame, and the application of an oscillating magnetic field manifests as a static term driving rotations about the x-axis of the relevant spin's Bloch sphere.

* consult your favorite NMR/ESR textbook for a derivation[74,75]

When the B_1 field is applied exactly at any of the four resonant frequencies between a pair of eigenstates, the result is a coherent Rabi oscillation between the two states.

2.5 Summary

In this chapter we have introduced a number of theoretical concepts relevant to the results presented in the chapters following. Most importantly, we established the single electron transport processes used to monitor the behaviour of electrons in low-dimensional nanodevices. We also determined the ground state characteristics of the single donor bound electron, and showed that the spin states may be accurately described in a simplified basis of product states.

3

Experimental techniques

The process to produce donor structures with atomic precision using a scanning tunnelling microscope (STM) is described in the first part of this chapter. We describe the sample preparation process, atomic precision lithography and the method by which electrical contact is made to the nanometre sized features. The chapter concludes with an overview of the cryogenic measurement set-up used to characterise and operate the donor devices.

3.1 Device fabrication

The devices presented in this thesis are made through a novel ultra high vacuum (UHV) process summarised in Figure 3.1. The silicon surface is cleaned and prepared by wet chemical etching (a), followed by a high temperature flash anneal (b) under UHV conditions, and passivation of the surface with a layer of hydrogen (c). Atomic precision structures are patterned by employing the STM as a lithography tool to remove parts

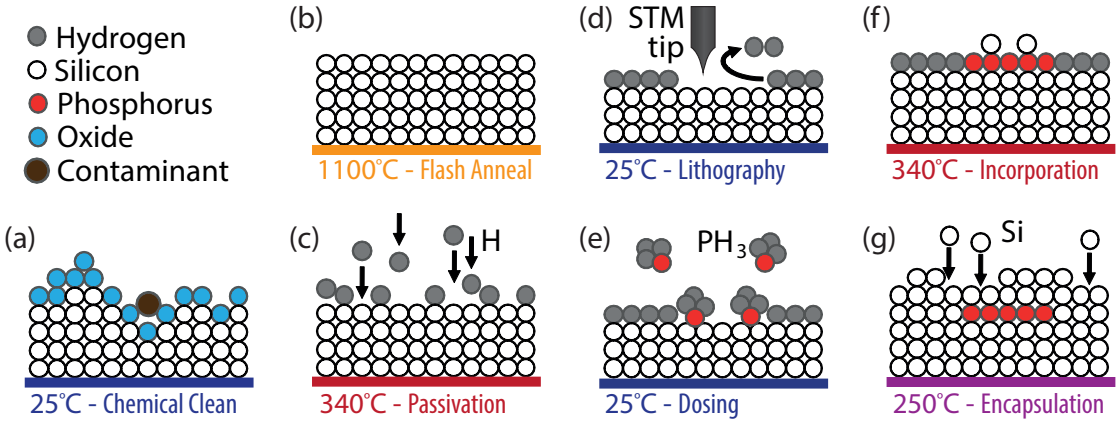

Figure 3.1: Atomic precision donor device fabrication scheme. (a) Silicon wafer is cleaned by a wet chemical process. The surface will be covered in a thin oxide layer, and be largely free of contamination. (b) A high temperature (1100°C) anneal removes residual contamination and the oxide layer, reconstructing an atomically flat surface. (c) The highly reactive silicon surface is passivated by a mono-layer of hydrogen, forming a lithographic mask. (d) The desired pattern is written into the mask by selectively desorbing the hydrogen mask with the tip of the STM. (e) The sample is dosed with phosphine gas, which will adsorb onto the surface within the lithographically defined areas. (f) At an increased temperature (340°C), the phosphine molecule dissociates, leaving the phosphorus atom incorporated into the silicon lattice. (g) The patterned layer is encapsulated by a layer of silicon (typically 50nm thick), embedding the donors in a bulk-like crystal environment.

of the hydrogen mask (d), allowing phosphine gas (PH_3) to adsorb onto the exposed silicon (e). The phosphorus donors are incorporated into the silicon crystal through a thermal anneal (f), and the donor layer is then overgrown with epitaxial silicon (g) before removal from the UHV system. The buried donor structures are then contacted using standard microfabrication techniques: etching vertical vias into the silicon, and depositing aluminium to form a low resistance ohmic contact on the chip surface that may be wire bonded to permit electrical measurements. We now discuss each of the steps in more detail.

3.1.1 Surface preparation

We use Czochralski grown [001] silicon wafers as a substrate*, with a background doping of boron to give a resistivity of $5 - 10\Omega$cm. The wafers are 300μm thick, and we cut each sample to 10×2.5mm to permit loading into the STM sample holder.

Registration markers

We begin the process by fabricating† a set of registration markers into the wafer, following the process developed by Ruess *et al.*[76]. These micrometre scale registration markers survive the high temperature anneal used to reconstruct the surface, which is critical to be able to align our ohmic contacts to the buried donor structures.

The samples are first oxidised, by growing a 50nm thick thermal oxide at 800°C in an oxygen environment, so that the markers can be produced with minimal contamination of the surface during the preparation sequence. We use a standard electron beam lithography‡ (EBL) process to define and develop a PMMA (poly-methyl-methacrylate) mask of the registration marker pattern, which is transferred to the oxide layer by etching in a buffered hydrofluric (BHF) acid bath (15:1 NH_4F:HF, 20%). The exposed silicon areas are etched to a depth of 300nm in a bath of TMAH (tetramethyl-ammonium hydroxide, 25%). The PMMA mask is then removed with acetone, and the thermal oxide with buffered hydroflouric acid (15:1 NH_4F:HF, 20%).

Chemical Cleaning

At this point, the substrate is cleaned in a three step process:

- A sulphuric peroxide mixture (3:1 H_2SO_4:H_2O_2) removes residual organic contamination
- A hydroflouric acid bath (1:10 HF:H_2O) removes any oxide from the surface
- An RCA standard clean 'SC-2' mixture (6:1:1 H_2O:HCl:H_2O_2) removes residual metallic contamination, and produces a thin native oxide layer protecting the wafer from incidental contamination before it is loaded into the UHV environment.

* wafer stock obtained from MMRC Pty. Ltd. † microfabrication was carried out within the Australian National Fabrication Facility's (ANFF) NSW node ‡ FEI/Phillips XL-30 scanning electron microscope

The wafer is rinsed in de-ionised water following each stage of the cleaning process.

Ultra high vacuum degassing and flash anneal

The substrate is loaded into the UHV chamber of the STM*, and the sample and its holder are degassed by heating to around 500°C in vacuum, in order to evaporate residual water and other contaminates. A current of $\sim$ 3A is passed through the sample, rapidly heating it to around 1100°C for one minute. To minimise contamination from secondary heating of the sample holder and apparatus, we divide the total anneal time into 4 windows of (20s,20s,20s,6s). This flash anneal performs two functions: it removes the native oxide layer; and it thermally excites the top layer of atoms, yielding an atomically flat surface with a low defect density when the substrate is slowly cooled to room temperature over several minutes.

Hydrogen passivation

Each silicon atom, with 4 valence electrons is bonded (with sp^3 type orbitals) to 4 neighbours in the bulk lattice, but at the surface, the situation is different. The reconstructed silicon (001) surface is characterised by a 2×1 unit cell. The bond lengths near the surface relax to position pairs of atoms closer together than they are in the bulk, termed 'dimers'. Thus, at the surface each atom is bonded to two atoms below, plus its dimer pair, leaving one free electron per atom, and a highly reactive surface.

We passivate the surface by exposing it to a flux of atomic hydrogen, produced by thermally cracking H_2 gas at 1400°C. We aim to produce a monolayer of hydrogen, with H termination of the dangling bond above every silicon atom. The substrate is heated to around 340°C for 6 minutes while a H pressure of 5×10^{-7}mbar is maintained in the process chamber. This temperature is in the intermediate range avoiding etching of the substrate – which occurs at room temperature[77], and thermal dissociation of H, and thus incomplete coverage – which occurs above $\sim$ 470°C[78].

* A Scientia Omicron variable temperature STM and integrated 'multiprobe' UHV preparation chamber

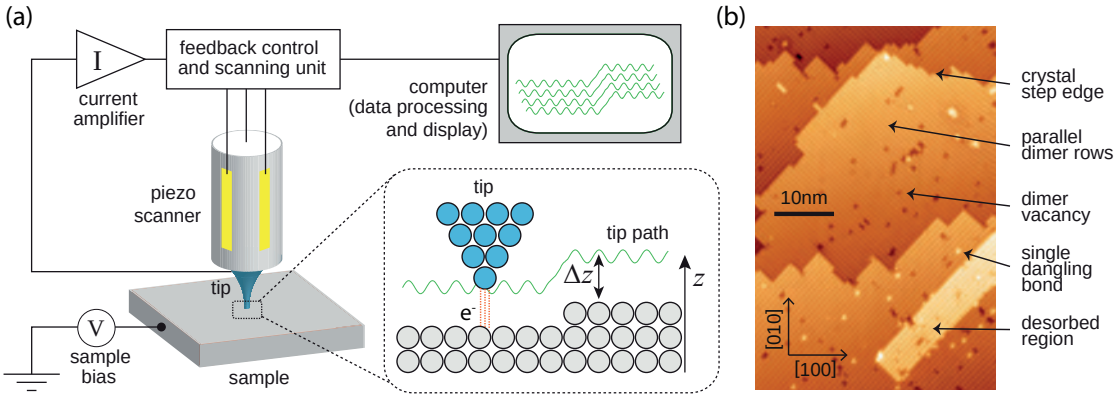

Figure 3.2: Scanning tunnelling microscope imaging and lithography. (a) Schematic showing the operation of an STM. A piezoelectric scanner moves the scanning tip across the surface, while monitoring the tunnel current flowing between sample and tip under an applied bias voltage in order to maintain a constant vertical separation z. Figure adapted from Fuechsle [81]. (b) An exemplary image of a reconstructed and passivated silicon [001] surface, with the brightness proportional to z. Common surface features and defects are shown, which are discussed in the text.

3.1.2 Atomic scale hydrogen lithography

The scanning tuinnelling microscope (STM) is central to our device fabrication strategy. The concept of using an STM as a lithography tool was introduced by Lyo and Avouris [79], and the application of the technique to a hydrogen passivation layer was shown by Lyding *et al.* [77] in the 1990s. O'Brien *et al.* [80] are responsible for complementing the atomic scale lithography process with a gaseous phosphorous deposition method, which we now employ.

The operational principle of an STM is sketched in Figure 3.2(a). A bias voltage V is applied between the sample and the STM tip (a tungsten wire etched to a final radius $\sim$ 5nm), which causes electrons to tunnel through the vacuum potential barrier between the tip and sample surface when the vertical gap Δz is small enough (on the order of pm). The measured current I is used as a feedback signal so that Δz may be kept constant while a piezoelectric scanner moves the tip in the x- and y-directions. The z height of the sample surface is defined by an equipotential surface which reflects not only the physical layout of atoms, but also the extent of the highest energy occupied conduction electron wavefunction at the surface of the substrate (lowest energy unoccupied states can also be imaged by reversing the sample bias).

Mode	bias voltage	tunnel current	spot size	scan speed
Imaging	-2.0V	100pA	-	1μm/s
Lithography				
– tunnelling	$+4.0$V	5nA	< 0.5nm	100nm/s
– field emission	$+8.0$V	30nA	~ 3nm	2μm/s

Table 3.1: Typical STM scanning parameters for filled state imaging, and lithography by the tunnelling mode and the field emission mode

Features on the silicon surface

Scanning the reconstructed and passivated silicon surface produces images such as the example shown in Figure 3.2(b). The image shows an area spanning four successive crystal planes, with edges visible when one plane comes to an end and the tip steps down to the lower plane. The dimers are oriented in parallel rows along the [110] and $[1\bar{1}0]$ crystal axes in alternating crystal planes (visible as clear lines in typical STM images such as Figure 3.2(b)).

The two most common defects[82] in the surface are: a dimer vacancy, where a pair of silicon atoms are absent from the surface layer – which appears as a dark rectangular space; and a single dangling bond, where the hydrogen termination is absent above one single silicon atom – which appears as a bright spot.

Controlled hydrogen removal

Hydrogen atoms are removed selectively by modifying the bias voltage and tunnel current. Exact values used vary for different scanning tips, but typical values are provided in Table 3.1. There are two distinct regimes for lithography: atomic resolution is obtained in a tunnelling mode, where the excess energy from inelastic tunnelling of many electrons removes a H atom by exciting a vibrational mode of the Si-H bond[77,83]; and a field emission mode, where electrons are emitted into the vacuum before striking the surface, each single electron having sufficient energy to free a H atom[84,85].

Figure 3.2(b) shows an example of narrow rectangular region where the hydrogen mask has been removed with tunnelling mode lithography. The area is 7 dimer rows wide, or 14 atoms, a typical scale used to write nanowire leads for source and drain reservoirs.

The bright colour reflects the larger vertical extent of the filled-state wavefunction of the dangling bonds above the bare Si, relative to the smaller wavefunction above a terminating H atom. The tunnelling mode lithography permits the precise placement of just one P donor[52], which we show in the following section is achieved by patterning a 3 dimer patch. The field emission mode is used to pattern long ($> 2\mu$m) nanowires extending away from the nanometre sized features of a device, terminating in large ($> 1\mu m^2$) contact pads. These allow reliable low resistance electrical contact to be made by later aligning external contacts to the patches with the $\sim$ 100nm alignment accuracy afforded by our registration markers.

3.1.3 Dopant incorporation and encapsulation

Following the lithographic patterning, we dose the surface with phosphine (PH_3) gas for 6 minutes at a chamber pressure of 5×10^{-9}mbar. This results in chemical adsorbtion of phosphine onto the exposed silicon surface. Note that the dosing is performed with the sample still on the STM scanning stage, allowing immediate imaging of the dosed surface. Figure 3.3(a) and (b) show an example of a small patch, only 3 dimers in size, before and after phosphine dosing. The phosphine molecules have chemically dissociated, with one H atom filling a dangling bond above a Si atom and the remaining PH_2 fragment bound to the other Si atom within one dimer, as illustrated in the first panel of Figure 3.3(c).

Phosphorus incorporation

The process by which phosphine dissociates on the surface is well documented[78,86,87]. The full chemical reaction requires an elevated temperature to overcome the activation energy, so we heat the sample to around 340°C for 1 minute. There are a number of dissociation reaction pathways[88], the most favourable being that shown in Figure 3.3(c).

- One of the PH_2 fragments recombines with the neighbouring H to desorb from the surface, leaving an un-terminated dimer (I)

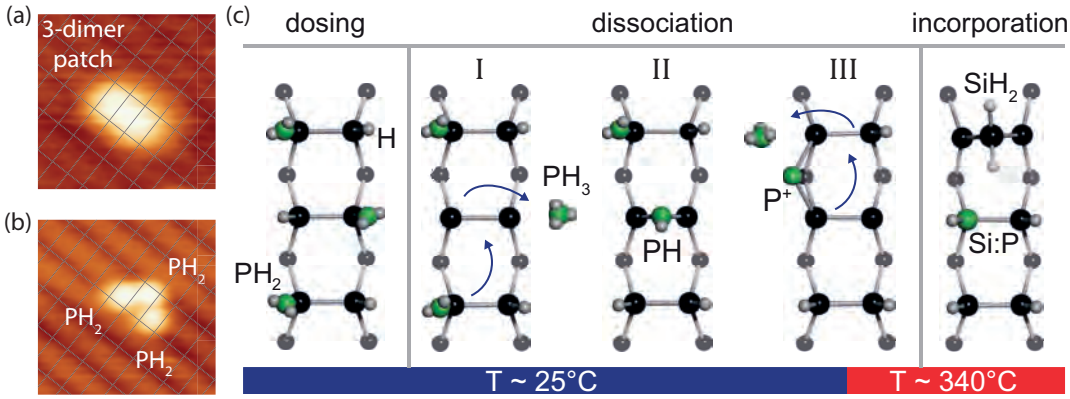

Figure 3.3: Phosphine dissociation and donor incorporation. (a) STM image of a three dimer lithographic patch, with a overlaid grid representing the dimer dimensions. The hydrogen termination has been removed from 6 adjacent Si atoms. (b) STM image of the same area after phosphine dosing. The clear change in appearance is due to the adsobtion of 3 phosphine molecules, which chemically dissociate into surface-bound PH_2 fragments.

- A neighbouring PH_2 further dissociates by transitioning to an interstitial position between Si atoms of the newly free dimer, leaving behind one H atom and resulting in a PH fragment, bonded to a pair of Si within a dimer (II)

- The interstitial PH donates its H to a neighbouring PH_2 fragment, allowing it to desorb, and leaving the P atom bonded across two dimers (III)

- The final step incorporates the P atom into a silicon lattice site, denoted Si:P, ejecting the original Si atom. This transition does not occur at room temperature, necessitating the thermal anneal at 340°C, which also accelerates the previous steps.

As can be seen in Figure 3.3(c), a minimum of 3 adjacent dimers are required for a P donor to fully incorporate. Larger exposed patches allow for a maximum final P density of $\sim 1/4$ of a monolayer, which is understood to be facilitated by additional desorption of H_2 during the incorporation anneal, which facilitates the transition to dissociation product III without loss of a PH_3 molecule.

Epitaxial silicon encapsulation

We activate the donors by growing an encapsulation layer ($25 - 50$nm thick) of silicon. Material is thermally sublimated by passing a current through a solid silicon source filament, growing single crystal silicon at a rate of around 0.15nm/min. During the growth the substrate is heated to ~ 250°C to ensure epitaxial crystal growth[89–91]. Lower temperatures or higher growth rates result in amorphous crystal growth and consequently poor donor activation and lower electron mobility within the δ-layer. Higher temperatures also produce a poor quality δ-layer, as the P donors become prone to segregation, moving with the surface as the silicon is grown.

The fabrication routine we have outlined produces metallic conduction within the patterned regions where the donor density is $\sim 2 \times 10^{14}\text{cm}^{-2}$. In a highly epitaxial bulk-like crystal, the donors are fully activated[91], producing an electrical carrier density $n_s \sim 2 \times 10^{14}\text{cm}^{-2}$, and a sheet resistivity of around $0.2\text{k}\Omega/^2$.

3.1.4 Microfabrication of electrical contacts

After removing a donor device from the UHV system, we use electron beam lithography (EBL), reactive ion etching (RIE) and physical vapour deposition (PVD) to produce electrical contacts, aligned to the buried donor patches with reference to the original registration markers[92].

- We use a PMMA mask and EBL to define a series of small ($\sim$ 200nm diameter) holes aligned to the $\sim 1\mu\text{m}^2$ phosphorus patches. Figure 3.4(a) shows an image of such a mask – the small holes are visible within the red circle.
- The holes are etched $\sim$ 70nm into the silicon by RIE etching* in a fluorine based gas mixture (1:2 SF_6:CHF_3) at a pressure of 5mTorr with a plasma power of 100W. This process etches silicon at a rate of 1nm/s.
- The first mask is removed, a second PMMA mask applied, and another round of EBL defines a pattern of surface contact wires, which taper from the scale of the

* Oxford instruments Plasmalab-100

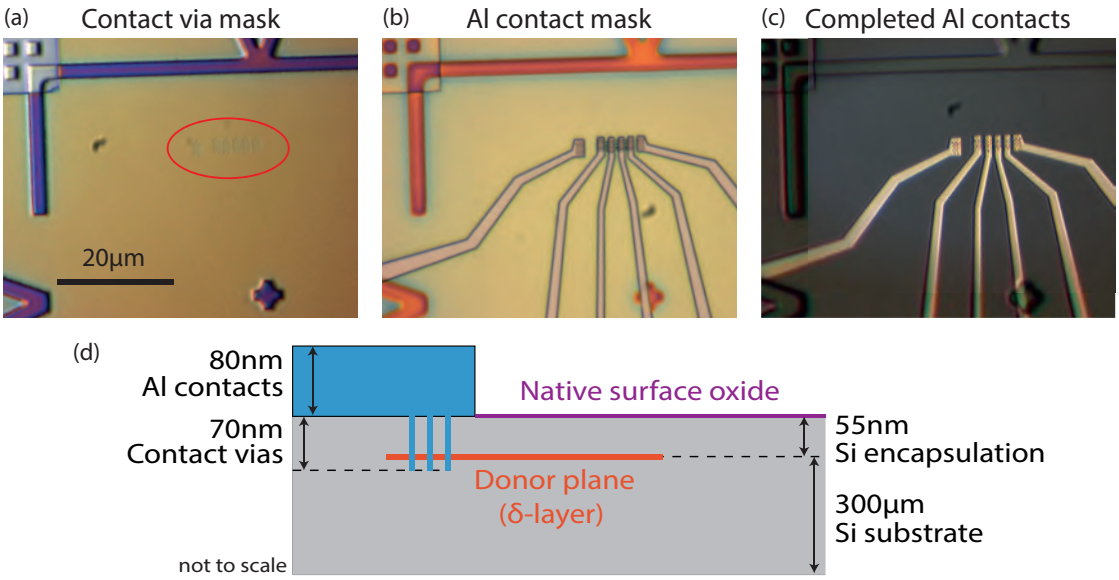

Figure 3.4: Making electrical contact to buried donor structures. (a) Optical image showing the developed PMMA mask before RIE etching of the vertical contact via holes (circled). Registration markers are visible around the image edges. (b) Optical image showing the developed PMMA mask before evaporation of the aluminium (Al) electrical contacts. (c) Optical image displaying the completed electrical contacts on the silicon surface, aligned to vertically etched via holes. The wires extend beyond the lower edge of the the image to $\sim$ 200μm sized bond pads. (d) Vertical cross-section of the contacting scheme, showing dimensions above and below the buried donor δ-layer. Low resistance contact is achieved by chemically removing the native oxide layer before the aluminium is deposited.

donor patches and vertical holes up to $\sim 200\mu$m, which is suitable for wire-bonding into the sample carrier for our electrical measurements. Figure 3.4(b) shows an image of such a mask.

- The exposed silicon surface is cleaned within an oxygen plasma (340mTorr, 50W for 2 minutes) to remove residual PMMA from the etched holes.

- The native surface oxide (which formes naturally on the silicon over around an hour in ambient conditions) is removed by etching in buffered hydrofluoric acid (15:1 NH_4F:HF, 20%) for 15 seconds.

- 80nm of aluminium is evaporated onto the exposed surface at a rate of 0.1nm/m in an electron beam PVD evaporator*

* Kurt Lesker PVD75

- The bulk of the metal is lifted off by soaking in N-methyl-2-pyrrolidone (NMP) for up to 1 hour to dissolve the underlying PMMA, leaving the structure as shown in Figure 3.4(c) – where bright areas are the aluminium metal contacts.

A schematic of the vertical structure at the end of this process is shown in Figure 3.4(d). The contact resistance achieved by this scheme is $< 100\text{k}\Omega$.

We have outlined the full fabrication process used to manufacture the donor devices we present in the following chapters. The next section briefly outlines the measurement techniques we employ.

3.2 Cryogenic Measurements

The various measurements throughout Chapters 4 and 5 were undertaken on a number of different dilution refrigerators with varied instrumentation, so we aim here to give a general sense of the measurement techniques we employ, and specific details relating to the individual experiments may be found in the appedices.

Initial measurements of a device are performed at a temperature of 4K in a liquid helium bath. The confinement within our donor structures (with quantum dots on the order of 1000nm^2 or smaller) is sufficient that the single electron transport regime is achieved at this temperature. This allows us to perform simple DC measurements of the charge stability conditions similar to the diagrams in Figure 2.5. Spin physics cannot be resolved however, since the electron Zeeman energy $\gamma_e B_0$ is less than $k_B T$ for magnetic fields B_0 even up to several Tesla. Thus we perform the bulk of our experiments in a dilution refrigerator*, which achieves a typical base temperature of $< 50\text{mK}$, and which is fitted with a superconducting magnet to provide the external magnetic field B_0.

Low pass filtering for noise reduction

In silicon, with its small spin orbit coupling, noise in the voltage applied to the gates and electron reservoirs within a device does not directly effect the spin states. It does however

* Oxford instruments Kelvinox-100 or Leiden cryogenics CF-500

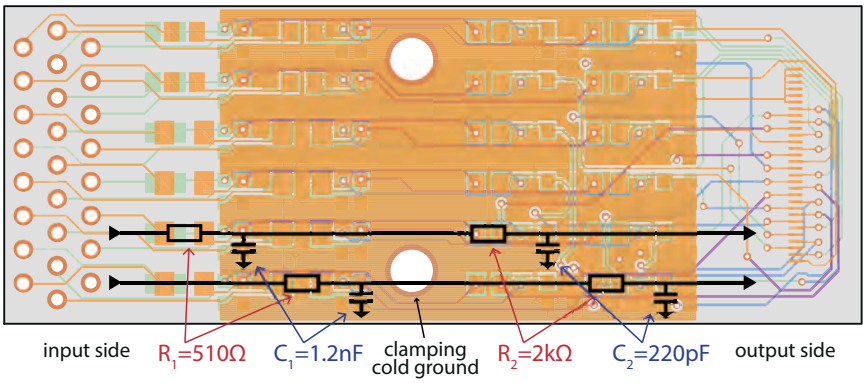

Figure 3.5: **Noise filtering for bias voltage lines.** Layout of the custom printed circuit board containing 24 individual signal lines with two stage RC low pass filters. The first and second stages are separated by a feed-through zone where all lines are electrically shielded between top and bottom ground planes. Colours represent the four conductor layers in order from top to bottom: orange, purple, blue, green.

degrade the measurement by broadening resonant tunnelling features. Therefore, in order to reduce voltage noise in our measurements, we pass all DC and pulse signals through a two stage RC filter. The resistors and capacitors are surface mounted lumped element components with values as indicated in Figure 3.5, and a low-pass cut-off of 150kHz.

Figure 3.5 shows the custom circuit board consisting of four signal layers (coloured orange, purple, blue and green from top to bottom). Between the two RC stages, all 24 signal wires are fed through the two internal layers, shielded by conducting ground planes in the top and bottom layers. This is done to enhance the high frequency filtering, by preventing radiated EM fields from transmitting high frequency noise through free space around the filter components, with the aim of producing an electrically quiet environment on the output side. The filters sit in a brass housing mounted in the wall of an effective Faraday cage that surrounds the device, and two large holes allow the board to be clamped in the centre, providing a low resistance, high thermal conductivity connection to the mixing chamber of the dilution refridgerator.

Wiring from room temperature to the filters is through twisted wire pairs. We keep one wire of each pair grounded, which effectively sheilds the other, minimising cross-talk between lines.

Control software

To control the various instruments we use a python environment based on the open-source 'QT-Lab' framework*. A range of routines were developed to facilitate the generation of time dependent voltage pulses and modulated resonant microwave signals and also for realtime acquisition of current signals.

Signal generation

DC voltage signals are generated by a voltage source and typically are divided by a factor between 5 and 50 with a simple resistive voltage divider at room temperature. This also allows the use of the full dynamic range of a source (typically 10V) whilst the required voltages for our in-plane gates are on the order of 100mV.

Pulsed gate signals are produced by an arbitrary waveform generator (refer to appendices for specific models used in each of the experiments) or high speed digital to analog converter. These signals are typically added to a DC voltage with a passive resistive adder at room temperature, and since we do not pulse at rates above $\sim$ 1kHz these signals are applied to the sample via the DC twisted pair lines, filtered to $\sim$ 150kHz as discussed above.

The radio frequency signals of Chapter 4 are produced with an AC signal generator and the reflectometry circuit described in that chapter. The AC signal is fed to the device by high frequency semi-rigid copper-nickel coaxial cable, attenuated at each thermal stage to dissipate heat and the associated thermal Johnson-Nyquist noise. The AC signal is finally added to a DC bias with an RC bias tee on a custom PCB at the mixing chamber stage before it reaches the device.

The microwave frequency signals of Chapter 5 are produced by a vector signal generator, which internally modulates the AC signal with modulation patterns we generate with an arbitrary waveform generator. The resulting signal is fed into the dilution refrigerator also through semi-rigid coaxial lines. Here we use a highly dissipative stainless steel cable in place of discrete attenuators at every thermal stage.

* developed at Delft University (available on Github)

Signal capture

The output signal that we measure is a current on the order of 100pA. We use a transimpedance amplifier* at room temperature to transform the current into a high impedance voltage signal. This typically introduces additional high frequency noise which we suppress with an active analog electronic Bessel filter† after electrically decoupling the signal line from the dilution refridgerator's cold ground reference with an isolating unity gain voltage amplifier‡. The amplified signal is then digitised for analysis.

3.3 Summary

In this chapter we have introduced the core experimental methods through which our precision donor devices are fabricated and measured, providing a basis for understanding the spcific details of each device and each experiment in Chapter 4 and Chapter 5.

* Femto DLPCA-200 † SRS SIM965 ‡ SRS SIM910

4

Single electron charge sensing by radio frequency reflectometry

One of the major challenges in scaling up to large arrays of addressable qubits is integrating enough readout sensors to monitor each donor based qubit, since physical space is limited by the close proximity of qubits required to enable two-qubit interactions. For donor qubits coupled using the exchange interaction, the separation may be as small as 10–20 nm, yet the highest fidelity readout sensor used to date, the single electron transistor (SET), requires significantly more real estate[55].

Spin readout relies on a spin to charge conversion process followed by charge state readout, and it is therefore the determination of the charge states that is the fundamental measurement required for most donor based quantum information processors. A typical planar, donor-defined SET is shown in Figure 4.1(a). The current flow through the SET is sensitive to the local potential landscape, so that the motion of a single electron on or off a nearby donor may switch the flow of current on or off. This can be seen in (b), where discontinuities run through the parallel conductance lines at two distinct angles, representing a change in the charge state of either of the two donors present in this device.

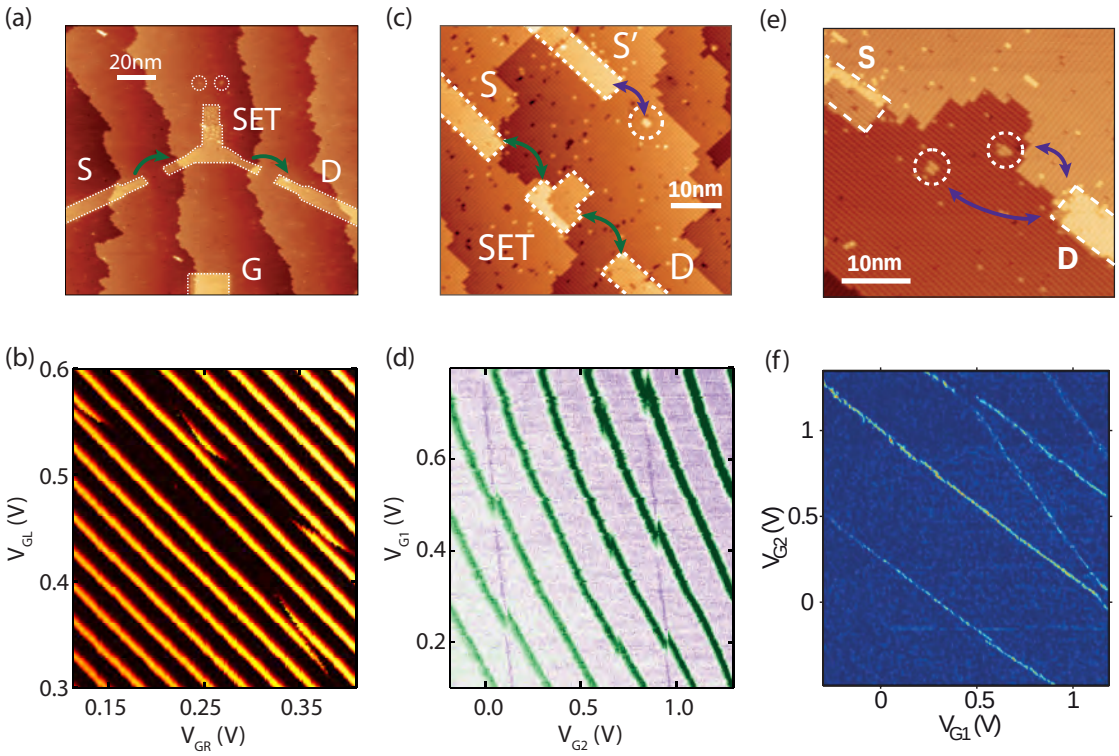

Figure 4.1: Charge sensors in planar donor devices. (a,c,e) STM images and (b,d,f) corresponding charge stability diagrams for three different charge sensing devices. (a) A typical SET charge sensor, capable of monitoring the charge state of a double quantum dot. The presence or absence of an electron on either small dot is sensed by the SET. An SET gate (G) is required to provide independent control of the SET potential, and so the entire structure fills over 120° of the radial space surrounding the donors. Current flow from source (S) to drain (D), as indicated with green arrows, may be switched on or off by a change in charge state, producing discontinuities in (b) the SET current as a function of gate voltages. Diagonal lines of high conductance represent the periodic switching of the SET due to Coulomb blockade, and discontinuities with two different slopes provide an indirect indication of charge state reconfigurations on each of the two donor dots. (c) A hybrid charge sensing device incorporating an SET alongside a reservoir (S') tunnel coupled to a single donor. We investigate multiple radio frequency charge sensing mechanisms in this device: AC tunnelling through the SET from source to drain as represented by green arrows, which produces (d) lines of conductance comparable to those in (b); but also AC tunnelling from S' to the single donor, as shown by the purple arrow, which produces clear lines directly showing the donor charge state transitions. (e) A double quantum dot device without an SET, where we show that charge sensing is still possible by monitoring the AC tunnelling from one reservoir (D) to each of the dots, as shown by the purple arrows. (f) The charge stability map clearly indicates the charge state transitions of each dot as lines with two distinct slopes. The absence of an SET simplifies the appearance of the stability diagram significantly.

In this chapter we shall describe two experiments that move beyond measuring the flow of current through an SET, to consider the reflection of radio frequency signals from nanoscale structures using a single terminal sensor. This strategy permits a much more efficient use of chip real estate as the single terminal charge sensor can be more readily scaled in contrast to a three terminal SET which consumes $\sim 120^{\circ}$ of the radial space surrounding the donors being sensed.

In the first experiment, we compare the visibility of the charge transitions of a deterministically placed single P donor, as seen in a reflected RF voltage signal and in a transmitted DC current. The device we use is summarised in Figure 4.1(c). The RF reflectometry measurements are performed using an electron reservoir (S') tunnel coupled to the donor, and concurrently, with a capacitively coupled single electron transistor (SET). The RF measurement allows direct observation of charge state transitions of the donor (continuous parallel purple lines in Figure 4.1(d)), in contrast to a more traditional SET current signal as in Figure 4.1(b) where the equivalent donor transitions are only observed indirectly by offsets in the parallel SET conductance lines. We show that the electrostatic coupling of our tunnel coupled reservoir is over 5 times greater than that typical for a capacitively coupled gate. We also extract a neutral phosphorus donor charging energy of 62 ± 17meV, consistent with previous measurements[53,69].

In the second experiment, we apply reflectometry techniques to a double quantum dot formed by two nearby donor clusters, consisting of 2 and 3 P donors respectively, shown in Figure 4.1(e) Without an additional charge sensor, in this device DC measurements allow observation of the donor state by monitoring electron transport through the two dots. As an alternative, we demonstrate charge sensing in this device via RF reflectometry. Figure 4.1(f) shows the clear charge stability diagram of the quantum dot charge states, obtained from the reflected RF signal, without the complication of numerous additional SET conductance lines. Using RF reflectometry we measure electron tunnel rates between the reservoir and donors, observing values from 100MHz to 22GHz as the number of electrons on one of the quantum dots is increased from 1 to 4. This technique also allows us to observe Pauli spin blockade, showing that single shot singlet-triplet measurement is possible using a single terminal sensor. By detuning the double quantum dot we demonstrate tunability of the exchange energy over 2 orders of magnitude, an important milestone in controlling the interactions between electrons in these precision donor systems.

Together, the work in this chapter shows that RF reflectometry, and in particular, single terminal dispersive sensing, is a powerful strategy, providing an alternative to DC charge sensor conductance based readout. We compare the strengths and weaknesses of both methods, but highlight the demonstrably smaller physical footprint possible with the RF technique. These results show that we can replace three terminal transistors by a single terminal dispersive reservoir, which plays the role of both control gate and sensor, promising for scalable donor qubit control and readout.

4.1 Radio frequency measurements in nanoscale devices

In this background section we introduce the motivation behind the development of high frequency charge detection techniques. We then present a theoretical overview of the AC electronics involved in the experiments that follow and describe the mechanisms at play in the context of a brief review of recent literature on RF charge detection in nanoelectronic devices.

4.1.1 The limitations of DC charge sensing

Measurement of single electron spin states has to date largely relied on spin to charge conversion followed by charge state readout through either a charge-sensing single electron transistor (SET) or quantum point contact (QPC). A QPC is a field effect device consisting of a buried two-dimensional electron gas (2DEG), locally constricted by electrostatic gates to form a short one dimensional constriction, producing a quantised set of transverse energy levels through which electrons may ballistically pass through the point contact. An example is shown in Figure 4.2(a). By tuning gate voltages to a point where an additional channel starts to become available, the conductance G of the QPC

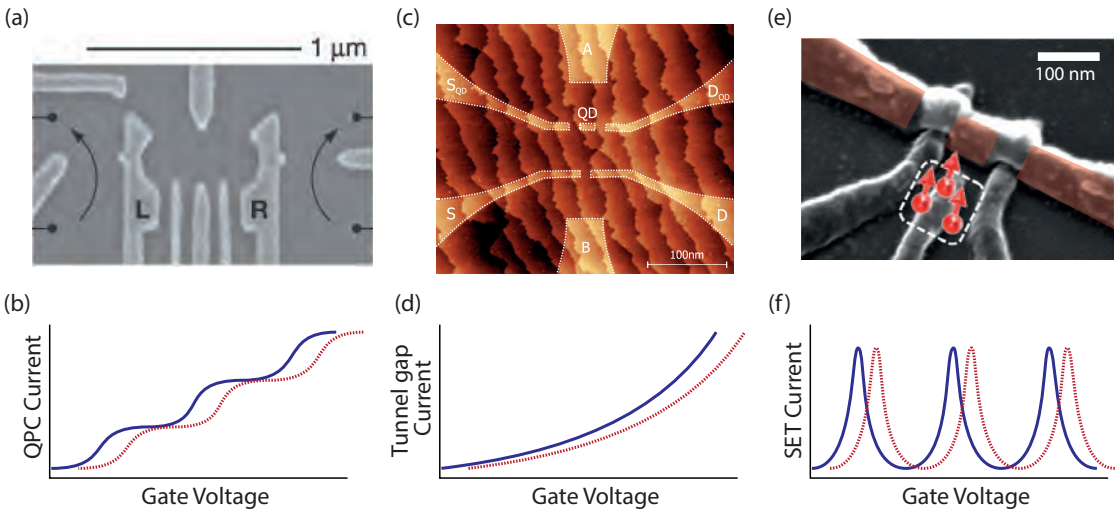

Figure 4.2: **DC charge sensing strategies.** (a,c,e) Images and (b,d,f) corresponding charge sensitivity diagrams for classes types of charge sensing devices. (a) A GaAs quantum point contact (QPC) formed by depleting a buried 2DEG with voltages on surface gates to form a 1D conductance channel. Two QPCs are shown left and right. Reproduced from Johnson *et al.* [93] (b) Conductance steps characteristic of a QPC. Increasing gate voltage lowers the energy of successive conductance channels, increasing the current flow. A change in the charge state of a nearby quantum dot is equivalent to a discrete change in gate voltage, effectively offsetting the conductance curve. (c) A planar, donor defined tunnel gap (lower half) and SET (upper half) in silicon, produced by STM lithography. Reproduced from House *et al.* [9]. (d) The conductance response of a simple tunnel gap. Increasing gate voltage gradually lowers the resistance, and similarly, a charge offset is equivalent to a discrete gate voltage shift. (e) A MOSFET-based single electron transistor (SET) formed by accumulating electrons in the silicon substrate beneath an oxide layer below the gate shaded red. Reproduced from Morello *et al.* [94] (f) Conductance peaks occur periodically as the gate voltage is increased as charge states of the SET island itself come into resonance with the source and drain. A charge state change external to the SET offsets the positions of all peaks.

becomes sensitive to the local electrostatic environment. As sketched in Figure 4.2(b), a discrete change in the charge state of a nearby quantum dot (switching the response between the blue and red lines) changes the current through the QPC.

A similar outcome can be achieved with a simple tunnel gap between two leads, where electrons tunnel through a barrier instead of travelling ballistically through a 1D mode. This type of device is shown (together with an SET) in the lower half of Figure 4.2(c) Here the electrostatic environment affects the barrier height, which in turn changes the transmitted tunnel gap current at a particular bias. Typically a tunnel gap type sensor provides a slowly varying and continuous signal across a range of gate voltages (red curve in Figure 4.2(d)), with discontinuities in this smooth background at fixed charge

degeneracy points where an electron tunnels nearby (switching the response to the blue curve).

The SET sensor consists of a quantum dot (QD) exhibiting Coulomb blockade (introduced in Section 2.3.1). SET devices based on electrostatically confined 2DEGs or those defined by regions of phosphorus donors behave in much the same way. Examples are shown in Figure 4.2(c,e). Here the current flow is a periodic function of the quantum dot potential, effectively zero for most configurations of the electrostatic environment while the SET is in Coulomb blockade, and taking a finite value when the gate voltages align a quantum dot transition potential to the lead Fermi levels (red curve in Figure 4.2(f)). Nearby charges capacitively, or through direct tunnel coupling, interact with the quantum dot. This shifts its electrochemical potential, often by a fraction of the SET's charging energy (blue curve), and capable of discretely switching the conductance from an on-resonance value to the blockade value.

Physical sensor size

All three of these charge sensor devices take up considerable space on a chip compared to the small size of a donor qubit. Two current carrying ohmic contacts are needed: a source and a drain, and often also a third gate terminal to be able to tune the sensor to a sensitive working point. This is not a problem in devices containing one or two qubits, but for more complex arrays of multiple qubits, the space surrounding each will be largely needed to accommodate interactions involving neighbouring qubits. Because donor qubits are atomic in size, a more compact sensor is desirable in scaling up towards a large-scale Si:P quantum computer.

Simply miniaturising the SET (for example) is not viable, since with decreasing quantum dot (or SET island) area, the charging energy increases, meaning that the peaks of Figure 4.2(f) become spaced more widely and consequently the sensor can only be sensitive at very few specific voltage settings. As an example, the SET in Figure 4.2(c) has dimensions of 17.2×8.5nm such that the separation between adjacent Coulomb peaks is ~ 80mV. A smaller SET island will only increase the peak separation, meaning that the sensor is 'blind' across a high proportion of all voltage settings.

The size of any 2 or 3 terminal sensor is additionally constrained in terms of the angular spread of its source and drain leads, because the two leads cannot be parallel

to one another at small distances, as this would allow a parasitic conduction pathway between the two leads that would be insensitive to charges within the device.

Noise and bandwidth

A major source of noise at low frequencies in many solid state electronic systems, is generally considered to be due to a background of two-level charge fluctuators. Increasing with the inverse of frequency, this effect is referred to as $1/f$ noise. DC charge measurements face the challenge of significant $1/f$ noise which can only be overcome by integrating over an extended time period such that the noise averages to zero. This averaging reduces the measurement bandwidth, limiting the time resolution of the sensor.

The measurement bandwidth is also limited by the fact that all the DC sensors detailed above measure the flow of current through a resistive circuit. The two tunnel barriers of an SET for instance must be on the order of $100k\Omega$ or greater to avoid lifetime broadening of the Coulomb peaks (where the uncertainty principle spreads the width of a Coulomb peak in inverse proportion to the average lifetime of an electron flowing through the SET island). This resistance together with the typical capacitive load of wiring between the SET at millikelvin and a room temperature current amplifier in an experiment (normally greater than 1nF), limits the bandwidth for DC operation of the SET, with an RC time constant of a few kHz (higher if the line capacitance can be reduced).

For improved sensor performance we therefore seek a method to reduce sensor resistance or wiring capacitance, operate at higher frequency, and with a smaller physical footprint. In this chapter we show that radio frequency reflectometry provides a route to improve in all of these areas. Underlying radio frequency reflectometry is the same fundamental idea used in laser interferometry, or in a lock-in amplifier. An AC signal is applied to a system, the signal is reflected with an altered amplitude and phase. Measuring the reflection alone provides limited information but by interfering the reflected signal with a copy of the original input in a so-called homodyne detection process, a complex valued reflection coefficient can be recovered. This homodyne signal can be engineered to sensitively respond to, in our case, changes in the charge state of the electronic system being measured. Before detailing the implementation in our precision donor devices, we present some theoretical background and a review of achievements in the literature.

4.1.2 Theory of LCR resonant circuits

An AC voltage signal $V_{in}(t) = V_1 \sin(\omega t + \theta_1)$ drives an AC current response $I(t)$ within a circuit, which manifests as a complex impedance Z to the incoming signal, related by Ohm's law $V_{in}(t) = I(t)Z$. The incoming signal is accordingly reflected by the system $V_{out} = V_2 \sin(wt + \theta_2) = V_{in}\frac{Z-Z_0}{Z+Z_0}$. Here Z_0 is the impedance of the transmission line used to deliver the signal to the system. If V_{out} is demodulated with a copy of the original AC signal in a frequency mixer, the output encodes the complex reflection coefficient $\Gamma = \frac{Z-Z_0}{Z+Z_0}$.

In order to gain full information of the complex response, two mixers are used in a combination called an IQ demodulator. The second mixer introduces a 90° phase offset before combining the signals. The first produces an output consisting of

$$V_I = V_1 V_2 \sin(\omega t + \theta_1)\sin(\omega t + \theta_2) \tag{4.1}$$
$$= \frac{V_1 V_2}{2}\cos\left((\omega t + \theta_1) - (\omega t + \theta_2)\right) - \frac{V_1 V_2}{2}\cos\left((\omega t + \theta_1) + (\omega t + \theta_2)\right) \tag{4.2}$$
$$= \frac{V_1 V_2}{2}\cos\left(\theta_1 - \theta_2\right) \tag{4.3}$$

where we have removed the high frequency component, since this is normally filtered out with a simple low pass filter. The phase shifted mixer on the other hand produces

$$V_Q = V_1 V_2 \cos(\omega t + \theta_1)\sin(\omega t + \theta_2) \tag{4.4}$$
$$= \frac{V_1 V_2}{2}\sin\left((\omega t + \theta_1) - (\omega t + \theta_2)\right) + \frac{V_1 V_2}{2}\sin\left((\omega t + \theta_1) + (\omega t + \theta_2)\right) \tag{4.5}$$
$$= \frac{V_1 V_2}{2}\sin\left(\theta_1 - \theta_2\right) \tag{4.6}$$

These two DC voltage signals V_I and V_Q represent the in-phase (real) and quadrature (imaginary) components of the complex reflection coefficient. These are often recast to

represent the amplitude $|\Gamma|$ and phase angle $\phi(\Gamma)$

$$\sqrt{V_Q^2 + V_I^2} = \frac{V_1 V_2}{\sqrt{2}} = \frac{{V_1}^2}{\sqrt{2}}|\Gamma| \tag{4.7}$$

$$\sim |\Gamma| \tag{4.8}$$

$$\tag{4.9}$$

$$\arctan(V_Q/V_I) = \arctan(\frac{\sin(\theta_1 - \theta_2)}{\cos(\theta_1 - \theta_2)}) = \delta\theta \tag{4.10}$$

$$\sim \phi(\Gamma) \tag{4.11}$$

4.1.3 Frequency dependant impedance in a resonant circuit

We now consider the effect of changing the resistance and capacitance within a simple resonant RLC circuit before moving on to discuss the underlying physical mechanisms that modify the resistance and capacitance of a nanoelectronic device.

The system of interest is embedded within a resonant LCR tank circuit. Consider first the impedance of a simple series circuit containing inductor L, capacitor C, and resistor R, as indicated in Figure 4.3(a).

$$Z = Z_L + Z_C + Z_R \tag{4.12}$$

$$= i\omega L + \frac{1}{-i\omega C} + R \tag{4.13}$$

In the simplest sense, with increasing drive frequency ω, the positive imaginary inductive impedance Z_L grows larger and negative imaginary capacitive impedance Z_C grows smaller. the resistive impedance Z_R is real and independent of frequency. These three components are sketched in Figure 4.3(c) on the complex plane. The total, $Z = Z_{LCR}$ follows a vertical trajectory as indicated by the grey line, moving up the page with increasing frequency, and crossing the real axis at the resonant frequency $\omega_0 = \frac{1}{\sqrt{LC}}$

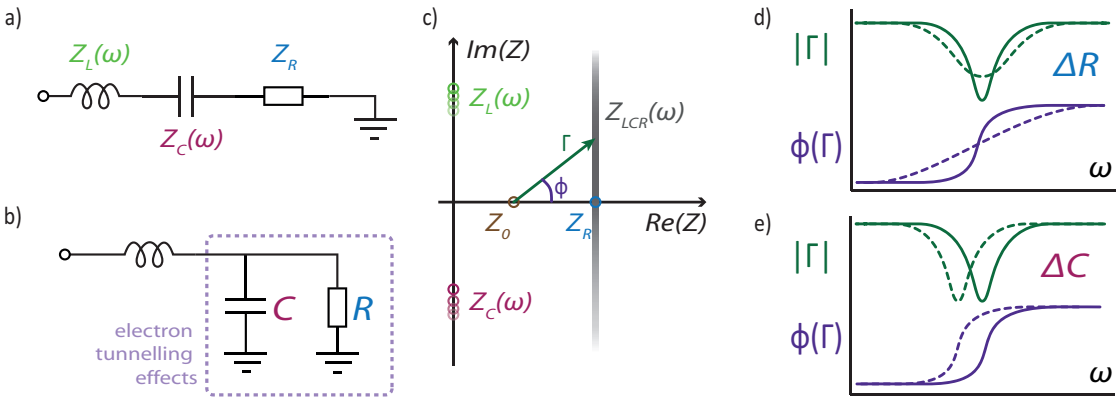

Figure 4.3: LCR resonant circuits as a sensor. (a) A simple series LCR circuit. (b) Idealised circuit model used in this chapter's measurements. The device is represented by the parallel resistance and capacitance, in series with a lumped element inductor. (c) impedance diagram on the complex half-plane. The sum of resistive, capacitive, and inductive impedances Z_{LCR} traverses a vertical locus as the drive frequency is increased. The reflection coefficient Γ depends reflects both the length and angle of a vector connecting Z_0 and Z_{LCR}. (d) Green and purple lines represent the magnitude and phase respectively of the reflection coefficient Γ as a function of drive frequency ω. A resonance occurs at ω_0 where the total impedance crosses the real axis, witha minimum in $|\Gamma|$ and an inflexion point in $\phi(\Gamma)$. The effect on the resonance curve is sketched for an increase in device resistance, the dashed line indicating a damping of the resonance. (e) Similar plot, but showing the effect of an increased device capacitance, shifting the resonant condition to a lower frequency.

where Z_{LCR} comes nearest to the (resistive only) $Z_0 = 50\Omega$. In measuring the amplitude and phase of the reflection coefficient, we observe the length and angle of the vector indicated with a green arrow in Figure 4.3(c), producing a pair of resonance curves as sketched in Figure 4.3(d,e). The width of the observed peak in $|\Gamma|$ is characterised by the dimensionless quality factor $Q = \frac{1}{R}\sqrt{\frac{L}{C}}$, with a lower resistance producing a higher Q and a sharper peak.

The real response of a nanoelectronic device is more accurately described by a different idealised circuit model shown in Figure 4.3(b) where electron tunnelling effects are described by a resistance and capacitance in parallel. The total impedance for this

circuit topology can be similarly determined.

$$Z = \frac{1}{\frac{1}{Z_R} + \frac{1}{Z_C}} + Z_L \tag{4.14}$$
$$= \frac{1}{\frac{1}{R} - i\omega C} + i\omega L \tag{4.15}$$
$$= \frac{R}{1 - i\omega CR} + i\omega L \tag{4.16}$$
$$= \frac{R + i\omega CR^2}{1 - i^2\omega^2 C^2 R^2} + i\omega L \tag{4.17}$$

From here we make two approximations which simplify the representation: $\omega CR \gg 1$, satisfied by our experimental parameters (since $\omega \sim 200\text{MHz}, C \sim 1\text{pF}, R \sim 20\text{M}\Omega$); and $\omega \simeq \omega_0$ since we are primarily concerned with behaviour near resonance.

$$Z = \frac{R + i\omega CR^2}{\omega^2 C^2 R^2} + i\omega L \tag{4.18}$$
$$= \frac{1}{\omega^2 C^2 R} + i\frac{1}{\omega C} + i\omega L \tag{4.19}$$
$$= \frac{L}{CR} + \frac{1}{-i\omega C} + i\omega L \tag{4.20}$$

Equation (4.20) is the same expression for the series circuit (Equation (4.13)), except that the resistive component is now given by an effective resistance $R_{\text{eff}} = \frac{L}{CR}$.

In summary, the response of the reflected RF signal is sensitive to a changes in both the resistance and capacitance of the device we are interested in sensing. We now consider three different ways in which such changes may arise, with reference to specific RF sensing devices in the literature.

4.1.4 Charge sensing based on RF signals

Here we review the state of the art in charge detection methods based on RF reflectometry signals. We discuss two classes of devices with increasing popularity in the nanoelectronic device community: the RF-SET (radio frequency single electron transis-

tor) and the dispersive gate sensor, as well as a third alternative with specific relevance to our atomic precision fabrication strategy – a dispersive tunnel-coupled reservoir.

The RF-SET sensor

The effect of a change in the system resistance is to narrow or broaden the resonance peak. In practice, rather than monitor the peak width by sweeping the drive frequency, typically the reflection coefficient is measured at a fixed frequency, most often on-resonance, and the increased or reduced reflection amplitude is interpreted as arising from a changed resistance within the system being sensed. The most common origin of a variable resistance is non-resonant tunnelling through an SET channel, and this dissipative process is the basis for the operation of an RF-SET.

The RF-SET was first introduced by Schoelkopf *et al.*[95], as a method to increase the real-time bandwidth of the SET as a charge sensor. The SET is inherently a high resistance device ($> \mathrm{M}\Omega$), and with wiring capacitance typically on the order of nF, the resultant RC time constant restricts measurement bandwidth of the DC-SET to a few kHz. This is not an intrinsic limitation of the SET itself, but of the DC measurement circuit normally used to amplify the current. By operating instead at an RF frequency with a resonant circuit, the wiring capacitance becomes unimportant, and therefore the RF-SET allows higher bandwidth measurements. The increased bandwidth was demonstrated in an aluminium SET shown in Figure 4.4(a), where standard double angle evaporation was employed to produce the tunnel junctions between source, island and drain.

The source-drain bias of the SET oscillates under an RF excitation applied to the drain. Therefore, relative to the potential of the SET island, an electron will tunnel onto the SET at a higher potential and tunnel off at a lower potential, dissipating the energy difference. Hence AC tunnelling manifests as an increased conductance, or a reduced resistive impedance R. With the circuit topology of Figure 4.3(b), R_{eff} is increased and this damps the resonance (as was illustrated in Figure 4.3(d)). The behaviour is seen in Figure 4.4(b), where dips in the reflected signal amplitude (rf power) correspond to coulomb peaks in a DC conductance measurement. Schoelkopf *et al.*[95] showed that the response was sensitive to single electron motion at a bandwidth of $\sim 100\mathrm{MHz}$.

The RF-SET has been implemented in metallic QDs[97], GaAs heterostructure QDs[98], silicon MOSFET QDs[99]. An additional benefit of the RF-SET was recently highlighted

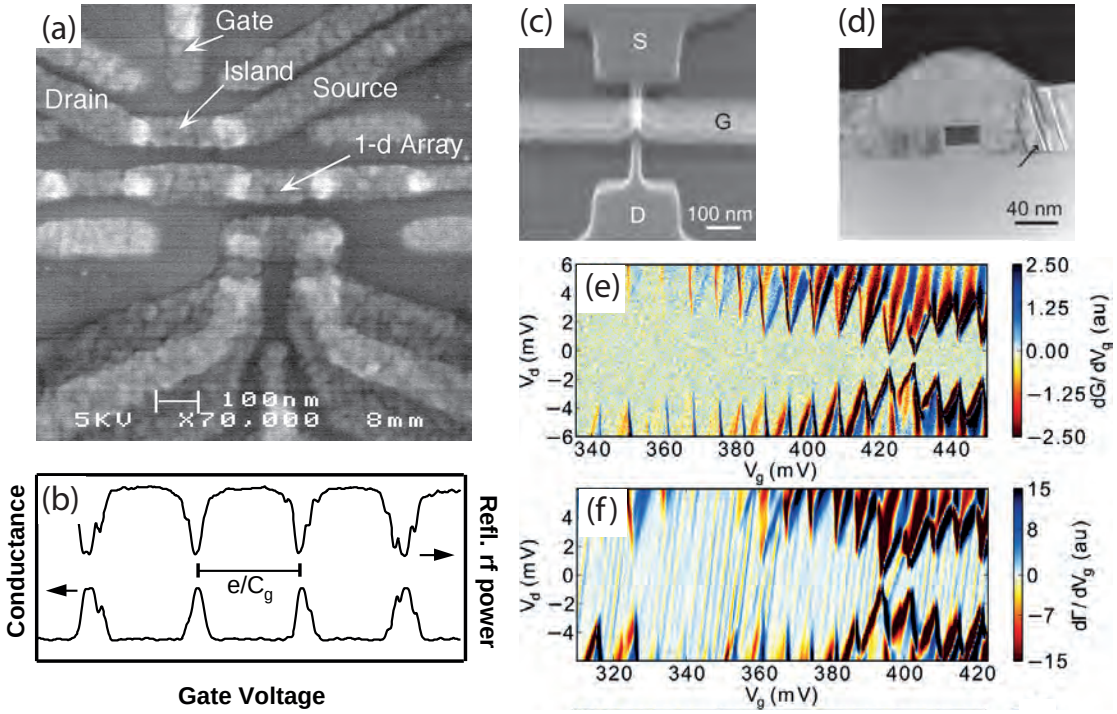

Figure 4.4: **High bandwidth sensing with the RF-SET.** (a) SEM image of an RF-SET formed by double-angle metal evaporation reproduced from Schoelkopf *et al.* [95]. The SET is comprised of Source, Island, Drain and Gate at the top of the image. (b) DC conductance and reflected RF power shown as a function of gate voltage. Coulomb peaks in the conductance signal (bottom curve) occur when the charging energy (e/C_g) is overcome allowing conduction through the SET island. These points correspond to a reduction in the reflection amplitude (top curve). Reproduced from Schoelkopf *et al.* [95]. (c) SEM image of a fin-FET transistor and (d) TEM image showing a cross-section of the same transistor, both reproduced from Villis *et al.* [96]. (e) DC conductance measurement showing coulomb diamonds due to the formation of a quantum dot in the transistor channel below pinch-off voltage. The blockaded region (for small V_d) shows no significant features. (f) RF reflected amplitude measurement of the same device, where resonances due to nearby charge traps are visible in the blockaded region as diagonal lines. (e,f) also reproduced from Villis *et al.* [96].

by Villis *et al.*[96], who used an RF-SET to detect the charging of dopant atoms within the channel of a fin-FET transistor, an effect that is not visible in bias spectroscopy transport measurements. The transistor used as the RF-SET can be seen in Figure 4.4(c,d). At negative gate voltage, the conductive channel between source and drain becomes depleted, forming an isolated island of charge. Addition of electrons to the SET island can be seen as Coulomb diamonds in Figure 4.4(e), a DC conductance measurement. The equivalent RF-SET measurement signal in Figure 4.4(f) reveals additional features within the Coulomb blockade region, that were attributed in this device to a charge trap within the wrap-around gate structure.

RF reflectometry combined with a single electron transistor can provide a high bandwidth charge sensing signal, sensitive to charge transitions occurring even with the SET itself in Coulomb blockade.

The dispersive gate sensor

The effect of change in the system capacitance within a resonant circuit is a shift of the resonance peak in frequency. Such a change in the capacitance arises within a device when electrons tunnel back and forth at a fixed energy (non-dissipatively) in response to an AC voltage, between charge states having different dispersion ($E(V)$) relations. This dispersive shift in the resonant frequency can be seen by monitoring the phase or amplitude of a reflected RF signal at a fixed drive frequency near to the resonant frequency.

Importantly, the non-dissipative AC tunnelling response can be observed by any conductor capacitively coupled to the charge states involved. This fact has been exploited to convert existing gates within a nanoelectronic device into a single terminal detector described as a dispersive gate sensor (DGS). The technique has been demonstrated using metallic surface gates defining QDs in GaAs quantum wells by Colless *et al.*[100], with a double quantum dot device shown in Figure 4.5(a). The blue highlighted R gate is coupled to a resonant circuit and has an RF signal applied, which induces AC tunnelling: between the two dots – corresponding to isolated points in the upper left of Figure 4.5(b); or between a dot and an electron reservoir – as evidenced by lines defining the charge state cells at higher gate voltages. The schematic of Figure 4.5(c) illustrates a stable point (orange), where the RF signal moves the system within the dispersion relation of one single charge state, in contrast to at a charge state transition (green), where the AC

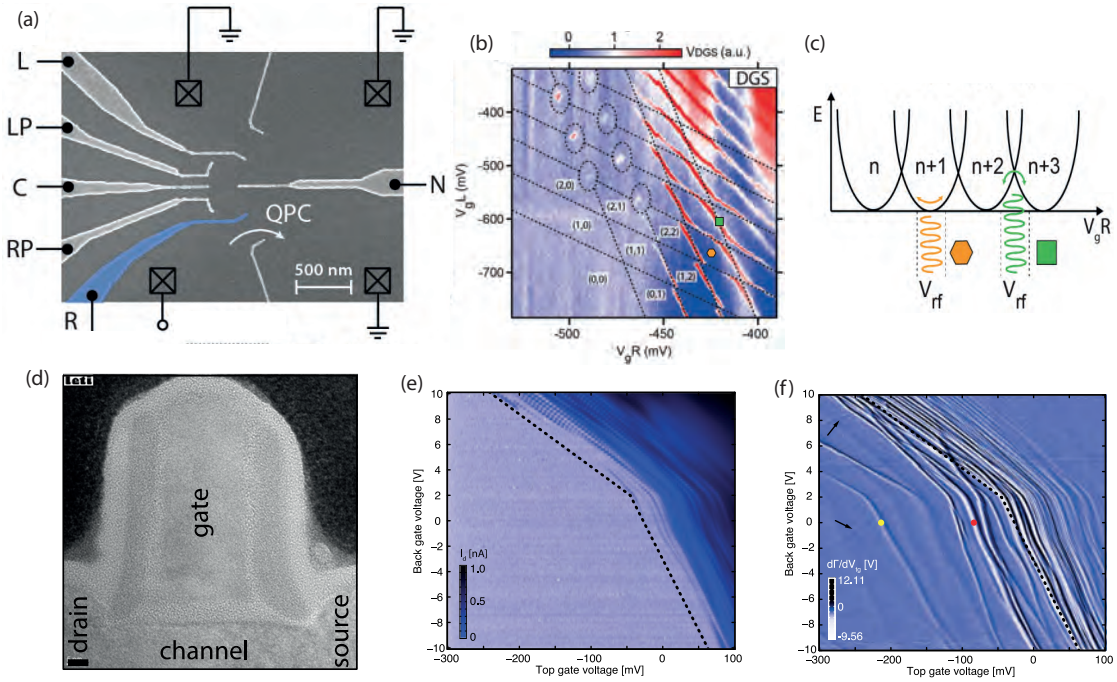

Figure 4.5: Dispersive gate sensing via a modified device capacitance. (a) SEM image of a GaAs double quantum dot. The quantum dots are formed by locally depleting a 2DEG under the gate structures. The blue highlighted gate is connected to a resonant circuit enabling its use as a dispersive gate sensor. (b) Reflected RF amplitude V_{DGS} shown as a function of L and R gate voltage. Lines with two slopes appear in the response corresponding to charge transitions of the two dots, where tunnelling from one of the electron reservoirs to a quantum dot in response to the applied RF signal contributes additional capacitance to the gate sensor. For lower electron numbers the dot to reservoir tunnel rate is too slow to be driven by the RF signal, and only fast inter-dot tunnelling signal remains. (c) Schematic showing the dispersion relations of subsequent quantum dot charge states. At degeneracy points (green), the RF promotes AC tunnelling and here the ground state energy does not follow the normal dispersion curve, manifesting an an added capacitance, compared to stable regions (orange) where the charge state is unchanged. (a-c) reproduced from Colless *et al.* [100] (d) SEM image showing a cross-section of a silicon fin-FET transistor, with the channel containing phosphorus dopants. The gate is coupled to a resonant circuit as a dispersive gate sensor. (e) DC conductance measurement showing the pinch-off point of the transistor marked by a dotted line, above this point several resonances indicating transport through specific dopants are visible as sharp conductance lines. (f) RF reflected amplitude measurement (the derivative is shown) of the same device, where multiple donor resonances are clearly visible in non-conductive region. (d,e,f) reproduced from Verduijn *et al.* [101].

voltage promotes AC tunnelling between two states with distinct dispersion curves. If the tunnel rate is comparable to or faster than the drive frequency, the system oscillates between the two states, and the change in charge in response to a change in voltage manifests as a so-called quantum capacitance $dQ/dV = C_Q$. This technique has been shown to be sensitive to single charge motion[102] with a bandwidth $\sim$ 8MHz

Effective use of the dispersive gate sensor was made by Verduijn *et al.*[101], using poly-silicon wrap-around gates surrounding the channel of a silicon fin-FET as shown in Figure 4.5(d). Comparing to a DC measurement in Figure 4.5(e), dispersive sensing with the wrap-around gate shown in Figure 4.5(f) reveals numerous charge transitions below the pinch-off point (dotted line in (e)) of the transistor. These lines represent donor transitions, not visible in transport measurements.

A major advantage of this sensor is that it doesn't require any additional structures be introduced to a device, since any gate already required to define the nano-structure or control the electrons may be used additionally as a sensor. Indeed converting every gate into a dispersive sensor is in principle possible, and combined with frequency multiplexing[103], and may provide a much more complete picture of charge motion within a device without a dedicated sensor device like an SET.

The tunnel coupled reservoir

As an alternative to the dispersive gate sensor which relies on capacitive coupling, a single terminal charge sensor can be made by placing a single metallic electron reservoir in direct tunnel-contact with a quantum dot. Such a tunnel coupled reservoir may sense charge transitions where an electron tunnels directly to/from the reservoir itself, providing a much stronger signal compared to the capacitively coupled dispersive gate sensor. More distant charge motion where tunnelling does not involve the reservoir can also be detected, just as it is by a gate sensor.

The direct tunnelling configuration was described by Persson *et al.*[104] as a single electron box (effectively one half of an SET), and depending on the tunnel rate and driving frequency, AC electron motion may produce a dissipative or dispersive response. A theoretical understanding of the dispersive response was developed by Gabelli *et al.*[105] and has been extended by others to the dissipative regime[104,106].

Between a quantum dot and an electron reservoir, the AC tunnelling resistance R_Q and capacitance C_Q depend on the dot-reservoir tunnel rate γ, the drive frequency ω, the

electron temperature T, the effective lever arm of the reservoir over the dot potential α', and the energy offset $\delta\mu = \mu - E_F$ between dot potential μ and reservoir Fermi energy E_F[105]

$$R_Q = \frac{4k_BT}{\gamma\alpha'^2e^2}\left(1+\frac{\gamma^2}{\omega^2}\right)\cosh^2\left(\frac{\delta\mu}{2k_BT}\right) \tag{4.21}$$

$$C_Q = \frac{\alpha'^2e^2}{4k_BT}\left(1+\frac{\omega^2}{\gamma^2}\right)^{-1}\cosh^{-2}\left(\frac{\delta\mu}{2k_BT}\right) \tag{4.22}$$

Now consider some limiting cases, taking $\delta\mu = 0$ to examine the response right at the charge transition point:

- In the slow tunnelling limit $\gamma \ll \omega$, C_Q goes to zero, and R_Q takes a maximum value of $\frac{4k_BT}{\gamma\alpha'^2e^2}$. This can be understood since the electron is unable to tunnel as fast as the driving signal so no charge motion occurs.

- Passing through $\gamma = \omega$, C_Q goes through an inflexion point, and R_Q is minimised at $\frac{8k_BT}{\omega\alpha'^2e^2}$. Tunnelling may now occur, but stochastically with a delay comparable to the period of the RF drive. The reservoir Fermi energy oscillates, and therefore tunnelling onto the dot is likely to occur with the maximum Fermi energy, and tunnelling off of the dot at minimum Fermi energy, thus the tunnelling in this regime dissipates energy.

- In the fast tunnelling limit $\gamma \gg \omega$, C_Q reaches a maximum value of $\frac{\alpha'^2e^2}{4k_BT}$, and R_Q also becomes large again. Here tunnelling is effectively instantaneous, occurring before the drive voltage reaches its peak value; at the same energy in either direction and so without energy loss. The dominant effect is in this case dispersive.

The following sections present the first RF reflectometry measurements in atomic precision donor defined planar nano-structures. First, in Section 4.2 we present a hybrid device which displays the combined and contrasted behaviour of a tunnel coupled reservoir alongside an RF-SET. Secondly, in Section 4.3 using a double quantum dot device with a tunnel-coupled reservoir, we demonstrate a reservoir tunnel-coupled to two donor quantum dots.

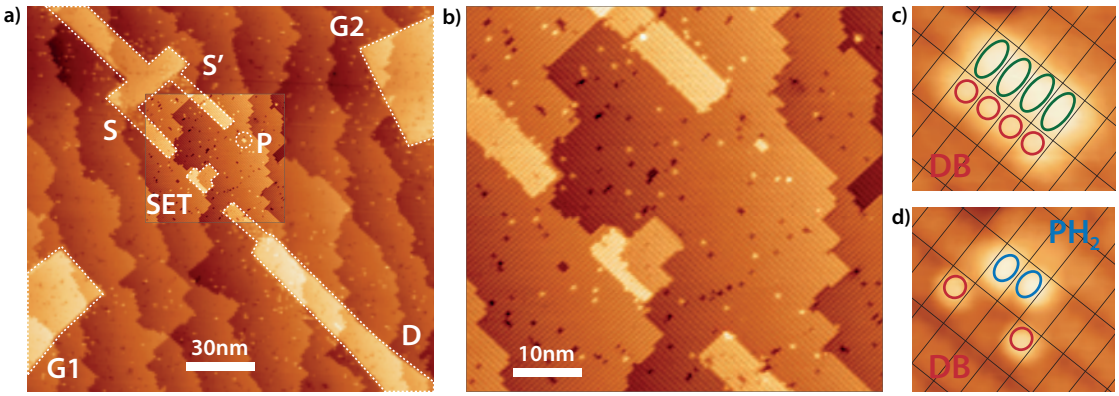

Figure 4.6: **A single donor with capacitively-coupled SET and tunnel-coupled reservoir.** (a) An STM image of the device, showing a hydrogen terminated silicon surface where hydrogen atoms have been removed with an STM tip to form the template for the creation of a single P donor capacitively coupled to an SET and tunnel coupled to the source reservoir. Reservoir (S‘) source (S) and drain (D) are labelled, as are two gates, $G1$ and $G2$ coupled respectively to the SET and donor. (b) Inner region imaged with atomic resolution. Single bright dots are non-reactive individual dangling bonds where one silicon atom is not terminated by hydrogen. Single dark dots are single atom or single dimer vacancies in the surface layer of the lattice, and will be filled during overgrowth. (c) STM image of the single donor incorporation site overlaid with the Si(2x1) surface atomic lattice grid, showing four clean adjacent dimers (green) before dosing and (d) after PH_3 dosing, showing two PH_2 fragments (blue). Red circles indicate single non-reactive dangling bonds.

4.2 A HYBRID SINGLE DONOR CHARGE SENSING DEVICE

To compare the operation of an RF-SET and tunnel coupled reservoir in a precision donor defined device, we use a hybrid layout, where a single lead acts as both the source terminal for an SET and also as a tunnel coupled reservoir for a single donor. The SET is designed to indirectly sense the charge of the single donor via the capacitive coupling between them, and the tunnel coupled reservoir is placed near enough to the donor to be in the fast-tunnelling limit, permitting dispersive sensing of donor charge transitions directly and independently of the SET. I fabricated the hybrid device with help from Eldad Peretz. Together with Matthew House, I designed the reflectometry circuit and we performed the following measurements together. The results of this section are published in Applied Physics Letters[1].

Figure 4.6(a) shows a scanning tunnelling microscope (STM) image of the hybrid

device created by STM hydrogen resist lithography. The image is of the lithographic pattern before phosphine dosing, and the inner region is shown in higher resolution in (b). Bright areas indicate where hydrogen atoms have been removed from the lithographic mask by the STM tip. We define a 75nm^2 donor based SET island placed $\sim$ 18.5nm away from the donor. We can operate this SET as a DC charge-sensor or as an RF-SET, allowing a direct comparison of the two operating modes in one device. The upper finger of the source terminal (S) of the SET is also tunnel coupled to the single donor (positioned 11.5nm away) so that it can act as a tunnel coupled reservoir (S‘). We will show later how we can independently resolve the RF-SET signal and the dispersive signal despite sharing a single terminal and RF resonant circuit. The drain (D) lead completes the SET channel and in-plane gates G1 and G2 tune the electrochemical potentials of the SET and P donor, respectively. Figure 4.6(c) shows a close-up image of the lithographic mask for the single donor site, where the bright area corresponds to twelve H atoms removed from a hydrogen terminated surface.

After dosing this surface with phosphine, in Figure 4.6(d), we see two PH_2 features identifiable by their height profile ($\sim$ 180pm). Annealing at 350°C causes one fragment to leave the surface and the remaining PH_2 fragment transitions to an Si-P hetero-dimer. The large exposed areas of the silicon surface that define the SET, reservoir, and gate electrodes are also phosphorus doped and annealed, resulting in metallic conduction with a carrier density[91] $n_{2D} = 2.5 \times 10^{14}\,\mathrm{cm}^2$. The planar device is then encapsulated with 50nm of epitaxial silicon and contacted with aluminium as described in Chapter Chapter 3. Based on the area of the SET and the 2D doping density, we know that the SET contains $\sim$ 185 P donors.

4.2.1 Amplitude and phase sensitive measurement circuit

With the circuit shown in Figure 4.7(a), which is attached to the source (S&S') we measure the reflection coefficient Γ of an RF frequency signal. The RF signal is injected through a directional coupler and the high pass side of a standard RC bias tee (R_B, C_B), to the resonant circuit consisting of a surface mount chip inductor L = 1200nH and

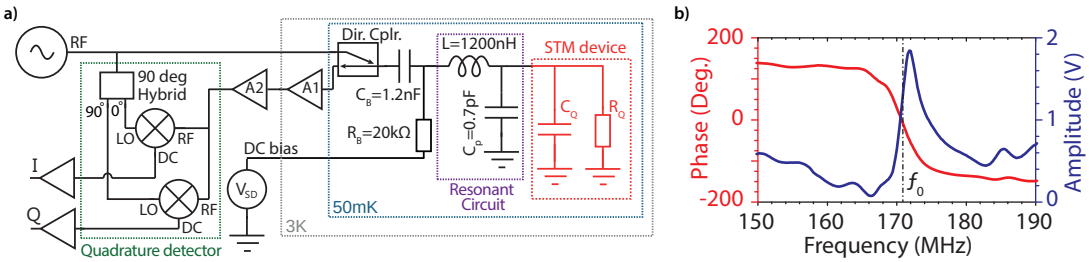

Figure 4.7: RF reflectometry setup, and tank circuit characterisation. (a) Schematic of the RF measurement circuit across different temperature stages, showing the applied RF signal injected through a directional coupler, the STM device and resonant circuit at millikelvin (mK), followed by amplifiers at the 3K stage and at room temperature (A1, A2) and a quadrature homodyne detection circuit. (b) The measured amplitude and phase of the reflected signal around the LC resonance at 170.9MHz for $V_{SD} = V_{G1} = V_{G2} = 0$, where the SET is in Coulomb blockade.

the parasitic capacitance to ground C_P due to the proximity of the signal carrying wire beyond the inductor to the ground potential. The RF circuit path at this point is wire-bonded to the source terminal of the device, represented in the circuit as the parallel capacitance C_Q and resistance R_Q and coloured red. The reflected signal passes back through the directional coupler and is routed to an amplifier at 4K (A1), and another at room temperature (A2). The amplified signal is then fed to a quadrature detector consisting of two mixers, using local oscillator signals offset by 90° to produce DC voltage signals representing the in-phase (I) and quadrature (Q) components of the reflection coefficient Γ. Further details of the hardware set-up and power levels are given in Section A.1.

Figure 4.7(b) plots the measured reflected amplitude $V_{out} = V_{in}|\Gamma|$ (blue) and phase $\phi(\Gamma)$ (red) of the reflected signal as a function of drive frequency with the device in Coulomb blockade, where its resistance is effectively infinite ($R_{\text{eff}} \approx 0$). The inflection point of the phase response occurs at $f_0 = \frac{1}{2\pi\sqrt{LC}} = 170.9\text{MHz}$. Knowing the value of the inductance, $L = 1.2\mu\text{H}$ allows us to determine the parasitic capacitance $C_P = 0.72\text{pF}$ and the resonator quality-factor. The quality factor of the resonance is found by taking the ratio of f_0 to the FWHM of the amplitude peak $Q = \frac{1}{R}\sqrt{\frac{L}{C}} = 46 \pm 10$. For most of the experiment, we fix the driving frequency $f = 172.0\text{MHz}$ (chosen to be near the peak of the amplitude signal) and observe variations in the phase and amplitude of the reflection coefficient. We estimate the applied RF power at the reservoir/source of the device is around $-90\text{dBm} = 20\log_{10}(V_{PP}/632mV)$, attenuated from +16 dBm at the

signal generator. This corresponds to an AC voltage within the device on the order of $V_{PP} \sim 20\mu$V.

4.2.2 A side-by-side comparison of DC and RF response

We now show a set of charge stability maps in Figure 4.8, simultaneously measuring (a,b) the DC current through the SET, (c) the reflected RF amplitude, and (d) the reflected RF phase signal, as a function of gate voltages V_{G1} and V_{G2} at a fixed $V_{SD} =$ 2mV. Diagonal lines of high current represent Coulomb peaks of the SET, separated by $\Delta V^{SET} = 240 \pm 3$mV, corresponding to the SET charging energy $E_C^{SET} = 10.2 \pm 0.5$meV (measured directly from the height of Coulomb diamonds in Figure 4.11).

From Figure 4.8(a), we can identify two lines of discontinuities having similar slopes (marked with blue dotted lines as a guide to the eye in (b)) associated with the donor $D^+ \rightarrow D^0$ and $D^0 \rightarrow D^-$ transitions. There is another discontinuity (green dashed line in (b)) which we attribute to a nearby charge trap 'T'. By considering the displacement of the SET conduction lines seen when crossing a transition, highlighted in the colour-coded insets, we can see that the trap produces a shift consistent with a mutual charging energy E_M of only 0.5meV compared to the donor mutual energy $E_M = 1.6$meV. This smaller mutual energy indicates that the trap is more weakly coupled to the SET, and thus farther away physically. This is confirmed by the lack of phase and amplitude response along the 'T' line. Note that at zero gate voltage the single donor is ionised due to the electrostatic presence of the surrounding gate electrodes, as seen in similar single donor devices[53,55]. In particular Fuechsle *et al.*[53] have measured the source and drain Fermi level in a similar device $\sim$ 80meV below the conduction band edge due to the high doping density within the device leads and gates. Although within an asymmetric potential landscape, the concept of a binding energy has little value, we see that in our device the first electron loads only after applying $\sim$ 200mV to gate $G2$ in agreement with previous results.

In the DC current map Figure 4.8(a), donor transition lines are only visible indirectly, by connecting discontinuities in the Coulomb peaks. We have highlighted these discontinuities in Figure 4.8(b) with blue dotted lines as a guide to the eye, yet without

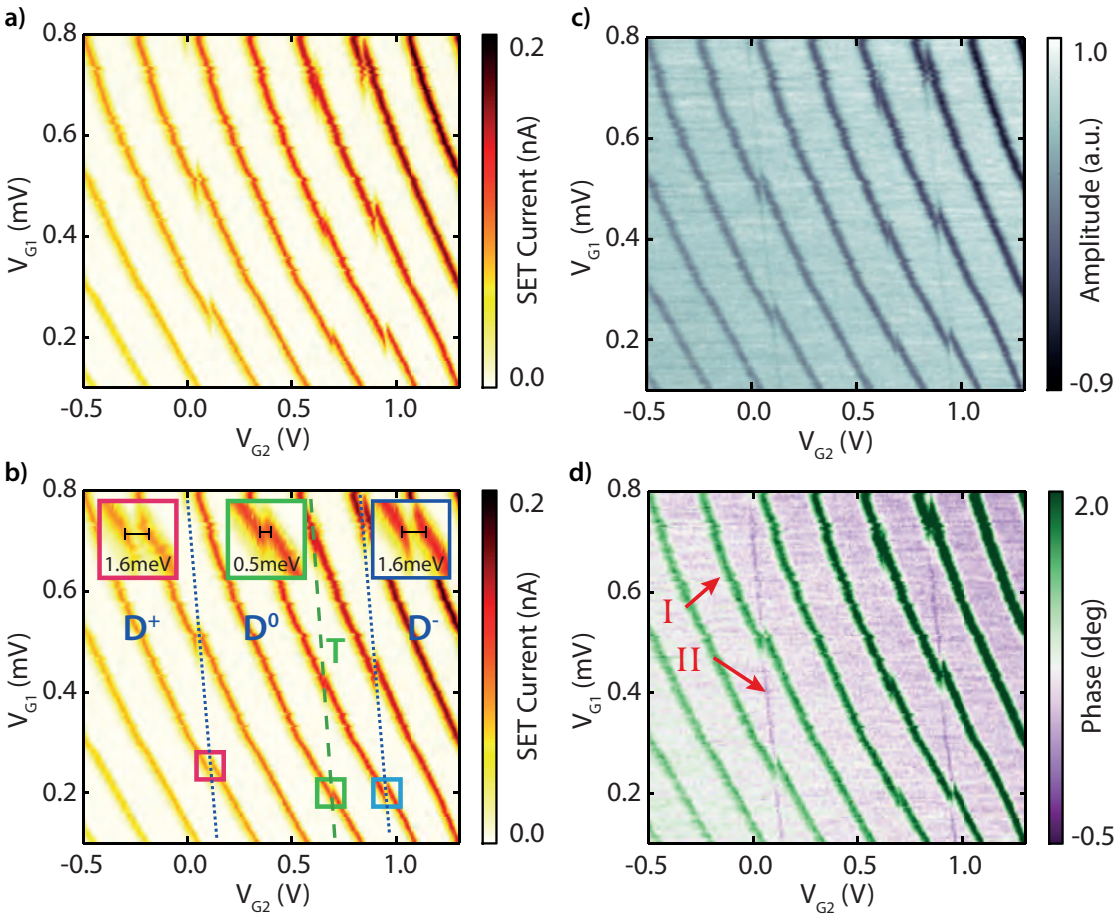

Figure 4.8: **Comparison of DC charge sensing and RF reflectometry.** Charge stability maps across the three charge states (D^+, D^0, D^-) of the donor comparing the different charge sensing signals: (a) DC tunnel current through the SET, (b) annotated version labelling the charge states of the donor and the transitions in blue. The green line marked T is due to an unintended charge trap. Insets show the charge offset at triple points, where the two discontinuities attributed to the donor have the same mutual charging energy offsetting SET conduction lines, whilst the line T has a smaller mutual energy. (c) Amplitude, and (d) phase of the reflected RF signal, as a function of the two gate voltages V_{G1}, V_{G2}. Features related to the dissipative (I) and dispersive (II) response of the resonant circuit are indicated.

these markers only the charge offset discontinuities are visible. In such a simple device identifying charge transitions indirectly from the discontinuities is trivial, but it is foreseeable that the feature identification of charge transitions between multiple donors may not be so straightforward in a future device containing many donor qubits. The RF measurements on the other hand are directly sensitive to the donor charge transitions, and continuous lines may be seen running (almost) vertically through Figures Figure 4.8(c,d). Not only does the reflected signal allow direct observation of where the charge transitions occur, but the response is different to that at the SET Coulomb peaks, because there are two mechanisms through which the applied RF signal produces a response within the device: a dissipative response, and a dispersive response.

Dissipative response (I) At the Coulomb peaks, an AC current flows through the RF-SET in response to the AC bias voltage. Since electrons dissipate energy in passing through the SET channel, this manifests as a finite resistance due to the 2-stage quantum tunnelling (not present when the SET is in Coulomb blockade). The presence of this finite parallel resistance R_Q damps the resonant circuit, generating a reduction in the reflected amplitude as seen in Figure 4.8(c). Since we drive the circuit at $f = 172.0$MHz, slightly above the natural resonance (located at $f_0 = 170.9$MHz), this also translates to a *positive* shift in the phase signal so that we observe green lines in Figure 4.8(d).

Dispersive response (II) Along the donor transition lines, an AC current flows between the source terminal and the P donor as electrons tunnel back and forth without losing energy, manifesting as a quantum capacitance C_Q. This has the result of lowering the resonant frequency which generates a reduction in reflected amplitude Figure 4.8(c), and a *negative* phase shift Figure 4.8(d), making the donor transition lines not only visible in the RF stability maps but also distinguishable from SET conduction lines.

Positive and negative shifts in the phase signal occur for the 172.0MHz drive frequency used to obtain the data of Figure 4.8. We next examine the effect of the RF drive frequency on each of the two AC tunnelling mechanisms.

4.2.3 Effect of driving frequency on SET and donor tunnelling processes

The dissipative (I) and dispersive (II) processes are illustrated schematically with arrows on the device image of Figure 4.9(a). We now further investigate the effect of varying the RF drive frequency f on these two processes, and the amplitude and phase response they generate in the resonant circuit.

The dissipative response, due to electrons losing energy as they tunnel through the SET, is to damp the resonance, and we sketch the effect in Figure 4.9(b). For frequencies above f_0 the phase of the reflected signal $\phi(\Gamma)$ increases (green arrow), and below f_0 the phase decreases (purple). In contrast, the dispersive response to tunnelling at a fixed energy between reservoir S' and the P donor is a shift of the resonance curve to lower frequency, illustrated in Figure 4.9(c). This reduces the phase of the reflection at all frequencies (purple arrow). The scale of the effects in these cartoons is exaggerated for clarity.

The stability map, shown again in Figure 4.9(d), displays positive/negative phase contrast between processes I and II because it is measured at a frequency above f_0. But the contrast changes as a function of frequency, as we show in Figure 4.9(e) by taking a cut along the V_{G2} axis that passes 3 SET lines and one donor transition. As expected, we observe a change in the sign of the response for the dissipative (I) RF-SET signal, which becomes negative for lower drive frequency. On the other hand the dispersive (II) response does not show this bi-modal behaviour, also as expected. In this plot the phase difference $\Delta\phi$ is referenced to the local background value which changes as a function of frequency and gate voltage.

Figure 4.9(f) shows the corresponding change in reflected amplitude $\Delta|\Gamma|$, normalized for each frequency. The dissipative (I) process manifests as an amplitude reduction across the entire responsive frequency band. The maximum change is only a 0.05% reduction, and is limited by imperfect impedance matching between the resonant circuit and transmission line. The amplitude response to the dispersive signal (II) is less, at only $\sim 0.01\%$.

Being able to discriminate between distinct tunnelling processes is a clear advantage of RF reflectometry over traditional transport current measurements, and will be of high value in understanding more complex future multi-qubit devices where multiple

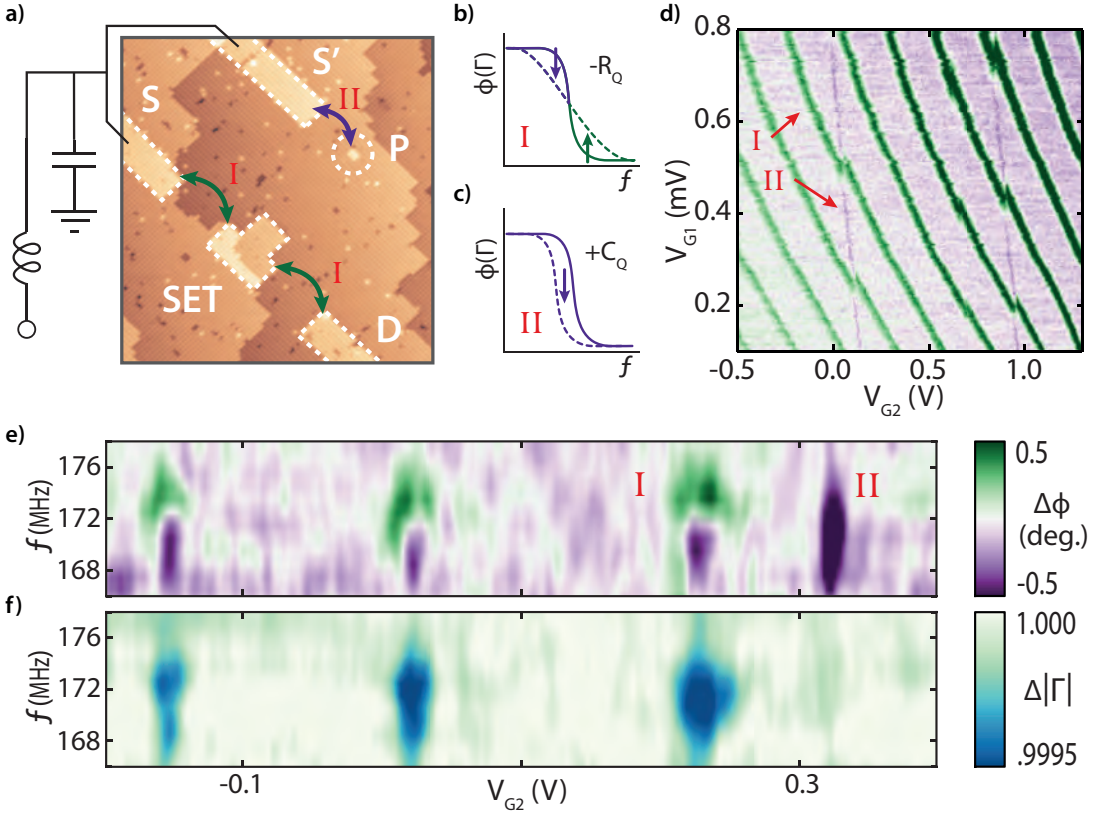

Figure 4.9: Frequency dependent response of a donor tunnel coupled to a reservoir and a nearby RF-SET. (a) STM image indicating the different AC tunnelling paths occurring (b) schematic representation of the frequency-dependent response to reduced device resistance through the SET channel when aligned to a Coulomb peak, and (c) equivalent schematic for increased quantum capacitance experienced at donor charge state transitions (d) phase response gate map (repeated from previous figure). (e) Phase response to a one dimensional gate (G2) scan, now as a function of the tank circuit driving frequency, showing the observed bipolar response to dissipative SET tunnelling (I), contrasted with a uniform phase reduction for dispersive donor-reservoir tunnelling (II). (f) Simultaneously recorded amplitude response showing a uniform dissipative signal where energy is absorbed by the SET and only a very weak response to dispersive resonance shift during donor tunnelling.

dissipative and dispersive tunnelling paths may exist.

4.2.4 Determination of the single donor charging energy

The two charge transitions of the donor are separated in gate voltage V_{G2} by a distance $\Delta V^P = 825 \pm 3\text{mV}$, as shown in Figure 4.10(a), and the separation between adjacent SET Coulomb peaks is $\Delta V^{SET} = 240 \pm 3\text{mV}$. At the triple points where the SET and donor charge transition lines intersect (an example is shown at high resolution in Figure 4.10(b)), there is a small offset in both lines, caused by the electrostatic interaction between the two charge islands — their mutual capacitance. We define these offsets schematically in Figure 4.10(c). The offset of $\delta V^{SET} = 38 \pm 3\text{mV}$ in the SET peaks due to donor charging events, and of $\delta V^P = 20 \pm 3\text{mV}$ in the donor transition potential due to SET charging lines can be used to calculate the mutual charging energy between the SET and donor E_M, and also the neutral donor charging energy E_C^P.

$$E_M = \frac{\delta V^{SET}}{\Delta V^{SET}} E_C^{SET} = 1.6 \pm 0.2\text{meV} \tag{4.23}$$

$$E_C^P = \frac{\Delta V^P}{\delta V^P} E_M - 3E_M = 61.7 \pm 17\text{meV} \tag{4.24}$$

Across the voltage span δV^P, three electrons are added to the SET, hence we subtract three times the mutual charging energy ($3E_M$) to give the single donor charging energy for the D^0 state $E_C^P = 61.7 \pm 17\text{meV}$. Despite the large uncertainty (due to the small value of δV^P) this charging energy is consistent with $45 \pm 7meV$ obtained with measurements of electron transport through an isolated P donor[53,69] and optical spectroscopy[69].

In calculating the donor charging energy we also obtain the lever arms α_{G2}^{SET} and α_{G2}^P relating gate voltage to SET and donor potentials. The full set of values are summarised in Table 4.1.

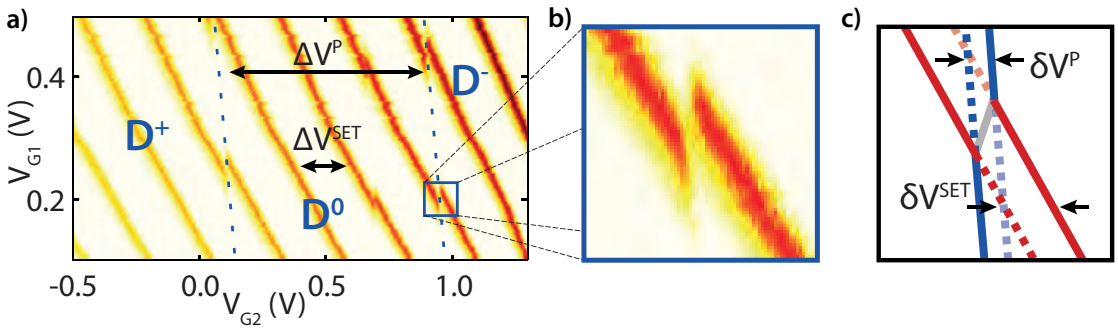

Figure 4.10: Determining the single donor charging energy from the observed charge transitions. (c) Gate map region indicating the voltage spans across one SET stability region δV^{SET}, and the D^0 donor charge state δV^P (b) Inset of a triple point, showing the charge offset due to the mutual capacitance between donor and SET. (a) Schematic showing charge degeneracy conditions around such a triple point. Red lines indicate SET transitions offset by δV^{SET}, for the cases where the donor is singly or doubly occupied, and blue donor transitions (offset by δV^P) for two SET charge occupancies. The donor charging energy is determined via measurements of the four voltage spans shown, as well as the SET charging energy taken directly from a standard Coulomb diamond measurement (see next figure).

SET parameters		donor parameters	
E_C^{SET}	10.2 ± 0.5meV	E_C^P	61.7 ± 16.5meV
ΔV^{SET}	240 ± 3mV	ΔV^P	825 ± 3mV
α_{G2}^{SET}	0.0425 ± 0.00215	α_{G2}^P	0.0807 ± 0.0216
δV^{SET}	38 ± 3mV	δV^P	20 ± 5mV
E_M	1.615 ± 0.151meV	E_M	1.615 ± 0.151meV

Table 4.1: Values of SET and donor charging energies, lever arms and mutual coupling energy

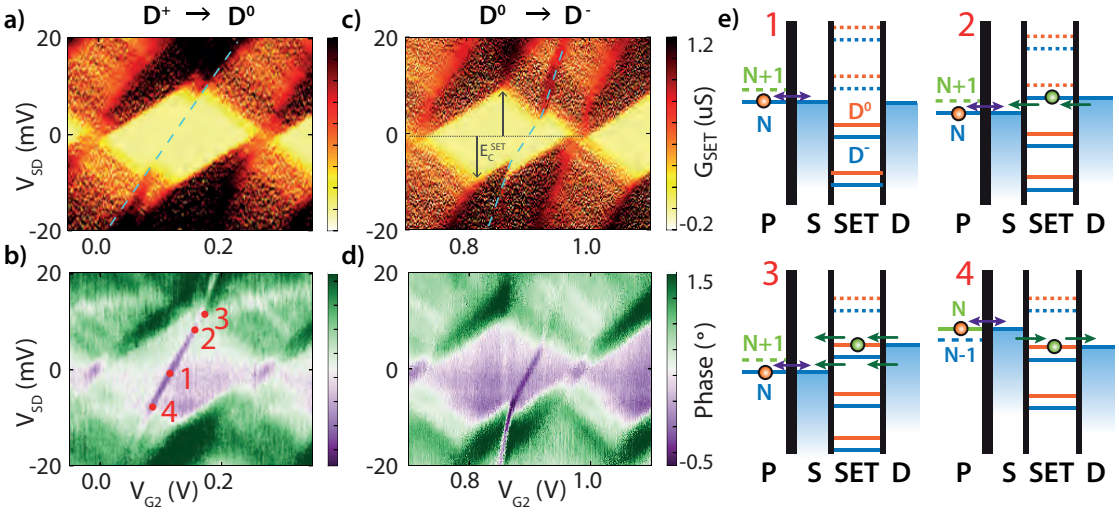

Figure 4.11: Coulomb diamond plots at the $\mathbf{D^+ \rightarrow D^0}$ and $\mathbf{D^0 \rightarrow D^-}$ donor transitions. Comparison of (a) DC SET conductance dI_{SD}/dV_{SD}, and (b) reflected phase shift signals at $V_{G1} = 100mV$ showing the $D^+ \rightarrow D^0$ transition and (c,d) similar plots for the $D^0 \rightarrow D^-$ transition. (e) Energy level diagrams for the 4 points marked in (b). Blue lines indicate electrochemical potentials of the SET when the donor is unoccupied (D^+), red lines indicate the electrochemical potentials of the SET when the donor is occupied (D^0), where the potential is increased by the mutual charging energy E_M. Likewise, the green line for the donor represents the electrochemical potential of the donor with an additional electron on the SET.

4.2.5 High bias interaction between donor and SET states

We can further examine the interaction between the donor and its reservoir by changing the reservoir voltage. Since the donor's reservoir and the source of the SET are one and the same in our device, this results in a Coulomb diamond scan. Figure 4.11(a,b) show the differential conductance $G_{SET} = dI_{SET}/dV_{SD}$ and reflected phase response, respectively, as a function of bias V_{SD} and donor-gate voltage V_{G2} for a region including the $D^+ \rightarrow D^0$ transition, whilst Figure 4.11(c, d) indicates the same for the $D^0 \rightarrow D^-$ transition. From the height of the Coulomb diamonds (marked in Figure 4.11(c)) we measure an average SET charging energy of $E_C^{SET} = 10.2 \pm 1.0$meV.

In both of these diagrams we observe a line passing diagonally through the diamond, with a positive gradient given by the ratio of relevant lever arms, corresponding with the $D^+ \rightarrow D^0$ and $D^0 \rightarrow D^-$ charge transitions

If we now consider the electronic configuration at four different source-drain bias points, shown schematically in Figure 4.11(e), along the donor transition line as marked in Figure 4.11(b) we can understand the differences between the DC SET conductance and reflected phase response.

- At position 1, in the centre of the Coulomb diamond, there is no source-drain bias and all SET transport is blockaded with an occupancy of N electrons. Here the donor $D^+ \rightarrow D^0$ transition is resonant with the source Fermi energy so tunnelling is allowed on and off the donor, giving additional capacitance and hence a negative phase response at this point in Figure 3(b), but no conductance response through the SET in Figure 3(a).

- At position 2, the SET $N \leftrightarrow N+1$ potential comes into resonance with the drain and current can flow through the SET, but only if the donor is in the D^+ state. Should the donor accept an electron, then the SET energy levels move up by the mutual charging energy (shifting from the blue ladder of potentials to the red) and current cannot flow until the donor bound electron tunnels away. This point defines the onset of DC transport when the donor is unoccupied. Therefore, in the region between positions 2 and 3, the conductance is non-zero only on the D^+ side of the donor transition.

- At position 3, there is enough source-drain bias that the electrochemical potential of the $N \leftrightarrow N+1$ transition, in both the ionized (blue) and occupied (red) donor configurations, is within the bias window. As a consequence tunnelling through the SET is allowed for both D^+ and D^0 donor states. Here, tunnelling to the donor is however partially suppressed in the presence of SET transport because the potential of the donor-source resonance is shifted up and down by E_M when there are respectively $N+1$ and N electrons occupying the SET. The result is that we do not observe a discrete jump in this resonance outside the Coulomb diamond but instead a gradual shift. This shift appears as an altered slope of the donor transition outside the Coulomb diamond, as highlighted by the guide-line overlaid on Figure 3(a,b), suggesting that the time averaged charge occupation of the SET is non-integer and varies with bias.

- At position 4 the $N-1 \leftrightarrow N$ SET resonance, conditional on occupation of the D^0 state, is aligned with the drain Fermi energy. Here blockade is initially lifted on the

D^0 side. With increasingly negative V_{SD}, AC charge motion is again suppressed, as the SET spends some time in both the $N-1$ and N electron state, again producing an apparent change in slope.

With a thorough understanding of the exact device geometry due to the precise nature of STM lithography, we are able to interpret dissipative and non-dissipative RF response mechanisms in this hybrid device, even when they occur simultaneously in the high bias regime of Figure 4.11.

4.2.6 Large lever arm of the tunnel coupled reservoir sensor

Purely capacitive coupling between a gate and a QD (such as our SET island, or donor) is parameterised by the lever arm – the ratio of electrochemical potential energy change to voltage change $\alpha = \Delta\mu/\Delta V$. An increase in gate voltage decreases the QD potential relative to a fixed Fermi energy, as illustrated in Figure 4.12(a) where an original ladder of charge state transition potentials (green) is shifted lower (purple) by an increased gate voltage ΔV, taking a potential $\mu \rightarrow \mu - \alpha\Delta V$. With two gates acting in such a manner, an increased voltage on the first can be compensated by an decreased voltage on the second, keeping the QD potential constant. As is the case for gate G1, G2 and the SET island, this compensation results in lines of negative slope in a stability map (such as Figure 4.8), with a gradient given by the ratio of donor lever-arms $-\alpha_{G1}^{SET}/\alpha_{G2}^{SET}$.

For a tunnel coupled reservoir however, there is an additional effect – the reservoir voltage also modifies the Fermi energy. As Figure 4.12(b) illustrates, the capacitive coupling electrostatically lowers the donor transition potential, just as it does for a standard gate, but the increase in voltage of the reservoir also directly lowers the Fermi level of the reservoir, and by a greater amount – the lever arm of this effect is unity. The overall response to an increase in voltage ΔV is then an *increase* in donor transition potential relative to the Fermi energy of the reservoir, directly in the opposite sense to a purely capacitive gate. This concept explains the positive slope of donor transitions previously seen in the reservoir/gate stability maps of Figure 4.11, since to compensate a positive change in reservoir voltage, a *positive* change in the gate voltage is needed to

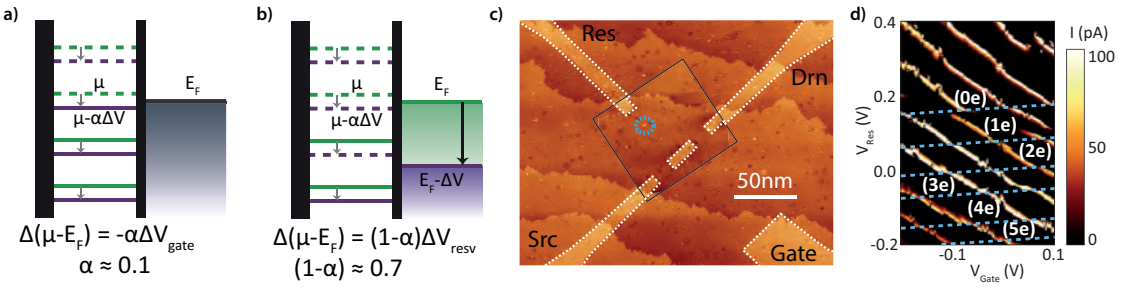

Figure 4.12: Large effective lever arm of the source reservoir on the donor potential. (a) Schematic of the standard response to a capacitively coupled gate lowering a quantum dot potential proportionally with the applied voltage. (b) Equivalent response to a tunnel coupled reservoir. Here the Fermi energy of the reservoir changes with the applied voltage, in addition to the weaker capacitive shift which is still present. The combination manifests as a large and negative effective lever arm $\alpha' = 1 - \alpha$ (c) STM image of a device with an independent reservoir tunnel coupled to a multi-donor cluster, which is also capacitively sensed by an SET consisting of island, source, drain and gate. (d) Stability map of the independent tunnel coupled reservoir device showing 6 parallel charge transitions, depleting 6 electrons from the QD within a reservoir voltage range of 400mV.

keep the donor potential fixed relative to the reservoir Fermi level. The average slope we measure over the two donor transitions $\alpha_{G2}^{SET}\ (1 - \alpha_{G2}^{P}) \sim 0.23$ indicates that the effective lever arm of the tunnel coupled reservoir is $(1 - \alpha)$~35%, considerably higher than typical gate lever arm values of $\sim 5\%$ for planar capacitive gates in donor-defined nanostructures[107,108].

Importantly, such a large lever arm would allow the three single donor charge states (D^+, D^0, D^-) to be accessible within a relatively small voltage range of <250mV on the reservoir. Increasing the source voltage this much in the hybrid device is impractical, but such a large lever arm in an independently tunnel-coupled reservoir presents opportunities to deplete multi-donor clusters to their last electron.

4.2.7 Depletion of a multi-donor quantum dot with an independent reservoir

Next we demonstrate the utility of an independent tunnel coupled reservoir in another precision donor device, where the reservoir is separated from the source terminal of

the SET. Figure 4.12(c) shows an STM image of this device, including a larger multi-donor quantum dot (circled in blue), directly and *independently* coupled to a reservoir at a distance of 15nm. We sense the charge state of this multi-donor QD with an SET $\sim$ 30nm away. Despite a number of unintentional charge traps producing spurious offsets in the gate/reservoir stability diagram, Figure 4.12(d) shows 6 parallel discontinuities, with the expected positive slope, demonstrating the ability add or remove 6 electrons from this multi-donor QD with a modest span of the reservoir voltage of $\Delta V_{Res} = 400$mV. For comparison, depleting a few-donor quantum dot by 6 electrons using a capacitively coupled gate requires a voltage span of over 1600mV[65].

Note that increasing the reservoir voltage reduces the number of electrons, and that beyond $V_{Res} = 200$mV, no further lines are seen by the SET charge sensor, indicating that the dot is fully ionised. This proof-of-principle demonstration highlights the benefit of tunnel coupled reservoirs in terms of strong control over the charge state of the coupled charge island.

The previous section has outlined the effective use of a reservoir with RF reflectometry to sense the charge state of the coupled charge island. The principal shortcoming of this device as a *spin* sensor is that the reservoir directly coupled to a donor qubit offers no way of directly performing an energy dependent single-shot spin measurement. This is because to establish the quantum capacitance, an electron must repeatedly tunnel to and from the reservoir, losing its spin identity in the metallic sea of electrons of the reservoir. One way around this is to use a pair of charge islands, and engineer the system so that the electron to be read out only tunnels locally between the two. We describe such a device in the following section.

4.3 A few donor double quantum dot device

RF reflectometry is particularly promising for spin readout in a double quantum dot configuration[109,110]. In the single dot dispersive sensing case as demonstrated above in Section 4.2, the localised electron from the donor is repeatedly made to tunnel to a reservoir, and another electron (of random spin) may tunnel back to replace it. As such,

it is not possible to detect the spin orientation – tunnelling will quickly become blocked by a spin down electron within just a few periods of the RF drive frequency, regardless of the initial spin state.

For a coupled double quantum dot system the two electron eigenstates in the (0,2) charge configuration are the singlet s and triplet t^-, t^0, t^+ states. If the double dot is detuned into the (0,2) charge state, both electrons must share the same spatial wavefunction and the resulting exchange energy raises the energy of the t^0 state relative to s. An AC voltage can be used to attempt the charge state transition as sketched in Figure 4.13(a). AC charge motion occurs for an electron pair with anti-parallel spins, by tunnelling into the s state, but not for spin-parallel electrons as the t^+ and t^- states are higher in energy. This situation is called Pauli spin blockade. The presence of the AC current between the quantum dots appears as a modified quantum capacitance C_Q to an RF tank circuit. The moving electron remains localised in the double dot system without ever tunnelling to the reservoir, and so the s/t readout mechanism illustrated in Figure 4.13(a) is a non demolition measurement (simply meaning that the measurement process leaves the state projected into the measured eigenstate), permitting a 'single shot' measurement of the combined two electron spin state.

In a double quantum dot device that was previously investigated using transport spectroscopy[56], we now use RF reflectometry to extract detailed information on the electron tunnel rate for each charge state of the two quantum dots, beyond what is possible with DC measurements. We then demonstrate the singlet/triplet spin parity readout method and show that we have control over the exchange interaction between the two electron spin states. The double dot device was initially fabricated by Bent Weber. I worked with Matthew House to add a resonant circuit for RF measurements and we conducted the following experiments together. Thse results have been published in Nature Communications[2].

Figure 4.13(b) shows an STM image of the lithographic mask used to define this double quantum dot device. Source (S) and Drain (D) allow the passage of current serially through the two QDs. Two gates (G1 and G2) control the electrostatic potentials of the two quantum dots (D1 and D2). The inner region is shown at atomic resolution in Figure 4.7(c), indicating the distances and the AC tunnelling paths examined in our experiment, from reservoir to each individual dot (purple arrow) and interdot tunnelling (blue arrow). The figure also shows the diagonal offset in the position of the two dots

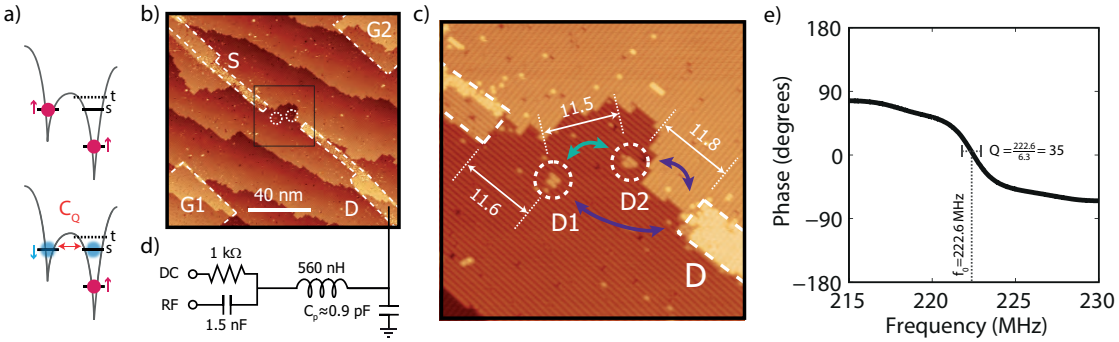

Figure 4.13: A double quantum dot device and RF measurement circuit. (a) Schematic energy level diagram for a double quantum dot at the (1,1) ↔ (0,2) charge transition. Tunnelling into the singlet ground state is not possible for electrons with parallel spins, but if the spins are opposite, AC tunnelling between the potential wells is possible, generating a capacitance C_Q. (b) STM image showing leads (S,D) and gates (G1,G2) surrounding the double quantum dot. An RF reflectometry circuit is attached to the drain terminal. (c) Simplified tank circuit schematic, showing the lumped inductor and parasitic capacitance which form a resonance at 222.6 MHz, and bias tee resistor and capacitor values. The external reflectometry circuit is similar to that shown in Figure 4.7 (d) High resolution STM image of the inner device region, showing the distances between source, D1, D2, and drain. The two dots are offset to allow independent control of the two QD potentials with the two gates.

with reference to the source and drain axis, which is optimised to provide independent electrostatic control over each dot by its respective gate[111]. The resonant circuit is connected to the drain, as shown in Figure 4.7(d), composed of a 560 nH inductor, which together with a parasitic capacitance, $C_P = 0.9\,\text{pF}$, forms a resonance at $f_0 = 222.6\,\text{MHz}$ with quality factor $Q \sim 35$. These values are obtained by measuring the reflected RF phase as a function of frequency in Figure 4.7(e). To allow DC biasing of the drain along with application of the RF signal, a simple RC bias tee is employed. The external measurement circuit is similar to that shown in Figure 4.7 in the previous section.

4.3.1 DC TRANSPORT THROUGH THE DOUBLE QUANTUM DOT

When we consider electron transport through a serially coupled double quantum dot, a DC current appears only near the triple points where three independent conditions that

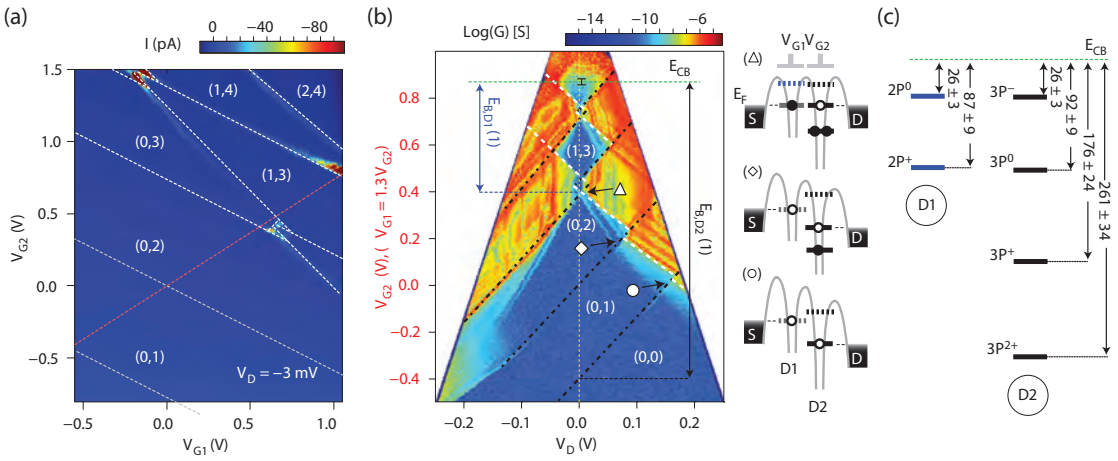

Figure 4.14: Electron transport spectroscopy in a double quantum dot. (a) Charge stability diagram displaying DC current through the double quantum dot at a source-drain bias of 3mV. (b) double quantum dot conductance as a function of bias voltage V_D and gate voltage along the red dashed line of part (a). The green dashed line at 0.86V on the gate axis, where Coulomb blockade fails, represents the conduction band energy and binding energies are measured relative to this point. White dashed lines with negative slope represent resonances between source Fermi level and a D1 transition potential, and black dotted lines resonances between drain E_F and D2 transition potentials. Insets show schematic energy level diagrams at the three locations indicated with triangle, diamond, and circle markers. (c) Measured binding energies for the 2P and 3P molecules in electron-volts, computed using the gate offset from E_{CB} scaled by the appropriate effective lever arm for the combined gate axis used. All parts of figure reproduced from Weber *et al.* [56]

must be met:

$$E_F^S \geq \mu_{D1}(N_1) \tag{4.25}$$

$$\mu_{D1}(N_1) = \mu_{D2}(N_2) \tag{4.26}$$

$$\mu_{D2}(N_2) \geq E_F^D \tag{4.27}$$

Here $\mu_{D_i}(N)$ represents the electrochemical potential for a transition on dot D_i between the N and $N-1$ electron charge state, and E_F^S and E_F^D the Fermi energy of source and drain respectively.

When these conditions are satisfied, small triangular regions of non-zero current arise as shown in the DC charge transport map obtained by Weber *et al.* [56] which we reproduce in Figure 4.14(a). The locations of individual charge transitions can be inferred by extending lines from the vertices of the bias triangles, to form the white lines displayed in Figure 4.14(a). These lines are a guide to the eye, and we note that the location of the

lowest two transitions are extrapolated by the following procedure: Figure 4.14(b) shows the DC transport current through the double dot as a function of source-drain bias and combined gate voltage taking a cut along the red line in (a). Here we see additional charge transitions appearing as 'shards' at the edges of the blockaded regions. Black dashed lines represent loading of an electron from the drain reservoir onto D2, and white dashed lines represent electron loading from the source to D1. By extrapolating a black line from the edge of the first shard, marked ∘ (where the energy level configuration is illustrated in the lower inset) through the $V_D = 0$ axis, we find the voltage where the first electron is loaded onto D2. The point where Coulomb blockade at zero bias breaks down (at the top of the plot) is taken to define the conduction band edge E_{CB}. The voltage distance to this point, converted to energy units by the appropriate lever arm, gives the binding energy of the first electron on D2 $E_{B,D2}(1) = 261\text{meV}$. The binding energies of each charge state can be extracted in a similar way to produce the spectrum shown in Figure 4.14(c). The electron numbers extracted are then mapped back onto the gate-gate map of Figure 4.14(a).

This method provides an estimate of the donor transition locations, but it is indirect, and so carries large uncertainties ($E_{B,D2}(1) = 261 \pm 34\text{meV}$).

4.3.2 Direct observation of single charge transitions with RF reflectometry sensing

In contrast, individual charge transitions of each quantum dot are clearly and directly visible with an RF reflectometry measurement, because AC tunnelling may occur when any one of the three resonance conditions (Equations (4.25) to (4.27)) is met. Figure 4.15 shows a comparison of the transport current (a) and changes in the phase (b) and amplitude (c) of the reflected RF signal as a function of the two gate voltages, all measured simultaneously. Without the need for guidelines as in Figure 4.14(a), the RF response directly shows the charge state transitions as bright lines. For example the phase response in (b) displays a clear line separating the (0,1) and (0,2) regions. The positions of these single dot charge transitions agree well with the positions estimated previously from the high bias DC measurements of Figure 4.14(b).

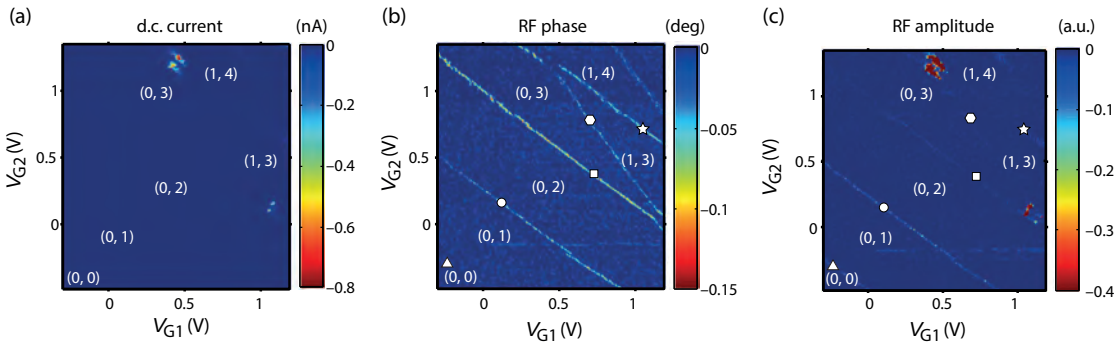

Figure 4.15: Improved visibility of single dot transitions in reflected RF phase and amplitude signals. (a) DC current, (b) RF phase change, and (c) amplitude offset relative to the background value. Numbers in brackets (N_1, N_2) indicate the number of electrons bound to D1 and D2 respectively. A bias of $V_D = -3$mV is applied. Transitions of the same dot appear as sets of parallel lines most clearly in the phase plot, except for at the lower electron number transitions where the amplitude signal is stronger. Shape markers denote transitions

4.3.3 Analysis of tunnel rates for different electron occupations

Variations in the dot-reservoir tunnelling rate can be distinguished with our RF reflectometry measurement because the relationship between tunnel rate and RF excitation frequency determines whether the response is dissipative (resistive) or dispersive (capacitive) in nature. Interestingly, in Figure 4.15, we see that most QD charge state transitions appear primarily in the phase response, except at the lower electron numbers, where they appear more strongly in the amplitude channel. Analysing these complementary pieces of information allows us to estimate the tunnel rates, providing valuable guidance on how to design future donor-based devices within a range of tunnel rates for optimal detection sensitivity and qubit operations.

To examine the tunnel rates in detail, Figure 4.16 plots the phase (a) and amplitude (b) responses of each of the five dot–lead transitions indicated with shape markers, as a function of the chemical potential of the dot relative to the Fermi level of the lead, $\Delta\mu$. Consider the first three of the transitions (hexagon, triangle, circle), one of D1 and the two lowest transitions of D2. Each have different peak phase and amplitude response, but

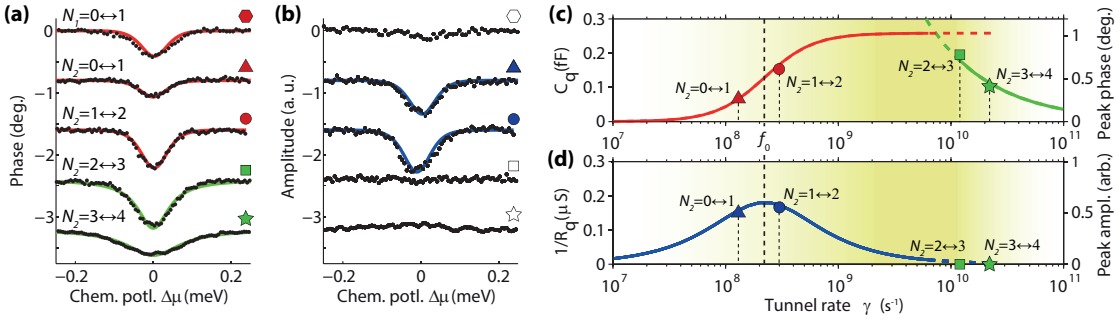

Figure 4.16: Tunnel rate determination by analysis of the reflected signal linewidths. Shape markers correspond to those in Figure 4.15. (a) Phase shift while scanning across each charge transition (normalised to a real energy detuning on the x-axis), each transition offset for clarity. Red curves on the lower electron number lines are fit to a thermally broadened model, green curves on the high electron number lines to a lifetime broadened model. (b) Amplitude response across the same transitions. Significant signal is only seen in the low electron number cases, where tunnel rates are on the order of f_0 (c) The extracted peak heights in the phase response for the $D2$ transitions plotted together, on a calibrated axis showing the expected quantum capacitance required to generate such a signal. (d) Equivalent analysis for the amplitude signal, mapped to the quantum conductance added by the AC tunnelling for each line in (b). The yellow shading represent the tunnel rate range where the dispersive phase response is greatest.

all three have the same width in $\Delta\mu$. This indicates that they are in the regime in which the width of the transitions is determined by the electron temperature, $\hbar\gamma \ll k_B T$, and the quantum capacitance and resistance are determined by Equations (4.21) and (4.22). At $\Delta\mu = 0$:

$$C_Q = \frac{\alpha'^2 e^2}{4k_B T}\left(1 + \frac{\omega^2}{\gamma^2}\right)^{-1} \tag{4.28}$$

$$R_Q = \frac{4k_B T}{\gamma \alpha'^2 e^2}\left(1 + \frac{\gamma^2}{\omega^2}\right) \tag{4.29}$$

We fit the measured peak response to estimate the tunnel rate γ for each transition.

- For the D1 transition, $N_1 = 0 \leftrightarrow 1$ (hexagon marker), the nonzero phase response indicates that the tunnel rate is at least on the order of the drive frequency, but it is still less than the thermal energy (as the peak is not thermally broadened). The lack of amplitude response can be explained because the AC tunnelling is occurring to and from the source lead, and reflectometry on the drain lead is insensitive to energy dissipation in the other half of the device. Consequently we estimate a tunnel rate $\gamma \sim 1 \times 10^9 - 1 \times 10^{10}\text{s}^{-1}$.

- The first transition of D2, $N_2 = 0 \leftrightarrow 1$ (triangle), has a reduced phase response but a significant amplitude response, an indication that the tunnel rate is close to the drive frequency $f_0 = 222.6$MHz. As such we estimate a tunnel rate of $\gamma \sim 1 \times 10^8 \text{s}^{-1}$.

- The second transition, $N_2 = 1 \leftrightarrow 2$ (circle), is similar but with a larger phase response, indicating a faster tunnel rate. We therefore estimate $\sim 2.5 \times 10^8 \text{s}^{-1}$.

The peak phase response of the two transitions of D2 are plotted together against the tunnel rate estimates as a red triangle and circle in Figure 4.16(c). The peak amplitude responses are plotted in Figure 4.16(d) along with red and blue curves that are an empirical fit to Equations (4.28) and (4.29) based on those two data points. Note that we plot the inverse of the quantum tunnelling resistance $1/R_Q$, since the conductance relates approximately linearly with the peak amplitude response.

In contrast, the two highest electron number transitions of D2, $N_2 = 2 \leftrightarrow 3$ (square) and $N_2 = 3 \leftrightarrow 4$ (star), have responses that are broader than the others in $\Delta\mu$, an indication that the tunnel rate is larger than the thermal energy, $\hbar\gamma \gg k_B T$. No amplitude response is expected in this regime since the AC conductance is effectively zero. Here the quantum capacitance can be defined as[106]:

$$C_Q = \frac{\alpha'^2 e^2}{\pi} \left(\frac{\hbar\gamma}{\hbar^2\gamma^2 + \Delta\mu^2} \right) \tag{4.30}$$

$$\tag{4.31}$$

By fitting this equation to these two transitions (green square and star), we estimate tunnel rates of $2.2 \times 10^{10} \text{s}^{-1}$ and $1.1 \times 10^{10} \text{s}^{-1}$, and these points are also plotted on Figure 4.16(c).

The tunnel rate analysis on the four D2 charge state transitions in particular demonstrates that tunnel coupling changes significantly for each electron transition, from $\sim$ 100MHz for the first electron to $\sim$ 22GHz for the fourth. As electrons are added to the few-donor quantum dot, the multi-electron wavefunction expands spatially[65,112,113]. Since the tunnel coupling depends on the wavefunction overlap, this produces a larger tunnel rate, exemplified in Figure 4.16(c,d). The yellow shading in the figure illustrates the full range of tunnel rates over which reflectometry detection is most favourable.

Frequency dependent response

We further examine the RF response at each of these five transitions, by measuring the reflected phase and amplitude over a range of drive frequencies out to 4MHz either side of the $f_0 = 222.6$MHz resonance, as shown in Figure 4.17. There are qualitatively three types of behaviour across the five transitions shown, and we show a schematic for each case representing the qualitative change in the resonance curve alongside each subplot.

- In the high tunnel rate case $\gamma \gg f_0$ (square, hexagon, star markers), the AC tunnelling between the dot and drain reservoir is non-dissipative, contributing only a quantum capacitance which lowers the resonance frequency. As we saw in Figure 4.9, a lower resonant frequency translates to a negative shift in the reflected phase for frequencies either side of f_0. This is observed in Figure 4.17(a,d,e). The amplitude peak due to the resonance also shifts lower in frequency, meaning that the amplitude increases below f_0 and decreases above f_0, which we observe as a bi-modal response in Figure 4.17(f,i,j).

- For the case of intermediate tunnel rate $\gamma \gtrsim f_0$ (circle marker), there is both a capacitive and resistive component to the response, but the capacitance dominates. The outcome is a negative shift in resonance frequency combined with a small damping of the resonance. We observe only a negative phase response in Figure 4.17(c), slightly skewed to frequencies below f_0. The amplitude response in Figure 4.17(h) only exhibits a very weak positive signal below resonance and a stronger positive shift at and above f_0.

- With a slower tunnel rate $\gamma \lesssim f_0$ (triangle marker), the resistive effect dominates instead. The result is significant damping with only a slight shift in resonance frequency. In Figure 4.17(b) we observe a weak bipolar signal confirming a damped resonance, and the amplitude response in Figure 4.17(g) is negative across all frequencies.

In summary, we have examined the relationship between electron tunnel rates and the resulting RF reflectometry response. For tunnel rates below the resonant frequency ($< 2.2 \times 10^8 \mathrm{s}^{-1}$), electrons cannot tunnel fast enough to respond to the RF drive voltage, and reflectometry is not an effective method. For large tunnel rates ($> 1 \times 10^{10} \mathrm{s}^{-1}$, e.g. $N_2 = 3 \leftrightarrow 4$), the measured phase shift becomes broader and smaller in magnitude as the

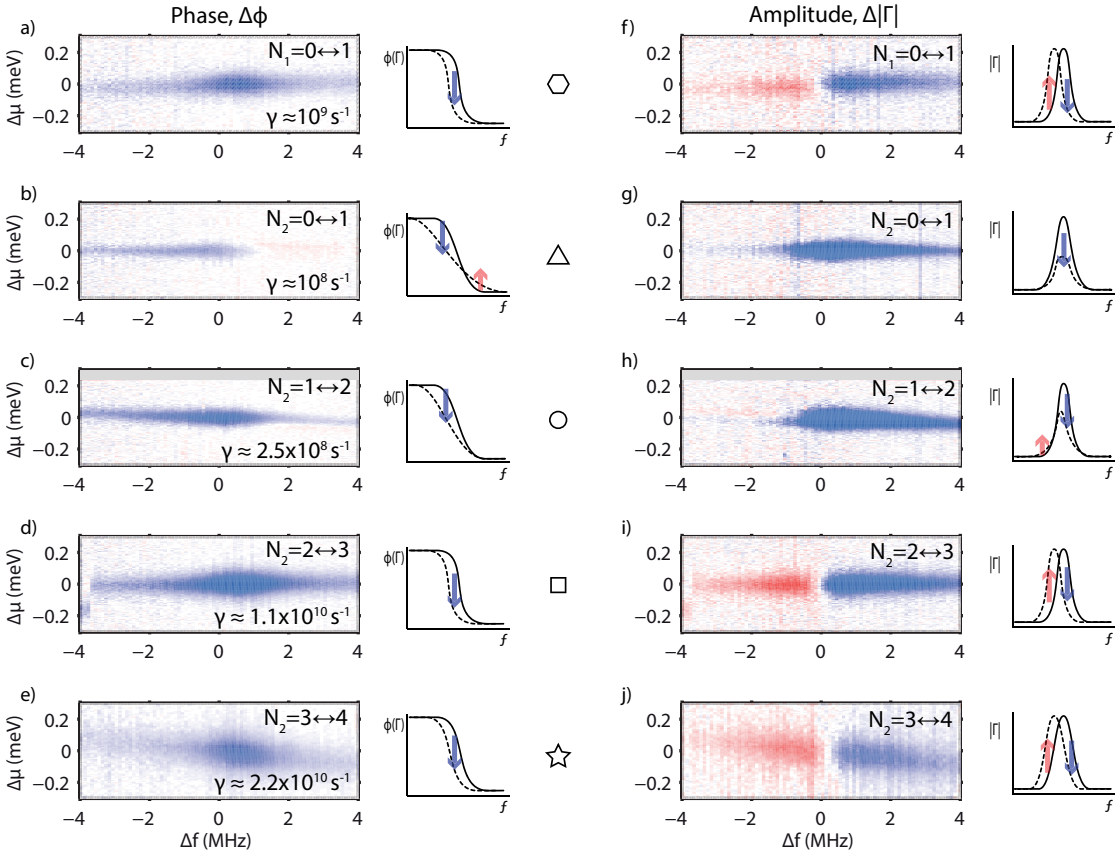

Figure 4.17: Frequency dependence of phase and amplitude response for different tunnel rates. (a-e) Phase shift while scanning across each charge transition, as a function of detuning potential and RF drive frequency. All but (b) show purely negative phase response. With a low tunnel rate, (b) shows a bipolar response above and below $\delta f = 0$ as here the dissipative resonance damping effect becomes significant. (f-j) Amplitude response across the same transitions. Significant asymmetric response is seen in the high tunnel rate cases (f,i,j) where the added C_Q shifts the system to a lower effective resonance frequency. Blue indicates a negative shift, red a positive shift relative to the background value.

quantum dot becomes less well confined, and the resonance becomes lifetime broadened. Future donor-based devices should be designed to have tunnel rates in the middle range for optimized RF detection. This optimal zone is shaded yellow in Figure 4.16(c,d) representing the range 1×10^8 to $1 \times 10^{10}\text{s}^{-1}$ in the current setup. The optimal range could however be broadened by reducing the electron temperature (which increases the effective quantum capacitance and phase shift) or lowering the resonant frequency of the reflectometry circuit (which allows for sensing of slower tunnelling events).

4.3.4 Pauli spin blockade and dispersive singlet triplet state readout

In DC transport measurements of this double quantum dot device, Weber *et al.*[56] previously observed Pauli spin blockade at the (1, 3) to (0, 4) charge transition, visible as a suppression of current at the triple point with bias voltage applied in one direction, but not the other.

Figure 4.18(a) and (b) show the two bias directions. In Figure 4.18(a), electrons tunnel from $D2 \rightarrow D1$, and since the (0,4) state is filled from the metallic drain reservoir, an electron with appropriate spin can form the (0,4)s singlet state. A strong DC current flows at the base of the bias triangles where the dot potentials are equal. However, in Figure 4.18(b), with the opposite bias, electrons must flow the other way $D1 \rightarrow D2$. If, in the (1,3) charge state, the single electron of D1 and the unpaired electron of D2 have parallel spins, the system is said to be in Pauli blockade, since tunnelling to the singlet ground state is forbidden by the Pauli exclusion principle. Only if the triplet excited states t^-, t^0, t^+ enter the bias window is the blockade lifted – as evidenced by the finite current seen at the point of the bias triangles in Figure 4.18(b). The distance from this point to the triangle's base provides a measure of the singlet triplet exchange energy for the (0,4) charge confiiguration $\Delta_{ST} = 8 \pm 1\text{meV}$.

Just as Pauli blockade can suppress DC current, it will also suppress AC charge motion, as has been observed by Schroer *et al.*[110] in an InAs nanowire device shown in Figure 4.18(c). Gates V_{LP}, V_M, V_{RP} are used to locally deplete the nanowire, confining single electrons to two quantum dots. With a resonant circuit attached to one end of

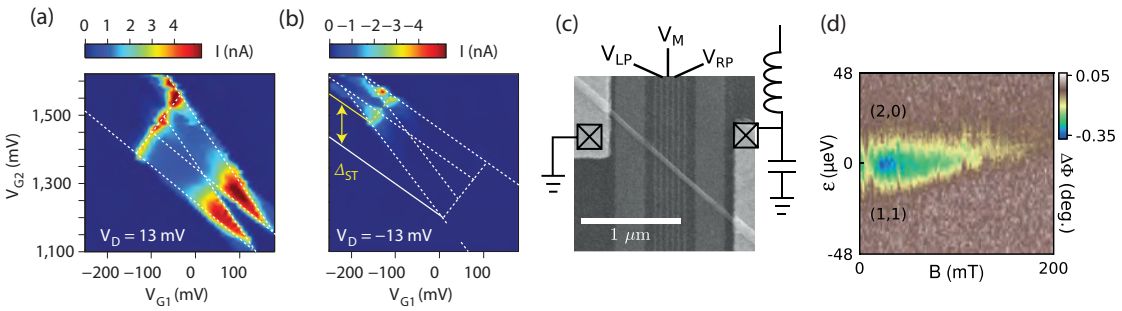

Figure 4.18: Pauli blockade and the singlet-triplet exchange energy in double quantum dots. (a) High bias DC transport current through our double quantum dot at the $(1,3) \leftrightarrow (0,4)$ charge transition. Bias triangles exhibit current flow for the forward bias case where electrons tunnel from the (0,4) state to (1,3) (b) Suppressed current within the bias triangles for the reverse bias, as tunnelling from (1,3) into (0,4) is only allowed if the single electron on D1 is anti-parallel to the unpaired third electron of D2, so that transport can proceed through the singlet ground state of D2. The system is Pauli blockaded by a pair of parallel spins, preventing current flow, unless the bias exceeds the singlet-triplet energy difference. Reproduced from Weber *et al.* [56]. (c) SEM image of a gated InAs nanowire double quantum dot device, with reflectometry circuit. Reproduced from Schroer *et al.* [110]. (d) Reflected phase signal of the InAs device at the (1,1) $\leftrightarrow$ (2,0) transition as a function of magnetic field. At zero field the groundstate of the two isolated spins is the s singlet, such that tunnelling between the charge states is allowed. With increasing field, the t^- triplet state energy decreases, eventually becoming the ground state, at which point the reflectometry signal disappears. Reproduced from Schroer *et al.* [110].

the nanowire, an RF signal drives AC tunnelling between the two dots, producing a quantum capacitance and associated phase shift signal as shown in Figure 4.18(d). Here the reflected phase signal varies as a function of magnetic field and the electrochemical potential detuning between the two dots $\epsilon = \mu_2 - \mu_1$. For zero magnetic field, the singlet state s is the spin ground state for both the (1,1) and (2,0) charge configurations, and when the potential of these states are equal, AC tunnelling is present – as evidenced by the phase shift due to the added quantum capacitance in the double quantum dot. As B increases, the energy of the t^- state is reduced, eventually becoming the spin ground state in the (1,1) configuration above $\sim$ 100mT, and beyond this point, AC tunnelling is suppressed by Pauli blockade – the quantum capacitance, and hence the phase shift, disappears.

In our planar donor defined double quantum dot, we operate with an additional 2 'spectator' electrons on D2, paired up with zero total spin, so the dynamics are the same as for a simple two electron system. Inter-dot tunnelling is a distinct process from dot-reservoir tunnelling, so we must now consider the relationship between quantum

capacitance and the interaction strength of the two dots.

The quantum capacitance for the singlet state at the inter-dot transition[109] obeys:

$$C_Q = -\alpha_\epsilon^2 e^2 \frac{\partial^2 E(s)}{\partial \epsilon^2} \tag{4.32}$$

$$= -\alpha_\epsilon^2 e^2 \frac{\partial^2}{\partial \epsilon^2}\left(\sqrt{(\frac{\epsilon}{2})^2 + t_c^2}\right) \tag{4.33}$$

$$= -\frac{\alpha_\epsilon^2 e^2 t_c^2}{4}\left(\sqrt{(\frac{\epsilon}{2})^2 + t_c^2}\right)^{-\frac{3}{2}} \tag{4.34}$$

where the detuning ϵ is the difference in energy between the (0, 4) and (1, 3) charge states, $\alpha_\epsilon = \alpha_{D1} - \alpha_{D2} = 0.32\text{meV/mV}$ is the geometric factor that relates ϵ to the voltage on lead D, α_{D1} (α_{D2}) is the effective lever arm of the drain reservoir over $D1$ ($D2$), and $E(s) = -\sqrt{(\frac{\epsilon}{2})^2 + t_c^2}$ is the dispersion relation for the singlet state, illustrated by the lower red line in the energy level diagram of Figure 4.19(a). In the diagram, an anticrossing is seen between the $(1,3)s$ and $(0,4)s$ singlet states with a width of $2t_c$. The tunnel coupling t_c defines the intrinsic interaction energy at zero detuning. The triplet states, which are all degenerate at zero magnetic field, do not anticross, since the $(0,4)t$ states are separated by a large onsite exchange $\sim 8\text{meV}$ as established in Figure 4.18(b).

We see the effect of the interdot quantum capacitance C_Q in Figure 4.19(b), showing the reflected phase response at the (1,3) $\leftrightarrow$ (0,4) transition. Taking a cut along the axis marked ϵ, produces the resonance curve plotted in (c). Since the phase response is proportional to C_Q, we fit the width of this peak to Equation (4.34) (red curve), providing a direct measure of the inter-dot tunnel coupling $t_c = 47 \pm 5\mu\text{eV}$. This improves on the estimate of $\sim 200\mu\text{eV}$ given by Weber *et al.*[56], which was based on a multi-parameter fit to resonant tunnelling data.

4.3.5 Control over the inter-dot tunnel coupling strength

In Figure 4.19(d), we repeat the measurement of the inter-dot transition with a magnetic field B=2 T applied. Here we see that the inter-dot phase response disappears

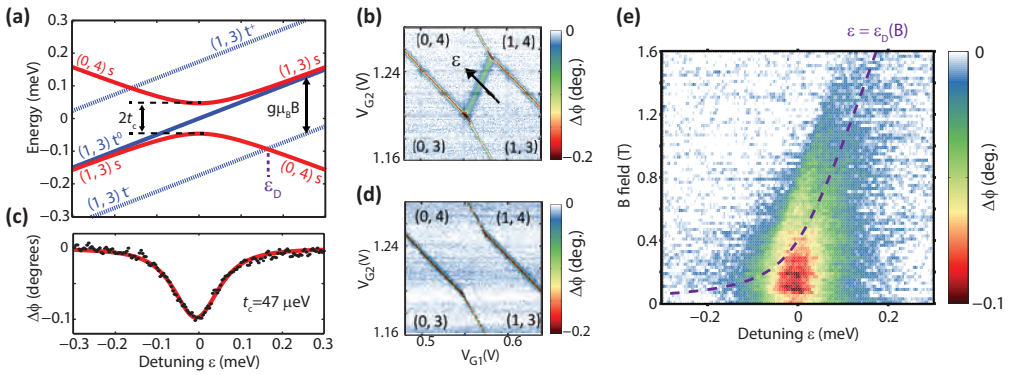

Figure 4.19: Readout of singlet and triplet spin parity states and inter-dot tunnel coupling measurement. (a) Schematic showing the eigenstates of the effective two electron system (assuming the first two electrons on D2 are non-interacting) as a function of the detuning energy ϵ (b) Phase response at the inter-dot transition between (1,3) and (0,4) charge states, reflecting localised AC charge motion. (c) Line trace cutting the inter-dot resonance along the black arrow in (a). Red line is a fit to Equation (4.37). (d) Suppressed phase signal in the same regions with the application of a magnetic field $B = 2$T (e) Transition from singlet to triplet ground state with increasing B field. The dashed line represents the degeneracy point ϵ_D.

completely. This can be understood because the magnetic field has lowered the $(1,3)t$ state in energy so that it is the ground state at $\epsilon = 0$. This state, shown by the blue line in Figure 4.19(a) has a linear dispersion relation, hence $\partial^2/\partial\epsilon^2 = 0$ and there is no quantum capacitance. In other words, Pauli blockade prevents tunnelling into (0,4) so there is no AC charge motion and no measured phase response in this case.

Finally, we examine the onset of Pauli blockade as the magnetic field is increased in Figure 4.19(e). The plot shows how the inter-dot phase response varies with respect to detuning energy and applied magnetic field. We map out the singlet–triplet ground-state transition, which occurs at a detuning ϵ_D as indicated in (a) at the intersection of the s and t^- lines. The phase response disappears at high B when the ground state of the system becomes the t triplet state. This crossing point occurs at a different magnetic field value for each point in detuning according to the equality:

$$E(t^-) = E(s) \tag{4.35}$$

$$\frac{\epsilon_D - g\mu_B B}{2} = -\sqrt{(\frac{\epsilon_D}{2})^2 + t_c^2} \tag{4.36}$$

$$B = \frac{2\sqrt{(\frac{\epsilon_D}{2})^2 + t_c^2} + \epsilon_D}{g\mu_B} \tag{4.37}$$

The dashed line overlaid on the phase data indicates this singlet–triplet degeneracy point $B(\epsilon_D)$ and is plotted by setting $t_c = 47\mu$eV as extracted above, and using the electron g-factor in silicon g=2. We see that the disappearance of the phase response matches well with the expected ground-state transition dependence on B and ϵ. The degeneracy line is asymmetric with respect to detuning, which we expect because the exchange energy $J = E(t^0) - E(s)$ is smaller when the electrons are separated in the (1, 3) configuration and increases as the detuning field pushes them towards the (0, 4) transition. The Zeeman energy at which the phase response disappears at each detuning point constitutes a direct measurement of the exchange energy across the charge degeneracy line, which changes from about 20μeV to 120μeV over the observed range in this measurement. Since we have seen[56] that the exchange energy is as high as 8meV at high detuning, these results demonstrate that we can control the exchange energy by almost 3 orders of magnitude in donor-based double quantum dots using monolayer-doped, in-plane gates.

These results show the promise of donor defined QDs towards the implementation of a two qubit gate operation, where the exchange interaction must be switched by at least 2 orders of magnitude with precise control in both time and energy[114]. Future work will develop precise time resolved control over J and address the competing effects of unwanted co-tunnelling in and out of the dots, as well as nuclear spin interactions which may impact coherent exchange coupling.

4.4 Conclusions and outlook

We have demonstrated complementary charge sensing methods in a deterministic single donor device fabricated at the atomic scale by STM hydrogen resist lithography. DC charge sensing with a capacitively coupled SET provides an indirect readout of the donor charge state, only visible at a discrete number of charge triple-points. In contrast, RF reflectometry provides fundamentally more information based on the quantum tunnelling capacitance and resistance that accompanies lossless and dissipative AC charge motion.

We have shown that a single terminal can function as electron reservoir, gate, and dispersive sensor. Using a hybrid device, we performed a direct comparison of the

charge sensing behaviour of the dispersive reservoir sensor to a traditional SET. The reflectometry signal provided clear distinguishability between our intentionally placed single P donor and an accidental charge trap. One significant advantage of the RF method is continuous sensitivity across the entire gate-space. Charging events can be observed at all degenerate points in the gate-space, not just at specific triple-points.

We demonstrated that the electrostatic coupling of a tunnel coupled reservoir is many times greater than that achievable with capacitively coupled gates. The large lever arm ($\alpha \sim 0.35$) we observed is desirable in terms of addressability in multi-qubit devices, and because it permits greater control over the charge state of a donor quantum dot within a smaller voltage range.

We showed, by analysing the amplitude and phase response of charge transitions across different electron numbers in a double quantum dot device, that RF reflectometry has potential to probe the tunnel coupling strength between donors or other electrically isolated structures.

We performed singlet-triplet state readout based on Pauli spin blockade using the RF reflectometry technique, and also demonstrated control over the exchange copuling from 20μeV to 120μev, an important first step toward achieving two qubit interactions in donor devices.

These considerations, as well as the small footprint of the dispersive reservoir sensor, position RF reflectometry as a crucial tool for scalable single electron charge sensing in atomic scale donor based qubit devices.

5

Addressable and coherent operations on interacting donor electron spin qubits

Single electron spin states have been observed in numerous single donor and few donor precision quantum dot devices in recent years, and in these devices extremely high spin readout fidelity ($> 99\%$) has been demonstrated using SET charge sensors[55]. The localised electron cannot be properly described as a qubit however, without the ability to *control* its spin state. This chapter details the achievement of qubit control using electron spin resonance (ESR) techniques, and the first demonstration of single qubit gates in an atomically precise donor nanostructure. With the long term goal of scalability in mind we have performed single qubit operations in a device architecture consisting of two qubits. This has allowed us to demonstrate a means of addressing individual qubit operations although they are separated by less than 20nm, and to observe the onset of interaction between two donor-defined qubits.

After a review of spin resonance experiments on phosphorus donor electron spins, and a number of schemes for addressing individual qubits, the results presented in this chapter concern two similar 'two qubit' devices, shown in Figure 5.1(a) and (g). In both, we employ a DC-coupled SET charge sensor, for single shot spin readout.

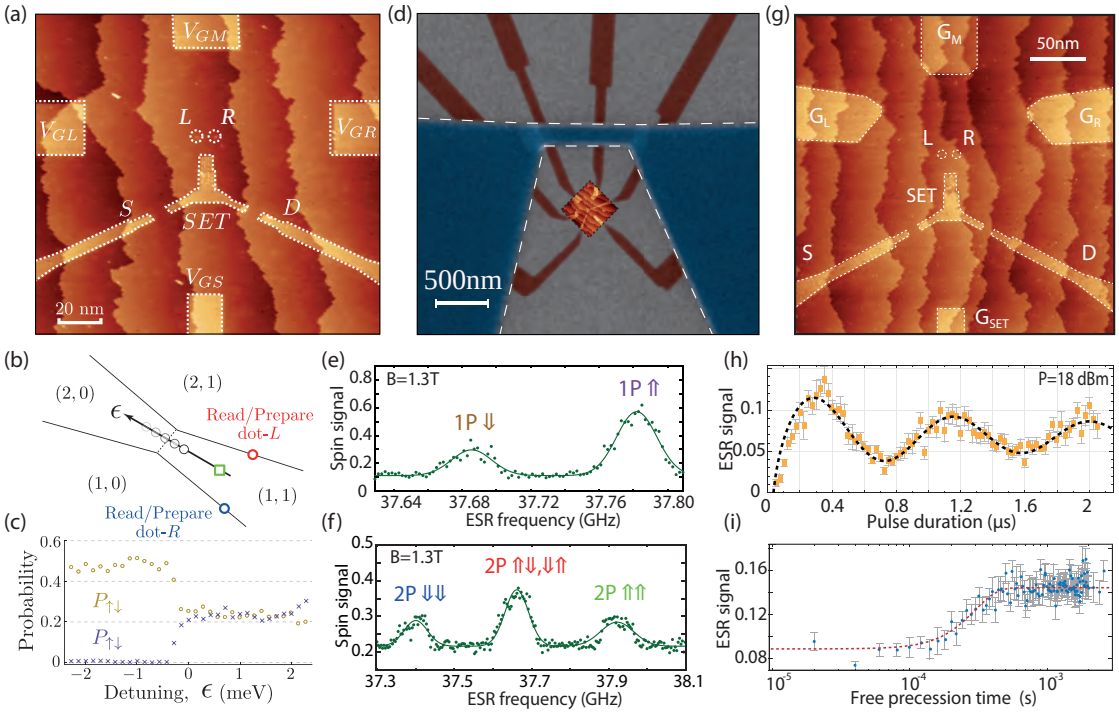

Figure 5.1: Overview of the devices and key results of this chapter. (a) STM image of the 1P/2P two qubit device used for the first two major results of this chapter. (b) Schematic stability diagram indicating operating points for independent readout and initialisation of the two qubits, and (c) anti-correlated spin states indicating the onset of a spin-spin interaction between them. (d) Fabrication of a microwave antenna registered to the location of the qubits. (e) Electron spin resonance spectrum of the 1P qubit showing two peaks – due to the spin up and down nuclear states. (f) the 2P molecule spectrum, showing three peaks – due to the four spin states of two nuclear spins (g) STM image of the second two-qubit device used for the final set of results in this chapter. (f) Coherent rabi oscillations of an electron spin state, and (g) the onset of decoherence as a function of time.

In the first part of the chapter we characterise the electron spin states of the device pictured in Figure 5.1(a) which is a 1P/2P double quantum dot device. We quantify the spin relaxation behaviour through independent initialisation and readout around the $(0, 2) \leftrightarrow (1, 1)$ charge state transition as indicated in Figure 5.1(b), and examine the onset of the exchange interaction between the two qubits as shown in Figure 5.1(c), critical in establishing a non-interacting regime in which to perform the following single qubit experiments.

In the second part of the chapter we describe the integration of a broadband microwave antenna, carefully registered to the atomic scale features, shown in figure Figure 5.1(d)

to apply an oscillating magnetic field and drive resonant electron spin rotation. We measure the electron spin resonance spectrum of the 1P and 2P qubits, characterising the hyperfine interaction between the qubit electron and its 1P or 2P donor host nuclei. The ability to selectively operate on a chosen qubit cannot be taken for granted, particularly with a spatial separation of < 20nm. Here we demonstrate the effectiveness of qubit addressability based on having a different number of donor atoms for each electron qubit, giving a unique in-built hyperfine energy, where each electron responds to a unique set of frequencies as illustrated in Figure 5.1(e,f).

The 1P/2P device was successfully characterised before an electrical discharge damaged the antenna. As a consequence, a nominally similar device, shown in Figure 5.1(g) was made. The latter part of this chapter demonstrates controlled spin rotations with a maximum Rabi frequency $\omega_R \approx 1.18$MHz, displayed in Figure 5.1(h). This coherent control allows us to measure the electron dephasing time $T_2^* \approx 300$ns and decoherence time $T_2 \approx 300\mu$s, shown in Figure 5.1(i) for the first time in a planar, donor-defined precision qubit device.

These results represent the first demonstration of full single qubit operation in a wholly donor-defined precision nanostructure capable of high fidelity initialisation and readout. Together with controllable interactions our results provide a major advance in the development of a donor-based atomic-scale quantum computer.

5.1 Electron spin resonance and decoherence in donor ensembles and single donors

To contextualise our results, we begin with a review of spin resonance measurements made on phosphorus donor electron spins in bulk silicon and more recent observations of electron spin qubit behaviour for single donors implanted within nanoelectronic devices.

5.1.1 Donor bound electron ensembles in natural and isotopically purified silicon

Electron spin resonance on an ensemble of donor-bound electron spins in bulk silicon is not a new technique, the first measurements were made in the late 1950s[115,116]. These earliest measurements provided values for the T_1 relaxation time of greater than 10s for temperatures below 4K and for the T_2 decoherence time, 240μs in natural silicon containing a phosphorus donor concentration of $3 \times 10^{16}\,\mathrm{cm}^{-3}$ and at 1.4K. Indeed these long (compared to other candidate qubit systems) relaxation and coherence times was one of the key motivations behind the seminal proposal of Kane[45] in 1998. More recent measurements with improved instrumentation and lower donor concentrations have provided extensive information about the mechanisms causing decoherence and relaxation at different temperature and donor concentration[117], isotopic purity of the silicon[118], and the angle of the crystal axes[119] relative to B_0. The measurements, at the simplest level, involve placing a sample containing a certain concentration of donors (in modern experiments typically on the order of $1 \times 10^{15}\,\mathrm{cm}^{-3}$) in a cryostat and within a large external magnetic field B_0. An AC magnetic field B_1 is applied perpendicular to B_0 in resonance with the Larmor precession of the electron spins, which in the rotating wave approximation appears as an effectively static magnetic field, and so causes the spins to rotate about the X axis in their rotating reference frame. Before an experiment begins the electron spins are in an equilibrium distribution, with some thermal excitations across the ensemble but the majority in the ground state, and so it is convenient to consider the ensemble average spin state. The measured 'echo intensity' signal in the following bulk ESR literature is due to the transverse component of the net magnetic moment of the ensemble precessing about the B_0 field and thereby inducing an AC current in a sensor coil.

Spin resonance pulse sequences

We briefly describe two canonical pulse sequences used to measure relaxation T_1 and decoherence T_2 timescales in bulk ESR experiments. These are shown in 5.2(a).

Hahn Spin Echo To measure the T_2 decoherence time, the B_1 field is pulsed on and off in a spin echo sequence named after its inventor[120] – shown in the top panel of

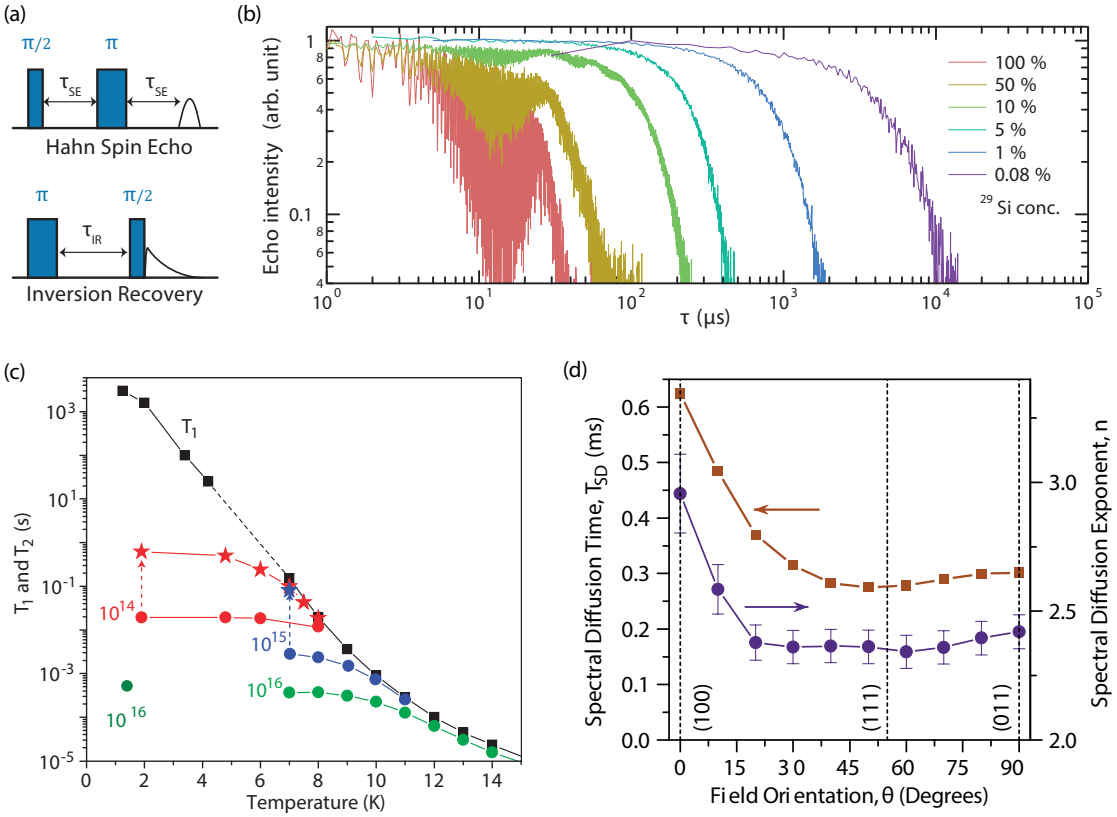

Figure 5.2: Electron spin coherence in bulk ensembles of ^{31}P donors. (a) schematic of the inversion recovery sequence commonly used to measure T_1 spin relaxation and Hahn spin echo sequence to measure T_2 spin decoherence. (b) Hahn echo data reproduced from Abe *et al.* [118] showing extension of the spin coherence out to beyond 1ms with reduced ^{29}Si isotope concentration. (c) T_1 and T_2 data reproduced from Tyryshkin *et al.* [117] indicating the dependence on temperature and donor concentration. Squares are T_1 values bounding the circular T_2 data points for high temperatures. At lower temperature the T_2 time saturates. Stars indicate measurements made to suppress residual dipole-dipole mediated decoherence (see text) (d) spectral diffusion limited T_2 data reproduced from [119] showing a dependence on magnetic field orientation relative to the crystal axes of the characteristic spectral diffusion time and decay exponent (see text)

5.2(a). This begins with a $\pi/2$ pulse to place the magnetisation vector in the transverse plane. Since each electron in the ensemble experiences a slightly different local B_0 field due to differing local nuclear spin environments and dipole interactions with other electrons, they all precess at different frequencies, dephasing over a wait time τ_{SE}. At this point a π pulse is applied to flip every spin, effectively reversing the direction of dephasing. Provided that each individual electron has remained independently phase coherent, after a second and equal wait time, all electrons in the ensemble will have recovered their individual phase offsets and the net magnetisation will produce a strong signal, the echo of the initial transverse magnetisation following the π pulse. If the wait time τ_{SE} is beyond the coherence time T_2 of the electron spins, the second wait period will not undo the effect of the first, and no clear echo will be observed. The initial echo intensity decays to $1/e$ the peak value when $\tau = 2\tau_{SE} = T_2$.

Inversion Recovery To measure the T_1 relaxation time, the B_1 field is pulsed on and off in an 'inversion recovery' sequence shown in the lower panel of 5.2(a). The sequence begins with a π rotation to invert the equilibrium ground state population, leaving a majority of electrons in the excited state. After a variable delay time τ_{IR}, a $\pi/2$ pulse projects any remaining excited spins onto the transverse plane where the net magnetisation vector precesses, emitting a rotating dipole field that excites a signal current in the sensor coil. For $\tau_{IR} < T_1$, the full inversion is seen in the readout signal, while for larger delay times the signal decays as relaxation processes recover the inversion before the second pulse occurs. A fraction $1/e$ of the peak signal remains when $\tau_{IR} = T_1$.

Spectral diffusion in isotopically natural silicon

A dominant cause of decoherence for donor bound electrons is the presence of uncontrolled magnetic field fluctuations due to the bath of randomly fluctuating nuclear spins surrounding the electron – termed the Overhauser field effect[121]. Silicon has three naturally present isotopes, two of which are spin free: ^{28}Si and ^{30}Si; only ^{29}Si, which has a natural abundance of 4.7%, has a nuclear spin 1/2 and contributes to Overhauser field fluctuations. Abe *et al.*[118] measured electron spin coherence in a series of samples – bulk P doped silicon with varying concentration of the ^{29}Si isotope, the result is reproduced

in Figure 5.2(b) which shows an echo intensity as a function of the wait time τ in a Hahn spin echo experiment. In 99.2% ^{29}Si, the coherence is extremely short-lived ($T_2 \approx 10\mu$s - red curve), natural isotopically abundant silicon (with around 5% ^{29}Si - teal curve) displays $T_2 \approx 200\mu$s, and when the ^{29}Si concentration is reduced to less than 1% (purple curve), the coherence is extended further to $>$ 1ms. The inverse relationship between ^{29}Si concentration and T_2 is attributed to 'spectral diffusion' caused by the fluctuating bath of ^{29}Si nuclear spins. Temporal fluctuations in the local B_0 field for each electron in the ensemble are caused by random flip-flops of pairs of nuclear spins interacting via the dipole-dipole interaction, in agreement with a theoretical model proposed by Witzel *et al.* [122] [123]. They argue that this mechanism persists also in the case of a single electron spin qubit in natural silicon [124] since the nuclear spin bath environment remains the same moving from an ensemble of many donor bound electrons to a single isolated electron. Decoherence in the prescence of spectral diffusion is described by a non-exponential echo intensity decay of the form [119]:

$$I = \frac{I_0}{\exp\left[2\tau_{SE}/T_{2e} + (2\tau_{SE}/T_{SD})^n\right]} \tag{5.1}$$

where a characteristic spectral diffusion time T_{SD} and the exponent n describe the spectral diffusion process, and the simple exponential term containing T_{2e} encompasses other residual decoherence effects. Both T_{SD} and n are sensitive functions of the electron wavefunction density at the flip-flopping nuclear spin sites. It was found by Tyryshkin *et al.* [119] (in a natural silicon sample with P donor density $8 \times 10^{14}\,\mathrm{cm}^{-3}$ and at 8K) that the exponent n varies between 2 and 3, depending on the crystal orientation in the magnetic field, as shown on the right hand axis (circles) of Figure 5.2(c). Here they also observed that the associated characteristic spectral diffusion time (left axis; squares) is maximised with the B_0 field aligned to the [100] crystal axis, reflecting the anisotropy of the underlying electron-nuclear dipole-dipole interaction as predicted by the theory.

Residual decoherence effects in isotopically purified silicon

Knowing that spectral diffusion is the dominant cause of decoherence in P donor electron spins at low temperature in silicon of natural isotopic abundance, the results above have motivated the use of isotopically purified ^{28}Si, to significantly extend the coherence time. Experiments by Tyryshkin *et al.* [117] have examined the remaining decoherence

after removing the majority of ^{29}Si – in samples with as little as 50ppm residual ^{29}Si. They measured the T_1 relaxation rate using the inversion recovery sequence as a function of temperature, observing variation by 8 orders of magnitude from $\sim$ 2000s at 1.2K to $\sim 20\mu$s at 15K, as shown by the black squares in 5.2(d). Relaxation is understood to be due to phonon mediated interactions between valley states – termed 'valley repopulation' at low temperatures[116], and dominated by a so-called Orbach process above $\sim$ 7K[125].

Figure 5.2(d) also displays T_2 measurements of three samples with varying P donor concentration (red: $1 \times 10^{14}\,\mathrm{cm}^{-2}$, blue: $1 \times 10^{15}\,\mathrm{cm}^{-2}$, green: $1 \times 10^{16}\,\mathrm{cm}^{-2}$) as a function of temperature, showing that the coherence time is T_1 limited above 10K. At increasingly lower temperatures, T_2 saturates at a value dependent on the P density. The red curve, with lower donor density saturates at a higher value of T_2. The inverse relationship shows that in the absence of a nuclear spin bath, the now dominant decoherence mechanism is an interaction with neighbouring donor electrons within the ensemble. The effect becomes weaker as the distance between donor sites increases, and hence the coherence time improves with reduced donor density, from the green circles, through blue, to red with the lowest P concentration. The saturation arises because of small instantaneous changes in one electron's effective B_0 field, due to the effect of other nearby electron spins being flipped (by the applied ESR echo pulses). The total effect for each spin is unique depending on the exact local arrangement of donors, and so is similar to spectral diffusion, yet changes only occur at the moments ESR pulses are applied, and so this effect is known as 'instantaneous diffusion'[126]. It is evident that instantaneous diffusion, unlike spectral diffusion, is not applicable in the case of a single donor spin – since there is no bath of nearby dipolar coupled electrons.

The starred data-points in 5.2(d) represent the application of a strategy to mitigate instantaneous diffusion by reducing the duration of the ESR pulses (replacing a 180° rotation with a 14° rotation), at the cost of a reduced overall signal intensity. The authors extrapolate their result (toward zero angle rotations) to claim an effective $T_2 = 1$s with infinitely short ESR pulses. Of course this is not practical, but by removing the effect of dipolar interactions with other donors, gives an idea of the timescale achievable with a single electron qubit ESR experiment, as opposed to an ensemble. This effect of instantaneous diffusion has been a motivating factor behind alternate strategies for reading out ensemble spin resonance signals electrically[127] or optically[128] (rather than detecting the magnetic moment directly), so that the density and total number of spins

can be reduced while retaining a signal strong enough to measure. The optical strategy in particular has been effective in achieving highly polarised initial states and consequently strong signals even with very low P concentration ($< 1 \times 10^{12}\,\mathrm{cm}^{-2}$), extending the current state of the art T_2 time for electrons to over 3 minutes[37].

5.1.2 Single electron spins in nano-structures

Performing a spin resonance experiment on a single electron requires the ability to measure the spin projection of the single electron. Although a single electron magnetic moment is too small to easily observe directly, the measurement can be done by mapping the spin state to a charge state and then observing the charge state with a device sensitive to single electron charges.

Single spin resonance pulse sequences

We now briefly describe three spin resonance experiments, using a single spin. These are illustrated in 5.3(a). The principal difference here compared to the ensemble case is that the readout relies on the longitudinal (Z) projection of the spin state, and not the transverse (X-Y) component, and that being a single quantum state, a single measurement can have only one of two outcomes. Hence the experiment must be repeated numerous times to determine the probability of projecting into either eigenstate. The set of repeated measurements forms a 'temporal ensemble', which can exhibit inhomogeneous broadening phenomena analogous to spatial spin ensembles, despite there being only one real electron spin present.

Rabi Oscillation To calibrate the strength of the applied oscillating magnetic field (Rabi field), cyclic rotations of the spin vector can be observed in two ways. A B_1 pulse is applied at a certain power level for a certain duration τ_{pulse} before being measured, as shown in the left panel of 5.3(a). The angle of rotation of the electron's spin vector, away from its initial state, is proportional to the product of the field magnitude and τ_{pulse}. Varying either one will change the Z-projection of the final state in a periodic way, producing oscillations in the measured spin.

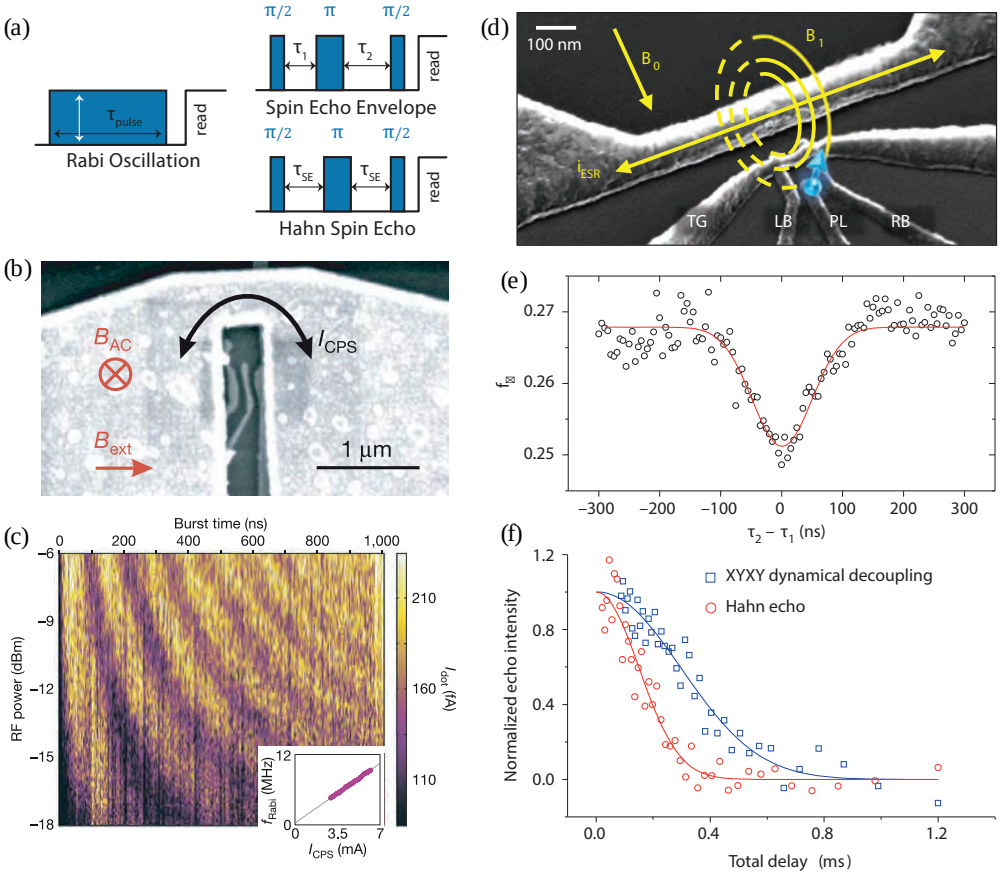

Figure 5.3: Previous studies of electron spin resonance on single electron spins in nanostructures. (a) Schematic diagrams outlining the Rabi driven spin rotation, spin echo linewidth, and Hahn echo sequences (see text). (b) Reproduced SEM image of the device used by Koppens *et al.* [30] showing the microwave antenna encircling the gate defined quantum dot beneath it. (c) Rabi oscillation data reproduced from Koppens *et al.* [30] illustrating the duration and power dependence of coherent electron spin rotations. (d) Reproduced SEM image of the device used by Pla *et al.* [49] showing how a single donor from amoung ~ 30 implanted P atoms is tunnel coupled to a readout SET, and next to a microwave antenna. (e) Spin echo envelope and (f) spin echo measurements reproduced from Pla *et al.* [49], measuring $T_2^* = 55$ns and $T_2 = 206\mu$s timescales of a single donor electron qubit.

Spin Echo Envelope To measure the T_2^* dephasing time, a spin echo sequence shown in the top panel of 5.3(a) is used. This begins with a $\pi/2$ pulse to place the magnetisation vector in the transverse plane. The temporal ensemble then dephases over an initial wait time τ_1. At this point a π pulse is applied to reverse any phase accumulation. By varying the secondary wait time τ_2, the shape of the spin echo can be observed. When $\tau_1 = \tau_2$, the phase accumulation will be fully cancelled out, and a final $\pi/2$ pulse returns the spin to a proper eigenstate before being read out. As the time difference $|\tau_1 - \tau_2|$ increases, the spin vector is not perfectly returned to an eigenstate, the $1/e$ point revealing the timescale over which the temporal ensemble dephases T_2^*.

Hahn Spin Echo To measure the T_2 decoherence time, the three pulse sequence is applied with equal wait times as shown in the top panel of 5.2(a). Although each electron in the temporal ensemble experiences a slightly different local B_0 field due to differing instantaneous local nuclear spin environments, the spin echo ensures that any phase accumulation is refocused. If the total wait time 2τ is beyond the coherence time T_2 of the electron spins, the second wait period will not undo the effect of the first, and no clear echo will be observed. The initial spin projection decays to $1/e$ the peak value when $\tau = 2\tau_{SE} = T_2$.

Single electron spin resonance in nano-electronic devices

The earliest quantum electronics experiments on single electron states were performed in gallium arsenide (GaAs), facilitated by the higher electron mobility achievable in that material[27,28]. Coherent rotation of a single electron spin within a nano-structured device was first achieved by Koppens *et al.*[30] in a GaAs quantum well, depleted locally by surface gates to form a single electron quantum dot. Their experiment was performed in a double quantum dot and Pauli spin blockade was used as a readout mechanism (a DC version of the technique presented in Section 4.3.4). Here they initialise into a spin-blockaded $(1, 1)$ triplet state where the two electron spins are parallel, and readout the combined spin state by attempting to move the system into the $(0, 2)$ charge state. Since the $(0, 2)$ triplet state is much higher in energy than the $(0, 2)$ singlet, in the absence of any driven spin rotation, the charge state does not change, but if one spin is rotated such that the two are antiparallel, the readout projects them into the (0,2) singlet and

the associated charge motion is sensed as a net current flow through the double quantum dot.

In this way, coherent rotation of the electron spin was observed by applying a microwave frequency signal, resonant with the Zeeman splitting, fed directly to an on-chip antenna seen in Figure 5.3(b). The resulting AC current through the end of the antenna generated an oscillating magnetic field B_1 at the QD location inside the loop of the antenna. The probability of projecting into the singlet state fluctuates as the rotation angle varies, producing so called Rabi oscillations as a function of both pulse duration and pulse power (illustrated in Figure 5.3(a)). Their Rabi oscillations as a function of both microwave burst time and microwave power is reproduced in Figure 5.3(c), with the inset plotting the Rabi frequency $f_R = \gamma_e B_1$ at each power setting by fitting a decaying sine wave to the data based on a phenomenological numerical model taking into account spectral diffusion by sampling from a Gaussian distribution of nuclear Overhauser field values. At the highest power (-6dBm) a π rotation was achieved in 54ns, indicating an effective $B_1 = 1.9$mT.

The singlet-triplet double dot readout method benefits from the large exchange energy (410μeV in their device) producing Pauli spin blockade, much larger than thermal excitations at 100mK, and allowing operation at small magnetic field and resonant microwave frequency (~ 100mT, ~ 0.5GHz). The same method has also been been used together with ESR in silicon quantum dots[129], to investigate the interaction of spin and valley states. The limitation of the Pauli blockade method is that a single shot measurement is in general not possible, because the readout signal is the net current produced by a train of repeated spin manipulation and readout sequences, and each sequence contributes on average approximately one electron to the measured current. This limits the maximum wait time during a spin echo experiment. Already at a repetition rate of 500kHz, the current contrast $I = ef$ is around 80fA, and any spin manipulation or echo sequence with a duration significantly greater than 1μs would reduce the current below measurable levels.

Despite this limitation, Koppens *et al.*[130] determined the dephasing time with a spin echo envelope sequence, finding $T_2^* \approx 30$ns. Additionally a Hahn spin echo experiment showed the T_2 decoherence time to be ~ 290ns, limited by spectral diffusion due to nuclear spin fluctuations. Note that in GaAs, there are no spin-zero isotopes of either atomic species, and hence spectral diffusion cannot be combated with isotopic purifi-

cation. Techniques have been developed however to dynamically polarise nuclear spins within the volume of a single electron quantum dot, suppressing spectral diffusion[33,131]. With careful timing of refocusing spin echo pulses to take advantage of resonances in the Larmor precession of the three nuclear isotope species (^{69}Ga, ^{71}Ga, ^{75}As) they could effectively rephase the nuclear spin bath, to extend the T_2 time in GaAs quantum dots to $> 400\mu$s[132,133].

Single electron spin resonance in silicon devices

Pla *et al.*[49] achieved electron spin resonance on a single electron hosted by a single, randomly positioned P donor in natural silicon. In this device, a small number of donors (30 in an area 90nm $\times$ 90nm) donor were implanted using a 14keV ion beam, into the substrate, prior to fabricating a MOSFET readout sensor above the donors. Here the readout mechanism did not involve a second electron, rather the Zeeman splitting was used directly to discriminate the spin states through spin dependent tunnelling to a many electron quanrum dot formed below the oxide layer in the MOSFET device, operating as a single electron transistor[94] to allow single shot measurements.

The microwave frequency B_1 signal was applied by a surface antenna, pictured in Figure 5.3(d). This antenna geometry was optimised to efficiently produce a B_1 field without causing heating or oscillatory electric fields[134]. This consideration was critical given the small Zeeman energy at 1.79T ($\sim 200\mu$eV) and moderate thermal energy at 300mK ($\sim 25\mu$eV), so as not to degrade the initialisation and readout operations. Being a donor electron bound to a ^{31}P nuclei, this experiment observed two resonance peaks separated by the hyperfine interaction energy A, one peak associated with the nuclear spin down state $\Downarrow$, one with the nuclear up $\Uparrow$. The maximum achievable B_1 field strength in their device, 0.12mT, was determined by extracting the rabi frequency from a Rabi oscillation experiment. Note that although this is less than the value achieved in the GaAs experiment outlined above, the microwave frequency here is on the order of 50GHz, compared to $< 1GHz$ used by Koppens *et al.*[30]. With a π rotation time of $\sim$ 75ns Pla *et al.*[49] performed a spin echo envelope experiment on the donor bound electron, shown in Figure 5.3(e). The negative peak is the maximum spin echo signal achieved when

$\tau_1 = \tau_2$, and a fit of the data to a Gaussian form (red curve):

$$f_\uparrow = C_1 - C_2 e^{-\left(\frac{\tau_2 - \tau_1}{T_2^*}\right)^2} \tag{5.2}$$

with fit parameters C_1, C_2 gives the dephasing time $T_2^* = 55$ns, beyond which the phase accumulation in the two delay periods are no longer equal and opposite.

Being natural silicon, spectral diffusion due to ^{29}Si nuclear spin fluctuations limits the coherence time just as it does in spin ensembles. Circular points in Figure 5.3(f) show the onset of decoherence in the spin echo signal following a Hahn echo sequence. For short times, the nuclear Overhauser field is approximately static and the sequence recovers any accumulated phase. For longer times, the echo becomes ineffective since flipping ^{29}Si nuclear spins result in unequal effective B_0 in the two halves of the sequence and coherence is lost. The decay (red curve) is fit to

$$f_\uparrow = C_1 - C_2 e^{-\left(\frac{t}{T_2}\right)^n} \tag{5.3}$$

resulting in a T_2 of ~ 200s, and an exponent $n = 2.1 \pm 0.4$, consistent with the spectral diffusion model[124].

The effect of fluctuating nuclear spins can be 'dynamically decoupled' from the electron spin by a series of additional echo pulses. These pulses correct for phase accumulation within shorter windows of time, thereby combating slow changes in the Overhauser contribution to B_0. There exist a whole family of dynamical decoupling pulse sequences to extend coherence in this way[135–137] (a common technique in NMR science). Pla *et al.*[49] demonstrate that T_2 may be extended with an XYXY echo sequence[138,139], replacing the single π rotation about the X-axis of the Bloch sphere used by the Hahn echo sequence (Figure 5.3(a)), with four π rotation pulses, alternately about the X and Y axes. As shown by the blue squares in Figure 5.3(f) this sequence extends the coherence to around 410μs.

Muhonen *et al.*[38] repeated these measurements for similar devices (again with a randomly positioned atom out of ~ 30 in a 90×90nm area) but with the donor atom embedded in isotopically enriched ^{28}Si, with only 800ppm residual ^{29}Si atoms. They achieved a considerable improvement in the coherence time of a single donor within a nano-device, similar to that previously observed for bulk donor ensembles by removing

the nuclear spin bath[36]. In two similar ^{28}Si devices Muhonen *et al.*[38] observed a five-fold improvement in the electron coherence time, achieving $T_2 = 1$ms in a Hahn echo experiment, extending to over 0.5s with the so called 'CPMG' dynamical decoupling sequence[136]. Muhonen *et al.*[38] also examined the decohrence mechanisms in their devices. Without numerous coupled electron spins (as there are in ensemble measurements) there is no significant instantaneous diffusion mechanism. At low temperature and B-field the T_1 time is greater than seconds[94], so the decoherence is not relaxation limited. The authors attribute the remaining decoherence to magnetic field noise intrinsic to small losses in the superconducting magnet and thermally generated noise producing kHz frequency fluctuations in the antenna's contribution to the B_0 field.

5.2 Addressability of donor-bound electron qubits

A critical requirement of any multi-qubit system is the addressability of each individual qubit site, so that gate operations applied to one qubit do not affect its neighbours. This selectivity cannot be taken for granted in donor systems where the spatial separation of qubits may be as small as $10 - 20$nm[54]. For spin qubits, addressability is achieved by selective detuning – ensuring each qubit experiences a unique and/or controllable effective Zeeman field B_0, and thereby a unique and/or controllable Larmor resonance frequency. Here we review several methods to achieve the required detuning proposed in the recent literature before outline the strategy we employ in this chapter.

5.2.1 Externally applied magnetic field gradient

Micromagnets offer one solution to addressing electron spin qubits. Used in GaAs[140–142] and SiGe[41,143] quantum dot devices, ferromagnetic cobalt micromagnets produce a slant-

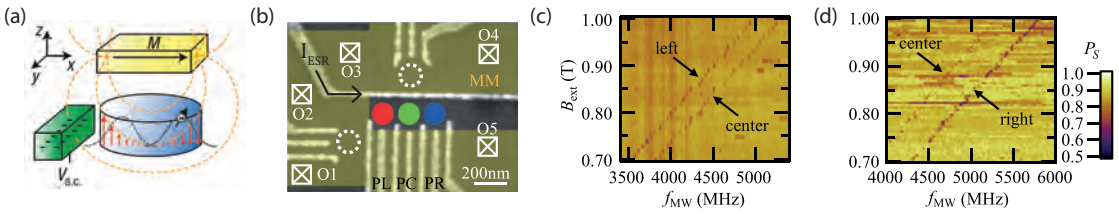

Figure 5.4: Detuning electron spin resonance with a micromagnet. (a) Schematic showing the slanting B field of a micromagnet (yellow) across a quantum dot (blue), used to produce an oscillating field (red arrows) when the electron is moved laterally by an AC voltage applied to a gate (green). Reproduced from Pioro-Ladriere *et al.* [142]. (b) GaAs device of Noiri *et al.* [144], displaying three gate defined quantum dots (red, green, blue). The yellow overlay indicates the footprint of the 250nm layer of cobalt forming the micromagnet. The upper white circle is a sensor quantum dot used to readout the triple dot charge state, and the wire passing above the quantum dots carries an AC current I_{ESR} that produces a B_1 field to rotate the electron spins. (c,d) Spin resonance maps plotting the probability of returning to the initial singlet state after an ESR pulse at frequency f_{MW} and in an external field $B_0 = B_{ext}$. Here only two dots are interacting at a time, so (c) shows resonance lines for the left and centre quantum dots, and (d) shows resonances for the centre and right dots. (c,d) reproduced from Noiri *et al.* [144].

ing Zeeman field at the location of the quantum dots, as illustrated in Figure 5.4(a). The technique was implemented first in quantum dots to facilitate electric dipole spin resonance (EDSR), where an AC electric field applied to a gate (green), moves the quantum dot (blue) wavefunction back and forth laterally within the slanting Zeeman field of the micromagnet (yellow). A confined electron therefore experiences an effective oscillating magnetic field as it is displaced, as indicated by the red arrows in Figure 5.4(a). The EDSR effect has been used as an alternative to direct ESR control over the spin of an electron, and is capable of driving extremely fast ($t_\pi < 10$ns) single qubit rotations[42,141].

Aside from engineering a B_0 gradient for the purpose of driving EDSR, Noiri *et al.* [144] employ a micromagnet, positioned on the surface of a GaAs triple quantum dot, to detune the ESR resonances of the three quantum dots. Their device is shown in Figure 5.4(b), and consists of three gate defined quantum dots, below a nanowire which carries a current I_{ESR} used to produce an oscillating magnetic field to drive single spin rotations via ESR. The upper white circle indicates the location of an RF-SET readout device, capable of sensing the charge state of the triple quantum dot system. Spin to charge conversion in their experiment is via Pauli spin blockade, and so a pair of electrons are initialised in the left and centre QDs into the ground-state of the micromagnet field $|\downarrow,\uparrow\rangle$. After an ESR pulse the spin pair is read out by trying to move the two electrons into one

QD. If the initial state has remained, the anti-parallel spins will form the low energy singlet, and the charge state change is detected by an RF-SET sensor, hence the high level background of Figure 5.4(c). If either electron, left or centre, has been rotated by resonant ESR excitation, there is a triplet component to the final state $|T^+\rangle = |\uparrow,\uparrow\rangle$ for example if the left spin has been rotated from down to up. In this case Pauli spin blockade prevents the two electrons from occupying the same QD, and a reduced readout signal is seen, producing two parallel lines, shifted by the detuning $\Delta B_0 \approx 50\text{mT}$ provided by the micromagnet. Figure 5.4(c) shows a similar pair of resonances, for the centre and right dots, who experience a greater Zeeman field difference, hence a larger separation. The authors have developed the technique further, recently demonstrating scalability of the scheme to four quantum dots[145]. The method may have limited applicability to donor qubits however, since the typical inter-donor separation is at least one order of magnitude less than that of electrostatically defined quantum dots. As a consequence, the detuning achievable with such a micromagnet field gradient, ΔB_0, may be less than the resonant linewidth due to spectral diffusion in natural silicon.

5.2.2 Dynamic Stark tuning with a variable electric field

The original donor based qubit proposal of Kane[45] posited the use of an 'A-gate' above each donor, designed to attract the electron wavefunction toward the surface and thereby reduce the wavefunction overlap at the donor site as sketched in the insets of Figure 5.5(a). The effect is to reduce the hyperfine coupling strength A, which modulates the nuclear resonance frequency with changing gate voltage as indicated by the plot. Although in Kane quantum computer the nuclear spins were designated as qubits and the electrons merely a means of detuning nuclei, the same idea can be applied if the electrons themselves are the qubits.

The mechanism, referred to as 'Stark tuning' (a general term for electric field induced detuning) was first demonstrated experimentally in bulk silicon using an ensemble of ^{121}Sb donors[147], observing a detuning of the hyperfine interaction A of 0.3% per MV^2/m^2. Calculations for phosphorus[148,149] have predicted a similarly strong effect of

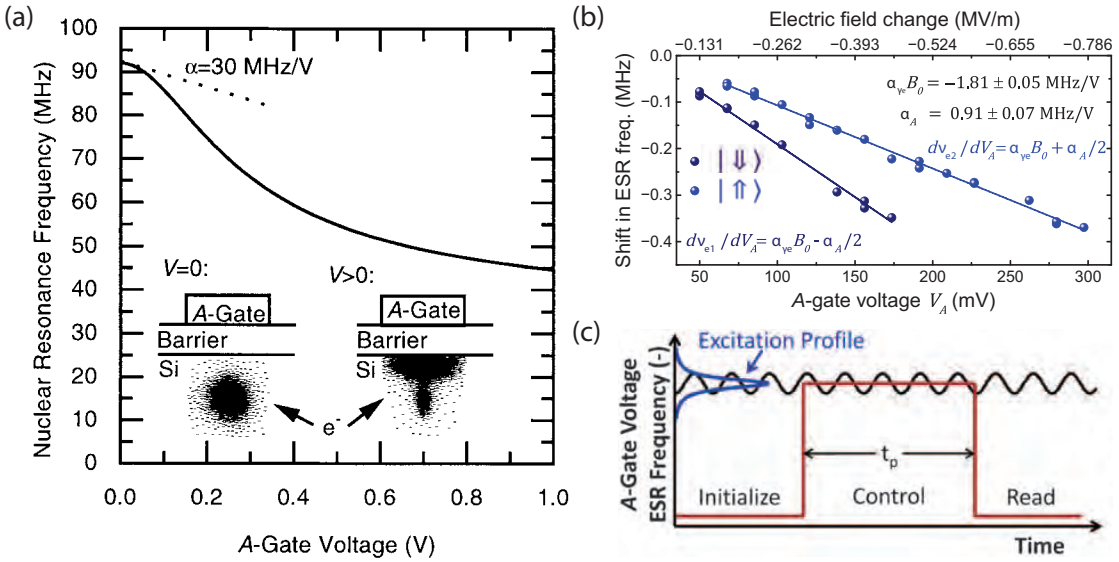

Figure 5.5: Stark tuning of the Hyperfine interaction. (a) Proposal for Stark tuning of the donor nuclear spin resonance frequency as a function of the voltage applied to an A-gate above the donor. Reproduced from Kane [45] The frequency is detuned from the $V = 0$ value as the bound electron is pulled further toward the silicon surface as pictured in the insets, reducing the strength of the hyperfine interaction. (b) Measured Stark shift of the resonance frequencies of a single electron bound to a P donor in ^{28}Si. The two lines correspond to the nuclear spin up and down states. Linear fits provide the stark shift coefficients for the hyperfine coupling (α_A) and gyromagnetic ratio ($\alpha_{\gamma e}$). (c) Scheme for pulsed ESR via dynamic Stark detuning in a continuous AC magnetic field. Spin control pulses are applied electrically to the A-gate, switching the electron spin in and out of resonance with an always-on oscillating B_1 magnetic field. (b,c) reproduced from Laucht *et al.* [146]

$0.2 - 0.3\%$ per MV^2/m^2. With a value of $A \approx 117$ in bulk silicon [71], at realistic device electric fields $\sim$ 1MV/m, the achievable Stark shift was expected to be less than the donor electron linewidth in natural silicon [118] ($\sim$ 6MHz), and so likely requiring ^{28}Si for the effect to be visible.

Laucht *et al.* [146] demonstrated Stark tuning with a single P donor in ^{28}Si. The measured ESR resonances are shown in Figure 5.5(b), the two lines showing the Stark shift of the two nuclear spin state resonances, labelled $|\Uparrow\rangle, |\Downarrow\rangle$. The resonant frequencies are given by:

$$\nu_{e1} = \gamma_e B_0 + \frac{A}{2} \tag{5.4}$$

$$\nu_{e2} = \gamma_e B_0 - \frac{A}{2} \tag{5.5}$$

where both $A = \alpha_A V_A$ and $\gamma_e = \alpha_{\gamma e} V_A$ are assumed to be linearly dependent on the A-gate voltage V_A. The fact that both resonances decrease with A-gate voltage indicates that the Stark effect on the gyromagnetic ratio γ_e is dominant over the hyperfine shift in their device. Fits to the data produce Stark shift coefficients $\alpha_A \approx 0.91\text{MHzV}^{-1}$ and $\alpha_{\gamma e} B_0 \approx -1.81\text{MHzV}^{-1}$. The authors relate these voltage dependent values to electric field via finite-element modelling of electrostatic fields in the device geometry, converting the hyperfine stark shift to ~ 2.4MHz per MV/m, consistent with theoretical expectations[149].

Further to observing the Stark shift, Laucht *et al.*[146] demonstrated its use in addressing an individual qubit in a 'global' control field, by applying an always-on oscillating magnetic field, so as to drive spin rotations, but detuned from the electron resonance. The scheme is illustrated in Figure 5.5(c), Since the maximum achievable resonance detuning is ~ 200 times greater than the electron's resonant linewidth of 0.5kHz in isotopically enriched ^{28}Si, there is effectively no B_1 field experienced by the qubit while it remains outside of the excitation profile. A voltage pulse on the A-gate then Stark tunes the electron into resonance with the driving field, for a duration t_p before again switching the electron out of resonance. Since the AC magnetic field may be left running continuously, it is easy to see that this method scales effectively to large numbers of qubits[47]. Each simply requires a dedicated A-gate to address the electron in and out of resonance with the global microwave B-field.

5.2.3 Intrinsic hyperfine detuning in donor molecules

An alternative to externally modulating the electric field to change the hyperfine interaction is to impart each qubit with an intrinsic hyperfine offset. Büch *et al.*[54] proposed a multi-qubit addressable architecture in which neighbouring electron spin qubits are hosted by small quantum dots where the confining potential for each is supplied by a small donor 'molecule'. Here the term 'molecule' refers simply to 1, or 2, or up to potentially several donors in close proximity (within the Bohr radius of P in silicon: 2.5nm), such that the electron wavefunction is spread over multiple nuclei. Single electron wavefunctions for example $1P, 2P, 3P$ and $4P$ molecules calculated by Wang *et al.*[150] using

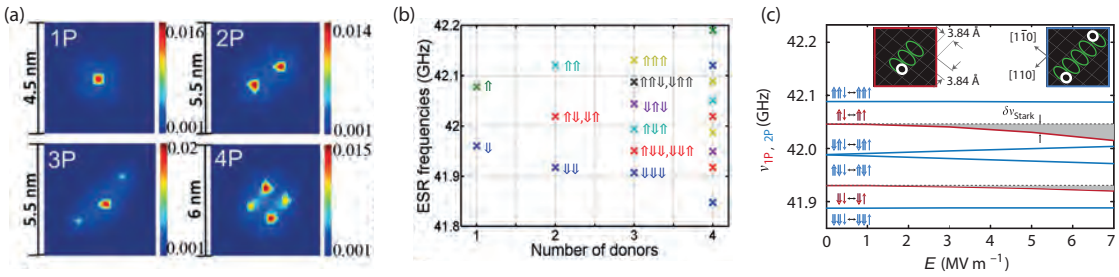

Figure 5.6: In-built hyperfine addressability of few donor molecules. (a) Simulated wavefunctions for 1P, 2P, 3P and 4P donor molecules, showing the probability density (in nm^{-3}) as a function of position. Reproduced from Wang *et al.* [150]. (b) Calculated single electron spin resonance frequencies for the 4 configurations in (a), in a Zeeman field $B_0 = 2$T. Nuclear spin states are labelled for the 1, 2 and 3 donor cases. Reproduced from Wang *et al.* [150]. (c) Calculated Stark shift of 1P and 2P electron spin resonance frequencies. Insets at top indicate the particular atomic configuration, with white circles indicating substitutional phosphorus in the square grid representing the silicon [100] crystal plane. The plot highlights a much larger intrinsic hyperfine difference between the two molecules than Stark shift in the single donor spectrum (grey shading). Reproduced from Büch *et al.* [54].

tight-binding model numerical simulations over a 30nm × 30nm multi-million atom domain[151] are shown in Figure 5.6(a).

The colour-maps plot the probability density distribution (in nm^{-3}), showing dense regions centred at the positions of the nuclei, connected by regions of lower but finite density. Based on the contact hyperfine interaction:

$$A = \frac{2\gamma_e\gamma_N\mu_0}{3}\sum_j^n |\Psi(\vec{R}_j)|^2 \tag{5.6}$$

proportional to the sum of the wavefunction densities Ψ over all n donor sites for each configuration, Figure 5.6(b) indicates the expected electron resonance frequencies in a magnetic field of 2T. Each donor molecule has a natural in-built 'address' in terms of its resonant frequencies. In the absence of an electric field there are two resonances for $1P$, three for $2P$, six for $3P$ and 9 for $4P$ and the nuclear spin states are labelled for the 1, 2 and 3 donor cases. Degenerate pairs such as $\Uparrow\Downarrow$ and $\Downarrow\Uparrow$ are split by an electric field, as indicated in Figure 5.6(c). Here we see the electron spin resonances expected for 1P (red) and 2P (blue) molecules as a function of E field, showing separation of the degenerate anti-parallel nuclear states with increasing E. The figure highlights an important limitation for single P-P addresability. The intrinsic hyperfine shift (separation between blue and red lines) between 1P and 2P molecules of ∼50MHz is significantly larger than

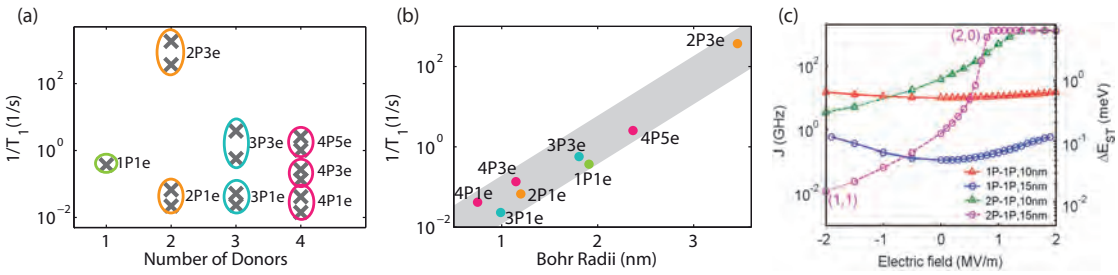

Figure 5.7: Long spin relaxation times and tunable exchange in few donor molecules. (a) Calculated electron spin relaxation rates $1/T_1$ for 1, 3 and 5 electron spin states in $1P$, $2P$, $3P$ and $4P$ donor molecules. Crosses indicate maximum and minimum values across various spatial configurations of the few P atoms. (b) The average relaxation rate in each set of configurations plotted as a function of the average representative Bohr radius of the molecule. (a,b reproduced from Hsueh *et al.* [152]) (c) Tunability in the exchange coupling J for qubits at a distance of 10nm or 15nm, in the case of symmetric single donors $1P-1P$, and asymmetric $1P-2P$ qubit pairs. The asymmetric cases display increased tunability as a function of electric field, up to 5 orders of magnitude as the charge state is detuned from (1,1) toward (2,0) in the 15nm separated $1P-2P$ case.

the achievable extrinsic Stark shift of <10MHz ($\delta\nu_{Stark}$ – grey shading), particularly at realistic electric fields ~ 3MV/m.

The strength of the hyperfine interaction depends not only on the number of donors, but also on the exact relative positions of the 2 (or more) donors confining the electron. Wang *et al.* [150] predict a variation in just the 2P hyperfine energy from a maximum of 387MHz – more than double the single donor value for a 2P cluster at the smallest separation of 0.4nm, down to 57MHz, roughly half single donor value at separation greater than ~ 4nm between the two P atoms.

Single electrons hosted by multiple donors are also expected to benefit from extended spin relaxation times T_1 compared to that of a single donor, since the deeper potential well provides stronger confinement and reduced interaction with the surrounding crystal lattice and weaker electron-phonon coupling [152]. Figure 5.7(a) plots the relaxation rate $1/T_1$ calculated by Hsueh *et al.* [152] by numerical simulation of the electron-phonon Hamiltonian for the (odd numbered) m electron spin-1/2 state bound in a molecule of $n = 1, 2, 3$ or 4 P donors (labelled $nPme$) in a B field of 2T. The exact values are sensitive to the relative positioning of donors within a molecule, and so crosses represent the extreme cases for molecules with small and large inter-donor separation. If we view the average relaxation rate as a function of the average molecular Bohr radii in Figure 5.7(b), we see that the rate is approximately proportional to the extent of the wavefunction,

Spin state	T_1 Theory (min − max)	T_1 Experiment	Reference
$1P1e$	2.5s	1.4s	Watson *et al.*[55]
$2P1e$	(15s − 50s)	6.7s	Watson[153]
$2P3e$	(0.5ms − 3ms)	20ms	Watson[153]
$3P1e$	(20s − 50s)	10s	Watson[153]
$4P3e$	(0.4s − 1s)	0.3s	Büch *et al.*[54]

Table 5.1: Comparison between calculated and measured T_1 spin relaxation times of few electron spin-$1/2$ states bound to few-donor molecules in a magnetic field $B = 2$T. Labels $nPme$ represent the m electron state bound to a n donor quantum dot

with a trend highlighted by the grey band. In general the single electron relaxation time T_1 is extended with increasing donor number, and for a fixed donor number, T_1 in extended with fewer electrons. Experimental values have been measured for several of these states, as listed in Table 5.1.

Furthermore, Wang *et al.*[154] showed that the asymmetric combination of a single P donor and a 2P quantum dot will provide greater tunability over the exchange interaction J between the two electrons than is possible with two single P donors. Ideally, in order to facilitate two qubit operations between donor electron spins, the exchange interaction between them should be controllable by several orders of magnitude between 'off' and 'on' values[114]. Early proposals[45,155] suggested to modify the tunnel barrier between two electrons with a so-called 'J-gate'. More recently schemes have been presented that rely instead on detuning the energy of the two electron states to modify the strength of exchange coupling[32,114]. To properly suppress interaction in the 'off' condition, at least two orders of magnitude control over J are required[114]. Wang *et al.*[154] performed atomistic tight-binding simulations of the J coupling between qubits as a function of electric field for a symmetric pair of qubits 1P-1P, and an the asymmetric pair 1P-2P. Figure 5.7(b) indicates the difference in tunability of J. In the $1P-1P$ situation, due to Coulomb repulsion between the electrons the overlap of the two electron wavefunctions remains small for realistic E-field values ($<$ 2MV/m), tuning J by only a factor of at most 2 at 15nm qubit separation (blue curve). Comparatively, the $1P-2P$ case displays substantially more tunability, particularly at 15nm qubit separation (purple curve), where J varies over 5 orders of magnitude from 11.6MHz to 1.3THz. This

enhancement in the tunability can be understood since the stronger confinement in the doubly charged 2P quantum dot assists in pulling the two electrons largely into the same potential well, significantly increasing the wavefunction overlap. A combination of 1P and 2P qubits is therefore very attractive in moving toward two qubit operations based on the exchange interaction, combined with an in-built hyperfine detuning of the single qubit ESR frequencies.

We next turn to our experimental results on precision donor devices in silicon. Following spin readout, relaxation, and correlation experiments on a two qubit device presented in Section 5.3, we show in Section 5.4.3 the fabrication of a broadband microwave antenna onto the same device. Section 5.5 outlines a series of robust measurement techniques used in Section 5.6 to measure spin resonance spectra of the two qubits. Finally Section 5.7 details coherent electron spin resonance measurements using a different two qubit device.

5.3 Spin initialisation and measurement in a double quantum dot device consisting of a single donor and 2P molecule

The double dot device presented in this section was fabricated by Matthew Broome and Sam Gorman. I was involved in the spin relaxation and correlation experiments together with Sam Gorman, writing the code to allow dual spin read-out, and performing the measurements. I then fabricated the ESR antenna and led all the spin resonance experiments of Section 5.6.

Figure 5.8(a) shows an STM image of a two qubit precision donor device, consisting of a single donor (1P) on the right (R) and a two donor quantum dot (2P) on the left (L), separated by 16nm, both coupled (at a distance of 19nm) to a larger quantum dot, acting as the island of a charge sensing SET. Bright regions represent metallic donor-defined conductive structures. The sensor dot is separated from source (S) and drain (D) leads by two tunnel barriers, forming the current pathway of the single electron

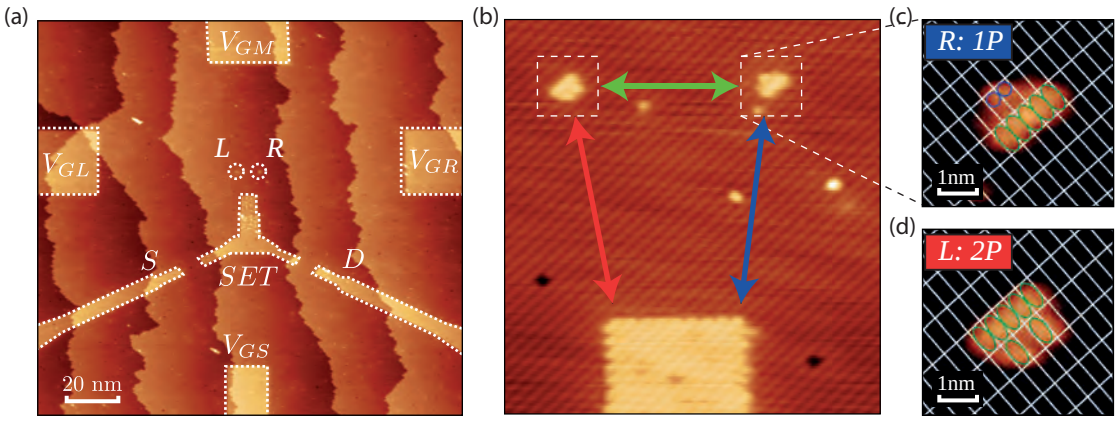

Figure 5.8: Atomic scale images of the 1P / 2P double quantum dot device. (a) STM image of the 1P-2P double quantum dot. The two dots, L (2P) and R (1P) are separated by 16nm and are 19nm away from the tip of a large single electron transistor charge sensor (SET). Source (S) and drain (D) leads allow the application of a bias voltage V_{SD} causing DC current to flow through the SET conditional upon the charge state of the two QDs. Voltages applied to gates GL, GM, and GR tune the relative and combined potentials of the quantum dots and a fourth gate GS allows independent tuning of the SET potential. (b) higher resolution image of the central region indicating where electron tunnelling is possible between the donor quantum dots and the SET, if the appropriate electrochemical potentials are aligned. (c) Silicon lattice constant dimer grid overlaid on an optimised atomic scale STM image showing the layout of exposed dimers and monomers in the left and (d) right donor sites before phosphine dosing.

transistor (SET), used for spin state readout via spin to charge conversion. Voltages applied to four gates (G_L, G_M, G_R and G_{SET}) tune the electrochemical potentials of the two donor qubits and the SET. The island of the SET additionally functions as an electron reservoir for the two small donor-defined quantum dots, with electrons loading via the SET as indicated by red and blue arrows in the higher resolution STM image of Figure 5.8(b), the green arrow represents inter-dot tunnelling, which may occur when the electrochemical potentials of the dots are aligned.

The number of donors incorporated at each of the two sites depends on the size of the patch exposed to the phosphine precursor during fabrication. The lithographic patch of the left dot is shown in Figure 5.8(c), overlaid with a grid representing the atomic lattice of the [001] crystal plane. Each rectangular cell represents a dimer – a pair of silicon atoms on the [001] surface that pull together to minimise their energy. The bright area in the image indicates that the hydrogen mask has been desorbed from 5 consecutive dimers along one row, with two separate desorbed dimers on the neighbouring row, highlighted in green. The right dot image of Figure 5.8(c) indicates also 5 consecutive

dimers desorbed, with two single atoms in the neighbouring row where the hydrogen has been removed leaving single dangling bonds. While it is understood from density functional theory models of the chemical process[78,87] that 3 adjacent free dimers are neccessary for the incorporation of a single phosphorus atom, with larger lithographic patches, we rely on a probabilistic analysis[81], indicating that the possible number of incorporated P atoms for a 5 dimer chain is 1-2. Whilst the STM fabrication routine does allow for deterministic verification of the exact number of incorporated donors[53], it involves an additional non-trivial imaging step which was not performed for this device. Instead we determine the donor number for each quantum dot by electrical measurement of the charging energy.

5.3.1 Donor number determination based on quantum dot charging energies

By analysing the charge stability diagram we are able to confirm that the left dot contains 2 phosphorus donor atoms, and the right dot a single P donor.

Figure 5.9(a) shows a composite charge stability map of the 2P-1P device over the full voltage range accessible. Each rectangular patch is a scan over left V_{GL} and right V_{GR} gate voltages for fixed values of $V_{G-SET} = 0.5$V and varying V_{GM} as indicated. Each patch is offset relative to the axes in order to align the charge transitions. Periodic diagonal lines of high current represent Coulomb peaks of the SET, and two sets of discontinuities in the SET lines are highlighted in red and blue, corresponding to electron transitions of the L (1P) and R (2P) donor quantum dots respectively. Crossing each of these lines from lower left to upper right adds an electron to the respective site. The charge states are labeled (n_1, n_2). Two additional discontinuities, marked T (green dashed lines) are due to an unintended charge trap in the vicinity of the SET. An avoided crossing (white box) between the two qubit transitions indicates a region where electrons can tunnel between L and R, in this case at the $(1,1) - (2,0)$ charge transition.

From the separation in gate voltage between successive charge transition lines, as indicated by the span ΔV_g^D for the right dot, we can compute the charging energy E_C^D – the energy needed to add an electron to the donor quantum dot. Since ΔV_g^D

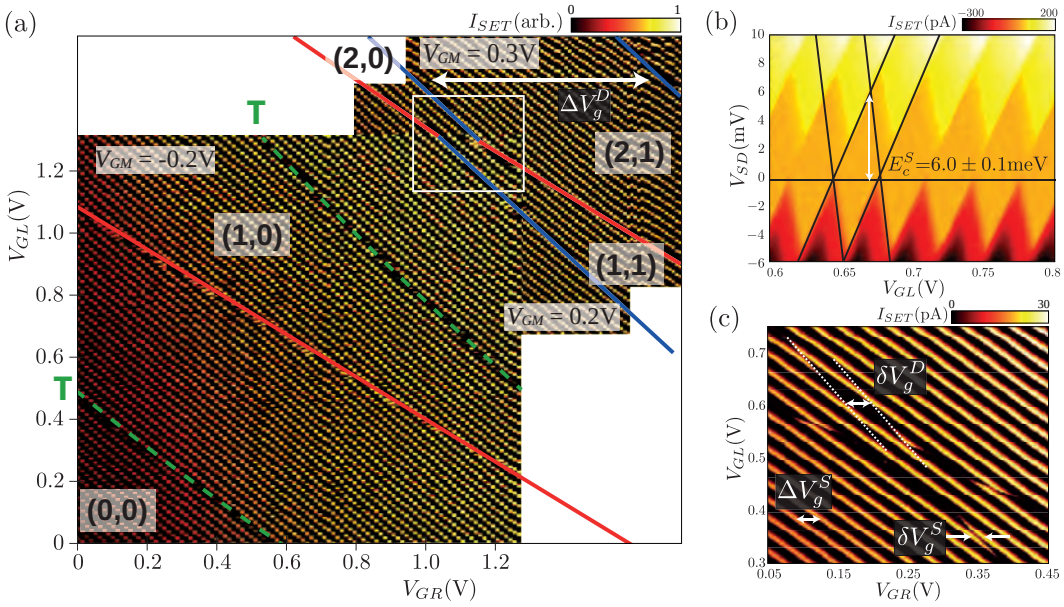

Figure 5.9: Charge stability diagram for a 1P/2P double quantum dot tunnel coupled to an SET. (a) Large scale stability map of the device, showing SET current as a function of gate coordinates. Individual tiles are scans in V_{GR} and V_{GL} as indicated by the axes. The three tiles from left to right have V_{GM} settings $-0.2, -0.2, 0.2, 0.3$V as marked. Donor charge transitions are marked in blue (red) for the left (right) quantum dot. and the charge state assigned to each region is marked in blue. Discontinuities marked T are attributed to an unintended charge trap. (b) Coulomb diamond stability map, showing SET current as a function of gate voltage V_{GL} and SET bias V_{SD}. The height of the diamond provides the SET charging energy E_C^S. (c) High resolution scan of the gate-space surrounding the (1,1) - (2,0) inter=dot charge transition (white box in (a)), indicating the charge offsets δV_g^S in SET and δV_g^D right dot lines corresponding to the mutual charging energy between them. Also marked is the gate span corresponding to the SET charging energy ΔV_g^S, and the equivalent span for the charging energy of the right dot ΔV_g^D is shown in (a). From these 3 stability maps, and the measured voltage spans, single electron charging energies of 43 ± 5meV and 65 ± 8meV, are obtained for the 1P and 2P dots respectively.

SET parameters		1P parameters		2P parameters	
E_C^{SET}	6.0 ± 0.1meV	E_C^{1P}	43.0 ± 5.0meV	E_C^{2P}	65.0 ± 8.0meV
ΔV_{GR}^{SET}	32.8 ± 2.0mV	ΔV_{GR}^{1P}	505 ± 5mV	ΔV_{GR}^{2P}	604 ± 5mV
α_{GR}^{SET}	0.183 ± 0.011	α_{G2}^{1P}	0.182 ± 0.012	α_{G2}^{2P}	0.108 ± 0.013
δV_{GR}^{SET}	17.1 ± 1.0mV	δV_{GR}^{1P}	15.6 ± 1.0mV	δV_{GR}^{2P}	12.4 ± 1.0mV
–	–	E_M^{1P}	3.0 ± 0.2meV	E_M^{2P}	3.3 ± 0.2meV

Table 5.2: Values of SET, 1P (R), and 2P (L) charging energies, lever arms and mutual coupling energy

is measured as a voltage, to convert this to energy units, we begin by determining the charging energy of the SET island E_C^S, which may be measured directly from a Coulomb diamond plot, shown in Figure 5.9(b). The height of the diamond gives $E_C^S = 6.0 \pm 0.1$meV. Figure 5.9(c) shows a high resolution stability map of the area around the $(1,1) - (2,0)$ charge transition, and by considering the SET line spacing ΔV_g^S, which corresponds to the SET charging energy, along with charge offsets due to the mutual charging energy between the SET and one of the dots (the right dot in this case) δV_g^S and δV_g^D, it is straightforward to relate the SET charging energy E_C^S to the donor-SET mutual energy E_M, and then to the donor quantum dot charging energy E_C^D. Using the method introduced in Section Section 4.2.4, we have:

$$E_M = \frac{\delta V_g^S}{\Delta V_g^S} E_C^S \tag{5.7}$$

$$E_C^D = \frac{\Delta V_g^D}{\delta V_g^D} E_M - n E_M \tag{5.8}$$

where n describes the integer number of electrons added to the SET over the span ΔV_g^D. The measured and computed values are shown in Table 5.2. We can apply the same procedure to the left dot also, and in this way we determine the charging energy for the $1 \rightarrow 2$ electron transition of the 2P and 1P qubit to be respectively 65 ± 8meV and 43 ± 5meV. These values are consistent with previously measured values of 2P[56,156] and 1P[53] donor quantum dots, and also consistent with the size of the lithographic patch based on the STM images of Figure 5.8. Therefore we can be confident that the left donor is a 2P molecule, and the right dot a single P donor.

5.3.2 Independent high fidelity spin readout of both QDs

Having described the device and its characterisation, we now demonstrate initialisation and independent readout of the spin states of the individual qubits. As an overview of the charge and spin states involved, Figure 5.10(a) shows a schematic of the energies of 0, 1, and 2 electron states in a finite magnetic field. Black lines indicate the energies of the available states, one of which is occupied at any one time. There is the trivial zero-electron state; two single-electron spin states: $|\uparrow\rangle$ and $|\downarrow\rangle$; and four two-electron spin states: $S = 1/\sqrt{2}(|\downarrow\uparrow\rangle - |\uparrow\downarrow\rangle)$, $T^+ = |\downarrow\downarrow\rangle$, $T^0 = 1/\sqrt{2}(|\downarrow\uparrow\rangle + |\uparrow\downarrow\rangle)$, $T^+ = |\downarrow\downarrow\rangle$.

We highlight four transitions between pairs of these states with green and pink arrows. These are the relevant transitions for spin readout of our two qubits. We describe two subtly different modes of spin to charge conversion, one to read out each qubit:

Single donor qubit readout via spin dependent unloading into the zero electron state

To measure the spin of R, the single donor quantum dot, we employ an single-shot readout technique based on energy-selective tunnelling[54,94]. The electrochemical potential of the single-electron transition between the $1e \leftrightarrow 0e$ charge states is split by the Zeeman energy in a static magnetic field of $B_0 = 2.5$T, giving two transition potentials $|\uparrow\rangle \leftrightarrow |0\rangle$ and $|\downarrow\rangle \leftrightarrow |0\rangle$ separated by an energy $\gamma_e B_0$. Whether an electron is able to tunnel from the donor to the SET reservoir therefore depends on its spin state, i.e. the readout is a spin-dependent *unloading* mechanism from R to SET. We perform a three level pulse sequence as illustrated in Figure 5.10(b), where we keep the SET potential (yellow solid line) aligned to the source and drain Fermi levels (grey lines at the right) during all three steps.

Ⓛ Load an electron of random spin onto the right dot (1P) by setting the potentials for loading an electron of either Zeeman state (green and pink lines) below the Fermi level of the SET (solid yellow line), such that an electron of either spin may tunnel to the donor. Once this occurs, the SET transition potentials are increased

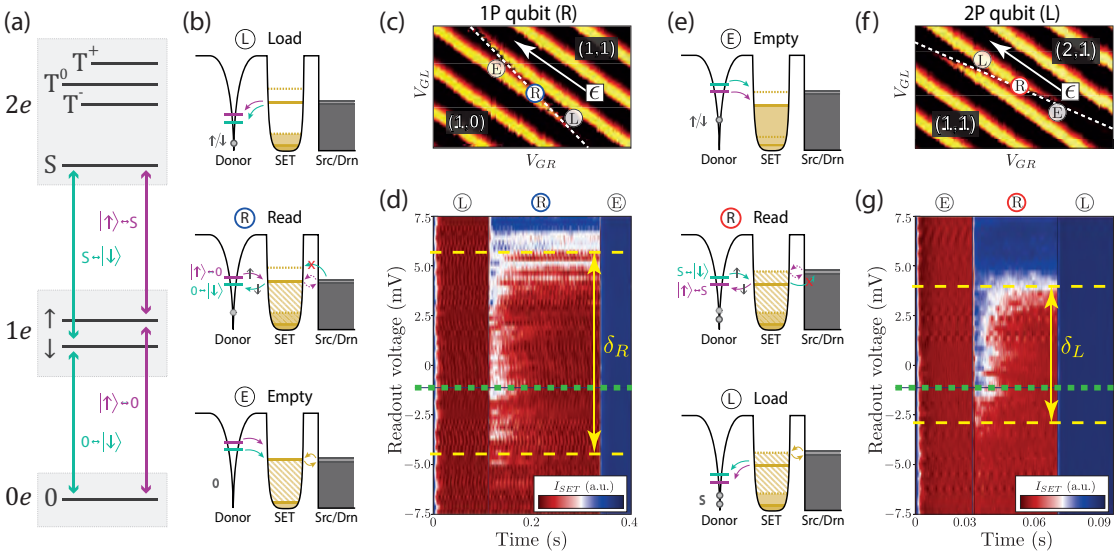

Figure 5.10: Individual donor quantum dot spin readout via spin dependent unloading and loading. (a) Schematic showing zero-, one- and two-electron charge and spin states, and the electrochemical potentials of four relevant transitions between them: $|\uparrow\rangle \leftrightarrow |0\rangle, |0\rangle \leftrightarrow |\downarrow\rangle, |\uparrow\rangle \leftrightarrow |S\rangle, |S\rangle \leftrightarrow |\downarrow\rangle$. (b) Electrochemical potential diagrams for the three stages of the spin readout sequence for the R qubit (1P). (c) small scale gate map defining the pulse levels (Ⓛ, Ⓡ, Ⓔ), relative to the SET conduction background, used to readout the R electron by spin dependent unloading (d) 1P spin-tail measurement. The average measured current response over 200 repetitions to the 3 level readout pulse sequence in a magnetic field of 2.5T highlighting the readout voltage range for successful spin discrimination δ_R. (e) equivalent potential diagrams for the L qubit (2P), where the readout proceeds by spin dependent loading into the two electron singlet state S. (f) gate map defining the levels for 2P spin readout. (g) 2P spin-tail, showing a $\sim$ 20-fold decrease in tunnelling times compared to the 1P qubit.

by the mutual energy, to the dashed yellow lines, and current can no longer flow through the SET. This can be seen in the gate map of Figure 5.10(c) – there is no SET current at position Ⓛ.

Ⓡ READ the spin, by aligning the Fermi level of the SET below the potential for unloading $|\uparrow\rangle \rightarrow |0\rangle$ but above that for unloading of $|\downarrow\rangle \rightarrow |0\rangle$. In such a configuration, the bound electron is able to tunnel to the SET only if it is in the spin excited state. This occurs probabilistically with a characteristic time $\tau_{\uparrow,off}$, and if so, current is then *temporarily* able to flow through the SET from source to drain as indicated by the dashed pink arrows. There is now an unoccupied $|\downarrow\rangle$ state available on the donor, and an electron will tunnel from the SET to fill the ground state within a characteristic time $\tau_{\downarrow,on}$, and at this point, the presence of the mutual energy

switches off the SET current, as the SET potential is inaccessible (green arrow with cross). At this point in the sequence, the spin is effectively initialised $|\downarrow\rangle$.

Ⓔ EMPTY the donor, by raising both Zeeman transition potentials above the SET Fermi level. This is to ensure the next repetition of the sequence is uncorrelated with the previous one. At this point, current will flow through the SET, as its potential is aligned with source and drain Fermi levels, and we correspondingly observe current at position Ⓔ in Figure 5.10(c).

During the READ phase, the presence of a transient current signal indicates the electron being measured was in the $|\uparrow\rangle$ state, however, the success of the readout sequence is sensitive to the exact voltage conditions during the READ phase. We determine suitable settings by performing an experiment where we scan the position of the Ⓡ level along an axis parallel to the SET lines (as indicated by the white arrow 'ϵ' in Figure 5.10(c)). The outcome is shown in Figure 5.10(d), which plots the average current response over 200 repetitions of the three level pulse sequence Ⓛ-Ⓡ-Ⓔ, at each readout voltage in a 15mV range across the donor transition. The characteristic shape we refer to as a 'spin-tail'. For large positive values of the readout voltage, Ⓡ $\approx$ Ⓔ, readout fails because either spin state will tunnel to the SET. The current switches on, and remains on, as evidenced by the blue band at the top of the plot. For large negative values, Ⓡ $\approx$ Ⓛ, readout fails because neither spin state may tunnel away from the donor. We observe low current (red) throughout, until reaching Ⓔ. At intermediate settings within a range marked $\delta_R = 10$meV, a transient current is observed at around 0.15s on the time axis, indicating successful spin to charge conversion and readout. There is some variation in the duration of this transient current (white region), indicating that the tunnel rate $\tau_{\downarrow,on}$ varies with the readout voltage. This is attributed to a non-uniform density of states within the SET[157]. Around 6mV there is a region exhibiting random telegraph signal (RTS) where resonant tunnelling occurs back and forth between the SET and the $|\downarrow\rangle$ ground-state for the duration of the READ phase. The green dotted line indicates the readout voltage used in the following experiments (-1.2mV). We calibrate the lever arm α_ϵ^R relating the voltage along the detuning axis (or readout voltage on the y-axis of Figure 5.10(d)) by relating the length of the spin tail, δ_R to the Zeeman energy $\gamma_e B_0$

(the range over which the spin-split potentials straddle the SET Fermi level)

$$\alpha_{\epsilon}^{R}\delta_R = \gamma_e B_0 \tag{5.9}$$

$$\alpha_{\epsilon}^{R} = 0.030 \pm 0.003 \tag{5.10}$$

We use this value later to calibrate the energy axis in a two electron interaction experiment.

2P DONOR QUBIT READOUT VIA SPIN DEPENDENT LOADING INTO THE TWO ELECTRON SINGLET STATE

For L, the 2P qubit, we use a slight variant of the readout method, first reported by Watson *et al.*[55]. The relevant charge transition for this qubit is $1e \leftrightarrow 2e$, and as indicated in Figure 5.10(a), this transition is Zeeman split also, with two transition potentials $|\uparrow\rangle \leftrightarrow |S\rangle$ (pink) and $|S\rangle \leftrightarrow |\downarrow\rangle$ (green) separated again by the Zeeman energy $\gamma_e B_0$. The difference is that here we utilise a spin-dependent *loading* mechanism, by attempting to add a second electron from the SET to L. Figure 5.10(e) illustrates the process for this readout sequence, where the SET potential, shifted by the mutual charging energy with the 2P qubit (yellow dashed line) remains aligned to the source and drain Fermi energy (grey lines) throughout.

Ⓔ 'EMPTY' one of two electrons from the 2P donor pair, by raising both transition potentials above the SET Fermi level, such that the charge ground state becomes (1,1) by randomly removing one of the anti-parallel spins which was part of the singlet state, leaving a random initial state $|\uparrow\rangle$ or $|\downarrow\rangle$. Removing the electron lowers the SET potential by an amount equal to the mutual charging energy, switching off the SET, and we observe in Figure 5.10(f) that there is no current flow at position Ⓔ.

Ⓡ READ the spin state, by aligning the Fermi level of the SET above the potential for the $|\uparrow\rangle \rightarrow |S\rangle$ transition potential but below that for $|\downarrow\rangle \rightarrow S$. In such a configuration, a second $|\downarrow\rangle$ electron can temporarily tunnel onto the donor pair (pink arrow), joining an existing $|\uparrow\rangle$ and forming a singlet, and by raising the SET potential by the mutual energy, switching on the SET current (pink dashed arrows). After a time $\tau_{\uparrow,off}$ the original $|\uparrow\rangle$ electron tunnels over to the SET

(blue arrow) leaving the spin ground state occupied, and switching off the flow of current. At this point in the sequence, the spin is effectively initialised $|\downarrow\rangle$.

Ⓛ 'LOAD' a second electron of the necessary spin to form a singlet state by setting both singlet transition potentials below the Fermi level of the SET. In this state, the SET current is on, as indicated by the non-zero current seen at position Ⓛ in Figure 5.10(f).

The same spin-tail experiment to calibrate a readout voltage is carried out in Figure 5.10(g) via this spin dependent unloading protocol, also referred to as 'D^- readout' since it was first applied to a single donor where the two electron negatively charged donor configuration is known as the D^- state. Note that the values on the time axis here are much smaller than in (d). The characteristic tunnel rates for the 2P dot's $1e \leftrightarrow 2e$ transition are around a factor of ~ 20 faster than in the 1P $0e \leftrightarrow 1e$ case, understandable given the larger orbital extent of the 2 electron wavefunction at a comparable distance from the SET. The measured spin-tail length corresponding to the Zeeman energy for the left donor dot is $\delta_L = 7\text{meV}$, providing a measure of the left dot lever arm along the detuning axis again by equating to the Zeeman energy at 2.5T:

$$\alpha_\epsilon^L \delta_L = \gamma_e B_0 \tag{5.11}$$

$$\alpha_\epsilon^L = 0.041 \pm 0.004 \tag{5.12}$$

The readout voltage used for the following experiments, -1.2mV is marked by a green dotted line.

A great advantage of using the combination of the standard unload-readout, and the D^- load-readout together in the following experiments is that we can perform single shot spin readout of both qubits from the $(1,1) \leftrightarrow (2,0)$ charge transition, without having to pulse gate voltages over a large voltage range to reach the $1e \leftrightarrow 0e$ transition of the left dot, a significant distance away ($\Delta V_{GR}^{2P} \approx 600\text{mV}$). Our dual readout avoids large voltage pulses which can generate significant cross-talk, reflections and charge instability within a device. We determine the average readout fidelity for the left qubit (2P) to be $96.2 \pm 1.1\%$, and for the right qubit (1P) we find $97.6 \pm 2.1\%$. The full fidelity analysis is presented in Section A.3.

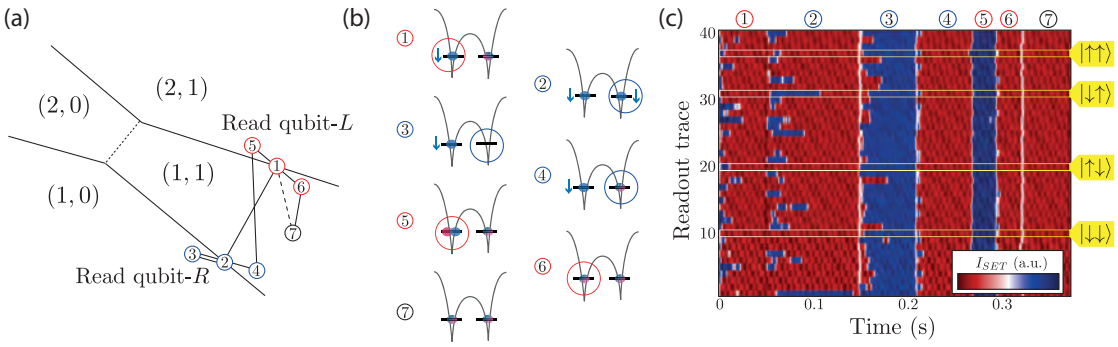

Figure 5.11: Gate pulse sequence for dual spin readout via spin dependent unloading and loading. (a) Schematic showing the full 7-level sequence required to randomly initialise both qubits. (b) Diagrams illustrating the effect of each of the 7 steps on the two qubit system – spin down states are indicated as blue, and spin-up as pink, uncertain states as a mixture. ① and ② initialise each qubit $|\downarrow\rangle$ as a consequence of the projective spin readout. ③ and ④ re-initialise the R qubit by first unloading its electron, then loading an electron of random spin. ⑤ and ⑥ re-initialise the L qubit by first loading a second electron to form the singlet state $|S\rangle$, then unloading one electron, leaving the other with random spin. ⑦ simply parks the system in the (1,1) charge state where there is negligible spin interaction. (c) 40 representative single-shot dual spin readout traces, with the full random initialisation sequence preparing the mixed state $\rho_{\updownarrow\updownarrow}$, with highlighted examples for each potential product state assignment.

5.3.3 Dual spin readout by sequential spin-to-charge conversion

The two readout sequences outlined above can be combined, as we show in Figure 5.11(a), which is a schematic of the charge stability diagram near the $(1,1) \leftrightarrow (2,0)$ charge state transition. It shows a 7-level pulse sequence defining the dual spin readout protocol used to measure both spins and then reinitialise them both into a random spin state. We arrange the order of steps to place the two readout phases first – ① = Read-L and ② = Read-R. We choose to read the qubit with the faster tunnel rate first, so as to minimise the time each spin has in which to relax before measurement. Hence we readout the faster 2P (L) qubit first, followed by 1P (R). As indicated by the cartoons in Figure 5.11(b), this leaves each spin initialised in the spin ground state $|\downarrow\rangle$ after the projective spin measurement (represented by blue down arrows).

After reading the states, the 1P qubit spin is randomised in steps ③ = Empty-R and ④ = Load-R. This process is shown in Figure 5.11(b) – first the electron is removed from the right dot (temporarily taking the system to the (1,0) charge state as seen in

Figure 5.11(a)), then an electron of random spin is re-loaded. Stages ⑤ = 'Load'-L and ⑥ = 'Empty'-L randomise the spin state of the 2P qubit next. Also illustrated in Figure 5.11(b), a second electron is loaded to the left dot, forming the singlet state $|S\rangle$ with anti-parallel spins (here the system is in the (2,1) charge configuration) before one of the two electrons is unloaded, leaving behind a random spin state in the left dot. Finally the ⑦ phase has the effect of simply 'parking' the system within the $(1,1)$ charge state region, where we expect there to be no spin-spin interaction.

We now describe four variations to this initialisation scheme, which we may use to prepare four different initial state mixtures ρ:

$\rho_{\updownarrow\updownarrow} = \frac{|\uparrow\downarrow\rangle\langle\uparrow\downarrow|+|\downarrow\uparrow\rangle\langle\downarrow\uparrow|+|\downarrow\downarrow\rangle\langle\downarrow\downarrow|+|\uparrow\uparrow\rangle\langle\uparrow\uparrow|}{4}$ The fully mixed state, where both spins are randomised after readout as described above, is generated by the sequence: ① (Read-L); ② (Read-R); ③ (Empty-R); ④ (Load-R); ⑤ (Load-L); ⑥ (Empty-L); ⑦ (Park). Stages ③ & ④ perform a random reinitialisation on the R qubit, by removing the single electron and re-loading one with a random spin. Stages ⑤ & ⑥ perform a random reinitialisation on the L qubit, by forming the two electron spin singlet state S, then removing one of the electrons at random.

$\rho_{\downarrow\downarrow} = |\downarrow\downarrow\rangle\langle\downarrow\downarrow|$ The simple sequence ① (Read-L); ② (Read-R); ⑦ (Park) prepares the two qubit system in the pure product state $|\downarrow\downarrow\rangle$ by projectively measuring both qubits, which at the end of each read phase leaves each spin in its ground-state, and then deliberately not re-initialising either with a random state.

$\rho_{\downarrow\updownarrow} = \frac{|\downarrow\uparrow\rangle\langle\downarrow\uparrow|+|\downarrow\downarrow\rangle\langle\downarrow\downarrow|}{2}$ the partially mixed state, with a random spin on the right qubit, but always spin-down on the left, is prepared by including steps ③ & ④, but not ⑤ & ⑥.

$\rho_{\updownarrow\downarrow} = \frac{|\uparrow\downarrow\rangle\langle\uparrow\downarrow|+|\downarrow\downarrow\rangle\langle\downarrow\downarrow|}{2}$ is prepared by excluding the right qubit randomising steps ③ & ④, and only re-initialising random states on the left qubit with steps ⑤ & ⑥.

Note that there is no gate pulse sequence to deterministically initialise either spin in the $|\uparrow\rangle$ spin excited state, doing so would require resonantly exciting the transition with an ESR pulse (the subject of following sections). A set of 40 single shot time traces using the first sequence, preparing $\rho_{\updownarrow\updownarrow}$, are shown in Figure 5.11(c), with highlighted example outcomes assigned to the four possible spin product states $(|\uparrow\uparrow\rangle, |\downarrow\uparrow\rangle, |\uparrow\downarrow\rangle, |\downarrow\downarrow\rangle)$ by yellow boxes and labels. The presence of a transient current 'blip' (blue) in phase

① indicates the left qubit was determined to be spin-up $|\uparrow\rangle$, and likewise a 'blip' in phase ② denotes a spin up $|\uparrow\rangle$ outcome for the right qubit. The blips durin the first readout phase (for the left qubit) are shorter due to the faster tunnel rate between the 2P molecule and the SET.

5.3.4 T_1 Relaxation measurements and verification of spin independence in the (1,1) charge regime

Importantly, the readout of electrons on each donor quantum dot should be independent of the spin-state of the other. That is to say, the exchange interaction at the position where readout is performed must be vanishingly small, such that no spin flip-flops occur during the readout time. This can be verified by performing a T_1 relaxation time measurement for each qubit, as shown in Figure 5.12. For these measurements we prepare the initial state $\rho_{\uparrow\downarrow}$ (i.e. a random spin on the left qubit, $|\downarrow\rangle$ on the right) in order to observe relaxation of the electron spin on dot L. The time delay in the 'parked' configuration ⑦ between initialisation and readout is varied, in order to allow excited state spins to relax to the ground state, and the remaining probability to measure each electron as $|\uparrow\rangle$, $P_{L\uparrow}$ and $P_{R\uparrow}$, is plotted in Figure 5.12(a). The left qubit spin-up probability $P_{L\uparrow}$ falls from $\sim 50\%$ to zero with increasing wait time.

Figure 5.12(b) plots the outcome of the equivalent experiment on the other qubit, beginning instead from the initial state $\rho_{\downarrow\updownarrow}$, to observe spin relaxation of dot R. In this case also, we see the excited state probability for the target qubit decay to zero, and we fit the data to simple exponential decay curves $P(t) = P_0 \exp(t/T_1)$. The initial randomly oriented spin on the left dot (Figure 5.12(a)) decays to the ground state with $T_1^{(2P)} = 2.9 \pm 0.5$s, and we see $T_1^{(1P)} = 9.3 \pm 2.4$s for the right dot (Figure 5.12(b)). This measurement was done at $B_0 = 2.5$T with the magnetic field oriented parallel to the device plane and aligned along the [110] crystal axis, as illustrated by the white arrow $B_z^{(1)}$ in Figure 5.12(c). Crucially, the spectator spin, which was initialised $|\downarrow\rangle$ remains so for all delay times, verifying that the exchange energy at our readout points in the (1,1) charge region is negligible and that there is no spin-spin interaction between the qubits over a timescale ~ 10s.

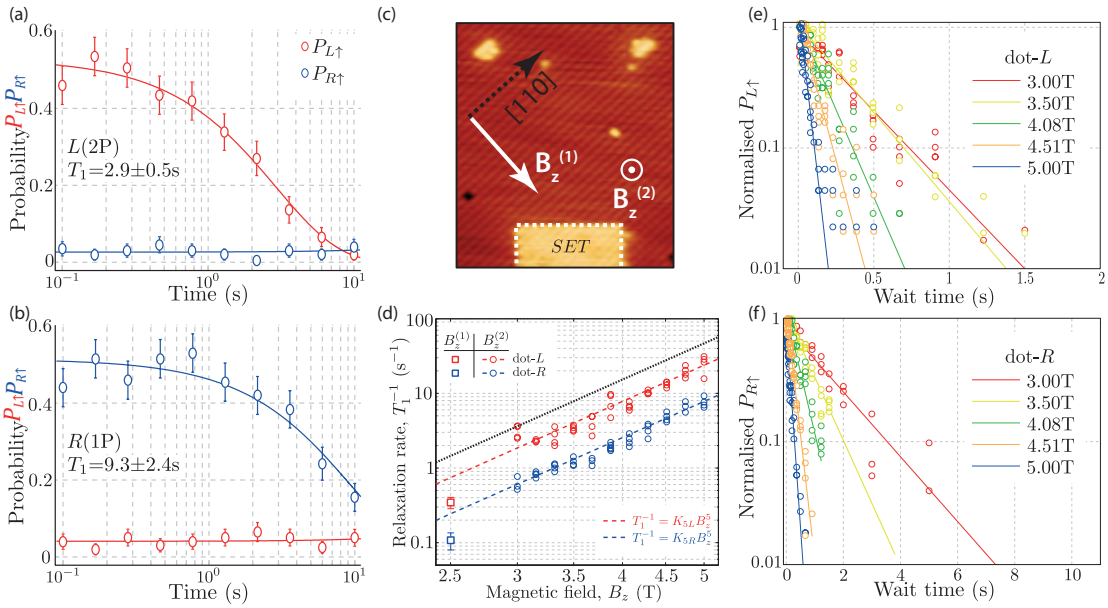

Figure 5.12: Independent single-shot spin readout and spin relaxation in 1P and 2P quantum dots. (a) T_1 spin relaxation measurement of the 2P electron, plotting individual spin up probability as a function of wait time. Note that the 1P spectator electron is always found $|\downarrow\rangle$ (b) T_1 measurement of the 1P electron, with similarly unaffected 2P spectator, both at 2.5T and with $B_z^{(1)}$ field orientation. (c) schematic indicating the two relative orientations of the magnetic field used in our measurements. (d) Summary plot of $1/T_1$ values for over a magnetic field range, illustrating the B^{-5} scaling of the relaxation time. The left dot (2P) relaxes around a factor of 3 faster than the right (1P). Multiple data-points indicate the uncertainty range across repeated measurements. Square data points at 2.5T correspond to (a) and (b). (e,f) Field dependence of the T_1 relaxation, for left and right qubits, with $B_z^{(2)}$ field orientation. With increasing magnetic field, the electron relaxes more quickly, and the probability falls toward zero at shorter wait times. The decay is exponential, and the fitted slopes at each field setting provide the T_1 values shown in (d).

We repeat the spin relaxation experiment at a range of magnetic field values from 3 to 5T, and on a second cool-down in the dilution refrigerator with an alternate orientation of the magnetic field to the crystal axis. Figure 5.12(c) indicates the second field alignment $B_z^{(2)}$, perpendicular to the device plane, along [001]. The measured relaxation rates as a function of magnetic field, $1/T_1$, are shown in Figure 5.12(d). Squares denote the $B_z^{(1)}$ alignment, and circles the field dependence study at $B_z^{(2)}$. We observe the expected relation $T_1 = KB^{-5}$ for donors, where the 5th power dependence is consistent with the theory of phonon mediated valley repopulation[116,158]. The exponential decay curves used to obtain the circular data-points are presented in Figure 5.12(e,f), where it is

easily observed that the spin relaxes to the ground state more rapidly at higher field, the probability to measure $|\uparrow\rangle$ falling to zero much faster for the blue 5T line than for the red 3T line.

We note that the $B_z^{(2)}$ trend-lines of Figure 5.12(d) pass well above the single data points at 2.5T along $B_z^{(1)}$ for both qubits, indicating that a shorter relaxation time appears to apply for the [001] alignment, evidence of anisotropy in the donor spin relaxation process[159,160]. An angular dependence of the T_1 relaxation rate has been observed in bulk samples[161], and has recently been investigated further by Weber *et al.*[162]. The black dotted line in Figure 5.12(d) shows the result obtained in previous single donor (1P) electron T_1 measurements[55,94], with a coefficient $K = 0.015\text{s}^{-1}\text{T}^{-5}$, obtained with a B_0 field aligned along [110]. We extract coefficients $K^{2P} = 0.0026 \pm 0.0001\text{s}^{-1}\text{T}^{-5}$, $K^{1P} = 0.006 \pm 0.0010\text{s}^{-1}\text{T}^{-5}$. Our lower coefficient reflects a longer T_1 time than the reference value.

Recent theoretical calculations by Hsueh *et al.*[152] using an atomistic tight binding approach suggest that multi-donor clusters should enjoy a longer relaxation time relative to a single donor, due to the single electron wavefunction being more tightly confined by the stronger Coulomb potential well, as discussed in detail in Section 5.2.3. At first glance, our results appear contrary to this understanding; we note that the 2P electron relaxes faster than the 1P electron in this device: $T_1^{(2P)} = 2.9 \pm 0.5\text{s}$, $T_1^{(1P)} = 9.3 \pm 2.4\text{s}$ (for the $B_z^{(1)}$ configuration at 2.5 T). However, the measurements were preformed in a different field orientation to the calculations of Hsueh *et al.*[152]. Since we know that there is a magnetic field orientation dependence of T_1 for single donors[161,162], it is likely that this is true for 2P molecules also. Our measured relaxation times are within around an order of magnitude of the theoretical predictions $T_1^{(2P)} \approx 35 \pm 15\text{s}, T_1^{(1P)} \approx 2.5\text{s}$[152], and other recent experimental measurements $T_1^{(2P)} = 6.7\text{s}$[153], $T_1^{(1P)} = 1.4\text{s}$[55]. Future work in needed to fully understand the interplay between field orientation and the crystal axes in 2P single electron quantum dots.

5.3.5 Controllable exchange interaction between two donor-bound electrons

The realisation of a two-qubit logic gate, and thus any sort of scalable qubit architecture, requires the ability to controllably turn on and off interaction between spin states. We now investigate the onset of the exchange interaction J as the double quantum dot is detuned from the (1,1) charge state into (2,0), as indicated in Figure 5.13. The experimental procedure is as follows:

- Initialise the two qubit system in one of the partially mixed state preparations $\rho_{\downarrow\updownarrow}$ [or $\rho_{\updownarrow\downarrow}$] as detailed in the preceding sections.
- Park the system in the (1,1) charge region, denoted by a green square in Figure 5.13(a).
- Pulse along the detuning axis ϵ toward (or beyond) the (1,1)-(2,0) charge transition, to a variable position marked by green circles in Figure 5.13(a).
- Wait at this location for 50ms, which is longer than both qubit tunnel rates, to avoid any transient behaviour.
- Pulse back to the starting location (Park)
- Readout the independent single spin states

From the individual single shot spin outcomes for each qubit we determine the joint probabilities P_{ij} for finding the two spins in the four possible product states: $ij \in \{\uparrow\uparrow, \uparrow\downarrow, \downarrow\uparrow, \uparrow\uparrow\}$, and these probabilities are plotted in Figure 5.13(d-f) as a function of the detuning energy ϵ – the position of the green circle in Figure 5.13(a) relative to the (1,1) – (2,0) charge degeneracy point which defines *epsion* $= 0$. We convert the gate voltage values of Figure 5.13(a) to energy units in via the combined effective lever arm along the detuning axis parallel to SET conduction lines $\alpha_\epsilon = \alpha_\epsilon^L + \alpha_\epsilon^R = 0.071 \pm 0.007$, determined by the lengths of the spin-tail plots in Figure 5.10. Hence the horizontal axes of Figure 5.13(d-f) are given in energyu units (meV).

In the case where $\rho_{\downarrow\updownarrow}$ is initialised (yellow circle markers), there are two randomly selected initial states, as illustrated in the upper-left and lower-left panels of Figure 5.13(b):

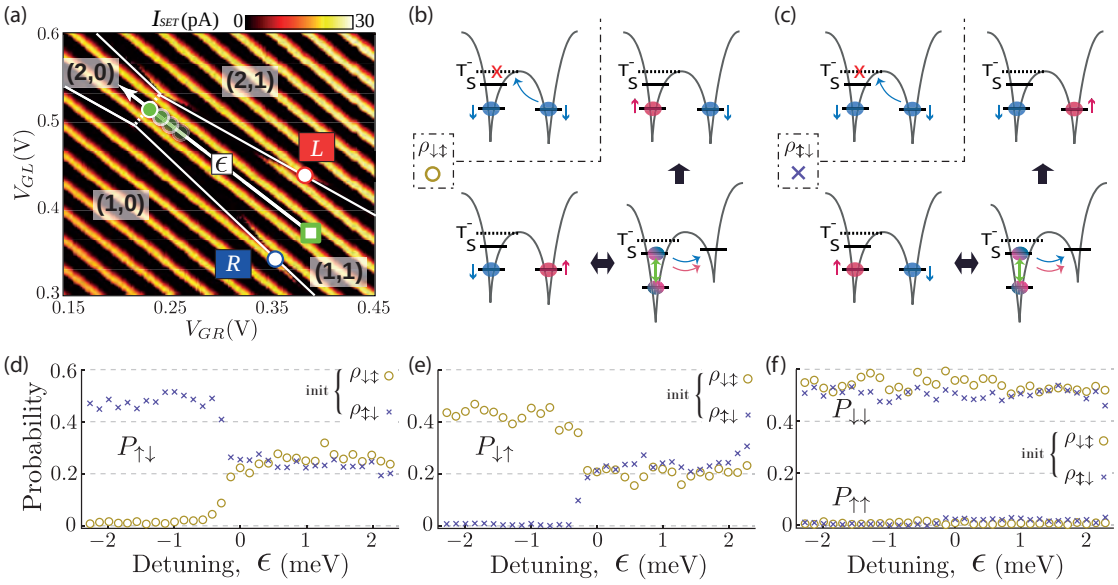

Figure 5.13: Tunable exchange interaction and independence of the two electron spins. (a) Pulse scheme for determining the onset of exchange interaction between two qubits. After initialisation, from the parked position in the (1,1) charge state (green&white square), a pulse is applied toward the (0,2) charge region (green circles), mapping the response along the detuning axis (ϵ). The following repetition of the sequence will involve reading out the individual spin states at positions marked by the red (L) and blue (R) circles. (b) Schematic of the effect of the exchange interaction on the initial state mixture $\rho_{\downarrow\updownarrow}$ where the left dot is deterministically $|\downarrow\rangle$ after initialisation. The two randomly selected initial states are shown in upper-left and lower-left panels. With both spins down (upper-left), detuning the system cannot move the two electrons together into the (2,0) state, as the T^- triplet state is much higher in energy than the S singlet. With anti-parallel spins, the S(0,2) state is accessible at positive detuning. With both electrons on the left dot as shown in the lower-right panel, the exchange interaction causes the spins to exchange rapidly, effectively randomising each individual electron spin, but always remaining anti-parallel. Thus, on return to the (1,1) charge state either $|\downarrow\uparrow\rangle$ or $|\uparrow\downarrow\rangle$ outcomes are possible, as indicated by the thick black arrows pointing into the upper-right and lower-left panels. (c) Similar schematic based on initialisation into the $\rho_{\updownarrow\downarrow}$ mixture. (d) Yellow circles [purple crosses] show the joint probability $P_{\uparrow\downarrow}$ of measuring the $|\uparrow\downarrow\rangle$ state after initialising in a $\rho_{\downarrow\updownarrow}$ [$\rho_{\updownarrow\downarrow}$] mixture and a 50ms exchange pulse, as a function of the detuning energy ϵ, (e) the joint probability $P_{\downarrow\uparrow}$ of measuring the $|\downarrow\uparrow\rangle$ state, and (f) likewise, $P_{\downarrow\downarrow}$ and $P_{\uparrow\uparrow}$ (labelled) under the same two initialisation conditions.

- The $|\downarrow\downarrow\rangle$ initial state (upper-left panel) is unaffected by the exchange interaction, since Pauli spin blockade prohibits the right electron from moving to the left dot. The state remains unchanged after the detuning voltage pulse. Since this state is initialised 50% of the time, we find in Figure 5.13(f), an average $P_{\downarrow\downarrow}$ value just over 0.5, which remains insensitive to ϵ

- The $|\downarrow\uparrow\rangle$ initial state (lower-left panel) on the other hand, is sensitive to the exchange interaction when the electron wavefunctions are made to overlap by increasing the detuning ϵ, and the spin anti-parallel (1,1) state hybridises with the S(2,0)[31,32].
  i) For values $\epsilon < -0.5$meV, there is no interaction and we observe in Figure 5.13(d), $P_{\uparrow\downarrow} \approx 0$, and in (e) $P_{\downarrow\uparrow}$ slightly less than 0.5
  ii) For values $\epsilon > -0.5$meV, the electron wavefunctions significantly overlap as both reside primarily in the left dot (lower-right panel) and the presence of the exchange interaction rapidly exchanges the two spins $|\downarrow\uparrow\rangle \leftrightarrow |\uparrow\downarrow\rangle$. The timescale for this spin exchange has been observed in silicon quantum dot devices to be on the order of MHz or faster[163]. Thus the effect over the comparatively long wait time (50ms) in our experiment is to randomise the spins when the electrons are finally separated again, leading to either final state $|\downarrow\uparrow\rangle$ (lower-left) or $|\uparrow\downarrow\rangle$ (upper-right panel). Hence, for positive ϵ we see that the probabilities in Figure 5.13(d) and (e), $P_{\uparrow\downarrow}$ and $P_{\uparrow\downarrow}$, are both around 0.25, representing a random outcome for each qubit, yet a clear anti-correlation between the two.

- We have repeated the experiment starting from the other initial state mixture $\rho_{\updownarrow\downarrow}$ (purple cross markers), and the equivalent state representation is shown in Figure 5.13(c), where the evolution is completely analogous to that described above for $\rho_{\updownarrow\downarrow}$, after switching the spin state labels for the two qubits.

The almost disctrete change in behaviour just below zero detuning energy is a clear indication of a controllable exchange interaction in our device, and a step towards a coherent two qubit gate. Additional quantum mechanical simulations based on the data collected in our experiment has recently provided an indication of the strength of the exchange coupling. Broome *et al.*[3] estimate a value of $\sim$ 200MHz at $\epsilon = 0$. This value is unfortunately too low to observe coherent exchange driven oscillations which would form the basis of a $\sqrt{SWAP}$ two qubit gate in this device.

The readout of random yet anti-correlated single electron spin states when we intentionally detune the double quantum dot system to positive detuning nevertheless demonstrates control over the exchange coupling in our two qubit device architecture. Having carefully verified the conditions under which our two spin qubits interact, we are in a position to operate each of them independently, confident that their exchange interaction is negligible around the single spin readout positions used in the remainder of this chapter.

5.4 Integrating a broadband microwave antenna onto an atomic-scale device

Following the spin relaxation and controllable exchange interaction experiments, the 1P-2P device was un-bonded and removed from its measurement package. The device was then reprocessed to integrate a broadband microwave antenna, to enable electron spin resonance experiments. First it is important to understand the technical requirements of the antenna, and for this we must consider the relevant energy scales and electromagnetic field profiles to optimise the antenna layout. We then describe the process by which the physical antenna is post-fabricated onto the existing device.

Measurements of the electron temperature in our dilution refrigerator set-up indicate a thermal energy $k_B \cdot 200\text{mK} \approx 20\mu\text{eV}$. As such, we require a Zeeman energy several times larger than this, to ensure that spin-to-charge conversion based on Zeeman-state dependant tunnelling remains effective. A magnetic field of 2.5T corresponds to a Zeeman splitting of $290\mu\text{eV}$ and is therefore suitable for high fidelity spin readout, $F_M \approx 97\%$ as we derive in Section A.3. However, given the gyromagnetic ratio for electrons in silicon $\gamma_e = 27.9\,\text{GHz/T}$, working at a magnetic field $B_0 = 2.5\text{T}$ would require spin rotation Rabi fields on the order of 70GHz. The electronic hardware to generate such high frequency signals is not readily available, so we must lower our Zeeman field. Single shot spin readout is not practical below 1T, as the Zeeman state splitting becomes comparable to the thermal energy. With a $\sim 1.5\text{T}$ field, spin readout is possible, but with a reduced

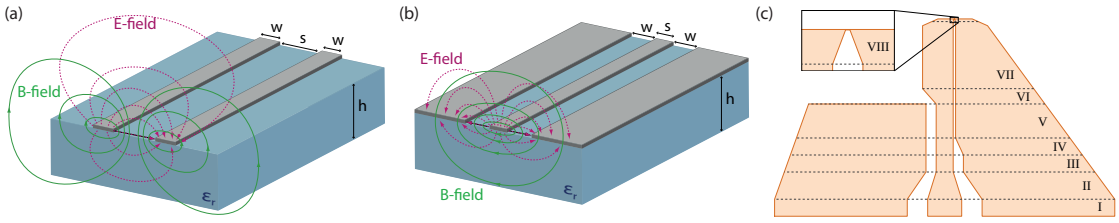

Figure 5.14: Microwave transmission geometries for exciting nanoscale devices. (a) Schematic of a coplanar stripline transmission line, indicating the dimensions and dominant electromagnetic field mode. (b) a similar schematic for a coplanar waveguide geometry, with a more tightly confined electromagnetic field mode. (c) Diagram indicating the tapered geometry of our antenna, transitioning from a coplanar waveguide to coplanar stripline and terminating in a short-circuit. Numbered sections are described in the text.

spin readout fidelity, in this device $F_M \sim 85\%$. The reduction is primarily due to an increased incidence of thermally excited spin-down states being mistakenly interpreted as being spin-up. Measurements in other precision donor devices have achieved higher measurement fidelity[55] (99% at $B = 1.6\text{T}$) by virtue of a more conductive SET, and therefore a higher signal to noise ratio than we have in the present device.

Therefore, for a viable electron spin resonance (ESR) experiment, we work in a B_0 field in the range 1.2T – 1.5T, corresponding to a Larmor resonance frequency in the microwave spectrum, around $\gamma_e B_0 \approx 40\text{GHz}$.

5.4.1 Microwave transmission line and broadband antenna geometries

At 40GHz the wavelength of radiation is on the order of millimetres and therefore the geometry of the transmission line used is critical for the effective coupling of the resonant spin control signal into a device. We now briefly introduce several electromagnetic transmission line structures relevant to transmitting microwaves in our experiment, before describing the optimised nanoscale broadband antenna used for our devices.

Co-Planar Stripline

A coplanar stripline consists of a dielectric substrate over which sit two thin parallel metal strips of width w separated by a distance s. This structure supports a guided TEM (transverse electro-magnetic) mode in the long wavelength limit ($\lambda \gg w$,s), where the two conductors carry equal and opposite alternating currents (thus termed a 'balanced' signal). A conceptual diagram of the general shape of the fields for the dominant mode in a coplanar stripline geometry is shown in Figure 5.14(a). The electric field is weaker within the substrate due to polarisation of the dielectric. The direction of the fields reverse every half-period along with the alternating current.

The characteristic impedance Z_0 for a coplanar stripline with conductor widths w, gap separation s on a dielectric substrate of height h and relative permittivity ϵ_r, as shown in Figure 5.14(a), is approximated as[164]:

$$Z_0 = \frac{\eta K(k)}{\sqrt{\epsilon_{eff}} K(k')} \tag{5.13}$$

$$\epsilon_{eff} = 1 + \frac{(\epsilon_r - 1)}{2} \frac{K(k')K(k_r)}{K(k)K(k_r')} \tag{5.14}$$

here η is the vacuum impedance ($120\pi\Omega$). K represents the complete elliptic integral of the first kind:

$$K(k) = \int_0^{\pi/2} \frac{d\theta}{\sqrt{1 - k^2 \sin^2 \theta}} \tag{5.15}$$

and the k-parameters depend on the waveguide geometry:

$$k = \frac{s}{s + 2w} \qquad k_r = \frac{\sinh^2(\pi s/4h)}{\sinh^2(\pi(s + 2w)/4h)} \tag{5.16}$$

$$k' = \sqrt{1 - k^2} \qquad k_r' = \sqrt{1 - k_r^2} \tag{5.17}$$

These expressions relate the geometry (w, s, h) to the stripline's impedance.

Co-Planar Waveguide

The coplanar stripline's magnetic and electric fields extend far from the conducting strips (green and pink field lines in Figure 5.14(a)). A more effective confinement of the E and B fields, and therefore a reduced loss per unit length is achieved with a so-called

coplanar waveguide geometry. This is a three conductor structure: one narrow center strip which alone carries an alternating current, and two wide ground planes either side, again laid over a dielectric slab. The groundplanes significantly reduce the lateral spread of the electric field, as illustrated in Figure 5.14(b).

Since this is the dual geometry to a coplanar stripline (two 'slots' as opposed to two strips), the form of the characteristic impedance is similar. The following expression[164], assuming infinitely extended ground planes, describes the coplanar waveguide impedance:

$$Z_0 = \frac{\eta K(k)}{4\sqrt{\epsilon_{eff}} K(k')} \tag{5.18}$$

in the limit of a thick substrate, $\epsilon_{eff} = (\epsilon_r + 1)/2$, so for silicon $\epsilon_{eff} \approx 6.5$.

Setting the impedance to 50Ω (to match the output impedance of the microwave source) and solving Equations (5.13) and (5.18) for s and w gives a solution set for the line widths w and separation s that will provide low loss transmission of microwave signals. The phase velocity of the transmission mode in either of the two structures is $\nu = c/\sqrt{\epsilon_{eff}} = 1.2 \times 10^8 \text{ms}^{-1}$, hence the wavelength at $f = 40\text{GHz}$ is around 3mm. We wish to avoid resonant behaviour of our transmission line, so an important consideration is the $\lambda/4 \approx 750\mu\text{m}$ resonance length. By keeping the size of our antenna less than this value we can avoid exciting standing waves, in order to produce an effectively broadband microwave antenna.

Nanoscale broadband microwave antenna

The design of the microwave antenna we use is based on the work of Dehollain *et al.*[134], and consists of a coplanar waveguide (CPW), transitioned gradually into a coplanar stripline (CPS) which terminates in a short circuit wire near to the qubit location. The layout is shown in Figure 5.14(c), defined by eight sections and Table 5.3 defines the dimensions of each section. The transition from a coplanar waveguide mode where the signal is unbalanced to a coplanar stripline mode where the signal is balanced, is referred to as a 'balun', and the shape of the balun transition is designed to minimise signal loss and reflection in several ways[165]:

- The shape in section I is large enough to allow wire-bonding to the centre conductor

Section	Transmission mode	s	w	length
		all dimensions in μm		
I	symmetric CPW	86	52	43
II	tapered CPW	–	–	69
III	symmetric CPW	43	26	43
IV	tapered CPW	43	26 / –	43
V	asymmetric CPW	43	26 / 6	86
VI	tapered CPS	6	–	39
VII	asymmetric CPS	6	78 / ∼100	160
VIII	symmetric CPS	6→1	∼40	7

Table 5.3: Nanoscale microwave antenna geometry: description of the eight successive stages forming the unbalanced-to-balanced signal transition in the microwave antenna design of Dehollain *et al.* [134] and the dimensions we have used.

- Section II tapers down to a smaller scale, condensing the electric and magnetic field modes in section III
- The coplanar waveguide is made asymmetric in section IV, so that the field becomes concentrated in the right-hand side of the waveguide throughout section V
- At section VI, the left ground-plane is discontinued, and the centre pin expands to form the left stripline
- The strip width remains large for section VII, to keep the current density low and therefore minimise resistive heating effects
- In section VIII, the antenna tapers toward the final short-circuit – a $\sim$ 100nm wide nanowire connecting the two striplines 1μm apart. The purpose of the short-circuit is to produce a large current density and thereby a large magnetic field at the end of the antenna where the donor qubits will be located.

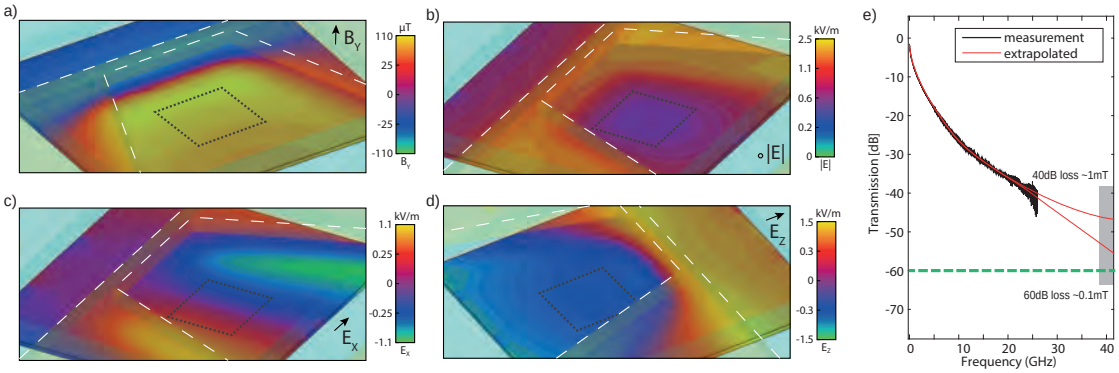

Figure 5.15: Finite element microwave field simulations. (a) Magnetic field B_Y and (b-d) electric field $|E|, E_X, E_Z$ simulations at 40GHz. The coloured panels plotting the fields are $2 \times 2\mu$m and lie 55nm below the silicon surface. White dashed lines indicate the position of the antenna. Grey boxes denote a 500×500nm target region where the ratio of magnetic to electric field is optimised. (a-d) reproduced from Hile [166] (e) Measured attenuation in the ~ 2.5m long stainless steel coaxial cable used to transmit the microwave signal into our dilution refrigerator. Red lines extrapolate the loss to 40GHz

5.4.2 Optimising antenna position by simulating the radiated magnetic and electric fields

We performed finite element field simulations[166*] of the B_1 oscillating magnetic field produced by our antenna geometry, in order to determine the optimal position of the antenna relative to the donor qubits so that the B_1 magnetic field at the donors' location is maximised. The simulated magnetic field within a $2 \times 2\mu$m area 55nm below the end of the transmission line/antenna is shown in Figure 5.15(a), for an antenna driving frequency of 40GHz. The plot indicates that the y-component (perpendicular to the antenna surface plane) of the magnetic field B_Y is stronger inside the loop of the antenna than outside, by a factor of ~ 4. This is understandable since the magnetic flux on the inside is concentrated into the limited area between the two coplanar stips and the terminating nanowire, where on the outside (top left of Figure 5.15(a)) there is no such flux confinement.

We aim not only to maximise the B field amplitude, but also to keep the E field small at the donor location. Large electric field fluctuations may lead to unintended ionisation of the donor during the spin resonance experiment, or adversely affect the SET charge

* These simulation results, obtained using *CST Microwave Studio* software, were presented as part of the author's Honours thesis[166], accepted for the award of another degree

sensor through photon-assisted tunnelling or charge pumping effects[167,168]. The associated electric field amplitude $|E|$ simulated for our antenna is shown in Figure 5.15(b). This plot indicates that within the antenna loop there is a region of minimal electric field $500\text{nm} \times 500\text{nm}$, as indicated by grey dotted lines – we take this as the target region in which we aim to position the donor qubits. Figure 5.15(c) and (d) show the in-plane E-field components E_X, E_Z, most critical for controlling unwanted tunnelling within our planar donor-defined nanostructure (a perpendicular electric field E_Y is expected to have a lesser effect since there are no metallic regions out of the plane for an electron to tunnel to). We see in (c) that there are two lobes of strong E_X below the edges of each stripline, and in (d) that a significant E_Z field component is projected beyond the end of the transmission line, further motivating the placement of our donor qubits within the antenna loop.

For the simulation, the transmission line's TEM mode was excited with a nominal input power of 1mW. To produce realistic field values in Figure 5.15, we scale the simulation results commensurate with realistic losses in the full transmission line between the microwave signal generator and the on-chip antenna, which is dominated by ~ 2.5m of stainless steel 2.2mm diameter (UT85) coaxial cable. We have measured the signal attenuation (at room temperature) in our coaxial cable up to 26GHz with a network analyser, as shown in in Figure 5.15(e). Extrapolating the loss curve suggests we can expect on the order of 50 ± 10dB of attenuation at 40GHz. The use of stainless steel provides good thermalisation of the cable at the cost of significant signal loss. We include an additional 10dB to account for further attenuation at cryogenic temperature and in the PCB launch adapter connecting coaxial cable to coplanar waveguide. Overall this produces an estimate of 60dB total attenuation, which is the value we have used to scale the simulation outputs to the values shown in the field plots of Figure 5.15(a-d). Based on this estimate, the expected B_1 field achievable within the target region is on the order of 0.1mT with a nominal input power of 1mW = 0dBm. Importantly, the electric fields we expect the antenna to generate are in the low kV/m range, orders of magnitude lower than typical DC electric fields in planar donor-defined devices which are on the order of several MV/m.

Having determined the optimal placement of an antenna relative to our donor qubits, we next describe the physical fabrication of such an antenna onto the surface of our 1P-2P double quantum dot device.

5.4.3 Fabricating a microwave antenna aligned to a precision 1P-2P double quantum dot device

The antenna post-fabrication process requires additional electron beam lithography with sufficient alignment accuracy to the buried atomic scale device to ensure the donor qubits will lie within the 500nm × 500nm target region specified above. This is achieved by reference to ∼ 350nm deep registration markers, visible as small squares in the corners, and long trenches around the edges of Figure 5.16(a). We know the relative position of our donor defined qubits relative to these markers with ∼ 100nm accuracy[76,92]. In the optical image of Figure 5.16(a) we see aluminium ohmic contacts to the buried donor plane fanning out to the top of the image, and the termination end of the microwave antenna, also aluminium, which extends from the lower edge of the image. These metallic structures are able to extend continuously over the alignment markers, since the anisotropic nature of the wet chemical etch producing the marker features leaves a smooth contour at a maximum angle of 54.7° down into the ∼ 350nm deep trenches[76].

Phosphorus donor defined nanowires extend from the gates and leads of the device, beneath the antenna and out toward contact regions where etched contact vias connect them to the aluminium structures. These phosphorus nanowires are false coloured (orange) in the SEM image of Figure 5.16(b) to show their relationship to the active region of the device (the STM image is reproduced here in Figure 5.16(c)), and the overlaid antenna, false coloured in blue. The external static magnetic field B_0 used in the following spin resonance experiments is oriented perpendicular to the out of plane oscillating magnetic field B_1, generated by the antenna as indicated in Figure 5.16(b).

A vertical cross-section of the final device is sketched in Figure 5.16(d). The antenna is separated from the phosphorus donor layer by a 55nm thick layer of epitaxial silicon, grown over the device in the initial STM-fabrication process, and also the native oxide layer which naturally forms on the surface when the chip is exposed to ambient atmosphere. In fabricating the aluminium ohmic contacts, this thin oxide layer is removed by etching in hydrofluoric (HF) acid prior to evaporation of the aluminium contacts, so that low resistance contact vias are realised by aluminium filling deep etched holes in the silicon. The HF etch process is omitted in the second metal evaporation process

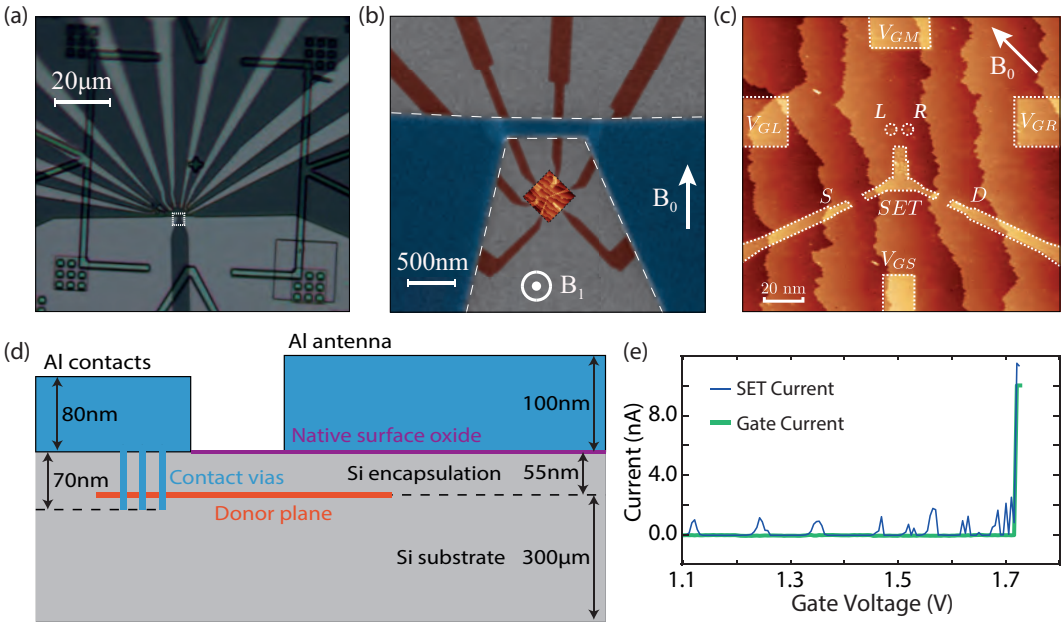

Figure 5.16: **Broadband ESR antenna alignment to buried donors.** (a) Optical image showing the relative position of the microwave antenna to the ohmic contact wires tapering out to bond-pads at the top of the image. Registration markers are visible around the edges. (b) Higher resolution composite image (white square from (a)). An SEM image shows the antenna – blue. The location of buried phosphorus leads are marked in orange, overlaid with reference to the registration markers. An STM image showing the SET and planar gate structures is shown to scale and with a positional accuracy relative to the antenna of ± 100nm (c) STM image of the donor plane of the 1P/2P device – the same image as in Figure 5.8 repeated here for convenience. (d) Vertical cross section of the device structure, indicating dimensions of the substrate, encapsulation layer, and surface aluminium contacts to the buried phosphorus donor structures as well as the aluminium antenna, which is electrically isolated from the donor plane. (e) Leakage current measured in a similarly fabricated device, showing no leakage up to more than 1.7V, and indicating that the leakage that does occur at this point is within the plane, and not vertically to the antenna.

when depositing aluminium for the antenna.

The combination of the silicon encapsulation layer and native oxide provides good electrical isolation, evidenced by the gate leakage measurement shown in Figure 5.16(e). This plot shows the onset of gate leakage current in a different but nominally similar device, where the antenna is grounded. As the in-plane gate voltage is increased, we see a series of Coulomb peaks in the SET current before the onset of some instability above 1.6V, and eventually electrical breakdown occurs beyond 1.7V. Critically, we see that at this point both the SET current and the Gate current sharply increase to > 10nA, evidence that the conduction pathway is from gate where the voltage is applied, to the drain of the SET, and not from the gate into the antenna. Therefore for normal operation of such devices at gate voltages below ~ 1.5V we do not expect current leakage between the donor plane and antenna.

5.5 A robust measurement scheme managing electrical and magnetic instability

Planar phosphorus donor defined nanostructures typically display lower levels of noise than many other material systems[169,170] because they are fully contained within a crystalline environment, with the electronic states far removed from any surfaces or material interfaces. However, in order to continuously measure over long periods of time (days), we find we must still must manage the effects of residual $1/f$ charge noise. Since we are working in natural isotopic abundance silicon, we must also manage the impact of fluctuations in the bath of ^{29}Si nuclear spins.

5.5.1 Correcting for electrical instability with an automated 2D realignment procedure

To stabilise our device against any electrical noise that may affect the quality of spin readout, we have developed an automated realignment algorithm capable of compensating for random shifts in the voltage coordinates of the donor and SET charge transition potentials due to low frequency charge fluctuations. The importance of this ability is highlighted in Figure 5.17(a), which displays a combined gate voltage scan where the voltage of three gates are varied simultaneously $V_{LMR} = V_{GL} = V_{GM} = V_{GR}$, to sweep over a single Coulomb peak, repeatedly over the course of $\sim$ 1hr (4000s). The resulting time-stability plot shows the effect of charge fluctuations, shifting the SET potential by around 2mV within this time-frame.

To perform spin readout we must operate at the intersection of the SET transition potential (a Coulomb peak) and the donor transition potential (a discontinuity), as indicated by the green dot marking the 2P qubit readout working point in Figure 5.17(b). To ensure that we meet these two requirements, we regularly perform a two dimensional (2D) realignment by scanning along the two axes marked: the tuning axis δ (blue arrow), and the detuning axis ϵ (pink arrow), and based on the outcome, update the voltage coordinates of our working point.

Peak Find A scan along the tuning axis δ, defined by the relation $V_\delta = \Delta V_{GL} = \Delta V_{GR}$ produces the trace shown in Figure 5.17(c). We offset this scan from the working point (by around 20mV) as indicated in Figure 5.17(b) so that the recorded Coulomb peak in this 'peak-find' scan is measured independently from the discontinuity at the donor transition. We filter the trace to smooth any noise and fit the curve to a set of peaks*, and take the peak position nearest to $V_\delta = 0$ to define the updated working point. This process ensures that the working point is aligned to the centre of the Coulomb peak, providing the maximum possible SET current I_M and hence an optimal signal to noise ratio for high fidelity single shot spin readout.

* using a continuous wavelet transform method[171] implemented in the Python Scipy library as `scipy.signal.find_peaks_cwt()`

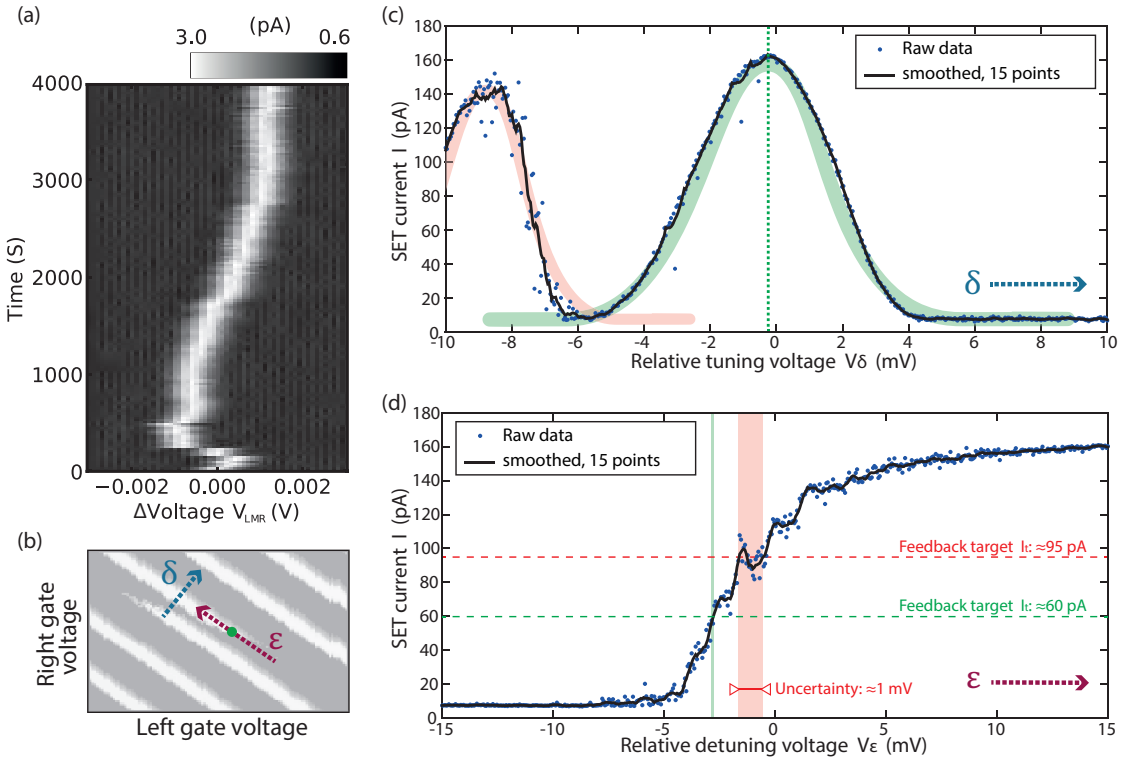

Figure 5.17: Two dimensional realignment procedure to stabilise against charge noise. (a) A low bias $V_{SD} = 0.3\text{mV}$ combined gate voltage scan using three gates (L,M,R) repeated over the course of 4000 seconds, showing variation in the position of a Coulomb peak by 2mV due to low frequency charge noise. (b) Stability diagram surrounding the operating point for spin readout of the 2P qubit, marked by a green dot. We monitor the effect of charge noise shifting this operating point in 2 dimensions, along the detuning axis ϵ parallel to SET peaks (pink), and across the tuning axis δ perpendicular to the SET peaks (blue). (c) Peak-find realignment procedure. A trace is taken along the blue line in (b). The resulting curve is smoothed and searched for peaks, the peak position closest to the previous working point is updated to be the new working point. (d) Edge-find realignment procedure. A trace is taken along the pink line in (b). The resulting curve is smoothed and the position where the curve crosses a selected target current value is updated as the new working point. The selected target current should be within a monotonic region of the curve (green) and not where fluctuations in the SET density of states make the selection of the working point ambiguous (red).

Edge Find A scan along the detuning axis ϵ, defined by the relation $V_\epsilon = -\Delta V_{GL} = \beta \Delta V_{GR}$ produces the trace shown in Figure 5.17(d). Here the coefficient $\beta = \alpha_{GR}^{SET}/\alpha_{GL}^{SET}$ determines the slope of the detuning axis to be parallel to the SET coulomb peaks as indicated in Figure 5.17(b), ensuring that the electrochemical potential of the SET island remains static for this 'edge-find' scan, and only the donor quantum dot transition potential is changed. Moving from negative to positive V_ϵ, an electron is added to the 2P quantum dot, switching on the SET current. In order to obtain a smooth curve, this scan must occur slowly compared to the electron tunnel time on and off the donor (which is $\sim$ 5ms for the 2P qubit shown here). By scanning slowly we average over the random tunnelling of the electron back and forth between the qubit site and the SET island over a 10mV range. The oscillatory features remaining in the smoothed trace of Figure 5.17(d) are not random fluctuations, but arise from the density of states of the SET, which for donor-defined SETs, has been shown to be non-monotonic[157]. Hence for our realignment protocol we must be sure to select a target current value I_t outside of the non-monotonic regions so that the uncertainty in V_ϵ is minimised. We then take the V_ϵ value where $I = I_t$ to define the updated working point. This process ensures that we maintain the electrochemical potential of the two Zeeman split transition potentials at uniform values above and below the SET Fermi energy so that the spin to charge transfer process remains consistent. Charge noise induced drift generates fluctuations in the spin readout fidelity, which we can combat with this 'edge-find' realignment protocol.

Prior to the development of the automated procedure, as for example with the spin relaxation measurements of Section 5.3.4, data was collected in small subsets with manual realignment of the working point several times per day. The combination of these two alignment processes allow reliable operation of the qubit over the course of many days with minimal manual input, a crucial development enabling the collection of the spin resonance datasets that follow.

5.5.2 Pulse sequence for spin resonance experiments incorporating continuous interleaved monitoring

In addition to performing our 2D realignment procedure at regular intervals (every $\sim$ 15min), we are also able to continuously monitor two feedback signals, associated with the tuning and detuning axes, that will indicate that either a 'peak-find' or 'edge-find' sequence is required. This monitoring effectively prevents systematic errors in the spin readout process which would arise if the working point drifts by a significant fraction of the Zeeman energy ($\sim$ 0.2mV) in between realignments. This secondary feedback protocol is integrated into the pulse protocol for spin initialisation, manipulation and readout, forming a 6 stage pulse sequence. We present here the timing used for the 1P qubit, optimised to the tunnel rate, but the operation of the sequence is equivalent up to the pulse timings for the 2P qubit.

Figure 5.18(a) shows the input voltage offset along the detuning (ϵ) axis, and Figure 5.18(b) shows an exemplary output trace of the SET current during one repetition of the sequence. Thirty additional example traces are shown in Figure 5.18(c). The steps executed are as follows, and each configuration is illustrated in Figure 5.18(d).

① **Plunge** The donor potential is lowered far into Coulomb blockade as shown in Figure 5.18(d-1) for the application of an ESR microwave pulse, which occurs at a time ($\sim$ 40ms) midway through this stage.

② **Read** The donor Zeeman state potentials are raised to straddle the SET Fermi level, enabling spin readout. The probability that a current 'blip' is due to a $|\uparrow\rangle$ electron tunnelling to the SET (pink arrow in Figure 5.18(d-2)) decays exponentially with increasing time. However, the probability for a thermally excited $|\downarrow\rangle$ to tunnel and cause an erroneous blip remains constant in time, therefore although this phase has a duration of 156ms, we restrict the spin readout discrimination routine so that only blips occurring in the first 76ms are assigned as $|\uparrow\rangle$.

③ **RTS** The donor potential is raised slightly above the read level such that the spin down state is resonant with the SET Fermi level as indicated in Figure 5.18(d-3). Here we observe a random telegraph signal (RTS) due to electrons tunnelling back and forth between donor and SET. By measuring the average value of the SET current $\langle I \rangle_3$ during this phase, over many repetitions (typically $>$ 200 single shots),

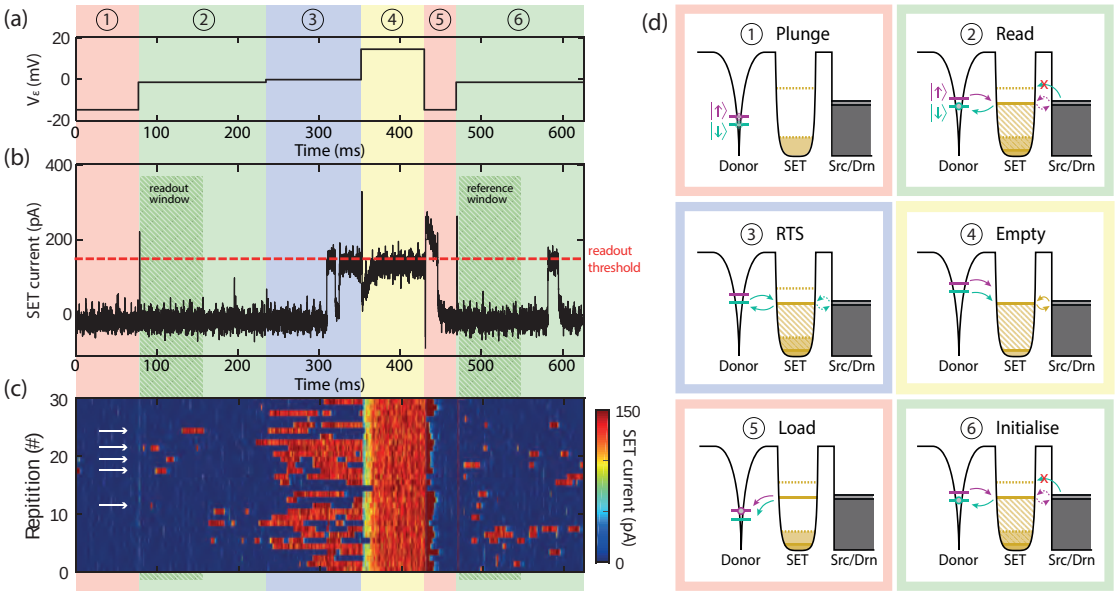

Figure 5.18: Pulse protocol incorporating continuous interleaved monitoring of charge stability. (a) A six stage pulse sequence of voltages defined on the detuning axis V_ϵ, as a function of time for spin resonance measurements of the 1P qubit, and (b) a sample SET current trace for a single-shot spin manipulation, readout, and re-initialisation sequence. The spin is determined to be $|\uparrow\rangle$ if the current trace exceeds the readout threshold level within the readout window as indicated. This sample shows a $|\downarrow\rangle$ outcome. (c) 30 single-shot current traces, 5 of which are $|\uparrow\rangle$ outcomes as indicated by white arrows. (d) Electrochemical potential diagrams corresponding to each of the six stages: ① plunge, ② read, ③ RTS, ④ empty, ⑤ load, ⑥ initialise.

we obtain a feedback signal equivalent to I_t (the target current for an 'edge-find' scan). Thus we are able to tell in real-time when the donor transition potential has shifted in the gatespace along the detuning axis. If $\langle I \rangle_3$ deviates from I_t by more than a specified tolerance (typically 10%), we trigger an 'edge-find' procedure as per Figure 5.17(d), to recover a proper working point.

④ **Empty** The donor potential is raised far above the SET Fermi level, causing the electron to tunnel to the SET. The SET current is expected to be high for this phase, with the SET Fermi level resonant with source and drain Fermi levels as shown in Figure 5.18(d-4). We monitor the average SET current value in this phase $\langle I \rangle_4$ as a feedback signal equivalent to I_M (the peak current from a 'peak-find' scan). If at any time $\langle I \rangle_4$ falls significantly (typically 15%) below the I_M value recorded in the most recent 'peak-find', we determine that the SET peak

has shifted in the gatespace along the tuning axis, and we trigger a 'peak-find' procedure shown as per Figure 5.17(c) to compensate.

⑤ **Load** The donor potential is lowered far below the SET Fermi level, loading an electron with random spin as shown in Figure 5.18(d-5)

⑥ **Initialise** The donor potential is held at the same read position as for step ②, and the presence of current blips within a 'reference window' is used to produce a reference spin-up probability. This reference value should remain consistent throughout the course of a spin resonance experiment, because it is based on the measurement of randomly loaded spins independent of the effect of any applied ESR microwave pulse during phase ①. At the end of this reference readout phase the spin is deterministically initialised $|\downarrow\rangle$ with high probability, as indicated by the blue arrow in Figure 5.18(d-6).

The continuous monitoring of the feedback signals $\langle I \rangle_3$ and $\langle I \rangle_4$ provide real-time information allowing the automated system to determine when low frequency charge noise causes the SET or donor potentials to drift. Execution of the two re-alignment procedures 'peak-find' and 'edge-find' corrects for the random drift, keeping the system fixed at a working point where high fidelity spin readout may be continuously carried out.

5.5.3 Adiabatic passage for reliable spin inversion in a fluctuating magnetic field

The electron tunnel rates are on the order of 100Hz (1kHz) for our 1P (2P) qubit, and as Figure 5.18 indicates, one single-shot readout sequence of the 1P qubit takes over 600ms. Over such timescales, greater than T_2, the nuclear Overhauser field is expected to fluctuate over the full inhomogeneous linewidth ($\sim$ 5MHz) as a result of spectral diffusion – the random evolution of the bath of 4.7% ^{29}Si nuclear spins. With a constantly fluctuating Larmor resonance frequency, performing electron spin resonance measurements at a fixed frequency is ineffective. A common strategy developed for both NMR and EPR is the adiabatic frequency sweep, or adiabatic passage pulse[172,173].

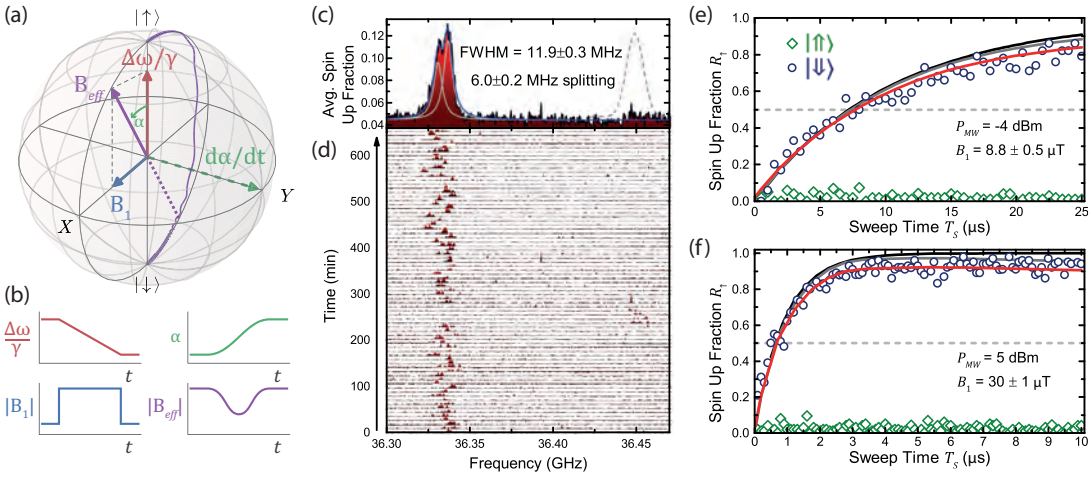

Figure 5.19: Adiabatic spin inversion. (a) Schematic showing the process of adiabatic spin inversion in a rotating frame syncronised to the instantaneous driving frequency ω at all times. The vector sum of B_1 and the detuning $\frac{\Delta\omega}{\gamma}$, indicated in purple as B_{eff} appears as the effective magnetic field experienced by the electron. When the rate $\frac{d\alpha}{dt}$ is small, the electron remains in the instantaneous eigenstate of $H \approx B_{eff}$ and follows the path defined by the purple line from $|\downarrow\rangle$ to $|\uparrow\rangle$ as the angle α increases from $0 \rightarrow \pi$. (b) Cartoon traces indicating the qualitative behaviour of the four quantities $\frac{\Delta\omega}{\gamma}, B_1, \alpha, B_{eff}$ as a function of time during the adiabatic inversion pulse. (c) Donor electron spin resonance spectrum in natural silicon measured by Laucht *et al.* [174]. The FWHM is due to hyperfine coupling with the ^{29}Si nuclear spin bath. (d) 75 individual frequency scans which, averaged together produce (c). The narrow peak in each scan shifts in frequency over $\sim$ 20MHz due to Overhauser field fluctuations. (e) Imperfect spin inversion occurs with a low power adiabatic inversion pulse at short sweep times (high chirp rate). Extending the sweep time makes the operation more adiabatic and thus the inversion occurs with higher efficacy. (f) Effective spin inversion occurs even at short sweep times when the power (B_1 magnitude) is increased. (c,d,e,f) reproduced from Laucht *et al.* [174].

In the simplest sense, an adiabatic passage simply involves 'slowly' sweeping the drive frequency of the B_1 field, such that is passes through the expected range of possible resonance frequencies. The result is an inversion of the spin state, from $|\downarrow\rangle$ to $|\uparrow\rangle$ or vice-versa. The meaning of 'slowly' is defined algebraicly below.

The effect of an adiabatic passage pulse on the electron spin can be understood by considering the effective Hamiltonian in the rotating frame, as illustrated in Figure 5.19(e). In the rotating frame, the Rabi field B_1 is considered to have a constant orientation along the X-axis, and we keep the amplitude fixed so that $B_1(t) = B_1$. Since the drive frequency deviates from the Larmor frequency by $\Delta\omega(t)$, there is an added effective magnetic field component along the Z-axis of magnitude $\Delta\omega(t)/\gamma$, the ratio of the frequency offset to the gyromagnetic ratio. Therefore at any instant, the total effective magnetic

field (shown by the purple arrow) seen by the electron spin is the vector sum of these two components:

$$|\vec{B}_{eff}(t)| = \sqrt{{B_1}^2 + \left(\frac{\Delta\omega(t)}{\gamma}\right)^2} \tag{5.19}$$

and the effective Hamiltonian can be written:

$$H(t) = \gamma_e B_1 \sigma_x + \Delta\omega(t)\sigma_z \tag{5.20}$$

The spin vector precesses, in the rotating frame, about the instantaneous $\vec{B_{eff}}$, and the $\vec{B_{eff}}$ vector itself rotates, over the course of the pulse, about the Y-axis at a rate $d\alpha(t)/dt$, where the angle $\alpha(t)$ (marked in green) changes according to:

$$\tan(\alpha(t)) = \frac{\Delta\omega(t)}{\gamma_e B_1} \tag{5.21}$$

$$\frac{d\alpha(t)}{dt} = \frac{d}{dt}\arctan\left(\frac{\Delta\omega(t)}{\gamma_e B_1}\right) \tag{5.22}$$

The qualitative shape of $\Delta\omega(t)/\gamma$, $|B_1(t)|$, $\alpha(t)$, and $|\vec{B}_{eff}(t)|$ is sketched in Figure 5.19(f). The choice of frequency modulation function is somewhat arbitrary. Different schemes exist employing various smoothly varying functions[175] for both the frequency offset $\Delta\omega$ and B_1 field amplitude as a function of time in order to tune the effective bandwidth and minimum required power for successful inversion. For simplicity we use a linear frequency chirp such that $\Delta\omega(t) = -\nu t$ for a chirp rate of νHz/s, we then have

$$\frac{d\alpha(t)}{dt} = \frac{\nu}{\gamma B_1}\frac{1}{1+\left(\frac{\nu t}{\gamma B_1}\right)^2} \tag{5.23}$$

The gradual rotation of $\vec{B_{eff}}$ from the positive Z-axis to the negative Z-axis, smoothly inverts the $|\downarrow\rangle$ and $|\uparrow\rangle$ eigenstates, since the electron will adiabatically follow the instantaneous groundstate – that is, with its spin parallel to B_{eff}.

If the angle α changes rapidly, a further effective field component arises along the Y-axis, with magnitude $\frac{1}{\gamma}\frac{d\alpha(t)}{dt}$, which has the effect of tilting $\vec{B_{eff}}$ out of the Z-X plane, and producing 'wiggles' in the path of B_{eff} as seen in Figure 5.19(e). The effect remains

small if the rate of change of the angle is small relative to the magnitude of B_{eff}

$$\frac{d\alpha(t)}{dt} \ll \gamma|\vec{B_{eff}}| \tag{5.24}$$

$$\frac{\nu}{\gamma B_1}\frac{1}{\left(1+\frac{\nu t}{\gamma B_1}^2\right)} \ll \gamma\sqrt{{B_1}^2+\left(\frac{\Delta\omega(t)}{\gamma}\right)^2} \tag{5.25}$$

$$\frac{\nu}{\gamma B_1} \ll \gamma B_1 \tag{5.26}$$

$$\nu \ll (\gamma B_1)^2 \tag{5.27}$$

where in moving to Equation (5.26) we have taken the maximum value of the LHS and minimum value of the RHS (both occurring at $t = 0$) in order to simplify the inequality. So long as the chirp rate is small compared to the square of the Rabi frequency, such a pulse executes an adiabatic passage, inverting the electron state, irrespective of the pulse duration or precise Larmor resonance frequency.

Laucht *et al.*[174] recently employed the adiabatic passage technique to perform high fidelity inversion of the electron spin of an implanted P donor within a silicon MOSFET device, in the presence of a fluctuating nuclear Overhauser field. Figure 5.19(c) shows the spin time averaged resonance spectrum they measured with conventional fixed-frequency ESR. The FWHM of the resonance peak is 11.9MHz, and reflects inhomogenous broadeneding due to spectral diffusion from the ^{29}Si nuclear spins. The double peak structure (at 36.33 and 36.34GHz) is interpreted to be due to the parallel and anti-parallel nuclear orientations of a single neighbouring ^{29}Si atom with strong coupling to the electron, or a second nearby ^{31}P donor. The dashed line on the far right shows the expected location of the other hyperfine resonance, but the ^{31}P nuclear spin was observed predominantly in the $|\Downarrow\rangle$ state. The peak in (c) is the sum of 75 individual frequency scans shown separately in Figure 5.19(d). In these individual traces the electron resonance appears with a much reduced linewidth of $\sim$ 1MHz on average, and with random fluctuations in the peak position.

To unconditionally excite the electron spin, irrespective of the instantaneous Overhauser field, Laucht *et al.*[174] applied an adiabatic passage pulse with the characteristics shown in Figure 5.19(b). The result is displayed in Figure 5.19(e). The plot shows the measured $|\uparrow\rangle$ probability $R_\uparrow$ after initialising the electron $|\downarrow\rangle$ before applying an adiabatic passage pulse. Here they use a nominal microwave power of -4dBm, and frequency

modulate the microwave signal linearly over a range of ±12.5MHz within the variable sweep time T_S. For short sweep times, the frequency sweep is non-adiabatic and the inversion ineffective, but as T_S is increased to 25μs the process becomes adiabatic, and the initially $|\downarrow\rangle$ electron spin state is inverted to $|\uparrow\rangle$ with probability approaching 1. As indicated by Equation (5.27), the frequency chirp rate ν which marks the transition from non-adiabatic to adiabatic depends on the square of the B_1 field amplitude. This dependence is demonstrated by the altered response seen in Figure 5.19(f). Here the same experiemnt is performed but with a higher microwave power of +5dBm, corresponding to a factor of ~ 3.5 increase in B_1, suggesting an increase in the limiting chirp rate by a factor $3.5^2 \approx 12$. The plot shows that the inversion probabiliy is maximised already at $T_S \approx 2.5\mu$s, reflecting a tenfold increase in ν consistent with the theory.

Building on the successful application of the strategy by Laucht *et al.*[174], we use similar adiabatic passage pulses to invert our electron spin in the following measurements.

5.6 Electron Spin Resonance of a single donor and 2P molecule

Using the feedback procedure and pulse scheme outlined in Sections 5.5.1 and 5.5.2 and the adiabatic passage technique of Section 5.5.3, we measure the electron spin resonance spectrum of our 1P and 2P qubits.

5.6.1 Single donor qubit hyperfine spectrum

The spin resonance spectrum of the single donor is shown in Figure 5.20(a) for $B_0 = 1.35$T. This data shows the fraction of $|\uparrow\rangle$ outcomes over 640 single-shot repetitions of the 6-stage pulse sequence of Figure 5.18 at each frequency value. During the Plunge phase, a microwave pulse is applied with a nominal power of +5dBm, frequency modulated with

a linear ramp of ±20MHz centred on the variable ESR frequency value plotted on the x-axis. Technical details of the experimental equipment used to generate the ESR pulse is given in Section A.4 The adiabatic passage is completed in a sweep time of 150μs, and therefore with a chirp rate $\nu = 0.27\text{THzs}^{-1} = 0.27\text{MHz}^2$. Orange arrows signify the frequency span of the adiabatic passage chirp relative to the frequency axis.

We observe two peaks in Figure 5.20(a) corresponding to the resonance conditions for driving transitions between electron states $|\downarrow\rangle \leftrightarrow |\uparrow\rangle$ when the single donor nuclear spin state is either $|\Downarrow\rangle$ (left peak) or $|\Uparrow\rangle$ (right peak). The transition frequencies here are separated by the hyperfine coupling strength A, given by:

$$\omega_{\Downarrow} = \gamma_e B_0 - \frac{A}{2} \tag{5.28}$$

$$\omega_{\Uparrow} = \gamma_e B_0 + \frac{A}{2} \tag{5.29}$$

as illustrated in Figure 5.20(b). The solid curve in Figure 5.20(a) is a fit to the sum of two Gaussian peaks:

$$f_{\uparrow} = f_0 + f_{\Downarrow} e^{\frac{-(\omega-\omega_{\Downarrow})^2}{2\sigma^2}} + f_{\Uparrow} e^{\frac{-(\omega-\omega_{\Uparrow})^2}{2\sigma^2}} \tag{5.30}$$

sharing a common peakshape parameter $\sigma = 11.8 \pm 0.8\text{MHz}$ corresponding to a width $\omega_{\text{FWHM}} = 2\sqrt{2\ln 2}\sigma = 27.8 \pm 2\text{MHz}$ and baseline $f_0 = 0.11 \pm 0.01$, but independent peak heights $f_{\Downarrow} = 0.18$ and $f_{\Uparrow} = 0.46$.

We measured a peak separation of $A = 96.5 \pm 2.5\text{MHz}$. This value is less than the 117.5MHz hyperfine splitting measured in bulk ensembles of P donors[71]. Similarly low values of A have been observed in ion-implanted samples[146]. The variation from the bulk value can be attributed to the Stark shift due to the electric field within our device, estimated to be $\sim$ 4.5MV/m at the 1P site (see Section A.5). For comparison, the spectrum obtained by Pla *et al.*[49] with a single P donor within a MOSFET device fabricated by high energy ion-implantation is shown in Figure 5.20(c), which shows two scans over the frequency range $\sim$ 10 minutes apart. In between the scans the nuclear spin has flipped, so that dark blue shows the $|\Downarrow\rangle$ state, light blue $|\Uparrow\rangle$. Due to the slow measurement time in our experiment (limited by electron tunnel rates between the donor qubits and the SET), it is not possible to record such a snapshot of each nuclear state individually. Figure 5.20(a) contains data collected continuously over $>$ 6 hours,

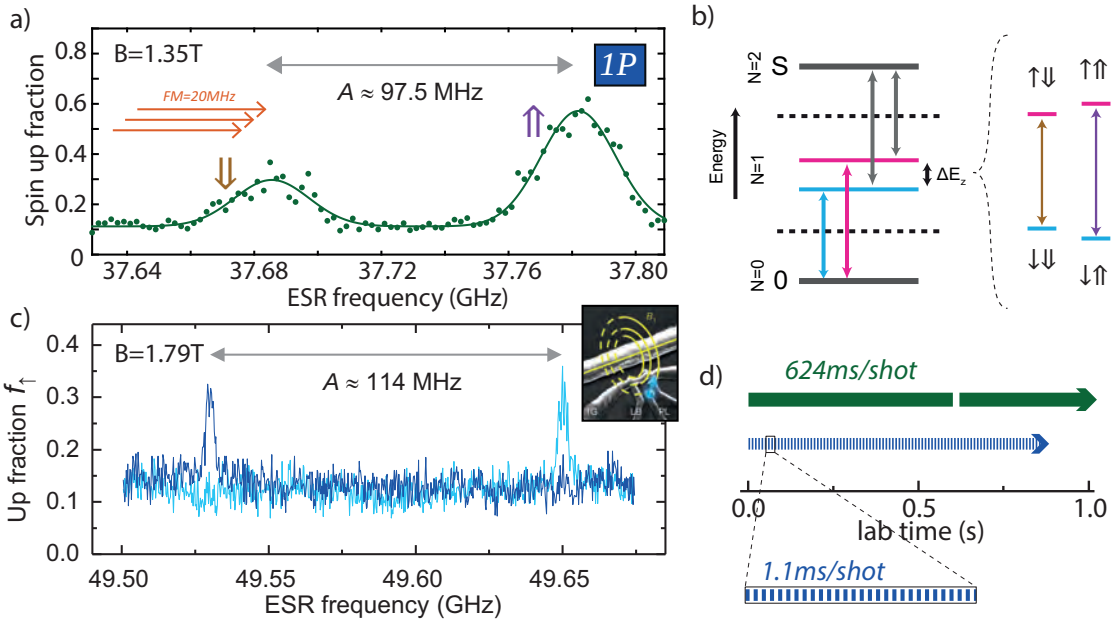

Figure 5.20: **Spin resonance spectrum of a single donor qubit.** (a) Spin up probability calculated from 640 repeated single shot measurements at each frequency, following a 150μs microwave pulse with an FM chirp depth of ± 20MHz and at $+5$dBm power. Measured at $B_0 = 1.35$T. (b) Schematic indicating the spin dependent unloading readout scheme as introduced in Section 5.3.2, and the driven transitions between pairs of combined electron-nuclear spin states. (c) Spin resonance spectrum reproduced from Pla *et al.*[49] for comparison. (d) Comparison of the single shot measurement time for (a) – green bars representing 624ms per single shot measurement and (c) – blue bars representing 1.1ms per shot.

and therefore we necessarily average over both nuclear spin orientations. The disparate measurement timescales are illustrated in Figure 5.20(d), the green segment representing the single-shot time for our 1P qubit (limited by the electron tunnel rate), and the blue band indicating that around 600 single-shot measurements were obtained by Pla *et al.*[49] in a comparable time.

Since no adiabatic passage frequency modulation is applied by Pla *et al.*[49], the linewidth of their peaks is considerably narrower in Figure 5.20(b) than for our experiment, reflecting the intrinsic broadening due to spectral diffusion of ~ 7.5MHz. The hyperfine splitting in Figure 5.20(b) of $A = 114$MHz is also seen to be nearer to the bulk value, although measurements in other implanted donor devices have shown values of the hyperfine energy A ranging from $96.9 - 116.6$MHz[38].

We now examine the nuclear spin dynamics observable in our measurement of the 1P

hyperfine spectrum, and discuss possible mechanisms changing the nuclear spin state. Figure 5.21(a) and (b) compare the 1P spectra observed at 1.35 and 1.55T. Solid dots indicate the overall average spin-up fraction $f_\uparrow$, obtained by averaging over several repeated frequency sub-scans. In each scan the order of points is randomised to average out any time dependent measurement artefacts. The individual sub-scan results are shown here as square markers of different colour, each coloured square showing $f_\uparrow$ for 80 sequential single-shot measurements within a single time-bin (80 shots $\times$624ms $\sim$ 50 seconds). By binning in this way we reveal further information about the nuclear spin dynamics.

Because $f_\uparrow$ is not consistent for data-points at the same frequency but in different time bins, we infer that with the smaller time binning we approach the timescale of nuclear spin flips. The smaller time bins preferentially sample either the nuclear $|\Uparrow\rangle$ or $|\Downarrow\rangle$ state rather than averaging equally over the two with each time bin. We are unable to explore the time dynamics on shorter timescales in this device, since the single-shot duration is limited by the tunnel rate of electrons between donor and SET, $\sim$ 100Hz for the 1P qubit, depending on the spin orientation and detuning voltage. A similar device with orders of magnitude faster tunnel rate would permit a more detailed study of nuclear spin switching dynamics.

We note that in Figure 5.21(a) the peak on the right (corresponding to the nuclear $|\Uparrow\rangle$ state) is more than twice the amplitude of the left (nuclear $|\Downarrow\rangle$ state), and in Figure 5.21(b) the left peak is almost entirely masked by the noise floor of dark counts ($f_0 = \sim 0.11$), indicating that there is some polarisation of the nuclear spin – the $|\Uparrow\rangle$ state is more likely to be seen than $|\Downarrow\rangle$. This polarisation is likely due to an inelastic electron-nuclear flip-flop process, pumped by spin resonant excitation at the $\omega_\Downarrow$ frequency[176,177]. The flip-flop mechanism is illustrated in Figure 5.21(c), where the electron spin 'flips' from $|\uparrow\rangle$ to $|\downarrow\rangle$, and the nuclear spin simultaneously 'flops' from $|\Downarrow\rangle$ to $|\Uparrow\rangle$. The total spin is thus conserved, and energy conservation is satisfied by the emission of a phonon Λ. Since the energy difference between the states is much larger than the thermal energy $\gamma_e B_0 \gg k_B T$, the reverse transition involving absorption of a phonon is suppressed. Any alternate cross-process involving the $|\downarrow\Downarrow\rangle$ and $|\uparrow\Uparrow\rangle$ states would require a change in total spin of ± 1 and so is forbidden by spin conservation.

This type of asymmetry in the occupation of nuclear spin states has been seen in single donor spectra previously by Pla *et al.*[50], where repopulation of the nuclear $|\Downarrow\rangle$

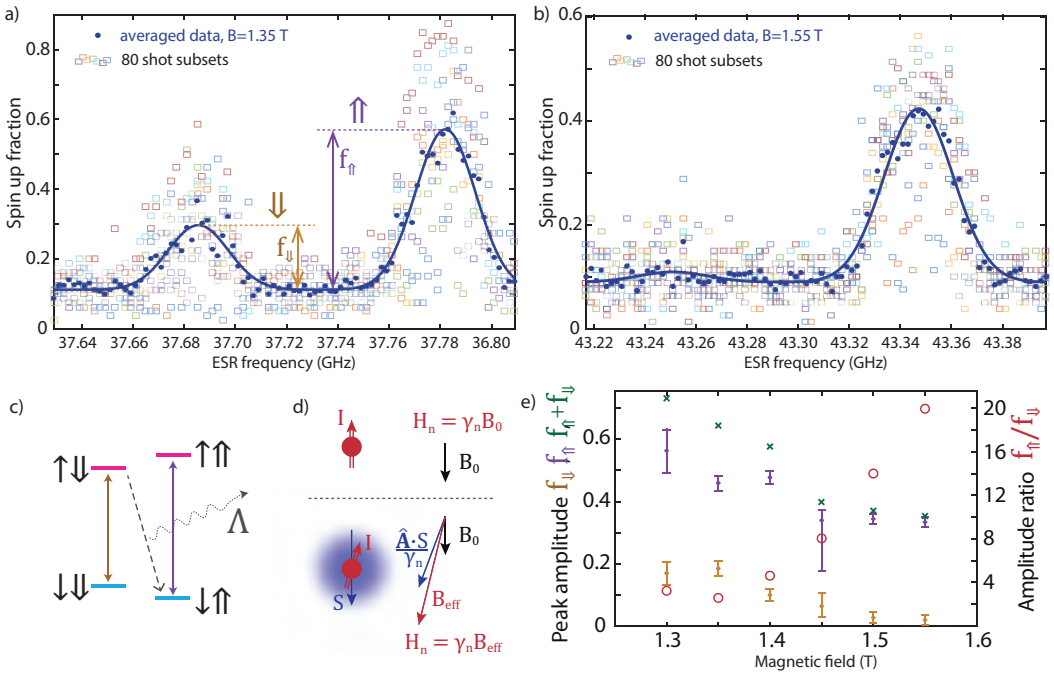

Figure 5.21: **Development of asymmetry in the 1P hyperfine spectrum with increasing magnetic field** (a) Average spin up probability at 1.35T, and short time binning of the same data set into 80 shot bins for each frequency. Coloured squares exhibit non-uniform scatter, departing from the average significantly at the resonance conditions, and indicating observation of nuclear dynamics at the binning timescale of $\sim$ 50s (b) Similar data for 1.55T. The left peak is notably suppressed due to a nuclear-electron flip-flop process, releasing the energy difference as a phonon. (c) Schematic of the flip-flop cross relaxation mechanism, emitting energy Λ to the phonon bath while conserving spin. (d) Ionisation shock may flip the nuclear spin when its effective magnetic field is non-adiabatically altered by the addition or removal of an electron. The anisotropic hyperfine interaction tilts the hyperfine field $\hat{A} \cdot S$ (e) Evolution of the two resonance peak amplitudes (tan, purple) as defined by arrows in (a), along with their sum (green) and ratio (red) as a function of magnetic field, displaying the gradual suppression of the low frequency resonance as the nuclear spin pumping process becomes more efficient.

state was observed and attributed to a process described as 'ionisation shock'. Here the effect of projecting the nuclear spin onto a time varying quantisation axis when loading and unloading electrons will result in a non-adiabatic change of eigenstate with some low but non-zero probability. We illustrate the concept in Figure 5.21(d), where the upper panel shows the nuclear spin I aligned (in this case anti-parallel) to the external field B_0 in the absence of an electron. With a Hamiltonian consisting only of the nuclear Zeeman term, $|\Downarrow\rangle$ and $|\Uparrow\rangle$ are perfect eigenstates. The lower panel shows the situation where the donor is occupied by an electron of spin state S. Here, the states $|\downarrow\Uparrow\rangle$ and $|\uparrow\Downarrow\rangle$ are not perfect eigenstates of the two spin Hamiltonian containing now a hyperfine interaction term. As defined in Section 2.4.1, the eigenstates for these two spin anti-parallel states evolve from the singlet and triplet states at zero field and are properly described as:

$$\left|\widetilde{\downarrow\Uparrow}\right\rangle = \cos(\eta/2)\,|\downarrow\Uparrow\rangle - \sin(\eta/2)\,|\uparrow\Downarrow\rangle \tag{5.31}$$

$$\left|\widetilde{\uparrow\Downarrow}\right\rangle = \cos(\eta/2)\,|\uparrow\Downarrow\rangle + \sin(\eta/2)\,|\downarrow\Uparrow\rangle \tag{5.32}$$

$$\tan(\eta) = \frac{A}{(\gamma_e + \gamma_n)B_0} \tag{5.33}$$

While the mixing angle η, describing the degree of approximation in assuming the simple product states as eigenstates (at a field of $B_0 = 1.55$T and hyperfine coupling $A = 96.5$MHz) is only $\sim 2.2 \times 10^{-9}$, the misalignment of eigenstates may be enhanced by the presence of an anisotropic component to the hyperfine interaction, which is in general defined by a tensor $\hat{A}$. The diagonal terms dominate, meaning that it is normally sufficient to consider a scalar approximation of A in what is called the contact hyperfine interaction. Small off diagonal tensor components, arising from anisotropy in the electron wavefunction for instance due to a non-zero electric field in the device, would allow the nuclear spin to experience an effective magnetic field component $(\hat{A}\cdot S)/\gamma_n$ that is not parallel to the external B_0 field, although the electron spin S is. By a combination of the two effects (non-zero mixing angle η, and anisotropic hyperfine $\hat{A}$) the quantisation axis for the nuclear spin changes instantaneously as indicated in the sketch of Figure 5.21(d) by B_0 and B_{eff} whenever the donor is ionised during the readout, feedback and initialisation sequence. Precession around these constantly switching axes allows the nuclear spin to flip back to $|\Downarrow\rangle$, providing an explanation for why we do not observe permanent occupation of the $|\Uparrow\rangle$ state, and complete supression of the lower frequency resonance peak, since the nuclear T_1 relaxation time for phosphorus donors is known to be on the

order of thousands of seconds at low temperature[178].

Further to the asymmetry in the amplitude of the two resonances, we observe a decrease in amplitude of both resonances at higher fields, as shown in Figure 5.21(e), which plots the amplitudes of the two resonance peaks for $|\Downarrow\rangle$ and $|\Uparrow\rangle$ as a function of B_0. Both peaks lose intensity with increasing magnetic field, and the lower line disappears almost completely within the noise floor at f_0 at $B_0 = 1.55$T. The reduction in overall spin-up fraction (the sum of up and down amplitudes, shown as green crosses) may suggest that the adiabatic passage is becoming non-adiabatic due to higher attenuation of the microwave signal at higher frequency, and consequently a reduced B_1 field strength. The change in *relative* peak intensity $f_{\Uparrow}/f_{\Downarrow}$ however, plotted with red ring markers and on the right side axis of Figure 5.21(e), suggests a process that is Zeeman energy dependent, such as the reverse of the 'flip-flop' cross-relaxation process discussed above. We were unable to measure at fields below $\sim$ 1.3T, because the Zeeman energy becomes comparable to the thermal energy of the system. If there are thermal phonons available with energy equal to the difference in $|\downarrow\Uparrow\rangle$ and $|\uparrow\Downarrow\rangle$ states, as is evidently the case in our device for the smaller magnetic field values, phonon absorption can mediate a 'flop-flip' transition, the reverse of the 'flip-flop' shown in Figure 5.21(c). As the field increases, and the Zeeman energy becomes larger, the rates of the two phonon mediated transitions diverge and the weighting of the two peaks becomes more asymmetric.

Understanding the nuclear spin dynamics is the first step toward utilising the nuclear degree of freedom as an additional or alternative qubit[50], or as a long lived quantum memory[37,179].

5.6.2 Hyperfine spectrum of the 2P qubit

The resonance spectrum measured for the electron bound to the 2P quantum dot displays instead three resonant frequencies, as Figure 5.22(a) shows. This data is based on 2000 single shots (with a faster tunnel rate than the 1P, more repetitions are possible with this qubit), and we indicate the fraction of these shots resulting in a spin-up outcome as a result of an adiabatic passage pulse with a power of +8dBm. As for the single donor qubit, the signal is frequency modulated over $\pm$20MHz in a sweep time of 150μs, giving

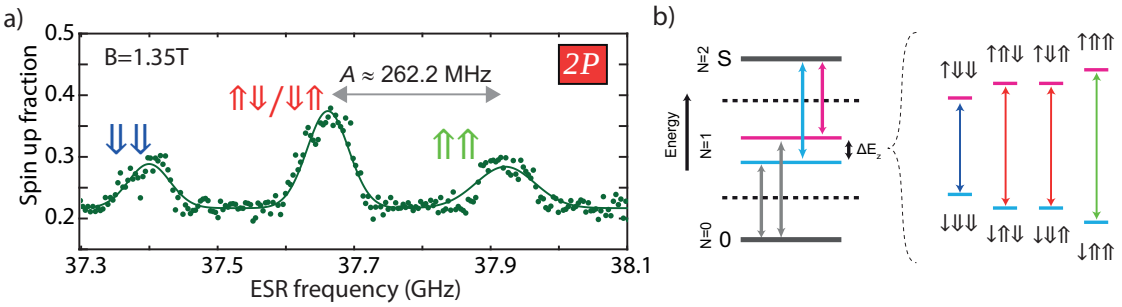

Figure 5.22: Spin resonance spectrum of the 2P molecule. (a) Spin up probability calculated from 2000 repeated single shot measurements at each frequency, following a 150s microwave pulse with an FM chirp depth of ± 20MHz and at $+8$dBm power cerntred at the frequency shown ($B_0 = 1.35$T). (b) Schematic energy level diagram indicating the readout scheme based on spin dependent loading into the 2 electron singlet state used for 2P qubit spin readout process as introduced in Section 5.3.2, and the driven transitions between pairs of combined electron-nuclear spin states.

a chirp rate of $\nu = 0.27$THz/s. The solid curve is a fit to the sum of three Gaussian peaks with common width:

$$f_{\uparrow} = f_0 + f_{\Downarrow\Downarrow} e^{\frac{-(\omega-\omega_{\Downarrow\Downarrow})^2}{2\sigma^2}} + f_{\Uparrow\Downarrow/\Downarrow\Uparrow} e^{\frac{-(\omega-\omega_{\Uparrow\Downarrow/\Downarrow\Uparrow})^2}{2\sigma^2}} + f_{\Uparrow\Uparrow} e^{\frac{-(\omega-\omega_{\Uparrow\Uparrow})^2}{2\sigma^2}} \tag{5.34}$$

from which we determine the parameter $\sigma = 30.5 \pm 2.0$MHz, related to the peak width $\omega_{\text{FWHM}} = 72 \pm 5MHz$. We also extract the baseline $f_0 = 0.21$, and peak heights: $f_{\Downarrow\Downarrow} = 0.072$, $f_{\Uparrow\Downarrow/\Downarrow\Uparrow} = 0.158$ and $f_{\Uparrow\Uparrow} = 0.067$.

The three peaks reflect the transition frequencies, sketched in Figure 5.22(b)

$$\omega_{\Downarrow\Downarrow} = \gamma_e B_0 - \frac{A_a}{2} - \frac{A_b}{2} \tag{5.35}$$

$$\omega_{\Downarrow\Uparrow} = \gamma_e B_0 - \frac{A_a}{2} + \frac{A_b}{2} \tag{5.36}$$

$$\omega_{\Uparrow\Downarrow} = \gamma_e B_0 + \frac{A_a}{2} - \frac{A_b}{2} \tag{5.37}$$

$$\omega_{\Uparrow\Uparrow} = \gamma_e B_0 + \frac{A_a}{2} + \frac{A_b}{2} \tag{5.38}$$

where A_a and A_b are the contact hyperfine interaction coefficients representing the electron wavefunction density at the location of the two donor sites (labelled a and b) of the 2P molecule. At zero electric field the $2P1e$ wavefunction is symmetric and the hyperfine interaction at the two donor sites is expected to be equal $A_a = A_b$, producing

two degenerate transition frequencies $\omega_{\Downarrow\Uparrow} = \omega_{\Uparrow\Downarrow}$.

With a finite electric field the electron wavefunction may be more densely concentrated at one site or the other, thereby breaking this degeneracy $A_a \neq A_b$. We estimate the E-field in our device (shown in Section A.5) for the operating point of the 2P qubit at around 4.3MV/m. This must have only a small effect on the two hyperfine strengths A_a and A_b, since we resolve only one central peak in the resonance spectrum. Therefore the energy separation between the two nuclear spin antiparallel states $|A_a - A_b|$ must be less than the width of the observed peak $\sim$ 30.5MHz in order to produce the three peak spectrum we observe.

The average peak separation, representing the hyperfine interaction energy A is 261 ± 10MHz, is over twice the single donor value, which is expected for a pair of donors with small spatial separation [150]. We will return to analyse this value in depth in Section 5.6.4.

Interestingly, we note that asymmetry in the peak amplitude for different nuclear spin configuration is absent in the 2P qubit's ESR spectrum. In Figure 5.23(a) at 1.35T and (b) at 1.55T we see an equal probability for each of the 4 nuclear spin subspaces, the nuclear $|\Downarrow\Uparrow\rangle$ and $|\Uparrow\Downarrow\rangle$ states being degenerate and indistinguishable, thereby producing a peak with approximately twice the amplitude of the $|\Downarrow\Downarrow\rangle$ and $|\Uparrow\Uparrow\rangle$ resonances. We also observe no strong magnetic field dependence of the peak distribution, as shown in Figure 5.23(c) which plots the three amplitudes as a function of B_0. This implies that either (i) the 'flip-flop' cross relaxation mechanism is suppressed, or (ii) that the 'ionisation shock' mechanism is enhanced, such that the nuclear state is randomised faster than it is polarised.

In order to investigate which of the two conditions (i) or (ii) is more likely, we perform an experiment where we repeatedly initialise an electron $|\downarrow\rangle$, excite the central resonance peak with an adiabatic passage pulse, and measure the electron spin, 40 000 times. This experiment allows us to determine whether the nuclear spin state is stable over the timescale of a single shot measurement sequence, which for the 2P qubit is 42ms (the time to complete the 6 level pulse sequence described in Section 5.5.2). The outcome is shown in Figure 5.23(d), where we plot a histogram of the number of times we observe N successive spin-up outcomes before the first spin-down reading. This is compared with a calculated Markovian histogram produced by a series of completely independent outcomes with the same overall probability of observing spin-up (the red dots). The inset plots the same statistics on a logarithmic scale. Figure 5.23(e) uses the same data set to

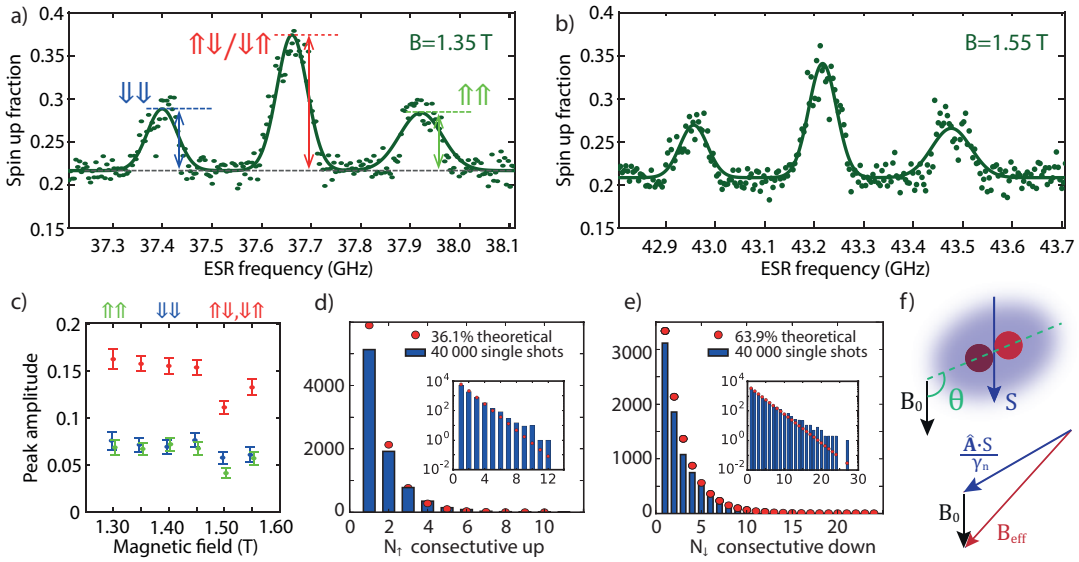

Figure 5.23: Populations of the 2P nuclear states remain independent of the magnetic field (a)Average electron spin up probability taken from 2000 single shot measurements at 1.35T, with peak amplitudes marked. (b) Similar data for 1.55T, with no significant shift in distribution of the peaks. (c) The three extracted peak heights for magnetic field values from 1.3 to 1.55T, showing no significant trend in the corresponding peak amplitudes. (d) Statistical analysis of the nuclear spin dynamics. We plot a histogram (in blue) of the number of times we observe N successive spin-up outcomes before the first spin-down, using a set of 40 000 single shot measurements all taken at the central resonance peak after an adiabatic inversion pulse. The red markers are the calculated distribution expected for a perfectly Markovian system (with no memory of the previous state). Inset plots the same histogram on a logarithmic scale for clarity. (e) a similar histogram of the count of N successive spin-down outcomes before the first spin-up, using the same data set.

plot the equivalent histogram of N successive spin-downs. We see very good agreement with the Markov model, showing that indeed the nuclear state has no long term memory and is randomised on the timescale of a single shot. This therefore indicates that the lack of state polarisation is likely due to an enhancement in the 'ionisation shock' mechanism (ii). This can be understood in the context of a 2P donor molecule by noting that the hyperfine tensor $\hat{A}$ is likely to be more highly anisotropic than in the single donor case, since the total electron wavefunction is not spherically symmetric.

We illustrate the effect of anisotropy in Figure 5.23(f). In the molecular frame, where the z-axis is defined by a vector passing through the two donor atom sites (green dashed line in Figure 5.23(f)), the full hyperfine tensor for each donor individually can be ex-

pressed:

$$\hat{A}' = \begin{pmatrix} A-d & 0 & 0 \\ 0 & A-d & 0 \\ 0 & 0 & A+2d \end{pmatrix} \tag{5.39}$$

$$A = \frac{2\gamma_e\gamma_N\mu_0}{3}|\Psi(r=0)|^2 \tag{5.40}$$

$$d = \frac{\gamma_e\gamma_N\mu_0}{10\pi}\left\langle\frac{3\cos^2\theta-1}{r^3}\right\rangle \tag{5.41}$$

Here the terms A and d represent respectively the contact and dipolar components of the hyperfine interaction, where r is the distance from the atom to a position within the extent of the assumed axially symmetric electron wavefunction. The right hand side of Equation (5.41) averages over the entire wavefunction, and θ defines the angle between the molecular axis and B_0. When this tensor is transformed into the frame defined by the B_0 quantisation axis, for large angles θ there will be significant off-diagonal terms, tilting the effective total magnetic field B_{eff} experienced by each nuclear spin in the presence of an electron. This tilt will (in general) be off-axis from the vector of B_0 which is the only magnetic field seen by the nucleus when ionised. This means the true eigenstates for the two charge states are less alike, and we would therefore expect to see enhanced nuclear spin randomisation by 'ionisation shock', consistent with our observations.

5.6.3 Gyromagnetic ratio and relative offset of the 1P and 2P resonances

Figure 5.24(a) plots the field magnetic field, B_0 dependence of the resonance frequencies for all 6 nuclear spin states across the two qubits: $\omega_\downarrow$ (brown), $\omega_\uparrow$ (purple), $\omega_{\Downarrow\Downarrow}$ (green), $\omega_{\Uparrow\Downarrow/\Downarrow\Uparrow}$ (red), $\omega_{\Uparrow\Uparrow}$ (blue). The values plotted are obtained from Gaussian peak fits to the recorded spectra at each magnetic field setting. The slope of the lines in (a) reflect the electron gyromagnetic ratio $\gamma_e = g\mu_B/h$. Planck's constant $h = 4.1257 \times 10^{-15}$eV/Hz and the Bohr magneton $\mu_B = 5.7884 \times 10^{-5}$eV/T are known constants[70], allowing us to extract the electron's g-factor. All lines give a mean gyromag-

netic ratio of $\gamma_e = 27.886 \pm 0.030$GHz/T corresponding to $g = 1.987 \pm 0.002$. However we note that due to experimental uncertainty in the calibration of our superconducting magnet, our measurement of g has a larger systematic uncertainty of 0.02. The final result – $g = 1.987 \pm 0.020$ is therefore consistent with the bulk g-factor of 1.9985[71]. This value confirms that we indeed see the resonance of our intentionally placed donors, since electrons bound to most types of lattice defects and surface state traps[180] are known to have a g-factor larger than 2.0.

For clarity, the insets Figure 5.24(b) and (c) display the hyperfine splitting of the 1P and 2P qubits respectively, by plotting the resonant frequency with the Zeeman term subtracted $\omega' = \omega - \gamma_e B_0$, to show that the hyperfine splitting is independent of magnetic field for both qubits. We extract an average hyperfine splitting of $A = \Delta\omega' = \omega'_{\Uparrow} - \omega'_{\Downarrow} = 97 \pm 10$MHz between the two single nuclear spin states of the 1P qubit, with a mean frequency offset from $\gamma_e B_0$ of $\bar{\omega'} \sim 176$MHz, corresponding to a magnetic field at zero frequency of $\sim$ 6mT. For the 2P qubit, the average hyperfine separation is $A = \Delta\omega' = (\omega'_{\Uparrow\Uparrow} - \omega'_{\Downarrow\Downarrow})/2 = 262 \pm 20$MHz, with a similar offset from $\gamma_e B_0$ of $\sim$ 131MHz in the $|\Uparrow\Downarrow\rangle$ / $|\Downarrow\Uparrow\rangle$ resonance. The large uncertainties are a product of the adiabatic passage strategy, which artificially broadens all resonances.

In Figure 5.24(c) we display also the 1P qubit resonances as faded dashed lines for direct comparison of the two spectra. We note the presence of an offset of $\bar{\omega'} - \omega'_{\Uparrow\Downarrow/\Downarrow\Uparrow} = \sim$ 45MHz between the central frequency of the two qubits. In magnetic field terms this corresponds to $\sim$ 1.6mT. The offset is constant for all magnetic fields measured, so cannot be explained by drift in the superconducting magnet over time. The two qubits are operated at different electric field configurations, 4.5 and 4.3MV/m for 1P and 2P but oriented in different directions (as outlined in Section A.5). A Stark shift of the hyperfine energy, $A(\vec{E})$ would affect the line separation $\delta\omega'$, but not the offset ω' (A terms cancel out in the definition of $\bar{\omega'} = (\omega'_{\Uparrow} + \omega'_{\Downarrow})/2$). One possible explanation for our observed offset is a Stark shift of the g-factor, where the gyromagnetic ratio itself is modified by an electric field $g(\vec{E})$, and this hypothesis is consistent with the uncertainty in our extracted g factors, as indicated in Figure 5.24(b) and (c), independently fitting the slope of the lines for the two qubits produces g factors (1.988 and 1.986) that differ by 0.2%. Although this difference is of the same size as the uncertainty in the extracted values, it is enough to explain a 45MHz shift on top of a $\sim$ 40GHz resonance frequency. Alternatively, the 1.6mT offset may be due to a small fixed local magnetic field gradient

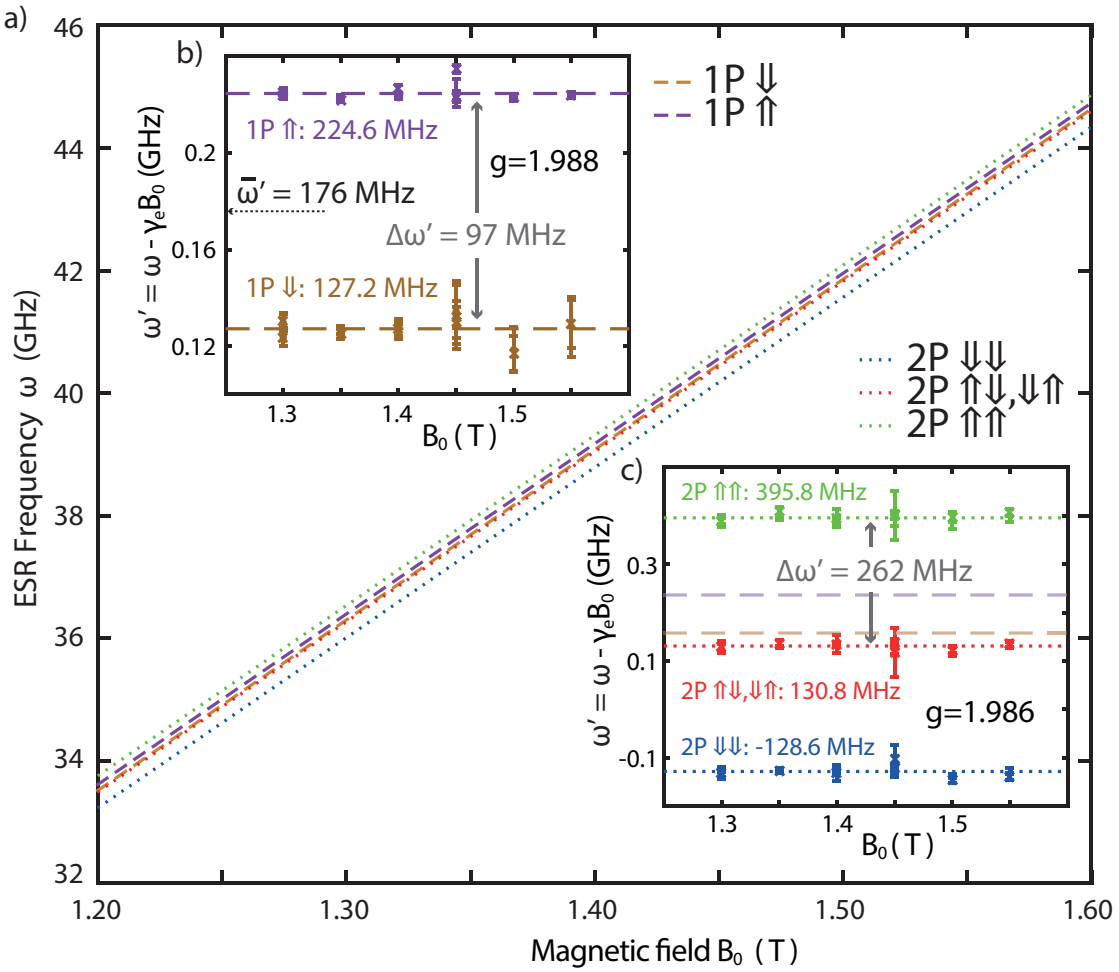

Figure 5.24: Comparison of resonance spectra for the 1P and 2P qubits as a function of magnetic field. (a) Gyromagnetic plot of the five resonant peaks of the two qubits measured from 1.25 to 1.55T. Independent fits to both qubit resonances converge with at a g-factor of 1.987 ± 0.02. Insets show the Hyperfine field offsets of the individual nuclear spin states of the 1P (purple & brown) and 2P (green, red & blue) qubits. Insets (b) and (c) display the resonance frequencies with the linear Zeeman term subtracted, showing more clearly the variation in hyperfine splitting for the 1P and 2P states. $\bar{\omega}'$ indicates the average offset for the 1P $|\Uparrow\rangle$ and $|\Downarrow\rangle$ lines.

across the two qubit sites, perhaps due to some external magnetic component within the dilution refrigerator.

We presented in this section the first electron spin resonance measurements on a precision donor device. The resonance spectra for our two qubits (1P and 2P) are unique, demonstrating that a combination of single donor and donor molecule qubits will permit addressable single qubit operations.

5.6.4 Determination of donor positions from the hyperfine spectrum

In Section 5.2.3 we summarised theoretical work by Wang *et al.*[150], who have used atomistic tight binding calculations to predict the hyperfine energies in 2P and larger donor molecules. This section describes results developed in collaboration with those authors, from the theoretical group of Rajib Rahman*, to understand the impact of both electric fields and the spatial configuration of donor atoms, on the spin resonance spectrum seen for our 1P and 2P qubits.

The 1P hyperfine splitting of 97MHz observed in our 1P qubit differs by 17% from the bulk value. This can be explained by the presence of a strong electric field within the nanostructure which modifies the electron wavefunction density at the donor site. The Stark shift for P donors in silicon is dominated by a quadratic term $\Delta A(E) = \zeta_A E^2 A(0)$, and has been measured[181] in bulk ensemble samples to have a value of $\zeta_A = -2.5 \times 10^{-3}\mathrm{m}^2/\mathrm{MV}^2$. Under our experimental conditions the E-field due to gate voltage settings is calculated to be 4.5MV/m (in Section A.5), which would translate to a ΔA of only 5% with this simple phenomenological quadratic shift. It should however be noted that our donor wavefunction is likely already perturbed by the electric field inherent to the surrounding nanostructure even without voltages applied to the in-plane gates. The background electrostatic potential has been seen to significantly modify single donor binding energies and shift chemical potentials by up to $\sim$ 100meV in similar donor defined devices[53,113]. It should also be noted that theoretical work on the Stark shift of donor hyperfine coupling to date has considered only vertical electric fields ionising a

* Electrical and Computer Engineering Department, Purdue University

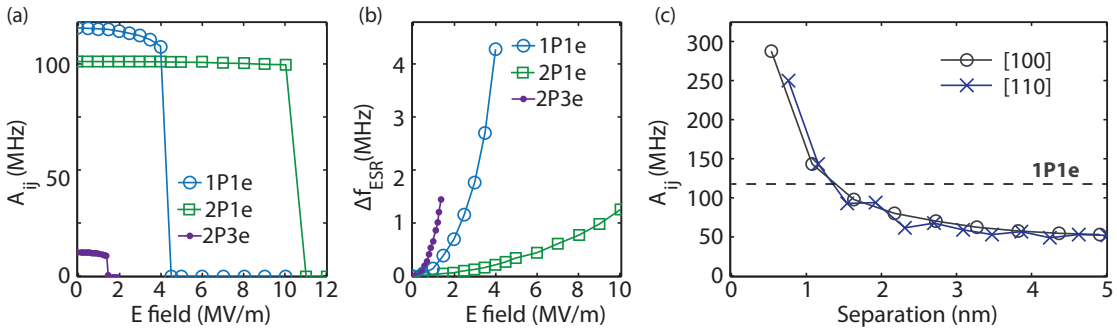

Figure 5.25: Simulated hyperfine energies as a function of electric field and donor atom separation. (a) Electric field dependence of the hyperfine interaction energy between $j = 1, 2$ donor nuclei and $i = 1, 3$ electrons, calculated numerically with an atomistic tight-binding method. (b) Variation in the ESR resonance frequencies as a result of the Stark shifted hyperfine energy in (a), illustrating the smaller effect for a 2P1e state relative to the single donor Stark shift. (c) Simulated hyperfine energy for a 2P1e state as a function of the spatial separation between the two donor atoms along two directions in the cryatal lattice. All parts reproduced from Wang *et al.* [150]

donor electron by drawing it toward a surface gate or reservoir, as found in MOSFET type nanoelectronic devices or the original Kane [45] qubit architecture. In our device however, the E field is primarily oriented in the plane parallel to the surface.

To illustrate the Stark shift effect, in Figure 5.25(a) we show numerical tight binding simulations by Wang *et al.* [150], computing the (vertical) electric field dependence of the contact hyperfine coupling A_{ij} between $j = 1, 2$ donor nuclei and $i = 1, 3$ electrons. The reduction in A_{ij} with increasing E field is on the order of $\sim$ 10MHz for the 1P1e case (blue circles) before the donor in the simulation is ionised at 4MV/m. Figure 5.25(b) shows the same data presented instead as the difference in electron spin resonance frequency Δf (for the cases where all donor spins are $|\Uparrow\rangle$). We note that this 1P1e simulation produces a Stark shift of a similar order of magnitude to that measured in our experiment. These calculations provide qualitative guidance, but we note that they do not capture fully the physics of our planar device where the electron tunnels not vertically through a 2-dimensional tunnelling cross section, but instead within the device plane to a small SET, through effectively a 1D tunnelling cross-section.

The 2P1e electron wavefunction is more tightly confined by the combined Coulomb potential well of two donor atoms and therefore is not as easily displaced by an electric field. Since the hyperfine energy depends on the wavefunction density, this results in a suppressed Stark shift – an almost constant value of A_{ij} up to the ionisation point

as shown by the green squares in Figure 5.25(a). However, a simulation of A_{ij} in a 2P quantum dot, as a function of the spatial separation of the two donor atoms, shown in Figure 5.25(c), indicates that we should expect the wavefunction distribution to be very sensitive to the exact position of the two phosphorus atoms. We see here that the hyperfine energy has a maximum of more than twice the 1P1e value, the enhancement due to the stronger Coulomb confinement when the donors are close together, forming a strongly hybridised molecular orbital with greater density at the donor cores. A_{ij} decreases as the donors are positioned farther apart, reaching $\sim$ 50MHz beyond a separation distance of 4nm, where the electron wavefunction resembles a linear combination of two non-interacting donor-bound states, in which each donor atom experiences approximately half the electron density as in the 1P1e situation. The exact calculated values differ slightly for the circle and cross markers, but the overall trend is similar for donors separated along [100] and [110] equivalent crystal axes.

In our 2P molecule the hyperfine splitting is 262MHz, suggesting (based on Figure 5.25(c)) that the two donor atoms of the 2P qubit are less than 1nm apart in our device. We turn now to a detailed analysis of the hyperfine energy in a range 2P quantum dots with different geometries of the two phosphorus atoms comprising the dot. Guided by the results of Wang *et al.*[150] we restrict ourselves to pairs of lattice sites within a distance of 1nm, but in a silicon lattice, a sphere of radius 1nm still encompasses around 200 atoms. Since our device is fabricated by STM lithography on the [001] plane, we are able to exclude a large proportion of sites. The donor phosphorus atoms are incorporated into the silicon crystal at the surface layer at fabrication time, and are then overgrown with epitaxial silicon after an incorporation anneal which prevents the donors from segregating up toward the surface during the silicon growth. The growth is also performed at low temperature, preventing thermal diffusion of the donors away from their original positions. Therefore we are primarily interested in donor pair geometries where both donor atoms lie in the fabrication plane. For completeness we have also considered configurations deviating by 2 monolayers above and below the plane in our simulations, and the full set of results can be seen in Section A.6.

Figure 5.26(a) shows the calculated hyperfine energy for a 2P quantum dot hosting a single electron, where we vary the separation r between the two P atoms of the quantum dot. Since the donors substitute for silicon within the crystal lattice, there are only discrete values of r which are valid. Large circles indicate the A values for configurations

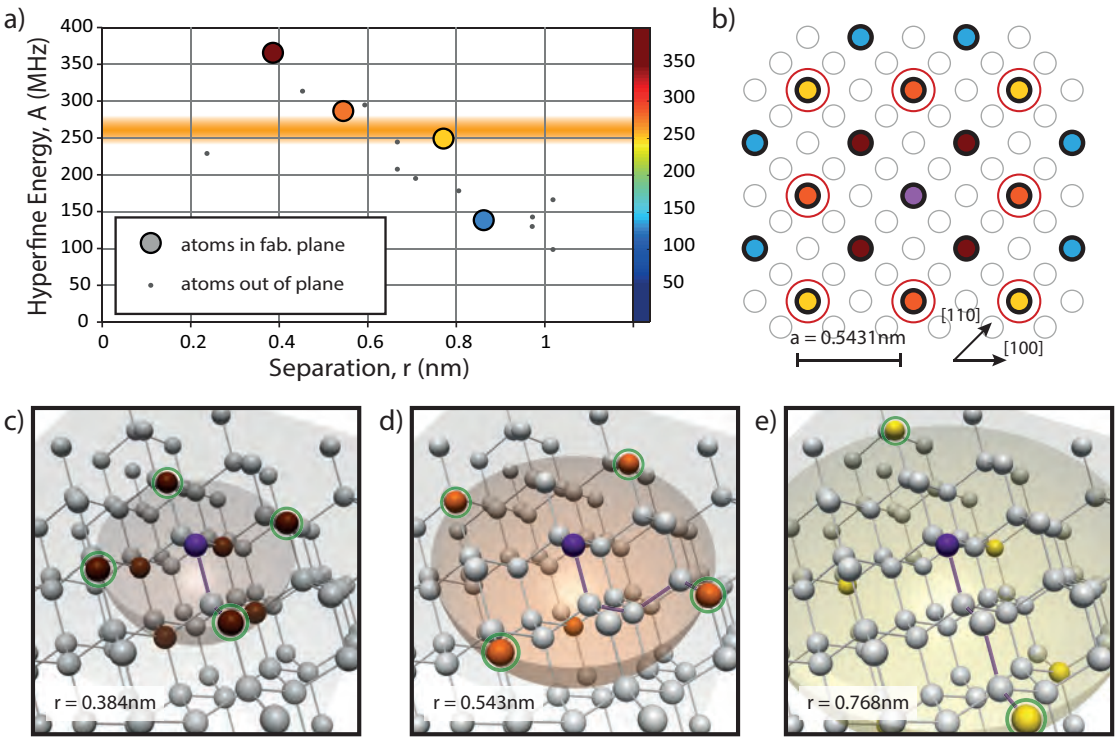

Figure 5.26: Intrinsic hyperfine energies for different donor configurations within a 2P molecule. (a) Simulated hyperfine interaction energy A, for atomic configurations of a 2P quantum dot with donor separation less than 1nm. Configurations with both donors in the fabrication plane are shown as large circular markers, configurations with a donor outside of the fabrication plane are represented by small grey dots. (b) Schematic showing the layout of the [001] crystal plane in which the device is fabricated. Atoms in this plane are shown coloured according to their relationship to the central purple reference site. Red rings denote 8 sites with a hyperfine coupling consistent with our measurement (262MHz). Grey circles represent atoms within the crystal lying in layers above and below the fabrication plane. (c,d,e) 3D images of the silicon crystal lattice, highlighting equivalent sites at three different separation distances from a reference site (purple). Transparent hemispherical shells mark the distances r given for each image. Green rings highlight atoms lying in the fabrication plane, and purple highlighted bonds show that the brown atoms in (c) are 2nd nearest neighbours to the reference site, and the highlighted atoms in (d) and (e) are 4th nearest neighbours. Site colouring corresponds to (a) and (b).

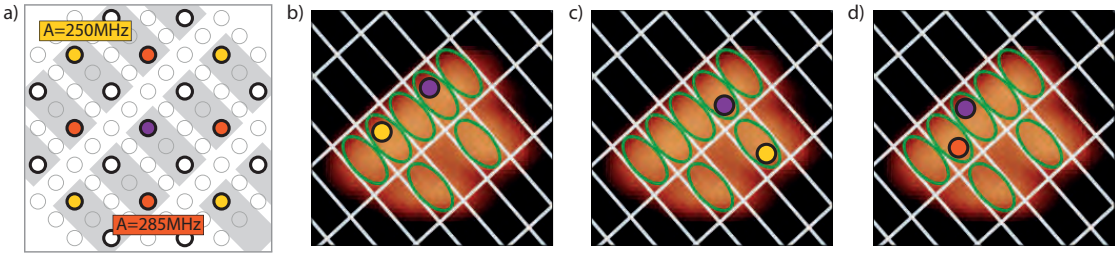

Figure 5.27: **Donor configurations consistent with the 2P lithographic patch.** (a) Schematic showing the layout of the [001] crystal plane in which the device is fabricated. Atoms in this plane are again coloured according to the hyperfine strength produced in a 2P molecule together with the central purple atom, as labelled. Grey circles represent atoms within the crystal lying in planes above and below the fabrication plane, and rectangles the surface dimer reconstruction present during fabrication. (b,c,d) Atomic resolution STM image of the 2P qubit's lithographic patch, interpreted as a total of 7 exposed silicon dimers marked in green. Three potential donor configurations from (a) lying within the patch are shown.

where both donors lie in the fabrication plane (the [001] crystallographic plane), and the colour of the circle denotes A according to the colour-scale on the right side of the plot. Small grey dots indicate A values for donor configurations where one of the two atoms is in a position lying above or below the fabrication plane, and the orange band represents the hyperfine energy measured experimentally for our 2P qubit device. The geometrical layout of the in-plane configurations of Figure 5.26(a) are displayed in Figure 5.26(b), which shows that there are several equivalent sites at a particular distance from the reference atom (coloured purple) due to the symmetry of the lattice. In fact there are many more configurations satisfying these four values of the inter-donor separation, where one atom lies far above or below the plane, as we show in Figure 5.26(c-e), three images showing the full layout of atoms in the silicon lattice in 3D. Taking the first donor of the 2P system as the purple reference atom, Figure 5.26(c) shows a hemispherical shell marking a distance $r = 0.384$nm, and indicating that there are 4 atomic sites at this distance which lie in the plane (marked by green rings) for which a second donor would produce a total hyperfine energy of ~ 360MHz. An additional 4 such sites are situated 2 monolayers below the plane (and there are 4 more above the plane – not shown). These (brown coloured) atoms are all second nearest neighbours to the reference site, as highlighted by the two purple shaded bonds. Figure 5.26(d) and (e) display similar hemispherical shells for fourth nearest neighbour groups of donor sites at separations of $r = 0.543$nm and $r = 0.768$nm respectively.

Provided our experimental value of $A = 262 \pm 20$MHz, only the eight orange and

yellow geometries in Figure 5.26(b) are possible representations of the configuration of donors in our device. These are consistent with the size of the lithographic patch that was fabricated. Figure 5.27(a) shows the planar configurations of Figure 5.26(b) which are consistent with our measured value – with calculated hyperfine energies $A = 250$MHz and 287MHz, along with a representation of the dimer reconstruction (grey rectangles), characteristic of the silicon surface during fabrication. Pairs of adjacent surface layer atoms move together forming dimers as the bond lengths near the surface change to minimise the total energy, but once the device is encapsulated with the silicon capping layer, the lattice returns to the fully symmetric diamond cubic structure.

The dimer pattern is overlaid on an STM image of the lithographic patch in Figure 5.27(b-d) – the bright areas in the image indicating the presence of dangling bonds which allow the phosphine to adsorb and incorporate into the lattice at those positions. We conclude from this image that five adjacent dimers in one row, and two single dimers in the neighbouring row were exposed to the phosphine precursor gas. As described in Section 3.1.3, the additional hydrogen atoms of the phosphine molecule (PH_3) are removed from the P atom by moving to occupy the surrounding dangling bond sites, therefore 2-4 adjacent exposed dimers are needed for the incorporation of one P atom. Dangling bonds are known to thermally migrate along the lattice rows at the $\sim 330°$C incorporation anneal temperature, providing a means by which a P atom may incorporate at a single isolated dimer location, provided there are additional dangling bonds nearby. We indicate one possible configuration of the two donor atoms (by the purple and yellow dots) within the lithographic patch in Figure 5.27(b), where there is sufficient space to permit the incorporation process. The potential configuration shown in Figure 5.27(c) relies on thermal movement of dangling bonds to permit incorporation at the initially isolated dimer in the lower row. Figure 5.27(d) indicates a third potential layout.

There are a number of alternate arrangements within the seven dimer lithographic patch consistent with our observed hyperfine spectrum. The guidance provided by the atomistic modelling enhances our understanding of the configuration of atoms within the 2P quantum dot, and has allowed us to reduce the number of possible atomic configurations from several hundred down to around ten.

5.6.5 Extracting the Rabi field strength from resonance peak amplitudes

Having determined the likely locations and distance between the P donors of the 2P qubit, and having measured the hyperfine spectra for both the 1P and 2P qubits, we now investigate the Rabi field strength. The strength of the oscillating Rabi magnetic field B_1 achieved in our experiment is analysed by measuring the change in the amplitude of a spin resonance peak as we vary the power of the microwave signal applied to the antenna. The result is shown in Figure 5.28(a), which plots in red the amplitude, or spin-up fraction relative to the background value, of the centre peak $f_{\Uparrow\Downarrow/\Downarrow\Uparrow}$ of the 2P qubit as a function of microwave power, specified in dBm at the signal generator. We see that for powers between 0 and 10dBm, the amplitude is rather constant at around 0.15, falling toward zero below 0dBm and also falling slightly above 10dBm. Values are obtained by fitting the measured spin resonance spectra using Equation (5.34). We note that the baseline of the Gaussian peak f_0 (shown in blue) remains constant within the fitting uncertainty at around 0.23. This is a clear indication that exciting the antenna even up to 15dBm does not change the spin up fraction off-resonance due to heating effects on the SET or due to AC electric fields overcoming Coulomb blockade to eject the trapped electron and reloading a random spin state. The high value of the baseline (more than the signal amplitude $f_{\Uparrow\Downarrow/\Downarrow\Uparrow}$) is due to poor initialisation and readout fidelity.

Also in Figure 5.28(a) we plot a simulation of the expected spin up fraction, normalised to our maximum measured amplitude (dashed grey curve). The simulation takes the adiabatic passage Hamiltonian of Equation (5.20), using parameters for the detuning profile $\Delta\omega(t)$ taken from the experiment: a frequency modulation span of $\pm$20MHz and sweep time $T_S = 150\mu$s, and thus a chirp rate of $\nu = 2.67 \times 10^{11}\text{Hz}^2$.

$$H(t) = \gamma_e B_1 \sigma_x + \Delta\omega(t)\sigma_z \tag{5.42}$$

We then integrate the time dependent Schrödinger equation:

$$i\hbar\frac{\partial\Psi(t)}{\partial t} = H\Psi(t) \tag{5.43}$$

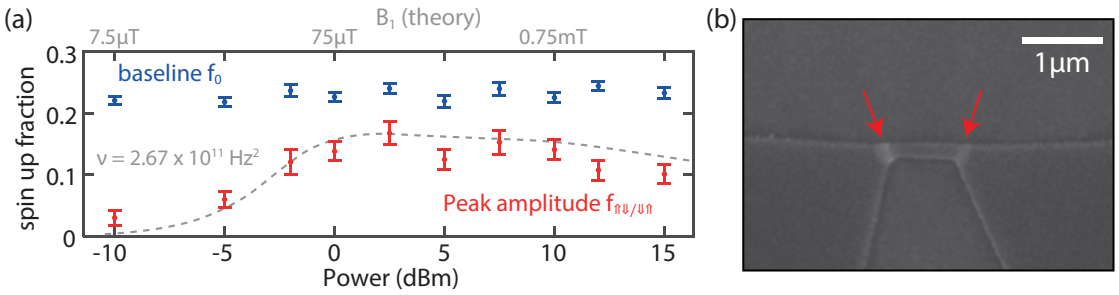

Figure 5.28: Microwave power dependence of the ESR peak amplitude. (a) Plot of the measured peak amplitude of the central resonance of the 2P qubit $f_{\Uparrow\Downarrow/\Downarrow\Uparrow}$ (red) and the baseline f_0 due to initialisation and readout errors (blue) as a function of the power of the applied microwave signal in a B field of 1.45T. Also shown in grey is a theoretical curve simulated using the adiabatic passage Hamiltonian and assuming a B_1 magnetic field of 75μT is achieved at 0dBm input power. (b) SEM image of the aluminium antenna taken after the measurements. Possible stress points are indicated

to determine the final state $\Psi(T_S)$, the z-projection of which describes the theoretical spin up fraction. We find good agreement with the experimental data when we set the oscillating Rabi magnetic field $B_1 = 75\mu$T at 0dBm power. This produces the theoretical plot shown (dashed grey curve), and associates the lower power axis with the upper B_1 field axis. Remarkably, the 1mW = 0dBm value of B_1 obtained in this way is only 30% different from the prediction of the finite element predictive modelling of the microwave frequency fields presented in Section 5.4.1.

Unfortunately, following the spin resonance spectrum measurements described in this section, an accidental electrical discharge event occurred, which could not be linked to any change in the hardware configuration or voltage settings. Indeed this shock occurred in the middle of a typical measurement sequence, at a time when nobody was present in the laboratory. Figure 5.28(b) shows an SEM image of the antenna after the event. We note indications of stress at the corners of the terminating nanowire (marked by arrows). Following the event, the device stability was reduced, and one of the in-plane gates (G_R) experienced large leakage currents when biased.

As a result, additional work toward coherent spin manipulation with the original 1P/2P qubit device was unsuccessful. Instead, a second two qubit device was produced, which we describe in the next section.

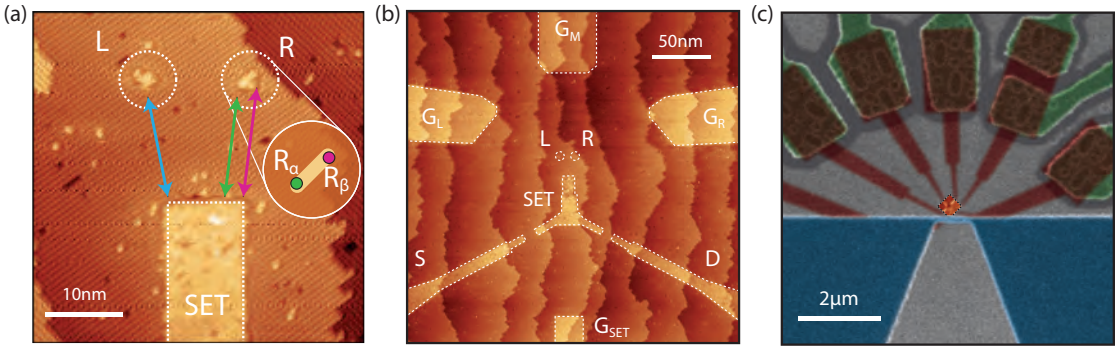

Figure 5.29: Integrated ESR antenna on a multiple quantum dot device. (a) STM image of the two intended qubit sites, tunnel-coupled to each other and to the readout SET. Three arrows indicate that after incorporation of the P donors, three quantum dots are formed, L, R_α and R_β. (b) STM image of the complete nanostructure, showing gates G_L, G_M, G_R and G_{SET} and the readout SET and its source (S) and drain (D). (c) False colour SEM image showing the relative positioning of donor-defined nanostructure (orange), ohmic contact patches (green) and ESR antenna (blue).

5.7 Coherent control of a few-electron spin state in a precision few-donor device

To continue toward the aim of controlled coherent spin state control of a single electron state, a second 2 qubit device, shown in Figure 5.29 was fabricated, nominally equivalent to the original 1P/2P qubit device. I fabricated this second double dot device and performed the spin resonance and control experiments detailed below, working together with Lukas Fricke.

Figure 5.29(a) is an STM image of the two few donor quantum dots, nominally 13nm apart, tunnel-coupled at a distance of 17nm to the readout SET. Three tunnelling pathways to the SET are shown, indicating that there are in fact three quantum dots present in the device, which we determine and explain based on electrical and spin measurements below. The lithographic patch for the site on the right (R) is eight dimers long, and we show later that donor incorporation into the site R has resulted in two electrically separate entities likely residing at opposite ends of the lithographic patch, which we denote R_α and R_β, with a strong tunnel coupling between them.

A larger-scale STM image in Figure 5.29(b) shows the four gates (G_L, G_M, G_R and G_{SET}) for tuning the quantum dot potentials, and the readout SET and its source (S)

and drain (D) reservoirs. The false colour SEM image of Figure 5.29(c) shows the location of the buried planar P doped metallic contact wires and patches (orange), contacted to the overlapping surface aluminium contacts (green) through vertical contact vias visible as circular structures in the overlapping areas, relative to the aluminium surface antenna (blue). The antenna fabrication procedure is as described in Section 5.4.3, the only significant difference in the layout of this new device being that the antenna is positioned such that the qubit sites lay $\sim$ 300nm *outside* the loop of the antenna.

5.7.1 Determination of charge states in the presence of an unintended third quantum dot

Figure 5.30(a) displays the full charge stability map for this new device, showing the SET current as a function of left and right gate (G_L, G_R) voltages for this scan $V_M = 750$mV and $V_{SET} = 300$mV. Diagonal lines of high current represent Coulomb peaks of the SET, where resonant tunnelling from drain to SET island to source is allowed. Discontinuities are seen in the Coulomb peaks when an electron tunnels to or from one of the donor quantum dots, changing the charge state. We highlight 6 such charge transitions: 1 for the left dot (L, blue); and 5 for the right dot. Of these 5, we identify 2 with the entity R_α (green), and 3 with the entity R_β (pink). Inter-dot charge transitions where the total number of electrons on the three quantum dots does not change are marked in white.

This assignment was achieved by careful analysis of the spin parity of each transition. A high resolution gate-map of the area surrounding location © is shown in Figure 5.30(b). We may determine the electron occupation numbers above and below the dot transition (the dotted line) by attempting a spin readout experiment. In Section 5.3.2 we introduced spin dependent loading and unloading sequences to enable spin readout.

- Consider first the spin-dependent Load applied to the transition in Figure 5.30(b). Starting in the N electron state at the red circle marker, we move along the detuning axis to the position marked with a red diamond at the border of the $N + 1$ electron region. If N is an odd number, then by doing so we should be able to read out the spin of the un-paried electron as illustrated in the left panel

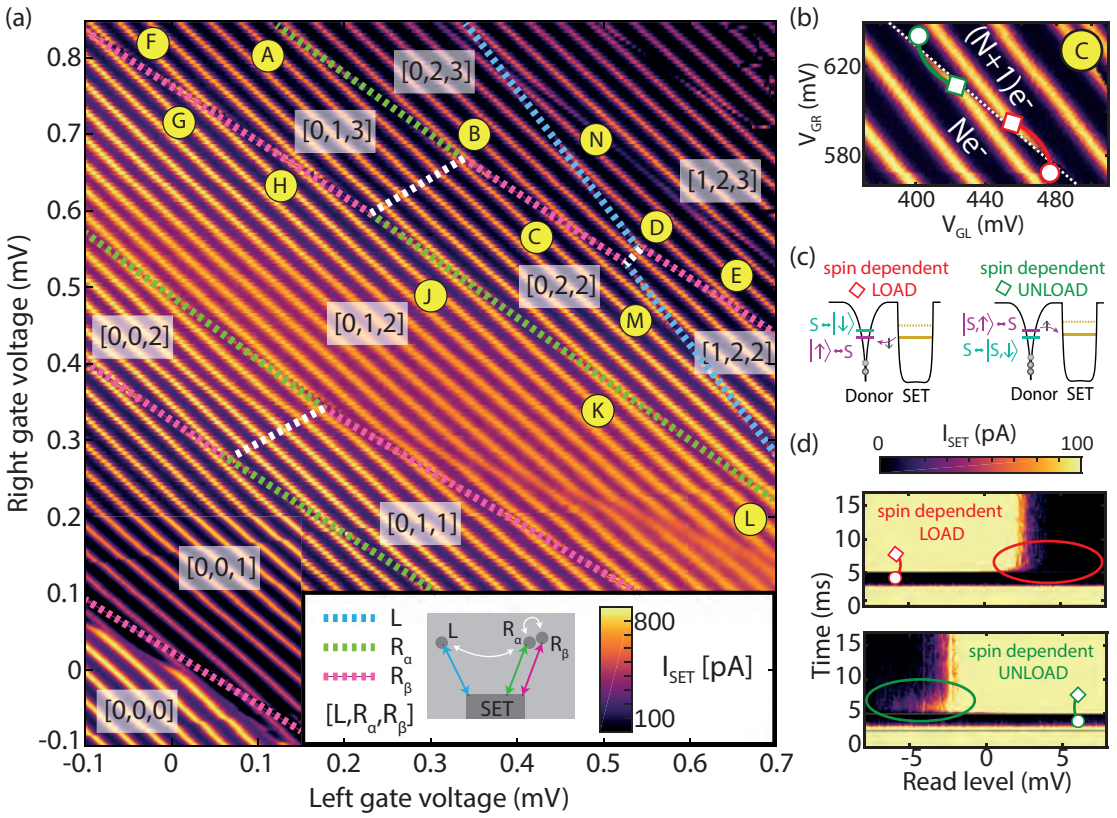

Figure 5.30: Charge stability map and charge parity confirmation with spin readout. (a) Charge stability map, plotting the SET current I_{SET} as a function of left and right gate voltages (with $V_M = 0.3$V, $V_{SET} = 0.75$V). Diagonal lines represent Coulomb peaks of the SET sensor, which are shifted by a charge state transition of one of the donor quantum dots. We highlight transition potentials for L, R_α and R_β dots with blue, green and pink dashed lines respectively. Inter-dot transitions are shown in white. Three-tuples indicate the assigned charge state for each stability region, giving the number of electrons on each of the three dots as $[L, R_\alpha, R_\beta]$. Yellow circles label discontinuities in SET lines where spin readout measurements are performed. (b) Detail plot of one such discontinuity Ⓒ, where we determine that the number of electrons on R_β changes from 2 to 3. (c) Two potential readout strategies. A spin dependent load process, where a singlet state is formed conditional on the existing un-paried spin state, if the addition of an electron brings the total to an even number. And a spin dependent unload process, where a singlet state (or zero electron state) is reached conditional on the existing un-paried state, if the unloading of an electron brings the total to an even number. (d) Result of attempting the two readout strategies at Ⓒ in a magnetic field $B_0 = 2.5$T. The unload process shows the characteristic 'spin tail' feature (circled in green), where the load does not, evidence that a singlet state with an even number of electrons is found by unloading, and not by loading an electron to R_β at location Ⓒ

of Figure 5.30(c). Here, if the initial state is a $|\uparrow\rangle$ the loading of an additional $|\downarrow\rangle$ electron will temporarily form a singlet state S, as indicated by the purple arrow. This change of charge state produces a current through the SET until the additional electron again unloads via the energetically accessible transition $S \rightarrow |\downarrow\rangle$, leaving the dot in the spin ground state. This transient behaviour cannot occur if N is an even number – the additional electron will simply load directly into the spin ground state, where it remains until the electrochemical potential is changed.

- Alternatively, we can apply the spin-dependent UNLOAD. Starting in the $N+1$ electron region at the green circle marker, we attempt to unload one electron by moving to the position indicated with the green diamond. If $N+1$ is an odd number, then this will allow readout of the un-paried electron as shown in the right side panel of Figure 5.30(c). In this case, if the un-paried electron is $|\uparrow\rangle$ it may unload from the dot as indicated by the purple arrow. This allows current to flow through the SET, until a new electron tunnels onto the dot to occupy the spin ground state. Similarly, the transient behaviour is impossible in the case that $N+1$ is an even number, thereby providing an indication of the charge parity.

Figure 5.30(d) shows the outcome of attempting the two readout types at ⓒ, for a range of values of the 'read level' (the exact position along the detuning axis of the diamond marker). We observe that the characteristic spin tail feature displaying transient current is present only when readout is performed using the UNLOAD process, a direct indication that the charge parity across this transition is N even, $N+1$ odd. Application of this spin readout parity test to the majority of the labelled locations Ⓐ to Ⓝ is summarised in Table 5.4.

We note for instance that Ⓐ and ⓒ display opposite parity, and therefore cannot be due to the same entity. As we do not observe further charge transitions at lower gate voltages, we determine that all three dots L, R_α and R_β contain zero electrons at $V_{GL} = V_{GR} = 0$, and the resulting assignment of charge states $[L, R_\alpha, R_\beta]$ shown on Figure 5.30(a) is consistent with the full set of parity measurements.

	readout type	tunnel time	dot assigned		readout type	tunnel time	dot assigned
A	LOAD	100μs	R_α	H	none	3ms	R_β
B	none	100μs	–	J	LOAD	800μs	R_α
C	UNLOAD	2ms	R_β	K	LOAD	500μs	R_α
D	–		–	L	–		R_α
E	UNLOAD	2ms	R_β	M	LOAD	100μs	L
F	–		R_β	N	–		L
G	UNLOAD	3ms	R_β				

Table 5.4: Spin readout parity analysis for charge state determination in a triple quantum dot system: showing the successful spin readout type and measured tunnel rate for each of 13 SET line discontinuities, and the resulting assignment of each transition to one of the three quantum dots. 'none' indicates that neither of the two readout methods produced a visible 'spin tail', and '–' simply indicates that spin readout measurements were not performed. The identity of G, L, N is unambiguous from the other measurements, and D occurs at an inter-donor charge transition.

5.7.2 SPIN RESONANCE ON A THREE ELECTRON DONOR BOUND STATE

Using the spin-dependent unload scheme at location ©, which corresponds to the 3 electron state of the dot R_α, we perform a spin resonance experiment. In Figure 5.31(a) we show the spin up fraction for 3750 single-shot spin resonance sequences where we apply a microwave burst at the indicated frequency, in this case without any adiabatic passage frequency chirp, but rather a single frequency pulse of duration $T_p = 330$ns. A magnetic field of 1.45T is applied. Scanning the frequency over a 700MHz range, we observe only a single resonance peak at $\omega_1 = 40.394 \pm 0.002$GHz. This is in contrast to the multiple lines seen for the single electon 1P and 2P spectra in the preceeding section. This suggests that the hyperfine coupling A is less than the peak width $\omega_{\mathrm{FWHM}} = 7.2 \pm 2.0$MHz from the Overhauser field induced spectral diffusion.

We fit the data, which is shown on an expanded frequency axis in Figure 5.31(d) to a Gaussian peak-shape:

$$f_\uparrow = f_0 + f_1 \exp\left(\frac{-(\omega - \omega_1)^2}{2\sigma^2}\right) \tag{5.44}$$

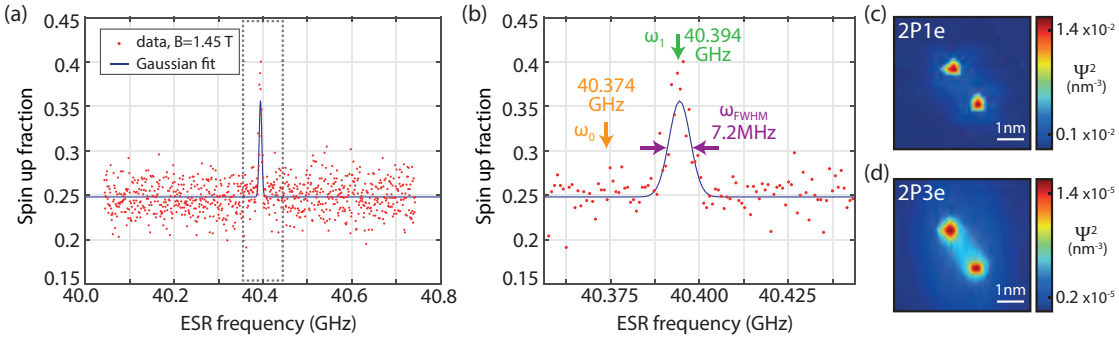

Figure 5.31: Spin resonance spectrum of the three electron state of R_α. (a) A scan over a 700MHz range, exhibiting only one single spin resonance peak. The data was collected with a B field of 1.45T, and a single frequency unmodulated microwave pulse of duration $T_p = 300$ns. (b) shows the central grey box expanded along the frequency axis. The resonance has a Gaussian lineshape 7.2MHz wide. On- and off-resonance frequencies ω_1 and ω_2 are marked. The spin up fraction at these frequencies are used to define an ESR signal intensity. The 1 electron (c) and 3 electron (d) wavefunction around a 2P molecule, expressed as the probability density Ψ^2, shown in a 2D slice through both donor potential wells. The 3 electron state is much more evenly distributed throughout the space between the nuclei and surrounding them, and consequently a lower density at the atomic core. (c) and (d) reproduced from [150].

We then find a peak amplitude in the spin up fraction, $f_1 = 0.105$ above a baseline $f_0 = 0.266$, and a peak width parameterised by $\sigma = 3.1 \pm 0.8$MHz, corresponding to the width $\omega_{\text{FWHM}} = 2\sqrt{2\ln 2}\sigma = 7.2 \pm 2.0$MHz. Without the adiabatic passage frequency modulation that was used in Section 5.6, this FWHM value represents the inhomogeneous line-width of the time ensemble of single-shots – the effect of spectral diffusion due to fluctuations in the nuclear Overhauser field.

Considering the Fourier transform of the resonance line-shape in Equation (5.44) allows us to link ω_{FWHM} to the dephasing time:

$$T_2^* = \frac{1}{\pi\sqrt{2}\sigma} \tag{5.45}$$

$$= \frac{2\sqrt{\ln 2}}{\pi\omega_{\text{FWHM}}} \tag{5.46}$$

This provides an indication that the three electron spin state bound to this small donor quantum dot dephases on a timescale $T_2^* \approx 73$ns, which is notably larger than the dephasing time of the single electron P donor bound state of 55ns recently measured by Pla *et al.* [49]. We return to discuss the reduced dephasing below, after first addressing

the question of why there is only one visible peak.

Extent and concentration of the three electron bound state

Wang *et al.*[150] have considered the effect of the number of bound electrons on the hyperfine energy A of few donor quantum dots. Using atomistic tight binding simulations (see Section A.6) they predict a reduction in A by a factor of ~ 10, for the three electron bound state (with $A \sim 49$MHz) compared to the single electron state (at $A \sim 370$MHz). The lower hyperfine energy of the 3e state is a direct result of the first two spin-paired electrons partially screening the Coulomb potential of the donor nuclei such that the third electron state is less tightly confined to the atomic cores. The difference is illustrated in Figure 5.31(c) and (d) which show 1 electron and 3 electron states bound to a 2P molecule with inter-atomic separation 1.58nm. The 2P1e state's electron density is concentrated mainly at the two donor sites, where it contributes to a strong contact hyperfine interaction. The larger light blue area seen in between the donor atoms for the 2P3e state is representative of the shallower potential well. The computed density Ψ^2 is on average around 3 orders of magnitude lower in Figure 5.31(b) relative to (a), and therefore the Hyperfine interaction, which depends on the overlap of electron and nuclear wavefunctions, is much weaker in the 3e case.

While the hyperfine coupling to the P donor nuclei typically determines discrete resonance splittings, broadening of resonances through the Overhauser field effect is ultimately a hyperfine interaction as well. This can be understood by considering the RMS average offset in Larmor resonance frequency $\sigma = \omega - \omega_L$ due to the electron's hyperfine coupling with the bath of N interacting ^{29}Si nuclear spins[122,182,183]:

$$\sigma \sim \sqrt{\sum_{j}^{N} \frac{A_j^2}{2}} \tag{5.47}$$

$$\sim \sqrt{\frac{A_{\mathrm{Si}}^2}{2N}} \tag{5.48}$$

where the hyperfine coupling to the j-th ^{29}Si nuclear spin A_j depends on the bound electron wavefunction overlap at that j-th atomic site, but the average over a large number N of such sites, can be approximated using the intrinsic hyperfine coupling for ^{29}Si atoms, A_{Si} defined by the overlap of just the periodic Bloch-function $U(\vec{R})$

component of the total wavefunction $\Psi(\vec{R}) = \Phi(\vec{R})U(\vec{R})$

$$A_j = \frac{2\gamma_e\gamma_N\mu_0}{3}\left|\Psi(\vec{R}_j)\right|^2 \tag{5.49}$$

$$A_{\mathrm{Si}} = \frac{2\gamma_e\gamma_N\mu_0}{3}\left|U(\vec{R}_j)\right|^2 \tag{5.50}$$

The approximation made for Equation (5.48) is asymptotically accurate in the limit of large N, and for donor quantum dot wavefunctions with a radius of several nm in natural silicon N is on the order of several thousand. The qualitative relation $\sigma \sim 1/\sqrt{N}$ therefore explains our observation of a longer dephasing time than seen by Pla *et al.* [49], since the three electron wavefunction of our quantum dot extends over a larger number of nuclei than the single donor single electron state. The additional sites draw the average total effect of the nuclear spin bath toward zero – although there is interaction with a greater number of nuclei, the fluctuations in the Larmor resonance frequency actually become less.

For use in the following sections we define an ESR signal intensity $I_{\mathrm{ESR}} = f_{\uparrow}(\omega_1) - f_{\uparrow}(\omega_0)$, simply taking the difference in spin-up fraction measured on-resonance and off-resonance as indicated by arrows at $\omega_1 = 40.394\mathrm{GHz}$ and $\omega_0 = 40.374\mathrm{GHz}$ in Figure 5.31(b). This provides a single number (I_{ESR}), encoding the effect that an applied pulse has on the electron spin state.

5.7.3 Coherent electron spin rotation and Rabi oscillations

By varying the duration of the microwave pulse T_p we control the rotation angle of the electron spin from its initial $|\downarrow\rangle$ state. In Figure 5.32(a-d) we display coherent Rabi oscillations in the ESR signal I_{ESR}, measured for four different values of the input microwave power as indicated. We observe that the oscillation amplitude decays with increasing pulse duration, and the oscillation frequency increases with the applied power.

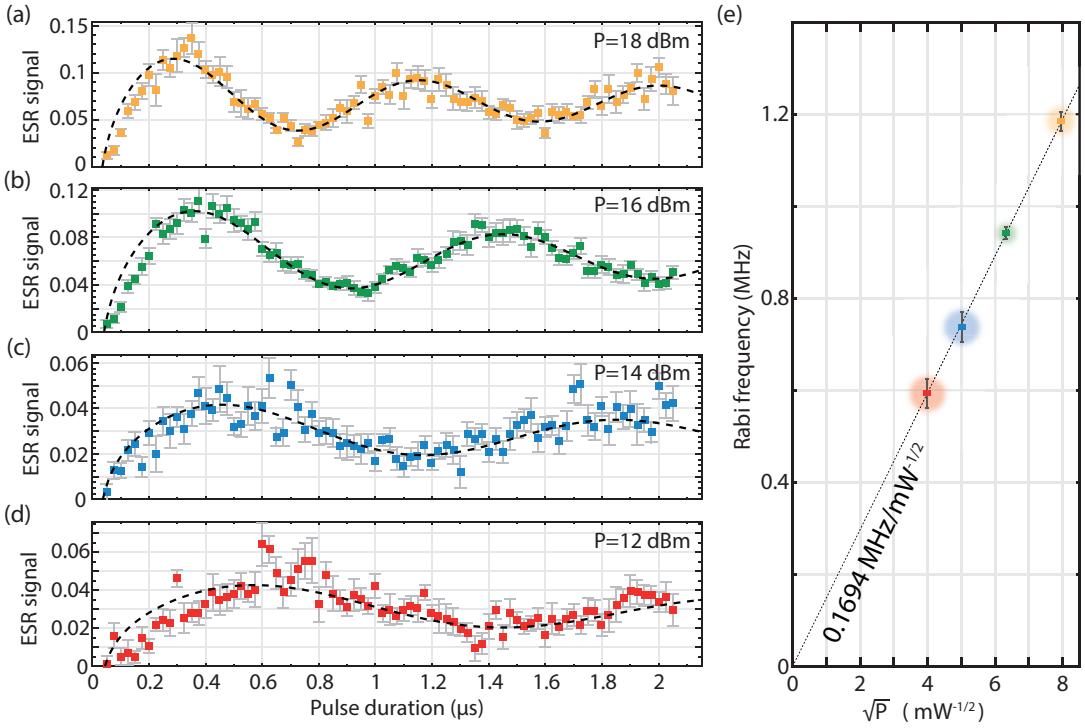

Figure 5.32: Coherent Rabi oscillations of a 3 electron spin-1/2 state (a) Rabi oscillations with a microwave power of 18dBm. There is a periodic recovery of spin-up probability with increasing pulse duration, although the oscillation amplitude decays with a non-exponential envelope. (b-d) With lower microwave power the frequency of Rabi oscillations is reduced, along with the maximum initial oscillation amplitude. (e) There is a square root dependence of the Rabi frequency on the microwave power P power, indicating that the Rabi frequency is proportional to the B_1 field strength. The maximum $B_1 \sim 50\mu$T observed at P = -18dBm provides a Rabi frequency of 1.3MHz, which is limited by the output power of the signal generator. (

We fit the data to a functional form[184,185]:

$$I_{\mathrm{ESR}} = I_0 - \frac{I_1}{\sqrt{T_p}} \cos\left(2\pi\omega_R T_p + \frac{\pi}{4}\right) \tag{5.51}$$

in order to extract the Rabi oscillation frequency ω_R. I_0 and I_1 are free fitting parameters.

We plot the resulting Rabi frequency ω_R against the applied power P in Figure 5.32(e). The Rabi frequency is linear in the oscillating Rabi magnetic field amplitude $\omega_R = \gamma_e B_{\mathrm{AC}}/2 = \gamma_e B_1$. Therefore B_1 scales linearly with the current through the nanowire at the end of our microwave antenna (by the well-known Biot-Savart law). The square

of the antenna current is proportional to the input power, and so we expect a power dependence, $\omega_R = \alpha\sqrt{P}$. This relationship is confirmed by our measurements as shown in Figure 5.32(e), with a coefficient $\alpha = 0.1694\text{MHz/mW}^{1/2}$. The highest Rabi frequency we achieved (at the maximum output power of our signal generator – 18dBm) was 1.184±0.020MHz. Extrapolating this value to 0dBm = 1mW gives a value of $B_1 \approx 12\mu$T. This B_1 value is lower than we estimated for the previous 1P/2P device in Section 5.6.5, by a factor of around 5. The outcome is remarkably consistent with the numerical modelling we presented in Section 5.4.2 if we additionally consider the exact placement of the antenna in this new device.

5.7.4 Understanding the electron spin dynamics in a fluctuating Overhauser field

We now justify the expression used to fit our Rabi oscillations, which is distinct from the well known Rabi formula. To do so, we consider the Rabi Hamiltonian for an electron spin, in the rotating Larmor frame and subject to a microwave magnetic field pulse of frequency ω_p and duration T_p. Such a pulse drives Rabi oscillations about the X-axis of the Bloch sphere at a frequency ω_R. We also consider in this model a fluctuating nuclear Overhauser field $\delta(t) = \gamma_e B_N(t)$ detuning the electron away from the expected Larmor frequency ω_L.

$$H_R = \omega_R S_x + \Delta\omega S_z \tag{5.52}$$

$$= \gamma_e B_1 S_x + (\delta(t) + \omega_p - \omega_L) S_z \tag{5.53}$$

We assume slow fluctuations of the Overhauser field, so that $\delta(t)$ is fixed for the duration of a single pulse T_p, and that $\omega_L \gg \omega_R$ so that the rotating wave approximation is valid. The expected z-projection of the spin (or fraction of spin up outcomes in a time ensemble) after such a pulse may be written:

$$f_\uparrow(T_p, \Delta\omega) = \frac{\omega_R^2}{2(\omega_R^2 + \Delta\omega^2)} \left[1 - \cos(T_p\sqrt{\omega_R^2 + \Delta\omega^2})\right] \tag{5.54}$$

Equation (5.54) is the standard Rabi formula*. Integrating this expression over a Gaussian distribution of Overhauser field detuning values δ (reflected in the lineshape of Figure 5.31) with standard deviation σ produces:

$$\bar{f}_{\uparrow}(T_p, \omega_p) = \int_{-\infty}^{\infty} \frac{1}{\sqrt{2\pi}\sigma} e^{\frac{-\delta^2}{2\sigma^2}} f_{\uparrow}(T_p, \delta + \omega_p - \omega_L) d\delta \tag{5.55}$$

This general form can be applied to describe both a 'strong driving' regime – where the detuning due to the Overhauser field is small relative to the Rabi frequency $\omega_R \gg \sigma$.; and a 'weak driving' regime – in the limit where the Rabi field strength is smaller than the detuning due to Overhauser field fluctuations $\omega_R \ll \sigma$ The evolution from one regime to the other has been studied at length theoretically[123,124,182,184–186], and since the analysis is not straightforward, we simply present the on resonance ($\omega_p = \omega_L$) outcomes in the two limits[141]. To clearly illustrate the properties of the two regimes, we additionally show a simple idealised numerical model of Equation (5.55) in Figure 5.33(a-c). The figures sketch ideal Rabi oscillations for a system with perfect initialisation and readout. Directly on-resonance ($\delta = 0$), the black dashed line describes spin rotation with a Rabi frequency $\omega_R = 1$MHz. Coloured lines show the effect of Overhauser field detuning with a Gaussian distribution of standard deviation σ, varied over the three plots (0.3MHz (a), 1MHz (b), 3MHz (c)). Detuning, positive or negative, always increases the Rabi frequency because the effective nuclear field $B_N(t) = \delta(t)/\gamma_e$ acts only in the Z direction, perpendicular to B_1.

'strong driving' produces a Gaussian decay envelope:

$$\bar{f}_{\uparrow}(T_p) = f_0 - f_1 e^{-\left(\frac{T_p}{T_2^{\text{Rabi}}}\right)^2} [1 - \cos(\omega_R T_p)] \tag{5.56}$$

Here, dephasing follows a Gaussian decay profile (exponential with a power of 2) parameterised by the Rabi dephasing time T_2^{Rabi}, which is distinct from the T_2^* and T_2 times because it applies only under the microwave driving field, which has its own distinct noise properties. In this regime, the initial amplitude of oscillations approaches 1, as sketched in Figure 5.33(a). In this simple model, each green line plots the sinusoidal evolution of a single trial from a state initialised $|\downarrow\rangle$,

* sometimes the $1 - \cos(\Theta)$ term is expressed instead as an equivalent $2\sin^2(\Theta/2)$.

undergoing uniform Rabi oscillations with a small relative random detuning σ selected randomly from a Gaussian distribution. A dashed black line shows the zero detuning behaviour, and the solid black line the ensemble average. Figure 5.33(d) displays the strongly driven spin rotation on the Bloch sphere and the process approaches the ideal X operator, cycling almost circumferentially between $|\downarrow\rangle$ and $|up\rangle$.

'weak driving' results in a power-law decay envelope, bounding oscillations which are shifted by a phase of $\pi/4$

$$\bar{f}_{\uparrow}(T_p) = f_0 - f_1\sqrt{\frac{\omega_R}{2\sigma^2 T_p}}\cos\left(2\pi\omega_R T_p + \frac{\pi}{4}\right) \tag{5.57}$$

This behaviour is characterised by a fast initial damping within the first period, followed by slow decay for longer pulse times, as we see in Figure 5.33(c) which is the same randomised trial by trial model. Trials which are further detuned from resonance travel a shorter cycle on the Bloch sphere (shown in Figure 5.33(f)), and consequently oscillate faster in time – an effect visible in (c). Interestingly, no detuned trial oscillates more slowly than the $\sigma = 0$ case (dashed sinusoid). The ensemble average reflects the fast initial damping of a square root decay envelope, and the onset of a $\pi/4$ phase shift is visible in the first few hundred nanoseconds in Figure 5.33(c). Despite the rapid initial decay, small oscillations persist for many cycles.

intermediate behaviour occurs when the detuning is approximately equal to the Rabi frequency. Figure 5.33(b) and (e) display properties of both regimes.

Given that our maximum Rabi frequency $\omega_R = 1.184$MHz is less than the Larmor frequency detuning due to spectral diffusion $\sigma = 3.1$MHz, we we expect that the 'weak driving' description should most closely describe our data. To confirm this, we plot in Figure 5.33(g) Rabi oscillation measurements extending out to $T_p = 3.6\mu$s. We have fit the data to three candidate functions: the strong driving Equation (5.56) (green curve), a modified version of Equation (5.56) with the square in the exponent replaced by a free-parameter power n (orange curve), and the weak driving Equation (5.57) (red curve). The green curve is a poor fit, decaying much faster than the data. The orange curve, locked to zero phase at zero time, does not accurately fit the period of the oscillation,

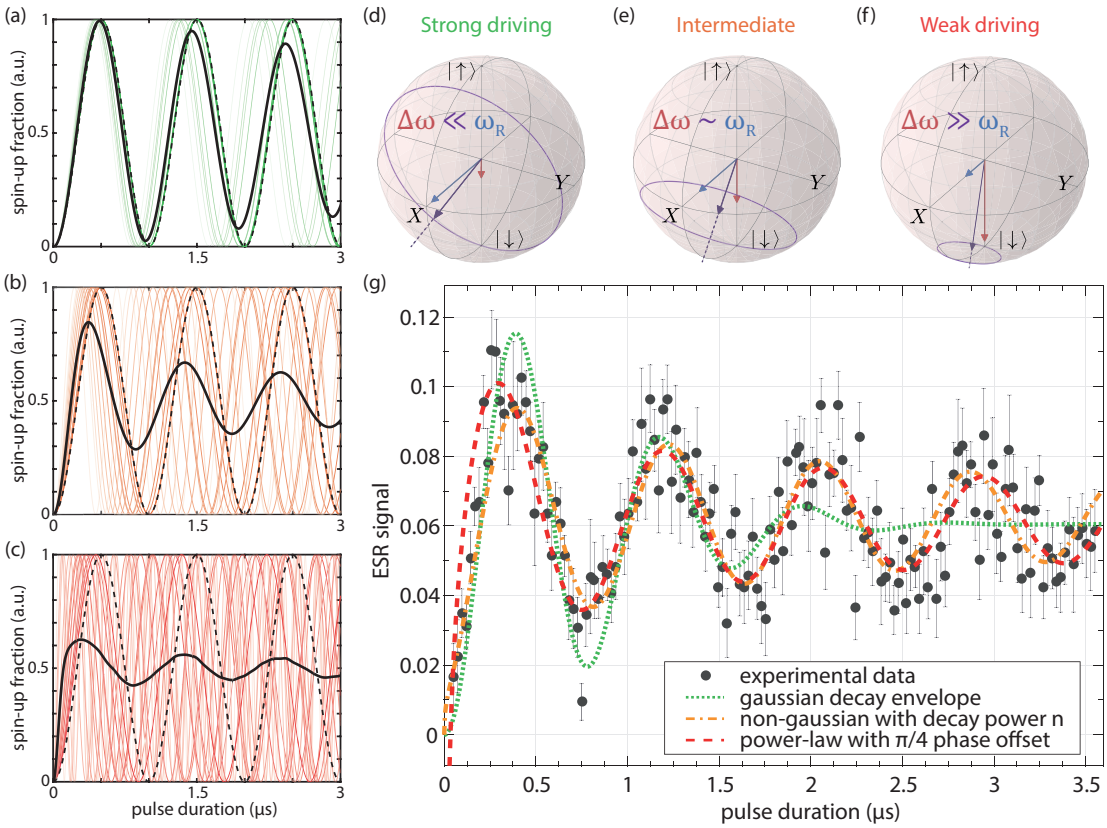

Figure 5.33: Rabi oscillations in the presence of random detuning. (a,b,c) Simple numerical model of Equation (5.55), plotting a number of detuned trials as coloured lines with intensity inversely proportional to the detuning. Dashed lines are the $\sigma = 0$ case, and solid black curves plot the ensemble average. Parameters used were: (a) $\sigma = 0.3\omega_R$; (b) $\sigma = \omega_R$; (c) $\sigma = 3\omega_R$. (d,e,f) Schematic Bloch sphere representations of the Rabi driving regimes. The red vector represents a frequency detuning, the blue arrow an oscillating B_1 magnetic field. The vector sum determines the axis of rotation. (g) Measured Rabi oscillations with a microwave power of 18dBm. Three fit functions are used: a sinusoid bounded by a Gaussian envelope (blue); a sinusoid bounded by a non-Gaussian envelope with exponent n (green); and a sinusoid bounded by power law envelope with a phase shift (red).

and in particular is visibly lagging behind the data above $T_P = 3\mu$s. The red curve is a better fit across the time domain we measured, with the greatest deviation near $T_P = 0$ where the approximations for Equation (5.57) are not fully met.

As a whole, Figure 5.33 illustrates the deleterious impact of Overhauser field induced dephasing. Without significant averaging (each point in Figure 5.33(g) is based on the average ESR signal over 750 single shot measurements), the coherent behaviour of our qubit would not be visible.

Although our limited Rabi field strength in this device means we cannot attain the strong driving regime which is far more preferable, since it partially overcomes dephasing caused by spectral diffusion, we nevertheless have shown we can perform coherent rotations of the electron spin. Reduced attenuation in the coaxial transmission line delivering the microwave signal, and adjustment to the antenna placement relative to the qubits will allow us to reach the strong driving regime in future experiments using isotopically natural silicon. Another strategy to mitigate the effects of the random nuclear spin bath is the spin echo, which we demonstrate in the following section.

5.7.5 Recovering electron spin dephasing using a spin echo sequence

The Overhauser field B_N not only affects the qubit during the application of a microwave pulse as we considered in the previous section, but also dephases the qubit whilst it is 'idle'. This dephasing can be overcome with a spin echo pulse sequence. We illustrate the sequence in Figure 5.34(a), where the pulse durations to achieve a π and $\pi/2$ rotation are determined from the first period of oscillation in Figure 5.33(a) by taking the time t_p at the peak value of I_{ESR}. The pulse sequence is:

Initialise by loading an electron $|\downarrow\rangle$ and then applying a microwave pulse of duration $t_\pi/2$ (the first blue coloured block). This has the effect of rotating the spin on the Bloch sphere, about the X-axis by an angle of $\pi/2$, into the X-Y plane. This is also represented in Figure 5.34(b) as the light blue arrow in the lower right.

Dephase for a wait time τ_1, in the absence of a microwave signal. The spin precesses about the Z-axis at a rate proportional to the instantaneous value of the Overhauser field $\Delta\omega \sim B_N$. Within the wait time the spin moves an angle described by $\tau_1\Delta\omega$ around the Bloch sphere as indicated by the red arrow in Figure 5.34(b). Depending on the orientation of B_N, this rotation may occur in either direction.

Flip the spin by an angle π about the X-axis, by applying a microwave pulse of duration t_π. This is indicated by the dark blue arrow in Figure 5.34(b).

Rephase for a second wait time τ_2, again without a microwave field. Assuming that the Overhauser field B_N has the same size and direction as it had for the first wait time, the phase angle accumulated in this second wait time $\tau_2\Delta\omega$, will return the spin to the Y-axis if $\tau_2 = \tau_1$, as is the case in Figure 5.34(b).

Project the qubit onto the Z-axis with a final $\pi/2$ pulse, as shown by the dashed blue line in Figure 5.34(b). When $\tau_2 = \tau_1$, this returns the qubit state to $|\downarrow\rangle$.

Read the spin state by performing the spin dependent UNLOAD procedure as discussed in Section 5.3.2.

Note that the rotation angles described by the light blue and dark blue arrows in Figure 5.34(b) are accurate only in the absence of the Overhauser field. B_N alters the path traced by the spin state, so the Bloch sphere diagrams presented represent the ideal case only.

As τ_2 and τ_1 diverge, the spin echo becomes less effective at rephasing the spin, and the final pulse projects the qubit to a point away from the ground state as shown by the yellow star in Figure 5.34(c). The error relative to perfect recovery of the $|\downarrow\rangle$ state is proportional to $|\tau_2 - \tau_1|\Delta\omega$. For an ensemble of such sequences with randomly distributed $\Delta\omega$, the average final state is approximately $|\downarrow\rangle$ for $\delta\tau = \tau_2 - \tau_1 = 0$ and tends toward the fully mixed state at large time differences. We perform such an experiment, with a fixed $\tau_1 = 3\mu$s () and show the results in Figure 5.34(d). Each point represents 30 000 single shot spin echo sequences (15 000 on resonance, 15 000 off resonance). We observe a clear envelope in the wait time difference $\delta\tau$ within which the ensemble of measurements is rephased by the echo sequence. We fit the measured ESR signal data to the function:

$$I_{ESR} = I_0 + I_1 e^{\left(\frac{\delta\tau}{T_2^*}\right)^2} \tag{5.58}$$

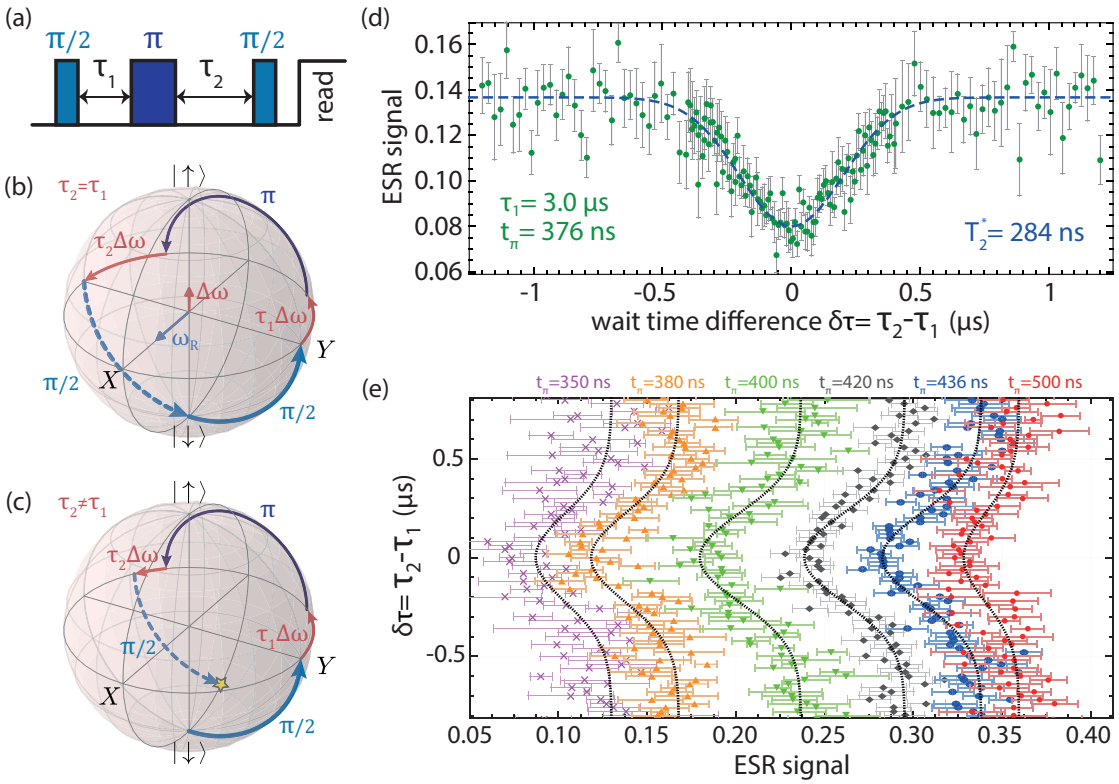

Figure 5.34: **Rephasing the electron spin with an echo sequence.** (a) Schematic of the spin echo envelope measurement sequence, where the second wait time, τ_2 is varied. (b) Bloch sphere representation of the effect of the sequence. The first $\pi/2$ pulse rotates the spin from $|\downarrow\rangle$ into the X-Y plane, initially along the Y-axis, where it accumulates phase at a rate given by the detuning $\Delta\omega$ integrated over a delay time τ_1. At this point, the central π pulse inverts the Y-component, so that after a second delay of equal time $\tau_2 = \tau_1$, the spin is refocused, arriving at the negative Y-axis regardless of the value of the detuning, assuming the detuning has remained the same for both delay periods. Under such a conditions, the final $\pi/2$ pulse rotates the spin back to the ground state. (c) When $\tau_2 \neq \tau_1$, the spin is not correctly refocussed, and the degree of error is proportional to the time difference $|\tau_2 - \tau_1|$ and also the detuning. (d) By repeating the sequence for different wait time differences, we observe a spin echo peak which has a width which describes the time it takes on average for the phase information to be lost due to the static detuning caused by B_N. This indicates the inhomogeneous dephasing time $T_2^* \sim 200$ns. (e) The spin echo envelope measured over a range of t_π settings from 350ns to 500ns, to observe the impact of rotation error. The largest peak amplitude is observed for $t_\pi = 400$ns, and the echo amplitude reduces with increasing rotation error at the extreme values. Traces are offset by 0.05 on the x-axis for clarity.

in order to extract a spin dephasing time $T_2^* = 284 \pm 22$ns. The value is larger than the $\sim$ 73ns estimate obtained in Section 5.7.2 from the width of the spin resonance peak in the frequency domain. We are uncertain of the origin of the discrepancy, though it may be related to power broadening in the resonance spectrum experiment which is suppressed in the spin echo as the pulse durations used are much shorter.

The angle of rotation achieved by a pulse of a certain duration depends on the instantaneous value of the Overhauser induced detuning. We now repeat the spin echo envelope experiment using different values for the microwave pulse duration t_π to obtain a qualitative picture of this effect. The result is shown in Figure 5.34(e), each line fitted also to Equation (5.58). Changing the pulse duration introduces additional rotation angle error on top of that caused by the Overhauser field. For small variations in t_p (between 400 and 440ns), we do not see a measurable decrease in the amplitude of the echo amplitude ($I_1 = 0.056$), as the change is comparable to the uncertainty due to the nuclear spin fluctuations. Modifying the time further does effect the final spin up probability, and at $t_p = 500$ns the amplitude is reduced to only $I_1 = 0.031$.

We have shown that despite significant spectral diffusion, and associated imperfections in the rotation angles achieved by our microwave pulses, a spin echo sequence allows us to recover the random phase accumulated over time due to the nuclear spin bath. In particular, we have found that the 3 electron state is more robust against dephasing than a single donor-single electron in natural silicon, with a longer T_2^* time by virtue of its greater overlap with nuclear spins in the substrate. In the section that follows we employ the spin echo technique to demonstrate arbitrary control over the Bloch sphere and measure the qubit decoherence time.

5.7.6 Applications of the spin echo: extending the coherence time and two-axis qubit control in a precision donor device

Having confirmed the effectiveness of the spin echo sequence in mitigating the dephasing due to the unknown instantaneous Overhauser field, we now perform a standard Hahn echo experiment, by fixing $\tau_1 = \tau_2$ and $t_p = 376$ns and varying the total wait time $\tau =$

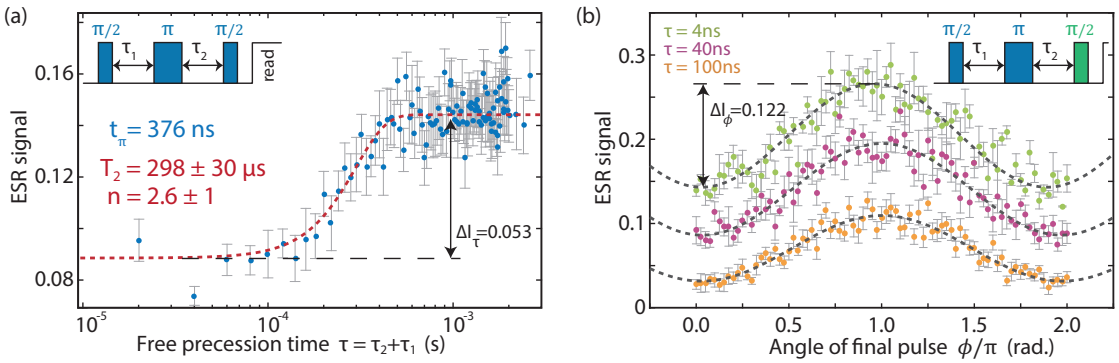

Figure 5.35: Recovering coherence with a Hahn spin echo sequence (b) Hahn spin echo experiment, plotting the recovery of a spin echo ESR signal as a function of total wait time τ. The inset illustrates the pulse sequence, with equal wait times. (c) Angular dependence of the echo recovery on the phase of the final $\pi/2$ pulse, displaying a sinusoidal shape, which demonstrates two-axis control over the Bloch sphere. The inset indicates the arbitrary phase of the final pulse, which is varied on the x-axis of the plot. Datasets for three different wait times are offset by 0.05 for clariy.

$\tau_1 + \tau_2$. The sequence is depicted in the inset to Figure 5.35(a). It is clear that the spin coherence extends well beyond T_2^* as the plotted echo signal intensity in Figure 5.35(a) shows, only starting to decay to the long-time equilibrium value beyond 10^{4-}s. We fit our data to the form:

$$I_{ESR} = I_0 + I_1 e^{\left(\frac{\tau}{T_2^{\text{Hahn}}}\right)^n} \tag{5.59}$$

where n, I_0, I_1 and T_2^{Hahn} are free parameters. In fitting the data we find that the Hahn echo sequence preserves the qubit coherence for a time $T_2^{\text{Hahn}} = 298 \pm 30\mu$s. The exponent we extract $n = 2.6 \pm 1$, is within the range found by Tyryshkin *et al.*[119] for spectral diffusion induced decoherence in P donor electrons in natural silicon.

Figure 5.35(b) demonstrates full control over the rotation angle on the Bloch sphere. We use a vector signal generator, allowing full control over the relative phase of the pulses within the spin echo sequence. By modulating the phase of the microwave pulse in the laboratory reference frame, the effect in the Larmor rotating frame is a rotation of the effective B_1 Rabi field within the X-Y plane. Delaying the phase ϕ by $\pi/2$ converts the final pulse into a Y-axis rotation. Delaying ϕ by π again rotates about the X-axis, but in the opposite direction. Therefore with $\phi = \pi$, the final state is (ideally) $|\uparrow\rangle$ at

the end of the spin echo sequence, in contrast with the $|\downarrow\rangle$ final state produced by the standard Hahn echo sequence used so far. The ESR signal amplitudes (I_1) seen in the spin echo experiments to this point have been approximately 0.053 ± 0.007, as shown in Figure 5.35(a) as ΔI_τ. This value of ΔI_τ reflects the evolution of the final state after the sequence from $|\downarrow\rangle$ at low wait time, to the fully mixed state at long times. We note that the amplitude of the sinusoidally varying ESR signal as a function of final pusle angle in Figure 5.35(b) is consistent with our expectations of a variable final state. The amplitude $\Delta I_\phi = 0.122 \pm 0.010$ shown for the $\tau = 4$ns dataset is approximately double ΔI_τ. This is only achievable if at $\phi = \pi$ the final state is indeed $|\uparrow\rangle$ as expected. This larger amplitude, together with the sinusoidal transition from one extreme I_{ESR} value to the other is strong evidence of arbitrary axis control of our electron spin state.

The ability to switch between X and Y rotations provides a basis for performing any arbitrary single qubit operation. With a π rotation time of $\sim$ 400ns and decoherence time of $T_2^{\mathrm{Hahn}} = \sim 300\mu$s, many operations are possible before the qubit decoheres. The biggest limitation is the random rotation error introduced by the nuclear Overhauser field. Increasing the Rabi driving strength, which is possible by improving the measurement set-up – in particular by reducing the loss in the microwave transmission line will reduce the severity of the errors, possibly by several orders of magnitude. Further improvement of the donor electron qubit ultimately relies on isotopic purification of the substrate to largely remove the nuclear spin bath.

Experiments with this device are ongoing at the time of writing, with several clear opportunities to explore, including electron spin resonance on one of the other donor quantum dots (L or R_β).

5.8 Conclusions and outlook

In this major results chapter we have demonstrated arbitrary axis coherent spin control in precision placed donors in silicon. To achieve this we have demonstrated a series of results:

- We have performed spin readout and spin resonance experiments on an atomic-precision donor-defined double quantum dot device, consisting of a single phosphorus donor and a 2P molecule – a pair of donors less than 1nm apart. Independent single shot electron spin readout of both qubits has demonstrated long T_1 relaxation times $\sim$ 10s. The combined spin readout scheme allowed an exploration of the controllable onset of spin-spin correlations when the system is detuned such that the exchange interaction between the two electrons becomes significant. This result is a first step toward developing a two qubit gate operation using donor bound single electron spins.

- We have detailed the integration of a broadband microwave antenna onto our planar device architecture, including numerical modelling of the GHz frequency electric and magnetic fields produced at the qubit sites. Combined with practical considerations of our measurement apparatus, the model has been successful in accurately predicting the oscillating magnetic field strength driving single qubit operations ($B_1 \approx 100\mu$T) to within an order of magnitude. To combat electrical noise and instability we developed an automated alignment procedure that tunes the electrostatics of a device to the optimal working point for high fidelity single shot readout, and monitors feedback signals to maintain stability over days, facilitating measurements over longer timescales. Magnetic field instability due to the fluctuating nuclear spin bath was combated using an adiabatic passage technique to permit clear electron spin resonance spectroscopy.

- We measured and analysed the spin resonance spectra of both single donor and 2P qubits, showing how the intrinsic hyperfine energy in donor molecules provides an in-built means of addressing multiple qubits. We measured values of $A^{(1P)} = 97$MHz and $A^{(2P)} = 262$MHz. Using tight-binding calculations of the wavefunctions, we were able to use the measured hyperfine spectrum to determine not only the distance separating the two donors of the 2P qubit, but also determine a small class of configurations for the two donor atoms of our 2P molecule consistent with our observations.

- We have additionally performed coherent spin resonance experiments with a second two qubit device. Here we utilise a three electron, spin $\frac{1}{2}$ state, believed to be bound to a 2P molecule, which displays a strongly reduced hyperfine coupling

to the donor nuclear spins, resulting in a single resonance peak at which which we drive Rabi oscillations. We confirm the expected power dependence of the oscillations and quantify spectral diffusion in the device due to fluctuating nuclear spins.

- We have used spin echo sequences to measure the pure dephasing time in this 3 electron system. We find $T_2^* \sim 300$ns, and are able to recover the dephasing, extending the qubit coherence time T_2 to nearly 300μs. Finally, we have also demonstrated full control over the Bloch sphere by modifying the phase of the microwave signal applied, to drive spin rotations about an arbitrary axis.

In conclusion, we have demonstrated many of the requirements for a viable, scalable qubit. We have identified the major limitation in our devices to be the ^{29}Si nuclear spins due to the use of a natural silicon substrate. These nuclear spins substantially degrade the qubit operations. Their effect could be mitigated to a large extent by increasing the strength of the oscillating magnetic field at the qubit by reducing loss in our microwave transmission line. Future work will proceed toward combining isotopically purified silicon with our fabrication procedure – which whilst challenging due to the incredibly small quantities of ^{28}Si material available is a subject of ongoing work within the research group.

6

Architecture for scalable error corrected quantum computing with donors

Large-scale quantum computing remains an ambitious goal, hovering in the future at a distance of one, or several decades depending on who you ask. Certainly the research community and an increasing number of commercial businesses are confident in the scaling prospects of several qubit implementations. At this point in the development of the field, a number of detailed theoretical proposals have emerged, presenting architectural designs for a large scale ($>$ 1000 qubit) quantum computer[187–192]. The key requirement at this scale is error correction, the ability to protect the quantum states from decoherence indefinitely, thereby facilitating computations with long run times. Conceiving the details of how this goal can be achieved at this early stage of qubit development is important, as it provides valuable guidance in the development of the fundamental qubit elements and their interactivity.

This chapter presents a plan for an error-corrected quantum computer implemented with precision donor qubits in silicon. First, we briefly outline the general error correction scheme we will use, known as the 2D surface code, along with a contextual survey of related architectures proposed for alternate qubit types. We then describe our proposed

physical layout realising the surface code topology, which consists of a two-dimensional lattice of donor qubits sandwiched between two vertically separated control layers forming a mutually perpendicular criss-cross gate array. We discuss the suitability of donor nuclear spin qubits for synchronous and parallel quantum operations, and the utility of the associated electron spin qubit in addressing subsets of the full quantum computer, as well as mediating interactions. We describe the details of executing single and two qubit gate operations, which we have designed to consist only of locally controlled electron tunnelling and global spin resonance signals.

Since the tunnelling process is key to this architecture, we present detailed numerical modelling of the charge state control possible with the geometry. Although electron tunnelling is inherently a stochastic process, we show that a combination of Zeeman and Coulomb energy splittings provide a latching mechanism which permits a 'phase matched' semi-deterministic tunnelling scheme which we have designed to preserve qubit coherence during required donor ionisation events.

In the context of recent experimental developments, such as those presented in Chapter 5 of this thesis, and with reference to the underlying theoretical literature[193,194] we have elucidated our surface code architecture to a level where it will be a useful guide in the short term, both for experimental tests demonstrating basic error correction in small numbers of qubits, and for higher level theoretical development concerning the operation of logical qubits within the surface code. Thus our results establish a viable roadmap for building a realistic quantum computer based on individual phosphorus donors in silicon.

6.1 Introduction to quantum error correction

Qubits, and even classical bits will experience errors during storage, transmission, or manipulation, due to imperfections in the physical hardware implementation. Environmental noise can change the state of a qubit or bit during computational operations, or whilst being stored in memory. Therefore detecting and correcting for such uncon-

trolled interactions with the bit or qubit's environment is important for any scalable system. We begin by looking at classical errors and error correction as an introduction to quantum error protection with the surface code.

6.1.1 Classical error correction and Hamming codes

In order to protect against processes that may interfere with the state of a bit, the simplest strategy is to store repeated copies of each bit. For instance, if we use three physical bits to represent one logical bit, the system can be protected against a single bit error. If the value is 1 (0), we store a 'codeword' $1, 1, 1$ $(0, 0, 0)$, and later we read the values of the three bits and if they are not all equal, say $1, 1, 0$, we simply take a majority vote and flip the dissenting bit back to its original value, recovering one of the valid codewords. Note that this simple 3-bit repetition code cannot protect against two or more errors. We could increase the number of copies, but doing so quickly becomes very inefficient, using most of the bits to hold a lot of redundant data. Rather, error correction schemes generally assume that errors occur with low probability, and will be corrected by the system fast enough to avoid an error propagating from a physical bit to a logical bit. This assumption gives rise to the concept of an error 'threshold'. If the rate of occurrence of single bit errors is below a certain value P_{th}, then the error correction system will be able to run arbitrarily long computations even in the presence of environmental interference. The value of P_{th} is normally specified as a probability per operation time, and depends on the particular system and the noise.

If we consider the 3-bit repetition code, it is rather inefficient, with only 1 bit out of three representing actual information. An optimally efficient extension of the repetition concept is the family of Hamming codes[195], where m data bits are interleaved with k parity bits to form a codeword of n bits. Each parity bit records the parity (or sum modulo 2) of a unique subset of bits in the codeword, allowing unambiguous determination of the erroneous bit or bits and therefore correction of the error. In general, a $[n, m]$ Hamming code is capable of correcting 1 bit flip error per codeword if the Hamming

condition is met:

$$2^k \geq m + k + 1 \tag{6.1}$$

This inequality requires that there be enough parity bits to describe $m + k + 1 = n + 1$ different outcomes, that of a single bit flip in any bit position, or none.

As an example, we describe the [7,4] Hamming code which uses $n = 7$ physical bits to protect $m = 4$ logical data bits against any single error. The code is specified by a generator matrix G which produces the codeword w from a data-word d, and a Hamming matrix H which produces a 'syndrome' s for any w.

$$\boldsymbol{w} = G\boldsymbol{d} \quad (mod\,2) \qquad\qquad \boldsymbol{s} = H\boldsymbol{w} \quad (mod\,2) \tag{6.2}$$

$$G = \begin{pmatrix} 1 & 1 & 0 & 1 \\ 1 & 0 & 1 & 1 \\ 1 & 0 & 0 & 0 \\ 0 & 1 & 1 & 1 \\ 0 & 1 & 0 & 0 \\ 0 & 0 & 1 & 0 \\ 0 & 0 & 0 & 1 \end{pmatrix} \qquad\qquad H = \begin{pmatrix} 1 & 0 & 1 & 0 & 1 & 0 & 1 \\ 0 & 1 & 1 & 0 & 0 & 1 & 1 \\ 0 & 0 & 0 & 1 & 1 & 1 & 1 \end{pmatrix} \tag{6.3}$$

For a given data-word $\boldsymbol{d}$, G establishes the parity bits such that $H\boldsymbol{w} = (0, 0, 0)$ in the absence of errors. A non-zero syndrome indicates an error has occurred, and since $\boldsymbol{s}$ contains three bits of information, it is sufficient to determine which of the 7 bits (or none) suffered the error. The canonical H matrix (which results in parity bits at position indexes that are powers of 2) produces a syndrome which is directly a binary representation of the position index of the erroneous bit.

An example codeword $d = (1, 0, 0, 1)$ is shown in Figure 6.1(a). The codeword is computed as $w = Gd = (0, 0, 1, 1, 0, 0, 1)$, which without any error will produce a syndrome, $s = Hw$ of $(0, 0, 0)$. We suppose an error occurs on the bit at position ⑤, flipping its value to 1 (shown in red) in the erroneous codeword $\boldsymbol{w'}$, and corrupted data d'. If the codeword is computed again from d', a different codeword is obtained w''. The syndrome $\boldsymbol{s} = H\boldsymbol{w'} = (1, 0, 1)$ corresponds to the difference between w' and w'', and is in fact the binary representation of 5, providing the index of the erroneous bit, and hence allowing the error to be unambiguously corrected to recover the original codeword w.

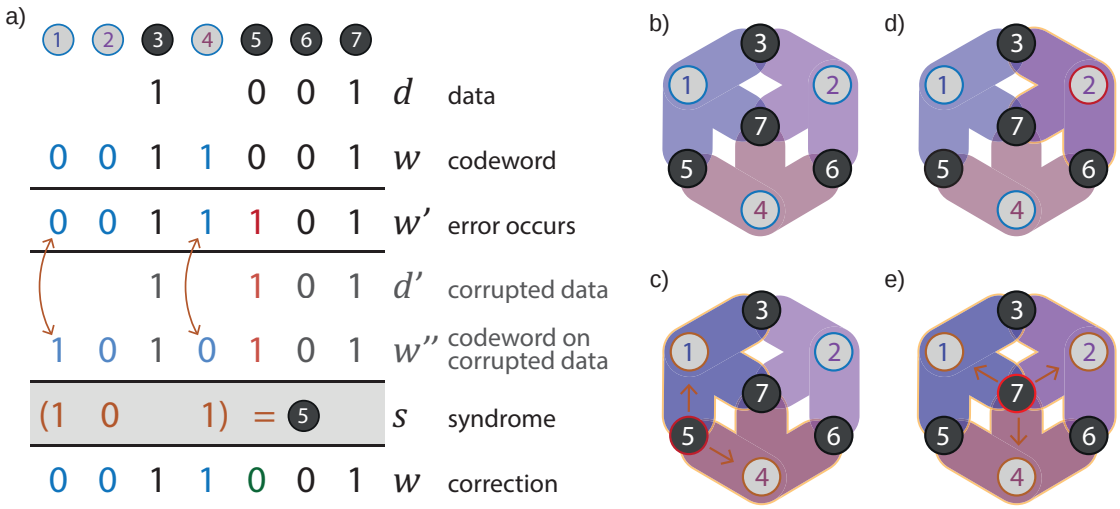

Figure 6.1: Classical error correction with the Hamming code. (a) Example of the classical Hamming[7,4] code algorithm, correcting one error in a 7 bit codeword, containing 4 bits of data. Data bit values shown in black, parity bit values blue. Top panel shows a starting codeword, with blue parity bits added to for a codeword. In the second panel an error occurs on the ⑤ bit (red). The third panel shows the outcome of computing the codeword on the erroneous data, with the error appearing on the ① and ④ parity bits; their changed values highlighted by orange arrows. The grey panel indicates that the syndrome encodes the error location: (1,0,1) is the binary representation of 5. And the final panel shows that the data in bit ⑤ can then be corrected (green). (b) Graphical representation of the Hamming[7,4] code. Data bits are dark circles, parity bits light circles, with coloured shading indicating which three data bits contribute to each parity check. (c) A single error on a data bit (red ⑤) causes a change in the value of two parity bits (orange). Here $\boldsymbol{s} = (1,0,1) \rightarrow$⑤. (d) A single error on a parity bit (red ②) changes only that one parity bit. Here $\boldsymbol{s} = (0,1,0) \rightarrow$②. (e) The special case of an error on bit ⑦ (red) causes all parity bits to change (orange). Here $\boldsymbol{s} = (1,1,1) \rightarrow$⑦.

The action of the syndrome measurement performed by the Hamming matrix H is displayed graphically in Figure 6.1(b), which shows data and parity bits as dark and light circles respectively. Each of the coloured shapes represents one row of H, and hence one bit of the syndrome. Note that each shape intersects with a unique subset of bits. Figure 6.1(c) illustrates the example case in (a), showing that an error on bit ⑤ affects two bits of the syndrome – the two shapes that intersect with bit ⑤. Figure 6.1(d) and (e) demonstrate the cases of an error occurring on a parity bit, which impacts only one bit of the syndrome, and the unique case of an error on bit ⑦, which intersects all three shapes, and produces the syndrome $(1,1,1)$.

Repeated application of the syndrome measurement followed by the appropriate correction to either data bit or parity bit 'stabilises' the code against single errors. Of

course for classical bits, determining the syndrome is as simple as reading the value of each bit and performing some matrix multiplication. With a quantum bit, this is not an option – directly measuring any qubit containing quantum data will project it into an eigenstate and collapse a superposition or destroy any entanglement it may share with other qubits. Fortunately, there is an indirect way of measuring the quantum parity, by instead only measuring an 'ancilla' qubit which has previously interacted with a set of data qubits, in analogy with the parity bits from the Hamming code after application of the G matrix to a set of data bits. Such a measurement is termed a 'stabiliser' operation. The result is that the combined system of (data and ancilla) qubits is partially projected into a certain subspace of the full Hilbert space, and we gain a measurement outcome – a syndrome – reporting the occurrence of any error that may have occurred, thereby allowing it to be corrected without needing to directly *look at* the qubit states[196].

6.1.2 Discretisation of arbitrary quantum errors by projective measurement

Calderbank, Shor & Steane[197,198] introduced quantum error correction with a general class of what are known, after the inventors names, as CSS codes, a close analogue of classical Hamming codes, the principal distinction stemming from the fact that the two-dimensional Hilbert space of a single qubit represents analog information that may suffer an arbitrary *analog* error, and not merely a digital flip from $0 \rightarrow 1$ or $1 \rightarrow 0$ as for a classical binary bit.

We illustrate a small analog error acting on a physical qubit state $|\Psi\rangle$ on the Bloch sphere in Figure 6.2(a). The combined effects of decoherence and relaxation may perturb $|\Psi\rangle$ by an arbitrarily small angle about an arbitrary axis. The key to quantum error correction is that we may consider such arbitrary rotations as a weighted superposition

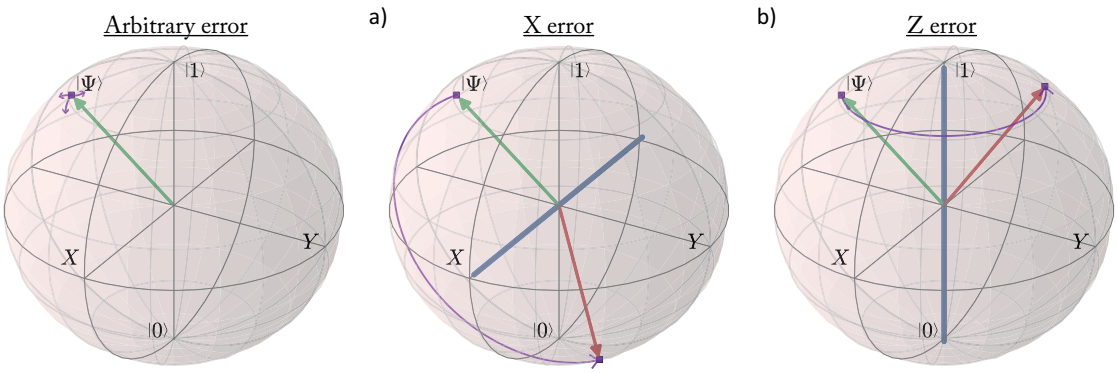

Figure 6.2: Discretised errors by projective stabiliser measurements. (a) Noise acting on a physical qubit can rotate a state $|\Psi\rangle$ (green arrow) on the Bloch sphere in an arbitrary way, as indicated by the small purple arrows. (b) The effect of a quantised X error, or (c) Z error on a qubit state $|\Psi\rangle$. Any state along the purple line is projected to one of the endpoints by a projective measurement following a stabiliser operation; and so the surface code effectively digitises errors.

of a basis set of large errors, for which we define operators based on the Pauli matrices:

$$\hat{X} = \hat{\sigma_x} = \begin{pmatrix} 0 & 1 \\ 1 & 0 \end{pmatrix} \qquad \hat{Z} = \hat{\sigma_z} = \begin{pmatrix} 1 & 0 \\ 0 & -1 \end{pmatrix} \tag{6.4}$$

$$\hat{Y} = -i\hat{\sigma_y} = \hat{Z}\hat{X} = \begin{pmatrix} 0 & 1 \\ -1 & 0 \end{pmatrix} \qquad \hat{I} = \begin{pmatrix} 1 & 0 \\ 0 & 1 \end{pmatrix} \tag{6.5}$$

An X-error, analogous to a classical bit flip, is described by a rotation of angle π about the X axis of the Bloch sphere, as we show in Figure 6.2(b). The second type we consider is an Z-error, a π rotation about the Z axis of the Bloch sphere, often termed a phase flip, as shown in Figure 6.2(c). Thus, relaxation effects normally quantified with a T_1 relaxation time can be considered as the source of X-errors, and dephasing effects typically described with a T_2 decoherence time can be similarly seen as generating Z-errors. The Y-error is the product of both X- and Z-errors. The identity operator describes the occurrence of no error.

Syndrome measurements made on ancilla qubits are designed to project small errors onto the basis of $(\hat{X}, \hat{Y}, \hat{Z}, \hat{I})$ error operators[193]. Under the assumption that the error rate is small, and indeed less than some threshold P_{th}, the probability of projecting the error to $\hat{I}$, and the qubit state back onto the original Ψ is almost unity. Conversely, the probability of projecting the error onto one of the non-identity error operators is low.

With this view of decoherence and relaxation as binary errors in the X- and Z-projections of a quantum state, the CSS quantum codes can be viewed as two nested Hamming codes, where one layer corrects X-errors and the other layer corrects Z-errors. The threshold value for CSS codes are on the order of $P_{th} \sim 10^{-6}$ to 10^{-4} depending on the details of the system: the operation and measurements times, and the number of qubits in the entire quantum computer[24,199]. The 2D surface code described in the following section is a special case of a CSS code. It is constructed on a two-dimensional lattice[200], where all the stabiliser operations are local, meaning that no interaction is necessary between non-neighbouring qubits. Additionally, it takes advantage of topology[201] so that even clusters of multiple errors are efficiently corrected unless they form an unbroken chain across an arbitrarily large region of the lattice. These properties, combined with a high error threshold of $P_{th} \sim 10^{-3}$ to 10^{-2} makes the surface code the most attractive known option for the implementation of fault-tolerant quantum computing.

6.1.3 Topological protection with the surface code

The surface code is constructed as an interleaved 2D array of data and ancilla qubits, grouped into two sets of cross shaped 'plaquettes' as shown in Figure 6.3(a). Each plaquette is centred on an ancilla qubit and includes its data qubit neighbour to the north, south, east, and west. Half of the plaquettes are designated as Z-stabilisers, half as X-stabilisers, as indicated in Figure 6.3(a) so that every data qubit is a member of two Z-stabiliser plaquettes and two X-stabiliser plaquettes. Together the two subsets form a set of stabiliser operations on plaquettes of qubits, that together define the 'surface' of the surface code:

$$\hat{\boldsymbol{Z}}_i = \hat{Z_N}\hat{Z_W}\hat{Z_E}\hat{Z_S} \tag{6.6}$$

$$\hat{\boldsymbol{X}}_j = \hat{X_N}\hat{X_W}\hat{X_E}\hat{X_S} \tag{6.7}$$

The execution of these operations require the standard Hadamard operation $\hat{H}$ to transform between the Z-basis and the X-basis, and the two-qubit CNOT (controlled

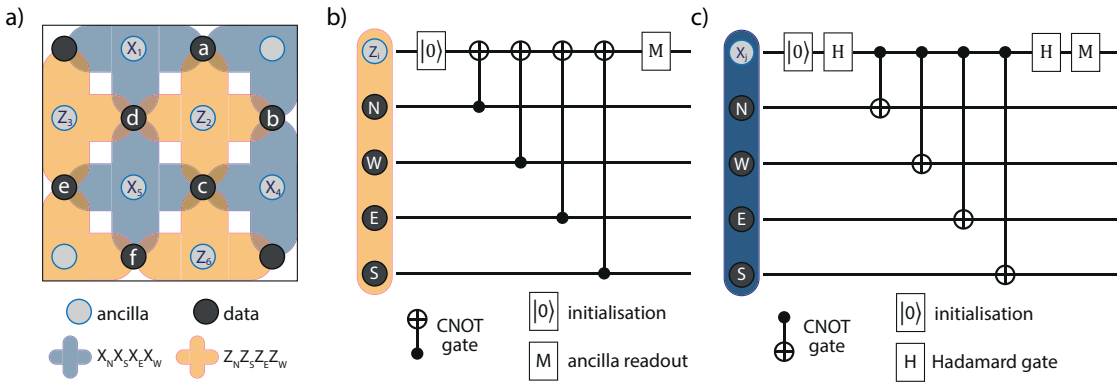

Figure 6.3: Syndrome extraction with projective stabiliser measurements. (a) The 2D surface code qubit layout. Ancilla qubits marked blue play a similar role to the parity check bits of the Hamming code, each one determining the eigenstate of combined X or Z operators acting on sets of neighbouring data qubits. (b) A Z-stabiliser operation on a single plaquette involves initialising the ancilla $|0\rangle$, entangling CNOT gates with each neighbouring data qubit (North, West, East and South) before projectively measuring the ancilla in the Z basis. (c) An X-stabiliser operation on a single plaquette involves initialising the ancilla $|+\rangle$, entangling CNOT gates with each neighbouring data qubit (North, West, East and South) before projectively measuring the ancilla in the X basis.

$\hat{X}$) operation $\hat{C}$ to entangle data qubits with ancillas:

$$\hat{H} = \frac{1}{\sqrt{2}}\begin{pmatrix} 1 & 1 \\ 1 & -1 \end{pmatrix} \qquad \hat{C} = \begin{pmatrix} 1 & 0 & 0 & 0 \\ 0 & 1 & 0 & 0 \\ 0 & 0 & 0 & 1 \\ 0 & 0 & 1 & 0 \end{pmatrix} \tag{6.8}$$

Z-stabiliser syndrome measurement

Figure 6.3(b) displays step by step the procedure for a Z-stabiliser operation using the i-th ancilla qubit:

- the ancilla is initialised in the ground-state $|0\rangle = \binom{1}{0}$
- a CNOT gate is applied with the ancilla as the target and its north (N) neighbour as the control, entangling them
- a CNOT gate is applied with the ancilla as the target and its west (W) neighbour as the control, entangling them

- a CNOT gate is applied with the ancilla as the target and its east (E) neighbour as the control, entangling them
- a CNOT gate is applied with the ancilla as the target and its south (S) neighbour as the control, entangling them
- the ancilla is measured in the Z-basis, projecting it to either $|0\rangle$ or $|1\rangle = \left(\begin{smallmatrix}0\\1\end{smallmatrix}\right)$.

The projective measurement of the ancilla indicates the parity of the four neighbour qubits in the Z-basis, and at the same time, partially projects those data qubits into an eigenstate of the combined operator $\hat{\boldsymbol{Z}}_i$.

X-stabiliser syndrome measurement

Likewise Figure 6.3(c) displays the procedure for an X-stabiliser operation using the i-th ancilla qubit:

- the ancilla is initialised in the ground-state $|0\rangle$
- a $\hat{H}$ operation on the ancilla produces the state $|+\rangle = \frac{1}{\sqrt{2}}\left(\begin{smallmatrix}1\\1\end{smallmatrix}\right)$
- a CNOT gate is applied with the ancilla as the control and its north (N) neighbour as the target, entangling them
- a CNOT gate is applied with the ancilla as the control and its west (W) neighbour as the target, entangling them
- a CNOT gate is applied with the ancilla as the control and its east (E) neighbour as the target, entangling them
- a CNOT gate is applied with the ancilla as the control and its south (S) neighbour as the target, entangling them
- the ancilla is measured in the X-basis, by first performing a $\hat{H}$ operation, then projecting it to either $|0\rangle$ or $|1\rangle$. This process indirectly achieves a projection onto $|+\rangle$ or $|-\rangle = \frac{1}{\sqrt{2}}\left(\begin{smallmatrix}1\\-1\end{smallmatrix}\right)$.

In this case the final projection gives the parity of the four neighbours in the X-basis, and projects them onto an eigenstate of $\hat{\boldsymbol{X}}_j$. Repeated application of $|\boldsymbol{Z}\rangle_i$ and $|\boldsymbol{X}\rangle_j$ across all plaquettes i, j maintains the surface in a simultaneous eigenstate of all the combined stabiliser operators.

Commutatativity of stabiliser operations

The protocol would be no good if the various stabilisers interfered with one another, destroying superpositions in each others' subspaces. Part of the cleverness of the surface code is that this does not happen. Although for a single qubit, $\hat{X}$ and $\hat{Z}$ measurement operators do not commute,

$$\left[\hat{Z}, \hat{X}\right] = \hat{Z}\hat{X} - \hat{X}\hat{Z} = 2\hat{Z}\hat{X} = 2\hat{Y} \tag{6.9}$$

all of the combined stabiliser $\hat{X_N}\hat{X_W}\hat{X_E}\hat{X_S}$ and $\hat{Z_N}\hat{Z_W}\hat{Z_E}\hat{Z_S}$ operators *do* commute with each other. This comes about because of the connectivity built into the plaquette geometry, stabilisers always share exactly two data qubits with any other stabiliser, cancelling out negative signs when the two pairs are commuted. And of course individual operators on different qubits always commute with each other. Taking two of the plaquettes labelled in Figure 6.3(a) as an example:

$$\begin{aligned}
[\hat{\boldsymbol{Z}}_i, \hat{\boldsymbol{X}}_j] &= \left[\hat{Z}_a\hat{Z}_c\hat{Z}_b\hat{Z}_d, \hat{X}_d\hat{X}_f\hat{X}_c\hat{X}_e\right] && (6.10)\\
&= \hat{Z}_a\hat{Z}_b(\hat{Z}_c\hat{X}_c)(\hat{Z}_d\hat{X}_d)\hat{X}_e\hat{X}_f && (6.11)\\
&\quad - \hat{Z}_a\hat{Z}_b(\hat{X}_c\hat{Z}_c)(\hat{X}_d\hat{Z}_d)\hat{X}_e\hat{X}_f \\
&= \hat{Z}_a\hat{Z}_b(\hat{Y_c})(\hat{Y_d})\hat{X}_e\hat{X}_f && (6.12)\\
&\quad - \hat{Z}_a\hat{Z}_b(-\hat{Y_c})(-\hat{Y_d})\hat{X}_e\hat{X}_f \\
&= 0 && (6.13)
\end{aligned}$$

The resulting state after interacting and projecting every ancilla is called the quiescent state of the surface, a state with strong entanglement between local qubits, and increasingly weak entanglement with distant qubits. With no errors, repeated stabiliser operations do not change the state, or the measured syndrome outcomes. Errors are detected by noting any change in syndrome measurements, and since each data qubit is a member of two X-plaquettes and two Z-plaquettes, the location and type (X/Z) of a single error can be unambiguously resolved.

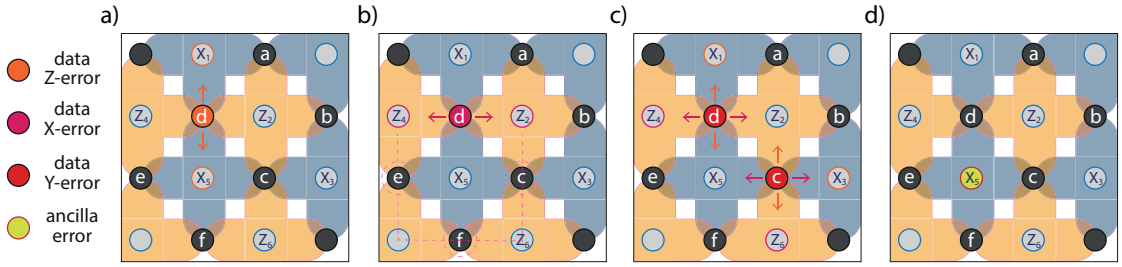

Figure 6.4: **Effect of X, Y and Z errors on syndrome measurements.** (a) A $\hat{Z}$ error at data qubit ⓓ propagates out to the two the X-stabiliser measurements labelled X_1 and X_5. (b) An $\hat{X}$ error at data qubit ⓓ propagates out to the two the Z-stabiliser measurements labelled Z_2 and Z_4. (c) A chain of two $\hat{Y}$ errors at data qubits ⓒ and ⓓ, appear in the X- and Z-stabiliser measurements at the ends of the chain. (d) An error occurring on any ancilla qubit appears as one isolated changed stabiliser measurement. It may also propagate errors across to neighbouring data qubits, which will be corrected in the following iteration of stabiliser measurements.

Some example error syndromes

We demonstrate a few examples in Figure 6.4 to give a sense of how the syndrome analysis reveals the location and type of errors that have occurred:

- In Figure 6.4(a) we consider a Z error at data qubit ⓓ. $\hat{Z}_d$ commutes with both $\hat{\boldsymbol{Z}}_2$ and $\hat{\boldsymbol{Z}}_4$ so the Z-stabilisers are unaffected. The effect on the two neighbouring X-stabilisers ($\hat{\boldsymbol{X}}_1$ and $\hat{\boldsymbol{X}}_5$) is to change their parity in the X-basis. Hence the interpretation of a syndrome consisting of two changed X-stabilisers either side of a data qubit, is that a Z-error has occurred at that data qubit. Applying the operator $\hat{Z}_d$ will map the state back to what it was before the error.

- In Figure 6.4(b) we consider an X error at data qubit ⓓ. $\hat{X}_d$ commutes with both $\hat{\boldsymbol{X}}_1$ and $\hat{\boldsymbol{X}}_5$ so the X-stabilisers are unaffected, and in this case the Z-stabilisers ($\hat{\boldsymbol{Z}}_2$ and $\hat{\boldsymbol{Z}}_4$) change parity. Hence the interpretation of a syndrome consisting of two changed Z-stabilisers either side of a data qubit, is that an X-error has occurred at that data qubit. Applying the operator $\hat{X}_d$ will map the state back to what it was before the error. There is a less likely alternative (actually there are many, of increasingly low probability) – indicated by the dashed pink line. A chain of X-errors on several data qubits (such as ⓔ, ⓕ, ⓒ), produces changed Z-syndromes at the endpoints of the chain. However, the surface code protocol always assumes the underlying error was caused by the most likely set of errors

(the shortest chain) using a matching algorithm[202], in line with the assumption of a low error rate. In fact, incorrectly assuming the wrong chain of errors between two endpoints also effectively corrects the error – the error operators combined with the mis-correction operators form a closed loop which turns out to be a product of stabiliser plaquette operators $\prod_j^{\text{loop}} \hat{\boldsymbol{X}}_j$ surrounded by the loop[203].

- In Figure 6.4(c) we consider the impact of a chain of two Y errors on the nearby data qubits ⓒ and ⓓ. $\hat{Y}_c$ changes the parity of all four surrounding syndrome plaquettes, as does $\hat{Y}_d$, but note that $\hat{\boldsymbol{Z}}_2$ and $\hat{\boldsymbol{X}}_5$ both have their parity changed twice, so these syndromes do not report any change. Only those syndromes at the end of the chain of errors change parity: $\hat{\boldsymbol{X}}_1$, $\hat{\boldsymbol{X}}_3$, $\hat{\boldsymbol{Z}}_4$ and $\hat{\boldsymbol{Z}}_6$, and this outcome can be traced back to the most probable source – two Y errors[202].

- In Figure 6.4(d) we consider the impact of an error on an ancilla qubit $\hat{\boldsymbol{X}}_5$. If the error occurs after the CNOT gates, it will only change the measured value of that ancilla (as shown). The other possibility is that the error occurs before one or more CNOT interactions, in which case, it may propagate errors back to the data qubits. These errors will simply be detected and corrected on the next iteration of the stabiliser operations.

In this way, multiple errors are detectable and correctable on a large surface[202], provided the density of errors is lower than the threshold for the surface code[25,204] $P_{th} \sim 1 \times 10^{-2}$.

In fact, it happens that detection of errors (type and location) is actually sufficient in the surface code, correcting them as they occur is not required. Since all errors have been discretised to full $\hat{X}$ or $\hat{Z}$ operations, which commute or anti-commute with all valid physical qubit operations within the surface code architecture, their presence may simply be tracked throughout the computation in classical software. If a second error of the same type on the same qubit is detected, the two will have effectively cancelled one another out ($\hat{Z}^2 = \hat{X}^2 = \hat{I}$). Otherwise, the appropriate corrective operator can simply be applied once to the physical qubit at the time of its eventual measurement whenever that may occur within the computation.

Qubits within the surface

Quantum information is encoded into the surface by constructing logical qubits – simply* 'holes' in the topological surface where stabiliser measurements are switched off in certain plaquettes. Then the quantum information representing the computation is effectively encoded into dimensions of the full surface's Hilbert space that are orthogonal to all of the active stabiliser operators.

We sketch an example of two such logical qubits in Figure 6.5(a), each one consists of a pair of holes. As there are two types of stabiliser plaquette, so there are two types of logical qubit. Omitting Z-stabiliser operations within two holes creates a 'double Z-cut' type qubit (left side of figure), which we show as two red rings surrounding holes within which all internal stabilisers are turned off completely, or modified to exclude qubits within the hole from their parity count. The edge of the hole must be completely defined by remaining X-plaquettes. The two holes are connected by a blue line marking a chain of data qubits from the boundary of one hole to the boundary of the other. The other type, the 'double X-cut' qubit, has an edge defined wholly by Z-plaquettes, but is otherwise equivalent – we mark it in inverted colours to show the different types.

Logical operations $\hat{X}_L$ and $\hat{Z}_L$ are related to chains of physical qubit operators encircling or connecting the pair of holes. We show the double Z-cut example in Figure 6.5(b). Executing a logical $\hat{X}_L$ requires a physical $\hat{X}$ operation on the full chain of data qubits connecting the two holes. Executing a logical $\hat{Z}_L$ requires a physical $\hat{Z}$ operation on the full chain of data qubits encircling *one* of the two holes. Measurements in the X- and Z- basis are similarly achieved by measuring the full chain of data qubits between or around the holes. If the chain is not complete, the repeated stabiliser operations will recover the initial logical state.

This is why the surface code is described as a topological protection scheme, large holes that are well separated are not sensitive to small, local sets (or chains) of errors – because the stabiliser protocol will counteract errors before a long-enough chain develops to form a logical qubit error. The subject of creating and operating on logical qubits within the surface is complex, and beyond the scope of this thesis. We have sketched some of the core concepts in Figure 6.5, but the reader is directed to a thorough review by Fowler *et al.*[194] for details. A crucial result in the literature concerning the surface

* it is not simple at all, aside from the realisation that one less stabiliser projection allows one more degree of freedom in the system

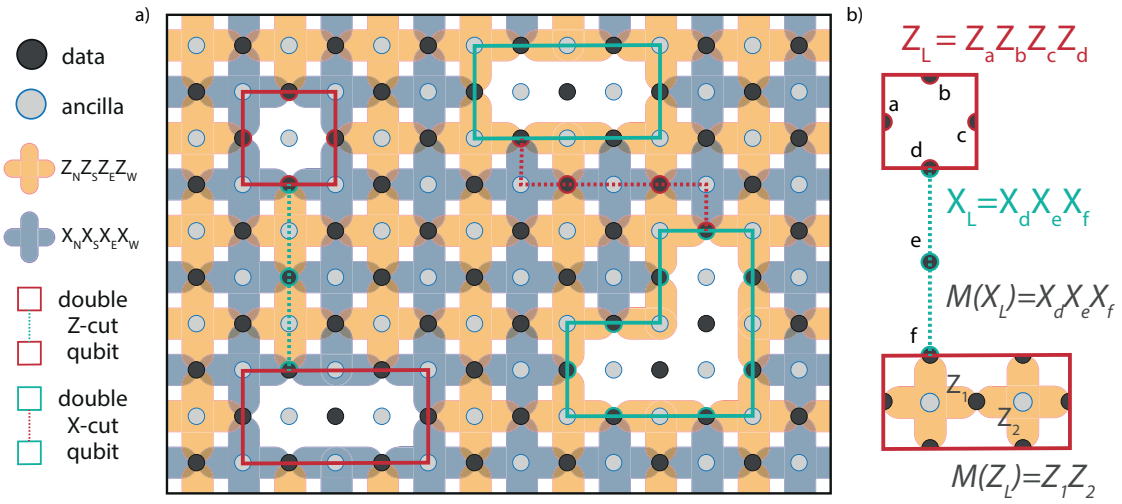

Figure 6.5: Creating logical qubits within the surface code. (a) Two logical qubits encoded in a surface. A pair of red rings marking areas of omitted Z-stabilisers joined by a blue line together form a 'double Z-cut' qubit. The complementary arrangement of two regions of omitted X-stabilisers is known as a 'double X-cut' qubit. Each hole may be arbitrarily large, and the two holes arbitrarily distant, increasing either size strengthens the fault tolerance. (b) Logical single qubit gates X_L and Z_L are achieved by chains of physical data qubit operations, completely around the perimeter of one hole ($Z_a Z_b Z_c Z_d$ for this Z-cut qubit example), or completely from the edge of one hole to the other ($X_d X_e X_f$ for this Z-cut qubit example). Logical state measurement involves the same chains, where each data qubit is measured in the appropriate Z- or X-basis rather than rotated about the Z- or X-axis.

code is that a complete and universal logical qubit gate set is achievable with only the following physical qubit operations[205]: $\hat{X}, \hat{Z}, \hat{H}, \hat{S} = \sqrt{\hat{Z}}, \hat{T} = \sqrt{\hat{S}}, \hat{C}$ and projective measurement in the Z-basis. The remainder of this chapter concerns the practicalities of implementing these operators in a scalable and manufacturable 2D donor array so that a surface code may be constructed using atomic scale qubits in silicon.

6.2 A survey of surface code architectures based on donor qubits

Compared to electrons in quantum dots, or even superconducting circuits, donor spin qubits are inherently uniform in terms of their energy levels, electronic confinement potential, spin-spin interactions[45]. Every ^{31}P atom is alike and there is no intrinsic variability from donor to donor. Thus, they permit a high degree of shared simultaneous control without needing to independently fine tune, or 'trim' each qubit into resonance. They also have been shown to posses exceptionally long quantum coherence times[37,38], high single-qubit gate fidelities[51] and in the long-term are expected to benefit from the proven scalability of silicon-based classical nano-electronics[34]. All of this provides a strong argument for the viability of donor qubits at scale. However, the two dimensional geometry required by the surface code poses formidable fabrication and control challenges, common to all solid-state semiconductor qubit types: The array must be 'dense' in the sense that each qubit must be able to interact with each of its neighbours, but this interaction must also be switchable – so that there is control over which qubits interact at each moment. However, the array must also be 'addressable', providing a means to act on a chosen qubit, pair of qubits or a chosen set of many qubits – which (at least naively) requires some dedicated control wiring or control field for every individual qubit. This would appear to be at odds with the dense nature of the array, since space is needed throughout to accomodate all these control elements in order to allow simultaneous operation of subsets of qubits in 'parallel', necessary to achieve the high surface code threshold error rate of $P_{th} \sim 0.01$. A number of proposals outlining strategies to meet these three challenges have appeared recently, and we shall describe three such approaches utilising donors in silicon below.

Mechanical re-positioning of qubits to control interactions

O'Gorman *et al.*[206] propose a mechanical system where matching arrays of data qubits and ancilla (or "probe spin") qubits are embedded as donor bound electron spins near to the surface in two physically separated substrates as shown in Figure 6.6(a). The two substrates are intended to be different types of spin qubits, for instance P donors in silicon in the data array and NV defect centres in diamond for the probe array.

The individual qubits in each substrate are far apart ($D \sim 400$nm) and non-interacting with their lateral neighbours, leaving sufficient surrounding space for individual control and addressing gates and readout sensors in each array. To facilitate qubit-qubit interactions, qubits in the ancilla substrate are mechanically aligned with the data qubits in the fixed substrate, bringing the electrons within $d \sim 40$nm of each other, where their magnetic dipole-dipole interaction becomes significant:

$$H_{\mathrm{dd}}(r = 40\mathrm{nm}) = \frac{\mu_0 g^2 \mu_B^2}{4\pi} \frac{\vec{S_1} \cdot \vec{S_2} - 3(\vec{r} \cdot \vec{S_1})(\vec{r} \cdot \vec{S_2})}{r^3} \tag{6.14}$$

$$\approx 0.8\mathrm{kHz} \tag{6.15}$$

Here the data and probe spin vectors $\vec{S_1}$ and $\vec{S_2}$ are separated in space by a vector $\vec{r}$, and g represents the electron g-factor. The dipolar interaction facilitates a CPHASE (controlled $\hat{Z}$) operation, which is be made addressable by initialising a certain probe spin in either the $|0\rangle$ or $|+\rangle$ state, switching the interaction off or on respectively.

Constant motion of the ancilla array as indicated in Figure 6.6(b) means that the total interaction is insensitive to the exact donor positioning, since the system integrates over a range of positions. After an appropriate interaction time the ancilla layer is then moved, shifting each ancilla over to the next data qubit it should interact with, and so on to complete the stabiliser operations required by the surface code. O'Gorman *et al.* [206] suggest that such a 4-step physical cycle can be completed in ~ 1.2ms for the dimensions mentioned, within the coherence time of donor-bound electrons and NV-centre electrons. There is a trade-off between the mechanical translation velocity, inter-substrate distance and qubit grid spacing parameters, all of which contribute to the speed of the quantum computer's operation.

Electrical shuttling of mobile electron qubits

Another scalable implementation of the surface code by Pica *et al.* [207] uses a combination of exchange and hyperfine interactions in a layout with widely-separated donor spin qubits. Here the qubits are transferred to interact with their 'distant' neighbours not mechanically but by electrically shuttling electrons around the processor. The layout is shown in Figure 6.6(c), and consists of a grid of bismuth donors which act as ancilla qubits, located beneath a mobile array of electrons confined to quantum dots at an interface. Surface gates act in parallel to shuttle the quantum dot electrons in unison

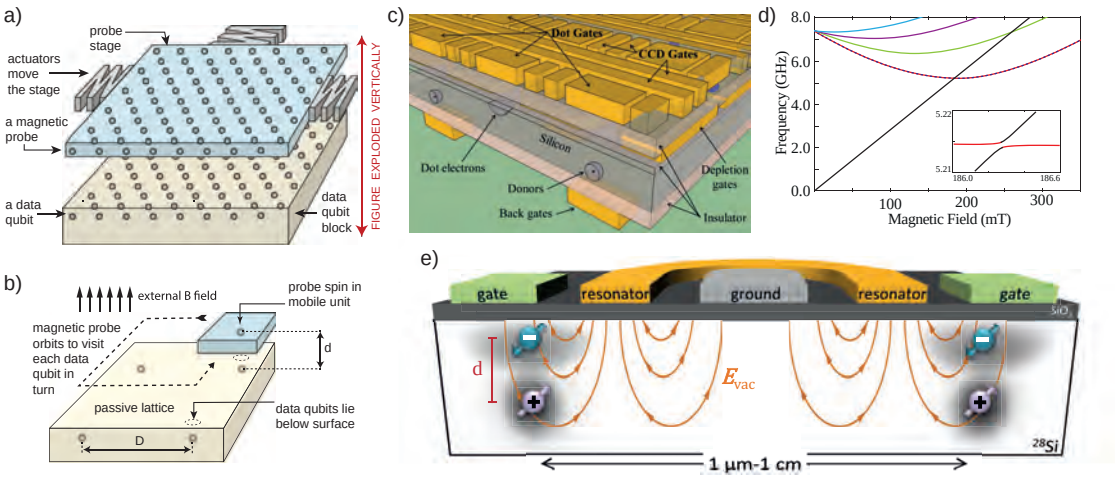

Figure 6.6: **Review of donor-based surface code architectures.** (a) **Mechanical positioning of qubits:** Two physically separate substrates, each containing an array of donor qubits. In this architecture the qubit interaction occurs via a CPHASE operation. Reproduced from O'Gorman *et al.* [206]. (b) Mechanical actuation of the ancilla/probe substrate to overcome large qubit separation ($D \approx 400$nm) in the passive data qubit lattice. The vertical separation may be as small as $d \approx 40$nm. Reproduced from O'Gorman *et al.* [206]. (c) **Electrical shuttling of mobile electron qubits:** CCD inspired hybrid donor/quantum dot architecture using bismuth donors. Interaction is based on fast adiabatic electron-electron SWAP operations and hyperfine mediated CNOT operations. Data qubits are electrically transported around the circuit. Reproduced from [207]. (d) Potential landscape, reproduced from [207] illustrating the hybrid donor/quantum dot double well, electrons adiabatically SWAP from one well to the other in response to back gate voltage pulses. (e) **Cavity coupling of qubits:** Another hybrid donor/quantum dot proposal, utilising cavity quantum electrodynamics to establish long distance coupling for two qubit gates, and fast electrical control to perform single qubit gates on a combined electron-nuclear 'flip-flop' qubit. Reproduced from [208].

(as in a standard charge coupled device – or CCD) between donors. Addressability is provided by a set of back gates.

On arriving at a donor location, the electron, which acts as a data qubit, the back gate voltage is changed to switch on an exchange interaction between the donor bound and quantum dot electrons. At this point the two electrons undergo an adiabatic $SWAP$ operation, driven by a magnetic field sweep over a span of $\sim$ 10mT. Figure 6.6(d) shows the transition frequencies between the spin 1/2 states of the dot electron (black line) and the spin 9/2 states of the Bi donor electron (other colours). Pica *et al.* [207] propose bismuth donors since the presence of an ESR clock transition (the frequency insensitive point on the red line around 200mT in Figure 6.6(d)) allows the adiabatic $SWAP$ (across the anti-crossing between the red and black states in the inset) to be

achieved within a small magnetic field sweep range ($\sim$ 1mT), and therefore quickly. In particular, the adiabatic nature of the interaction makes the scheme insensitive to variation in the precise donor placement.

With the data and ancilla qubits now encoded in the donor nuclear and electron spin states, a CNOT operation as required for the surface code stabilisers is achieved by simply exciting one of the four electron-nuclear transition frequencies with an NMR or ESR pulse. The electron state is adiabatically swapped back into the quantum dot and the surface gates shuttle it on to interact with the next donor as required to build the plaquette operators.

Cavity coupling for long distance interactions

A third mechanism for achieving an interaction between distant qubits is the electric dipole-dipole interaction, which has been proposed by Tosi *et al.*[209]. They describe a 'flip-flop' qubit configuration, where the qubit basis states are the donor electron-nuclear total spin zero states $|\Uparrow\downarrow\rangle$ and $|\Downarrow\uparrow\rangle$. Relying on the Stark effect which couples the hyperfine energy to the electric field experienced by the donor, an electric dipole spin resonance (EDSR) transition can be driven by an oscillating electric field E_z.

The EDSR effect is enhanced at the ionisation point, where the electron wavefunction is partially displaced from the nucleus toward the interface due to the gate-induced electric field (of around 4MV/m). This displacement generates a static electric dipole which may be used to couple two such 'flip-flop' qubits. In essence, the combined spin state is coupled to the electron orbital state by the Stark shift of the hyperfine energy, so that the orbital state has a spin-state-dependent electric dipole moment $\mu_e = ed$. Here e is the electron charge and d the average displacement of the interface-confined wavefunction away from the donor core, as shown on the left of Figure 6.6(e).

The electric dipole-dipole interaction permits an entangling $\sqrt{\text{SWAP}}$ gate between two 'flip-flop' qubits, either directly dipole-coupled at a distance between 100 to 500nm, or via a quantum electrodynamics – coupling two dipoles indirectly through a resonator cavity that supports coherent microwave frequency photons. This idea can be seen in Figure 6.6(e), and Tosi *et al.*[209] estimate that the qubit to cavity coupling strength can be as high as $g = 3$MHz with realistic device parameters, allowing two qubit operations on the order of 1μs even over distances of up to several cm.

Concept	O'Gorman *et al.*[206]	Pica *et al.*[207]	Tosi *et al.*[209]
Data Qubit	Static array of P donor electron states	Mobile electrons in silicon quantum dots	P donor electron-nuclear 'flip-flop' basis states
Ancilla Qubit	Mobile array of a different donor species (or NV cenres in diamond)	Fixed Bi donor nuclear spins	P donor electron-nuclear 'flip-flop' basis states
1 Qubit Gates	Electron spin resonance	Electron spin resonance	Electric dipole spin resonance (via Stark and hyperfine)
2 Qubit Interaction	Magnetic dipole-dipole	Exchange and hyperfine	Electric dipole-dipole
Control of Coupling	Mechanical motion	Electron shuttling	Cavity quantum electro-dynamics
Area per Qubit	$0.16\mu\text{m}^2$	$> 1\mu\text{m}^2$	$0.01 - 0.25\mu\text{m}^2$

Table 6.1: Scalable architectures using donor spins: a summary of the critical details of three scalable qubit proposals utilising donor spins to implement the surface code.

The three designs discussed in this section, and summarised in Table 6.1, deliberately avoid the challenge of dense donor placement, and conform to the required minimum physical volume for the fanout of individual qubit control elements and readout wiring. These schemes achieve qubit interactions not by proximity, but by mobilising electrons (or their dipole fields) to cross the large distances between qubits. In the remainder of this chapter we present our core result, taking the opposite strategy, and exploiting the ability of STM lithography to fabricate atomic scale structures so that we can place donors near to each other, greatly simplifying the layout of the qubit array, and minimising the number of different control components that must be integrated.

6.3 A dense surface code array based on local interactions between donor qubits

We propose a surface code architecture[6] consisting of three layers of precision donor-defined nanostructures in isotopically purified ^{28}Si. In the central layer, quantum information is encoded on the long-lived nuclear spin states of ionized phosphorus donors, $|\Uparrow\rangle \rightarrow |0\rangle$, $|\Downarrow\rangle \rightarrow |1\rangle$, which are arranged in a 2D square array. Electron spins are used only as a resource to enable addressable operation of the nuclear spin qubits, and to enable two-qubit interactions.

The scheme is illustrated in Figure 6.7(a), which shows the correspondence between the conceptual surface code topology of plaquettes (on the left), and the physical construction (on the right). The proof-of-principle STM image (right of Figure 6.7(a)) demonstrates our ability* to perform atomic-scale lithography to place single P donors at the appropriate positions on a 30nm grid, with a readout SET island a distance of $\sim$ 15nm from every donor, each SET multiplexed across 4 donor sites. Qubit interactions are achieved by controlling the charge state of each donor in an addressable way, and transferring the nuclear spin state to the donor-bound electron spin, allowing neighbouring qubits to interact via direct magnetic dipole-dipole coupling.

In the upper plane, long continuous parallel control lines will alternate as source (S) and gate A (GA) structures, and in the bottom plane, and perpendicular to those above, additional control lines alternate as drain (D) and gate B (GB) wires, as indicated in Figure 6.7(b). The computer operates at millikelvin temperatures in a background static field of $B_0 \sim 2$T, and also within a homogeneous global AC magnetic field $B_1 \sim$ 1mT for ESR and NMR spin control, values based on recently achieved experimental conditions[38,134].

The lateral separation of control lines matches the donor grid spacing of (nominally) 30nm, and the layers are registered to one another so that a mono-layer SET is aligned vertically to each intersection of S and D lines, as shown in Figure 6.7(c), forming a grid of vertical single electron transistors, which facilitate electron loading/unloading as well as electron spin readout. A single P donor is located at the centre of each unit cell defined by the boundaries of GA, GB, S, and D lines, as indicated in Figure 6.7(d). Donors are

* image provided by Joris Keizer

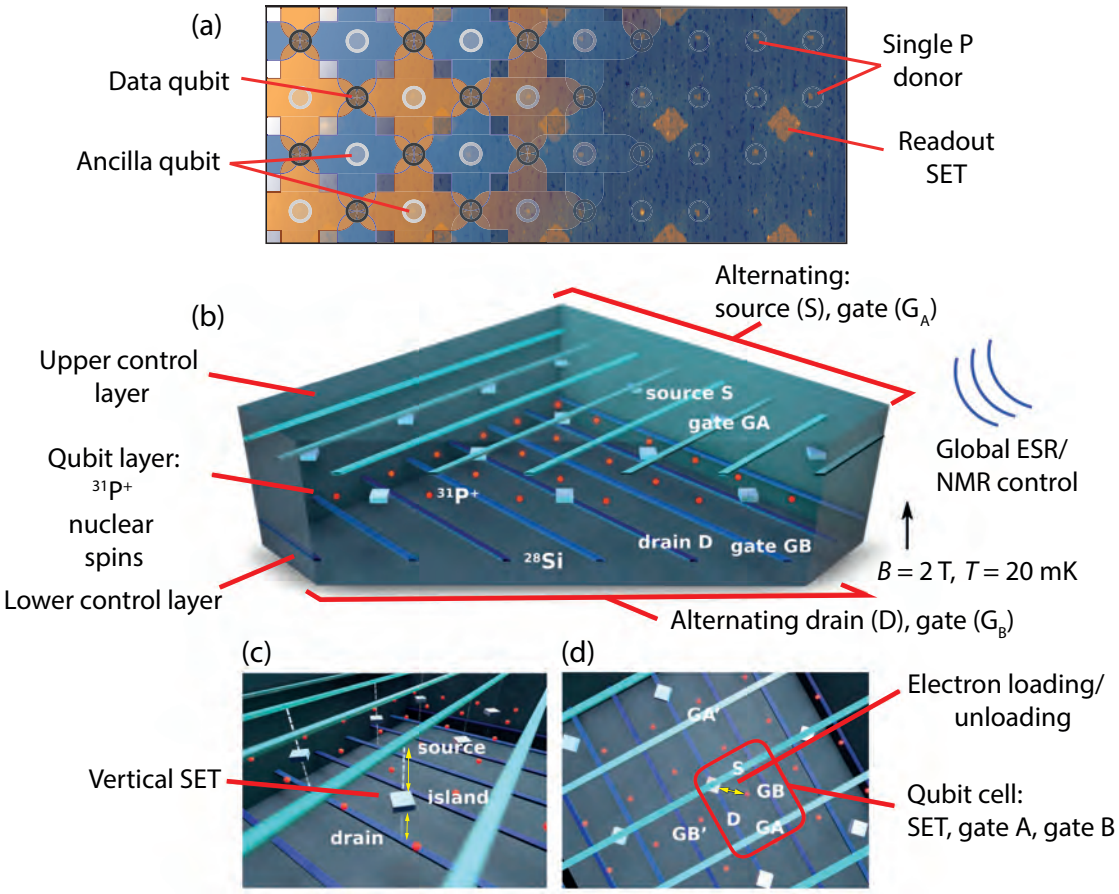

Figure 6.7: Implementing the surface code with atomic precision donors in silicon. (a) Schematic labelling the required 2D array of alternating data (dark) and ancilla (light) qubits to implement the surface code, with Z-stabiliser (orange) and X-stabiliser (blue) plaquettes shown, overlaid onto a real STM image demonstrating atomic scale lithography defining the central layer. Bright orange diamonds indicate areas to be phosphorus doped for the readout SET islands, and small patches (of 6 desorbed atoms in the H mask) to incorporate a single donor. (b) Representation of the layered 3D layout proposed. The central layer contains the donor qubit array as well as a shared SET island for each set of 4 qubits. The upper layer contains alternating parallel source and gate lines, and the lower layer alternating drain and gate lines. Lines in the top and bottom layers run perpendicular to one another. The entire structure sits in a static magnetic field at millikelvin temperatures, within a global ESR/NMR cavity. (c) Many-donor diamond-shaped SET islands are aligned at the intersection of source and drain lines above and below, forming a grid of vertical SETs, each indexed by a unique combination of source and drain line coordinates. (d) Electrons are made to tunnel to any selected donor qubit from the nearest SET island when activated by a unique combination of line voltages on the control lines (S, D,GA, GB, GA', GB') surrounding the qubit unit cell.

tunnel-coupled to their nearest SET (yellow arrow indicates potential electron motion), but only capacitively coupled to the nearby control lines.

With this geometry, an array of 25×10^6 physical qubits is realisable within an area of $150\mu\text{m} \times 150\mu\text{m}$. Such an array would require independent control over only 10^4 control lines, far less than in a comparably sized processor with independent control gates for each qubit, as is the case for the designs surveyed in Section 6.2. Thus we describe our architecture as dense, and remarkably efficient in it's control wiring.

Having described our motivation and the fundamental concept behind the plan, we detail in the following sections how such an architecture can be fabricated, the single qubit operations, initialisation and measurement, two-qubit interactions, and provide an analysis of its expected performance in terms of timescales and error rates. A small team of researchers actively worked on the development of the surface code architecture presented. Charles Hill was in charge of the overall conceptual design of the array, CNOT gate and phase matched loading mechanism. My role was in the determination of a viable geometry, determination of the electrostatic conditions required for qubit activation and to physically realise the operations needed for the CNOT and phase matched loading scheme. The proposal was published in Science Advances[6].

6.3.1 Fabrication of multi-planar atomic precision devices

The ability to pattern multiple vertically separated layers of donor structures in silicon, forming fully epitaxial, 3D devices, was recently demonstrated by McKibbin *et al.*[210]. Their results, across two different dual-layer devices, showed that inter-layer vertical electron transport, and also purely capacitive gating are both possible by careful 3D design.

The first device demonstrated vertical transport from layer to layer. Figure 6.8(a) and (b) show STM images of two donor defined nanowires $\sim$ 400nm long. These wires are oriented perpendicularly in two lithographic planes separated vertically by 45nm. The lower wire in (a) is 15nm wide and the upper wire of (b) 30nm wide at their crossover point. A 3D schematic of their layout is shown in Figure 6.8(c), which also shows the

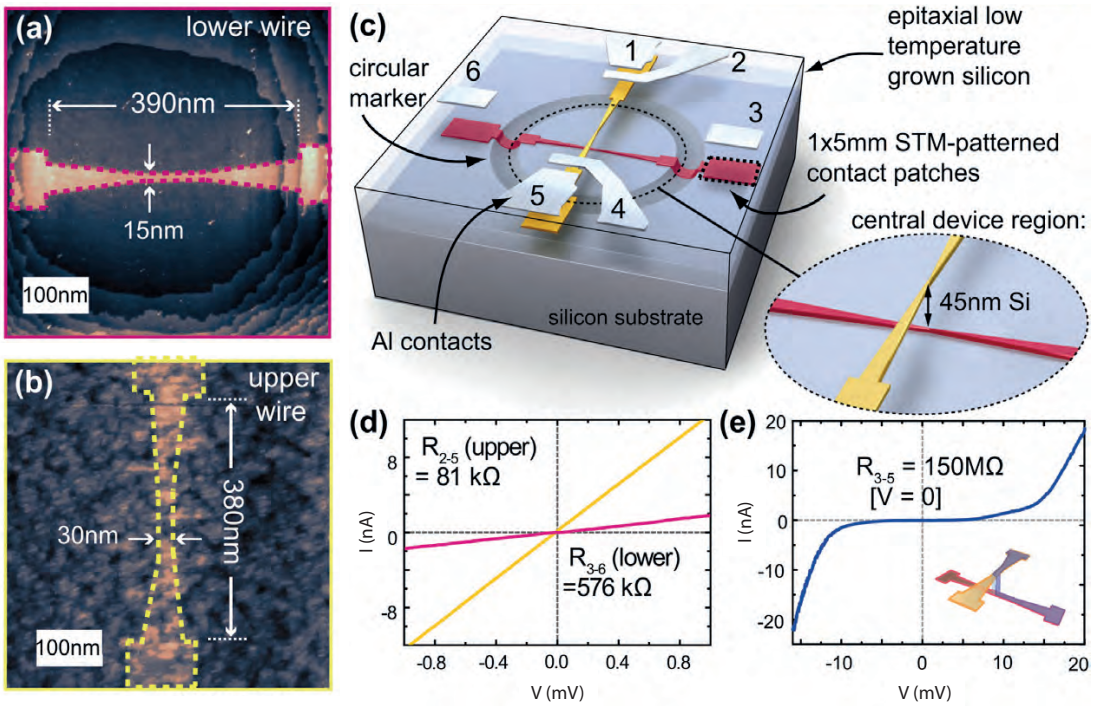

Figure 6.8: 3D multi-planar atomic scale device fabrication by STM lithography. (a,b) STM images of the lower and upper layers of a perpendicular nanowire device, bright regions indicating P dosed regions. While the lower layer (a) is smooth, with clear visibility of the atomic terraces, the upper layer (b) is fabricated on a low temperature overgrown surface, with roughness $\sim 0.7nm$. (c) 3D schematic of the perpendicular nanowire device, aligned with the aid of a circular etched registration marker. The inset indicates the vertical separation of 45nm. (d) Resistance measurements of the upper and lower nanowires, with the thicker upper layer wire displaying a lower resistance than the thin lower wire as expected. (e) Resistance measurement of the vertical conduction pathway from one wire to the other, providing a low bias resistance of $150\text{M}\Omega$ All parts reproduced from McKibbin *et al.* [210].

circular alignment marker which McKibbin *et al.* [210] used to align the two wires such that their overlapping area is $\sim 15 \times 30$nm.

The lower (upper) nanowire exhibits Ohmic conduction with a resistance of $576\text{k}\Omega$ ($81\text{k}\Omega$) as indicated in Figure 6.8(d) – the difference in resistance being due to the greater cross-sectional width of the upper wire. In Figure 6.8(e) we observe that although the two wires are electrically separated, the application of a bias voltage between them will cause a current to flow vertically between the layers, with a resistance of $150\text{M}\Omega$, substantially higher than the wires themselves, but comparable to the resistance of typical single-plane SETs [107].

In the second two-layer device with a considerably larger inter-layer vertical separation

of 120nm, McKibbin *et al.*[210] showed that the current flow between layers becomes negligible (with resistance $> 640\text{G}\Omega$) up to a breakdown voltage of ~ 1V. This result indicates that it is possible to create electrically isolated wires in separate vertical planes, which, if the separation is small, will permit vertical current flow, or which, with larger separation can provide capacitive coupling only, in order to act as a gate for a donor or SET island below or above.

One key limitation identified by McKibbin *et al.*[210] is that the second layer of lithography must be performed on a low temperature grown silicon surface. The low temperature requirement is to minimise vertical segregation of donors out of the lower layer. As shown in Figure 6.8(b), such surfaces have a roughness of ~ 0.7nm, larger than the dangling bond height of ~ 0.14nm which defines the contrast of the patterned features. As a consequence, the upper nanowire was patterned in a high voltage field emission mode[85], which does not allow atomic resolution lithography.

Recent developments by Keizer *et al.*[211] provide a solution to create a flat second surface for atomic precision lithography, using a rapid thermal anneal procedure. The optimal procedure consists of two steps: growth of a room temperature 'locking layer' to prevent dopant segregation out of the first lithographic layer, followed by heating to reduce surface roughness and anneal out crystal growth defects.

Figure 6.9(a) shows secondary ion mass spectrometry measurements of the donor concentration as a function of depth for four different locking layers. The sharpness of the green curve indicates that a 'locking layer' of only 9 monolayers (~ 3nm) of room-temperature grown silicon is already effective in suppressing dopant segregation, with $> 75\%$ of the P atoms of a full 2D delta-layer confined within a layer 1.0nm thick. Room temperature silicon growth is known to introduce vacancy defects which can result in lower electrical activation of the donor layer. To investigate the effectiveness of a rapid thermal anneal to heal such defects, Keizer *et al.*[211] performed magneto-transport measurements of the active carrier density in samples which were annealed differently. In Figure 6.9(b) we see the measured 2D carrier density n_S is maximised for an anneal at 500°C for 14s, but reduces for longer or higher temperature anneal conditions. This can be understood as increased lateral diffusion of donors occurs with additional thermal energy, producing electrically inactive P–P dimers.

Figure 6.9(c) displays STM images of the resulting surfaces corresponding to a number of the data-points in (b). We note the that the electrically optimal settings (500°C, 14s)

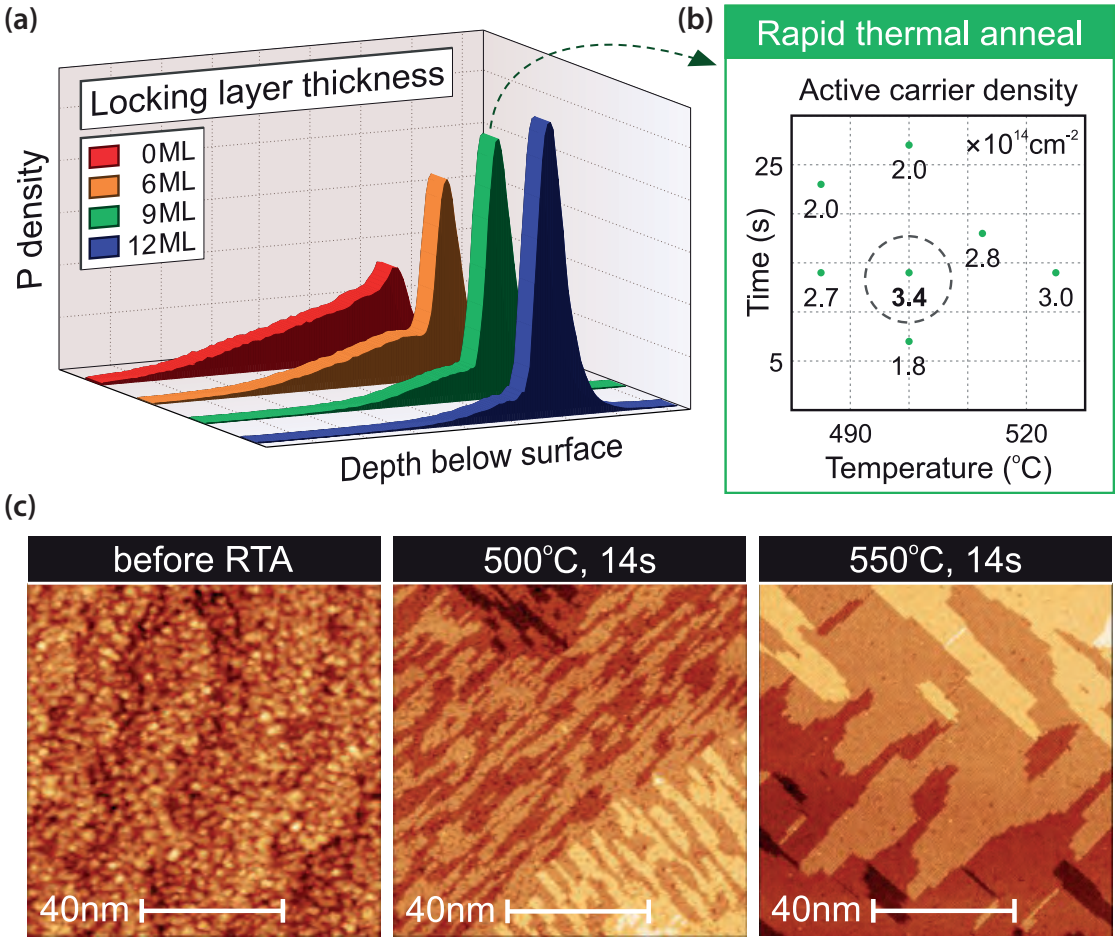

Figure 6.9: **Surface preparation for multi-layer STM lithography.** (a) Secondary ion mass spectroscopy, measuring the P donor concentration as a function of depth below the surface for 4 different 2D delta-doped samples, each encapsulated by a room-temperature 'locking layer' of varying thickness (from 0 to 12 monolayers). Thicker layers suppress dopant segregation, as shown by the higher peak and less uniform distribution in the green and blue curves. (b) The measured active carrier density is sensitive to the parameters of a rapid thermal anneal, and is maximised for $500°$C and 14s. (g) STM images of the resulting surfaces after low temperature growth of silicon followed by a rapid thermal anneal, with differing temperature and duration as indicated in each panel. Without the rapid thermal anneal the surface is rough on the scale of individual atoms, but a 14s anneal at $550°$C recovers a planar surface suitable for performing atomic scale lithography. All parts reproduced from Keizer *et al.* [211]

do not correspond to the smoothest surface (centre panel). However, these measurements from Keizer *et al.*[211] are all based on a thin ($\sim$ 3nm) layer. We expect that by growing a substantially thicker locking-layer, and separating the lithographic planes by $\sim$ 40nm, a higher temperature anneal of $\sim$ 550°C, will produce an acceptable surface flatness as in the right-most panel of Figure 6.9(c), without diffusion processes limiting the electrical activation of donors.

For our surface code architecture, we envisage an extension of this multi-layer fabrication technique to three planes: two control layers above and below a central layer of donor qubits. With the basic geometry and fabrication strategy laid out we now proceed to a physical description of the surface code's qubit operations: single-qubit gates, initialisation and readout, and two-qubit gates.

6.3.2 Qubit activation and single qubit gate operations

We make a distinction between 'Memory', and 'Active' operational modes of the individual physical qubits, with distinct definitions of the qubit basis states in each mode. In the non-interacting 'Memory' mode, both data and ancilla qubit states are encoded on the long-lived $|0\rangle = |\Uparrow\rangle$ and $|1\rangle = |\Downarrow\rangle$ spin states of the ionised spin-$\frac{1}{2}$ ^{31}P nucleus, a configuration illustrated in Figure 6.10(a). The qubit Hamiltonian in the memory state simply describes the Zeeman energy of the nuclear spin in a magnetic field:

$$H_{memory} = -g_N \mu_N \vec{B_0} \cdot \vec{I} \tag{6.16}$$

$$= \gamma_N B_0 I_Z \tag{6.17}$$

where $g_N = 1.13$ is the nuclear g-factor for phosphorus[212], μ_N is the nuclear magneton, $g_N = 17.3$MHz/T the resulting nuclear gyromagnetic ratio, B_0 the static magnetic field defining the Z-axis, and I_Z the Pauli Z-operator acting on the nuclear spin. The NMR transition frequency between the eigenstates $\nu_0 = \gamma_N B_0$, is indicated in Figure 6.10(b). Driving an oscillating magnetic field B_1 (perpendicular to B_0) at this frequency would cause single qubit rotations of all the 'Memory' qubits in parallel, but we do not intend to

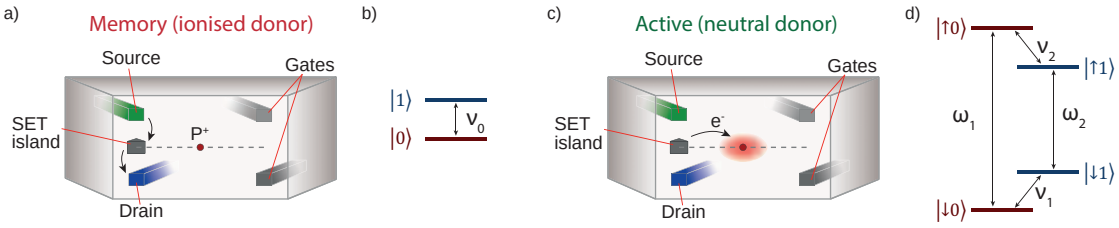

Figure 6.10: Qubit activation via the hyperfine interaction. (a) A cross-sectional view showing one donor next to a vertical SET. Ionised donors are idle, non-interacting qubits which we say are in the 'Memory' mode. With no bound electron, interactions with the environment are weak. (b) The ionised 'Memory' states are separated by the nuclear Zeeman splitting, with a resonant frequency ν_0 (c) Loading an electron from an SET onto a donor, switches on the hyperfine interaction, producing four two-particle states across which the quantum information can be manipulated. (d) The two particle spin product states, with conditional state transitions driven by resonances ω_1, ω_2 at microwave frequency (GHz) and ν_1, ν_2 at radio frequency (MHz).

drive such rotations*. Instead, the long T_2 coherence time of the ionised donor, ~ 1.8s[38] simply provides long-lived storage of the quantum information for timescales beyond the operational timescale of the architecture. Whilst qubits are idle – that is, when they are not being operated on during the course of the computation or surface code stabiliser cycles, the are left in the 'Memory' state.

Qubit activation

A specific qubit is 'activated' (deactivated) by loading (or unloading) an electron, which tunnels to a donor from the nearest SET as illustrated in Figure 6.10(c). This process switches on a hyperfine interaction that serves to shift the qubit energy levels, making them distinct from the 'Memory' qubit states. The modified Hamiltonian now consists of an additional electron-Zeeman term and a hyperfine interaction term:

$$H_{active} = -g_N \mu_N B_0 \vec{B_0} \cdot \vec{I} + g_e \mu_B B_0 \vec{B_0} \cdot \vec{S} + A\vec{I} \cdot \vec{S} \tag{6.18}$$

$$= \gamma_N B_0 I_Z + \gamma_e B_0 S_Z + A\vec{I} \cdot \vec{S} \tag{6.19}$$

where $g_e \approx 2$ is the electron g-factor in silicon[71], μ_B is the Bohr magneton, $g_e = 27.9$GHz/T the resulting electron gyromagnetic ratio, A is the hyperfine interaction

* Although we note that operations on memory qubits could be utilised to universally apply dynamical decoupling pulses to all the nuclear spins, and extend the coherence time further.

energy related to the electron wavefunction density at the donor core, and S_Z the Pauli Z-operator acting on the electron spin. $\vec{I}$ and $\vec{S}$ are the full spin vectors for nuclear and electron spins respectively.

With a finite magnetic field ($\sim$ 2T) the Zeeman energy is greater than the thermal energy ($\gamma_e B_0 > k_B T$) and electron loading is always into the $|\downarrow\rangle$ ground state. The finite field also permits a large field approximation (such that the eigenstates are well approximated by the spin product states – see Section 2.4.1) so for the 'Active' mode, the qubit basis becomes initially $|0\rangle = |\downarrow\Downarrow\rangle$ and $|1\rangle = |\downarrow\Uparrow\rangle$*.

The four distinct resonance frequencies between eigenstates displayed in Figure 6.10(d) correspond to:

$$\omega_1 = \gamma_B B_0 + \tfrac{A}{2} \qquad \omega_2 = \gamma_B B_0 - \tfrac{A}{2} \tag{6.20}$$

$$\nu_1 = \tfrac{A}{2} + \gamma_N B_0 \qquad \nu_2 = \tfrac{A}{2} - \gamma_N B_0 \tag{6.21}$$

Coherently driving only ν_1 or ν_2 (ω_1 or ω_2) allows for conditional rotations of the nuclear (electron) spin, dependent on the state of electron (nucleus), and so these resonances are used to implement two qubit interactions in the form of electron-nuclear CNOT gates. Alternatively, simultaneously exciting a pair of transitions allows the implementation of an unconditional rotation of one of the spins.

A global spin control field may be applied to electron and nuclear spins of all donor qubits currently in the 'Active' mode by a combined ESR (electron spin resonance) and NMR (nuclear magnetic resonance) pulse producing an oscillating magnetic field of amplitude B_ω / B_ν, described by the generalised Hamiltonian:

$$H_{global}(t) = \sum_{\nu=\nu_1,\nu_2} \gamma_N B_\nu \left[X_\nu(t) \cos(\nu t) I_X + Y_\nu(t) \sin(\nu t) I_Y \right] \tag{6.22}$$

$$+ \sum_{\omega=\omega_1,\omega_2} \gamma_e B_\omega \left[X_\omega(t) \cos(\omega t) S_X + Y_\omega(t) \sin(\omega t) S_Y \right] \tag{6.23}$$

Where the in-phase X and quadrature Y components of the four resonant signals may vary with time to execute rotations of arbitrary angle about arbitrary axes.

* single arrows represent the electron spin, double-beamed arrows the nuclear spin

Single qubit gates

For a nominal field strength of $B_1 = 1\text{mT}$, the corresponding nuclear spin π rotation time is $t_\pi = \frac{\pi}{2\pi}\frac{1}{\gamma_n B_1} = 21\mu\text{s}$, so we define the standard single qubit gate set required (in addition to a two-qubit CNOT) for universal computation in the surface code formalism[194] as follows:

X gate: A π rotation of the nuclear spin about the X-axis of the Bloch sphere in the usual rotating frame is defined by the operator $\hat{X} = \left(\begin{smallmatrix} 0 & 1 \\ 1 & 0 \end{smallmatrix}\right)$. With the electron spin in the $|\downarrow\rangle$ state, the pulse to achieve this is simply:

$$\begin{aligned} X_{\nu_2}(t) &= 0 \\ Y_{\nu_1}(t) &= 0 \\ Y_{\nu_2}(t) &= 0 \end{aligned} \qquad X_{\nu_1}(t) = \begin{cases} 0 & t < 0 \\ 1 & 0 < t < t_\pi \\ 0 & t > t_\pi \end{cases} \tag{6.24}$$

Z gate: A π rotation about the Z-axis of the Bloch sphere is achieved indirectly with a combination of X- and Y-rotations $\hat{Z} = \hat{Y}\hat{X} = \left(\begin{smallmatrix} 1 & 0 \\ 0 & -1 \end{smallmatrix}\right)$. The pulse to achieve this (with $X_{\nu_2} = Y_{\nu_2} = 0$) is:

$$X_{\nu_1}(t) = \begin{cases} 0 & t < 0 \\ 1 & 0 < t < t_\pi \\ 0 & t > t_\pi \end{cases} \qquad Y_{\nu_1}(t) = \begin{cases} 0 & t < t_\pi \\ 1 & t_\pi < t < 2t_\pi \\ 0 & t > 2t_\pi \end{cases} \tag{6.25}$$

H gate: A π rotation about the tilted Hadamard axis (in the X-Z plane, tilted by an angle $\pi/4$ from the Z-axis) of the Bloch sphere is also achievable with a combination of X- and Y-rotations $\hat{H} = \frac{1}{\sqrt{2}}(\hat{Y} + \hat{X}) = \frac{1}{\sqrt{2}}\left(\begin{smallmatrix} 1 & 1 \\ 1 & -1 \end{smallmatrix}\right)$. One decomposition of this operator into X and Y rotations is specified by:

$$X_{\nu_1}(t) = \begin{cases} 0 & t < 0 \\ 1 & 0 < t < t_\pi \\ 0 & t > t_\pi \end{cases} \qquad Y_{\nu_1}(t) = \begin{cases} 0 & t < t_\pi \\ -1 & t_\pi < t < \frac{3}{2}t_\pi \\ 0 & t > \frac{3}{2}t_\pi \end{cases} \tag{6.26}$$

S gate: A $\pi/2$ rotation about the Z-axis $\hat{S} = \sqrt{\hat{Z}} = \left(\begin{smallmatrix} 1 & 0 \\ 0 & -i \end{smallmatrix}\right)$. This can be achieved with

the sequence:

$$X_{\nu_1}(t) = \begin{cases} 0 & t < 12t_\pi \\ 1 & 12t_\pi < t < t_\pi \\ 0 & t > t_\pi \end{cases} \qquad Y_{\nu_1}(t) = \begin{cases} 0 & t < 0 \\ 1 & 0 < t < \frac{1}{2}t_\pi \\ 0 & \frac{1}{2}t_\pi < t < t_\pi \\ -1 & t_\pi < t < \frac{3}{2}t_\pi \\ 0 & t > \frac{3}{2}t_\pi \end{cases} \tag{6.27}$$

T gate: A $\pi/4$ rotation about the Z-axis $\hat{T} = \sqrt{\hat{S}} = \left(\begin{smallmatrix} 1 & 0 \\ 0 & e^{i\pi/4} \end{smallmatrix}\right)$. We pulse the NMR field according to:

$$X_{\nu_1}(t) = \begin{cases} 0 & t < 12t_\pi \\ 1 & 12t_\pi < t < t_\pi \\ 0 & t > t_\pi \end{cases} \qquad Y_{\nu_1}(t) = \begin{cases} 0 & t < 0 \\ 1 & 0 < t < \frac{1}{2}t_\pi \\ 0 & \frac{1}{2}t_\pi < t < t_\pi \\ -1 & t_\pi < t < \frac{3}{2}t_\pi \\ 0 & t > \frac{3}{2}t_\pi \end{cases} \tag{6.28}$$

For exactness we've specified particular decompositions of these physical gate operators – other alternatives exist and may be used instead. We note that the flexibility of H_{global} in our implementation allows for additional pulse optimisation and other robust control sequences[213] as required by the noise specifics of the real system.

The single qubit rotations specified above can operate simultaneously and in parallel for any and all qubits across the array that are in the 'Active' mode. Importantly, driving any of these 'Active' transitions does not affect any 'Memory' mode qubits due to the detuning provided by the hyperfine interaction ($\nu_0 \neq \nu_1 = \nu_0 + \frac{A}{2}$). Since the binary shift in hyperfine energy due to the presence of an electron on the donor toggles a nuclear spin in and out of the set of qubits addressed at any one time for the application of a global single qubit gate, it simply remains to addressably activate the desired qubits prior to the application of H_{global}.

6.3.3 Addressable activation and readout of the nuclear spin qubit

A fuller treatment of the exact procedure in terms of timing and control line voltages are provided in Section 6.3.6 and Section 6.3.5 below, but here we provide an overview of the process by which qubit activation (electron loading), deactivation (unloading) and qubit readout is addressed to a target donor. Although the number of control lines is always less than the number of donors in our 2D array, it is possible with a novel combination of control line voltages to load an electron to one target donor only, while leaving all its neighbours ionised and in the 'Memory' mode.

Activation and deactivation

Figure 6.11(a) shows a small section of the array surrounding an individual activation operation which is achieved by applying voltages to the proximal gates (S, D, G_A, G_B, G'_A, and G'_B) to create a local electrochemical potential variation to move an electron from SET to donor. A small negative bias is applied to both S and D, raising the Fermi energy of the SET island at their intersection (the dark grey diamond) relative to all other surrounding SETs (faded grey diamonds). At the same time, a combination of positive voltages applied to gates G_A and G_B (dark grey), and negative voltages on G'_A and G'_B (light grey), tilts the potential landscape surrounding the SET, lowering furthest the electrochemical potential of the target donor to exactly meet the Fermi energy of the SET. At this point the electron Zeeman ground state is accessible and a spin down electron tunnels from the SET to the donor – and now the targeted nuclear spin qubit is in the 'Active' mode.

Deactivation is simply the opposite process, where the electron is made to tunnel off the donor, returning the nuclear spin qubit to the ionised 'Memory' mode. Both the activation and deactivation processes are designed so they can be applied in parallel to a large number of qubits across the 2D array, by simultaneously adjusting the voltages on multiple sets of control lines. The parallelism of gate operations is discussed in more detail later in the chapter (Section 6.3.7).

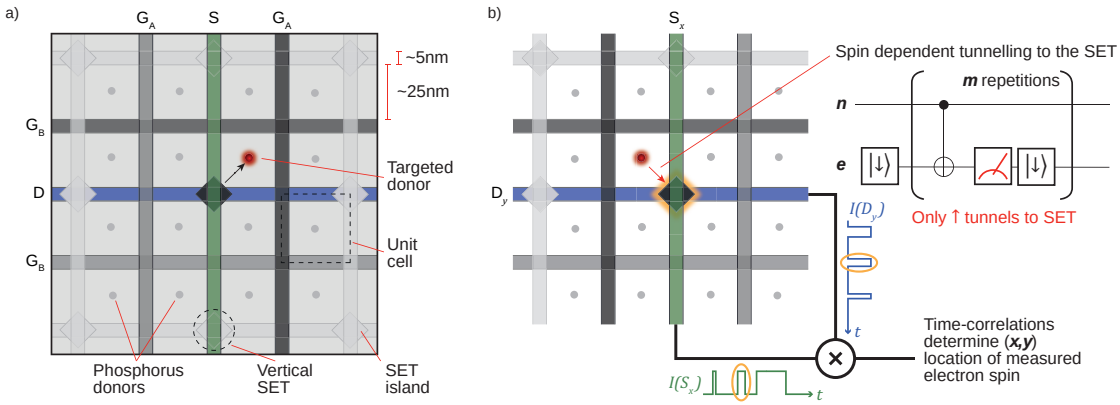

Figure 6.11: Addressable qubit activation and readout. (a) Top view of the criss-cross layout, showing intended dimensions of the structure, and highlighting the selective activation of a single targeted qubit. An electron is made to tunnel from an SET island to the intended donor by combined and unequal voltage pulses on the set of surrounding gates and source/drain lines ($S, D, G_A, G_B, G'_A, G'_B$). (Details of the voltages and the full electrostatic response are shown later) (b) Qubit readout is conducted by first mapping nuclear spin onto electron spin, then reading the electron state with spin to charge conversion. The repeated $CNOT_{N-e}$ gate is achieved by a simple π-pulse at the ω_2 frequency, and the subsequent electron readout is by Zeeman energy selective tunnelling of the electron to the SET island, generating a current flow through the vertical SET channel. Time correlating transient current pulses on each pair of source/drain lines allows addressable readout, even in parallel across the qubit array. The non-demolition nature of the repeated readout sequence overcomes individual readout errors.

Nuclear state measurement via electron state readout

Nuclear spin readout is achieved by mapping the nuclear spin state onto the electron spin state. Here a simple excitation of the ω_2 transition frequency flips the electron spin conditional on the nuclear spin being $|1\rangle = |\Downarrow\rangle$ (effectively an nuclear-electron controlled-X gate $CNOT_{N-e}$). By subsequently projectively measuring the electron spin state, we perform a quantum non-demolition measurement on the nuclear spin qubit, meaning that the nuclear eigenstate measured as the outcome remains a good description of the system after the measurement, and so the sequence can be repeated many times, increasing the measurement fidelity. The full procedure is shown in standard quantum circuit notation on the right side of Figure 6.11(b).

Electron spin readout itself (represented by the red measurement icon in Figure 6.11(b)) is achieved in exactly the opposite way to activation of the donor. For readout we bring the control voltages (of lines S, D, G_A, G_B, G'_A, and G'_B) back to the point where the SET island's Fermi energy is resonant with the donor's charge state

transition potential, where only the Zeeman excited state has sufficient energy to tunnel away from the donor. With the SET configured as a charge sensor, this charge motion is observed as a transient current flowing through the vertical SET channel, present until another electron tunnels back onto the donor, occupying the spin ground state.

Since the architecture is designed to perform operations in parallel on multiple qubits within the 2D array, this readout procedure can take place at many SET locations across the array simultaneously. Thus each source line, and each drain line involved in the group of simultaneous qubit readout operations will carry a time dependent current which is the sum of time dependent current signals from a number of SETs along the length of that particular line. However, the electron tunnelling process (from donor to SET) is stochastic and so each SET will switch on and off at slightly different times within the full duration of the readout phase. Therefore by time-correlating discrete changes in the current between a pair of source and drain lines, the (x, y) coordinates of the SET involved and therefore the individual donor responsible for each transient current 'blip' among many qubit being read-out at once, can be inferred. This is illustrated in Figure 6.11(b), where example current traces of a particular pair of source and drain lines are shown. Only the 'blip' circled in yellow is present in both traces, indicating its origin as the SET highlighted in yellow at the intersection of S_x and D_y. This time-correlation process has some chance of failure, if for example multiple SET signals are indistinguishable within the measurement bandwidth. Ambiguity can be resolved through repetition because the nuclear readout is a non-demolition measurement and can be repeated many (m) times, and the probability of such time collisions decreases exponentially with m.

6.3.4 Two qubit gate operation mediated by the electron-electron dipole interaction

The interaction underpinning the two-qubit Control-NOT (CNOT) gate between neighbouring qubits is based on natural electron-electron spin interactions and controlled by the timing of electron load/unload operations. Here, we explicitly consider the case of

dipole-mediated gates, which is the dominant interaction at a separation of 30 nm. At smaller spacings, the faster exchange interaction would dominate.

In the absence of bound electrons, the spin-dipole interaction between the nuclear spins of memory qubits is negligible. However, when electrons are loaded on adjacent sites, the spin-spin interaction between activated donor pairs increases by more than six orders of magnitude because of the larger magnetic moment of the electron ($\gamma_e \sim 2 \times 10^3 \gamma_N$). The dipole-dipole Hamiltonian describing the interaction between two electon spin vectors S_1 and S_2 can be written:

$$H_{dd}(r = 30\text{nm}) = \frac{\mu_0 g^2 \mu_B^2}{4\pi} \frac{\vec{S_1} \cdot \vec{S_2} - 3(\vec{r} \cdot \vec{S_1})(\vec{r} \cdot \vec{S_2})}{r^3} \tag{6.29}$$

$$\sim 1.9\text{kHz} \tag{6.30}$$

Where the maximum value of the dot-products (unity), provides the interaction timescale of 1.9kHz, the frequency at which the target spin rotates about the Z-axis conditional on the control spin being in the excited state. The CNOT gate executes a conditional rotation of angle π, so we can estimate the required CNOT duration as $\frac{\pi}{2\pi} \frac{1}{1.9\text{kHz}} \sim 260\mu\text{s}$.

The CNOT gate

The sequence of operations involved in the CNOT gate between any pair of neighbouring nuclear spin qubits (typically one data qubit and one ancilla within a surface code plaquette) is described in Figure 6.12. Our CNOT gate can be understood at the highest level as two Hadamard gates directly applied to the target qubit through global control on the nuclear spin, sandwiching a controlled $\hat{Z}$ operation, which occurs in the electron spin subspace. We now examine each step of the gate procedure in detail:

- The target qubit n_1, which may begin in an arbitrary (potentially entangled superposition) state, is activated by loading a $|\downarrow\rangle$ electron e_1 from the nearest SET island(Figure 6.12(a)).

- A pair of simultaneous ESR pulses at ω_1 and ω_2 achieve a $\hat{X}(e_1)$ operation unconditional on the spin of n_1, flipping the target electron e_1 spin to the $|\uparrow\rangle$ state (Figure 6.12(b) – pink arrows). This has the effect of addressing the target qubit

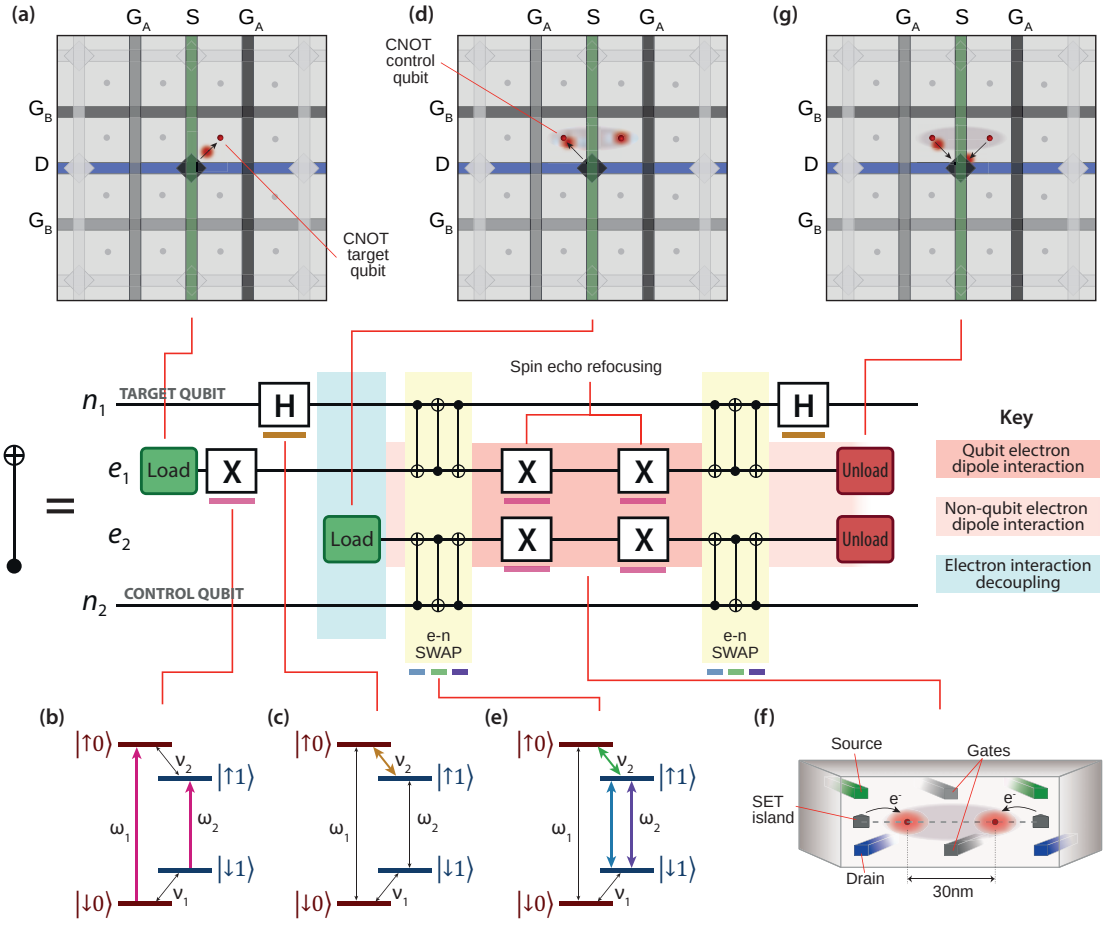

Figure 6.12: **Procedure for a two qubit gate via electron-electron interaction.** (centre strip) Overview of the physical $CNOT_{n-n}$ 2 qubit gate between a target nuclear spin n_1 and control nuclear spin n_2, with time running from left to right. (a) activation of the target qubit, by electron tunnelling (b) detuning of the nuclear qubit n_1 by unconditional excitation of the electron spin e_1 (driving ω_1 and ω_2) (c) Hadamard gate on the nuclear qubit n_1 (driving ν_2), as required to map the CPHASE operation to the desired CNOT (d) activation of the control qubit by electron loading. At this point, electron-electron decoupling begins, to suppress interaction until the electron and nuclear states are swapped. (e) swapping of qubit states onto the electron spins for both control and target qubits (by driving ω_2 then ν_2 then ω_2 again) (f) dipole (or exchange) mediated electron-electron CPHASE interaction. During this time (comprising the bulk of the gate duration), a spin echo sequence is applied to constantly re-phase the electron spin states (driving ω_1, ω_2). This rephasing operation commutes with the interaction operator so does not interfere with the two qubit gate. (g) deactivation of the two qubits following re-swapping electron and nuclear spins and a final Hadamard gate for the target nuclear qubit to complete the CPHASE to CNOT mapping.

nuclear spin independently from the control qubit nuclear spin by shifting its resonant frequency from ν_1 to ν_2.

- The control qubit nuclear spin undergoes a Hadamard gate $\hat{H}$, driven at its new resonant frequency ν_2 (Figure 6.12(c) – brown arrow). This exchanges the X- and Z- projections of the n_1 qubit state.

- The control qubit n_2 is activated by loading an electron e_2 (Figure 6.12(d)). To suppress electron-electron spin interaction until it is desired, a continuous magic angle spin-spin decoupling pulse sequence[214]* may be applied during the loading time.

- Electron and nuclear spin states are swapped, transferring the qubit coherences from nuclei to electrons. This is done with a sequence of three electron-nuclear CNOT gates[178] (between n_1 and e_1 and between n_2 and e_2 as indicated in the yellow shaded regions in the centre strip of Figure 6.12), consisting of 3 pulses timed to execute π rotations, driven at resonance frequencies ν_2, ω_2, ν_2 in that order (Figure 6.12(e) – blue, green, purple arrows)

- At this point the quantum information is transferred onto the electron spin states and the interaction between qubits has begun. By virtue of the initial inversion of the control electron e_1, the two nuclear spins now occupy orthogonal eigenstates $(n_1 : |\Uparrow\rangle ; n_2 : |\Downarrow\rangle)$ which means the two electron spins' resonant frequencies are detuned from one another $(e_1 : \omega_1; e_2 : \omega_2)$. This detuning effectively suppresses electron flip-flops (as would occur in the case of a SWAP-type gate), and only phase is accumulated via the dipole interaction. The accumulation of phase on the target qubit depends on the Z-projection of the control qubit, which appears as an effective magnetic field component adding to or subtracting from B_0 (Fig-

* magic angle decoupling is a well-known NMR technique using a pulse sequence to achieve a time-averaged interaction Hamiltonian of zero $\langle H_{dd} \rangle = 0$. There are numerous families[215] of pulse sequences capable of averaging the dipole-dipole interaction of the two electrons to zero.

ure 6.12(f)). Thus the interaction achieves a controlled-Z rotation:

$$\widehat{CPHASE} = \begin{pmatrix} 1 & 0 & 0 & 0 \\ 0 & 1 & 0 & 0 \\ 0 & 0 & 1 & 0 \\ 0 & 0 & 0 & -1 \end{pmatrix} \tag{6.31}$$

accumulating a relative phase of π after a time $T_{\text{CPHASE}} \sim 250\mu$s. During the interaction period, the dephasing effect of any inhomogeneity in B_0 can be corrected by applying a Carr-Purcell spin echo sequence of refocusing electron X rotations*. This is possible because the X-gate commutes with the Control-Z interaction, and so we ensure that the electron qubit dephasing is limited by the longer T_2 time (> 1ms) in preference to the bare $T_2^* \approx 270\mu$s dephasing time[38].

- after the interaction period the electron-nuclear states are swapped back with a repeated ν_2, ω_2, ν_2 sequence of conditional π pulses, storing the computational qubit states back into the nuclear spins.
- the final Hadamard gate $\hat{H}$ is applied to the target nuclear spin n_1, addressed by ν_2 which only excites the control qubit.
- the target and control qubits are de-activated by sequentially removing the two electrons (Figure 6.12(g))

As spin control is carried out by global RF and MW fields, the CNOT gate can be carried out on many pairs of qubits in parallel through the multiplexed control lines. The activation of the target qubit followed by the control qubit occurs in sequential steps and hence can be carried out on neighbouring qubit cells.

Provided the overall electron-electron interaction strength J is much smaller than the hyperfine interaction A, the same pulse sequence applies to a CNOT gate mediated by exchange interactions. With the control qubit and target qubit having distinct transition frequencies, this CNOT gate design also allows for the inclusion of an interaction correction protocol, for example, BB1-based schemes[138,216], or other optimised control sequences[217,218] which can provide robustness to unknown variations in the spin-spin

* The CP refocusing sequence is a simple extension of the Hahn echo, consisting of $\hat{X}$ operations repeated at times $(2k-1)\tau_{CP}$ for a chosen integer k, where τ_{CP} satisfies $(2k)t_{CP} = T_{CPHASE}$

interaction (dipole or exchange), and provide additional protection against any residual uncertainty in donor placement precision. These are optimisations, and beyond the scope of this thesis.

We have described the full sequence required to perform a CNOT gate between two physical qubits encoded in the nuclear spins of donors in our 2D array. We now discuss the details of the operating points in terms of realistic gate voltages.

6.3.5 Electrostatic requirements of the one and two qubit gates

To understand the level of gate control required for the selective activation/deactivation of individual donor qubits and pairs of adjacent donor qubits, we carried out 3D simulations of the electrostatics of our proposed control structures. As a starting point, it is known that the built-in electric field due to the presence of highly doped donor-defined gates modifies the bound state wavefunction within the donor Coulomb potential wells, raising its ionization energy $\sim$ 80meV above the conduction band edge at equilibrium as has been observed in a single atom transistor[53,113]. Hence, we assume that at zero gate bias all qubits are expected to be in the ionised memory state.

From this starting point we calculate the shift in energy of every charge state in response to variations of the voltages on the control lines. The process consists of two stages: first, computing a capacitance matrix by solving the Poisson equation numerically over the array geometry; and second, simulating a charge stability map with the constant interaction model to give a sense of realistic voltage levels needed to activate qubits and operate the array as we intend. This is a fully classical model, and does not account for the true quantum mechanical binding energies. The method has proved to be an accurate way of predicting device characteristics in donor defined nanostructures[107,111].

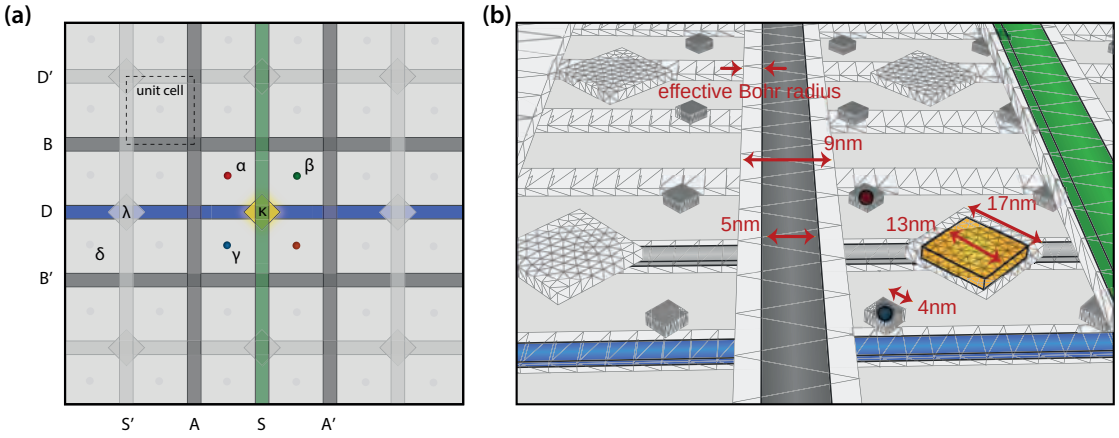

Figure 6.13: Modelling the capacitive coupling between elements of the donor array. (a) A limited model of the full 2D array consisting of 36 unit cells, and 59 electrical elements in total. We compute the strength of capacitive interactions on the full set of elements shown, and then using the resulting capacitances, model the electrochemical potential of the coloured (non-faded) set of control lines, donors and SETs. (b) A representation of the panellised geometry used as input to the FastCap2 capacitance solver. Dimensions are shown, and we expand the lithographic dimensions to account for the $\sim$ 2nm Bohr radius of electrons in silicon.

Computing the capacitance matrix of a small array

The Maxwell capacitance matrix:

$$C = \begin{pmatrix} C_{\Sigma 1} & -C_{12} & \dots & -C_{1m} \\ -C_{21} & C_{\Sigma 2} & & \\ \vdots & & \ddots & \\ -C_{m1} & & & C_{\Sigma m} \end{pmatrix} \tag{6.32}$$

may be calculated for any physical arrangement of m electrically independent conductors within a dielectric medium. The general algorithm for determining the full set of coupling capacitances C_{ij} and self capacitances $C_{\Sigma i}$ involves solving the Poisson equation $\nabla^2 V = \frac{\rho}{\epsilon}$ in order to compute the total charge induced on each conductor i ($Q_i = \int_i \rho$) in response to a change in the electrostatic potential of each conductor, V_j. We use the FastCap2 solver[219] to numerically evaluate C. The software decomposes the surface of each conductor into discrete 2D panels, and uses a multi-pole expansion to efficiently compute the total electrostatic potential at each panel.

Consider, as shown in a Figure 6.13(a) a single SET island (yellow) and its four

Elements	C_{ij}	Value (aF)	C_{ij}	Value (aF)
donor-SET	$C_{\alpha\kappa}$	0.625	$C_{\alpha\lambda}$	0.095
donor-SET	$C_{\beta\kappa}$	0.625	$C_{\beta\lambda}$	0.013
source-SET	$C_{S\kappa}$	1.01	$C_{S\lambda}$	0.211
gate-SET	$C_{A'\kappa}$	0.66	$C_{A'\lambda}$	0.080
donor-source	$C_{S\alpha}$	0.235	$C_{S\beta}$	0.235
donor-source	$C_{S'\alpha}$	0.093	$C_{S'\beta}$	0.024
donor-gate	$C_{A\alpha}$	0.256	$C_{A\beta}$	0.085
donor-donor	$C_{\alpha\beta}$	0.064	$C_{\gamma\beta}$	0.018
donor-donor	$C_{\delta\alpha}$	0.005	$C_{\delta\beta}$	0.001

Table 6.2: Electrostatic capacitances in the surface code array. Simulated capacitances in attofarads (10^{-18}F), between selected pairs of elements as marked in Figure 6.13. Donors: $\alpha, \beta, \gamma, \delta$; SET islands: κ, λ; control lines: S, S', A, A'.

surrounding donors (red, blue, green and orange). To be sure we capture all relevant interactions and avoid boundary effects, we also include qubit unit cells surrounding the four central cells, out to next-nearest neighbours – 36 cells in total. We build a geometric model of this small sample of the 2D array, composed of a number of 2D panels defining the boundaries of conducting elements. A representation of the panellised input geometry is shown in Figure 6.13(b), where we extend the size of the STM patterned structures by the Bohr radius of an electron in silicon, to represent the extent of the electronic wave function. Here the geometric parameters used are: Bohr radius = 2 nm, mono-layer gate width = 5 nm, SET island = 13 x 13 nm^2, donor-SET distance = 15 nm, planar gate pitch = 30 nm, and gate layer separation in the vertical direction = 40 nm. Then using FastCap2 we generate the full capacitance matrix considering such an array of 36 unit cells, comprising 36 donors, 9 SET islands, and 14 control lines – 59 elements in total. Representative capacitance values are provided in Table 6.2.

Current STM lithography techniques allow P donor placement with an accuracy to within 1-2 lattice sites ($<$ 1nm)[53], so ultimately we must consider the effect of the positional uncertainty on electrostatic gate coupling. We varied the individual donor positions by ±1nm in the x- and y-directions and find that only a small variation occurs in the coupling capacitances: $\sim$ 5% in $C_{P-\mathrm{SET}}$ the SET to donor coupling; $\sim$ 1% in

$C_{P-\mathrm{S/D}}$ the source/drain line to donor coupling; and $\sim 0.5\%$ in $C_{P-\mathrm{G}}$ the gate line to donor coupling.

In the output C matrix, there are many vanishingly small entries, since nearby elements screen the electric field of more distant ones, and thus interactions with nearby elements dominate the electrostatics. This allows us to make a simplification and use a smaller sub-matrix for the second part of our analysis. We retain all 14 control lines but only the single central SET and 4 surrounding donors for the subsequent constant interaction model ground-state mapping, reducing the matrix size to 19×19.

Simulation of the charge stability diagram with realistic gate voltages

A breakdown electric field threshold of $\sim$ 10MV/m has been observed in experiments using mono-layer Si:P nanostructures[56,65]. Therefore, we anticipate a gate pitch between parallel nanowires in each plane of 30 nm will safely allow an operational voltage bias range of $\pm$250mV. We show in this section that one-qubit and two qubit gates can be achieved well within this limitation, opening the possibility for closer qubit placement. This is done by identifying the combinations of the bias voltages applied to source, drain, and gate control lines at which electrons can be selectively loaded/unloaded from an SET island to activate/deactivate single qubits at a targeted position, without activating/deactivating neighbouring qubits, as well as bias points for activation of a second adjacent qubit as required for the CNOT gate.

We consider the electrostatic energy in a particular charge state represented by an integer vector $\vec{n}$ listing the number of electrons on each of the 4 donors and the central SET (which we collectively term charge-islands), and under gate voltage conditions represented by a vector $\vec{V}$ listing the voltages on all the 14 control-lines. The total energy can be written[67] as:

$$E = \frac{1}{2}\vec{Q}^T C_{nn}^{-1}\vec{Q} \tag{6.33}$$

$$\vec{Q} = C_{nV}\vec{V} - q_e\vec{n} \tag{6.34}$$

where the vector $\vec{Q}$ describes the total induced charge on each of the charge islands, composed of an integer number of electrons of charge q_e, plus capacitively induced charges due to voltages on each of the control-lines (and $\vec{Q}^T$ is the transposed vector). The ma-

trices C_{nV} and C_{nn} are sub-blocks of the complete capacitance matrix C. $C_{nV} = C_{Vn}^T$ describes charge-island to control-line capacitances, C_{nn} charge-island to charge-island mutual capacitances, and C_{VV} the cross capacitances between control lines.

$$C = \begin{pmatrix} C_{nn} & C_{nV} \\ C_{Vn} & C_{VV} \end{pmatrix} \tag{6.35}$$

The expression in Equation (6.33) does not consider the effect of tunnel coupling within the system of charge islands, so we make one a modification to the C_{nV} matrix. Additional electrons are provided to the system of 5 charge-islands (SET and 4 donors) from the source and drain nanowires, and this means these control lines $l = S, D$ have a strong effective lever-arm $\alpha'_{il} = 1 - C_{il}/C_{\sigma i}$ over the islands i they are indirectly tunnel-coupled to. To include the effect of tunnel coupling into our model we replace each $C_{il} \to \bar{C}_{il} = C_{\sigma i} - C_{il}$.

The C_{nn} sub-block must be inverted to compute the total energy, then given the inverse C_{nn}^{-1} we simply iterate through the set of possible charge states $\vec{n}$ to find the lowest energy charge state at every point in a set of gate voltage coordinates $\vec{V}$. By marking the boundaries between different charge ground states we produce a simulated gate-space map.

Figure 6.14(a) shows a schematic of the area surrounding an SET and its four tunnel-coupled donors, each colour-coded to the simulated gate-maps in the other sub-figures. We define plunge and tilt voltage axes representing the following combinations of bias voltages on the control lines:

$$V_{\text{plunge}} = V_S - V_{SD} = V_D \tag{6.36}$$

$$V_{\text{tilt}} = 2V_{G_A} = -2V_{G'_A} = V_{G_B} = -V_{G'_B} \tag{6.37}$$

The effect of these two voltage combinations can be seen in the simulated gate-space map of Figure 6.14(b).

As we reduce V_{plunge}, moving down along the left edge from 0, we observe a series of yellow lines (I, II), each indicating an additional electron being added to the SET. With $V_{\text{tilt}} = 0$, the equal capacitive coupling of each of the four donors (red, blue, green and orange) to the lines S and D means that at a point around $V_{\text{plunge}} = 15$ (marked III) the four donors are activated essentially all at once, with no addressability. In order

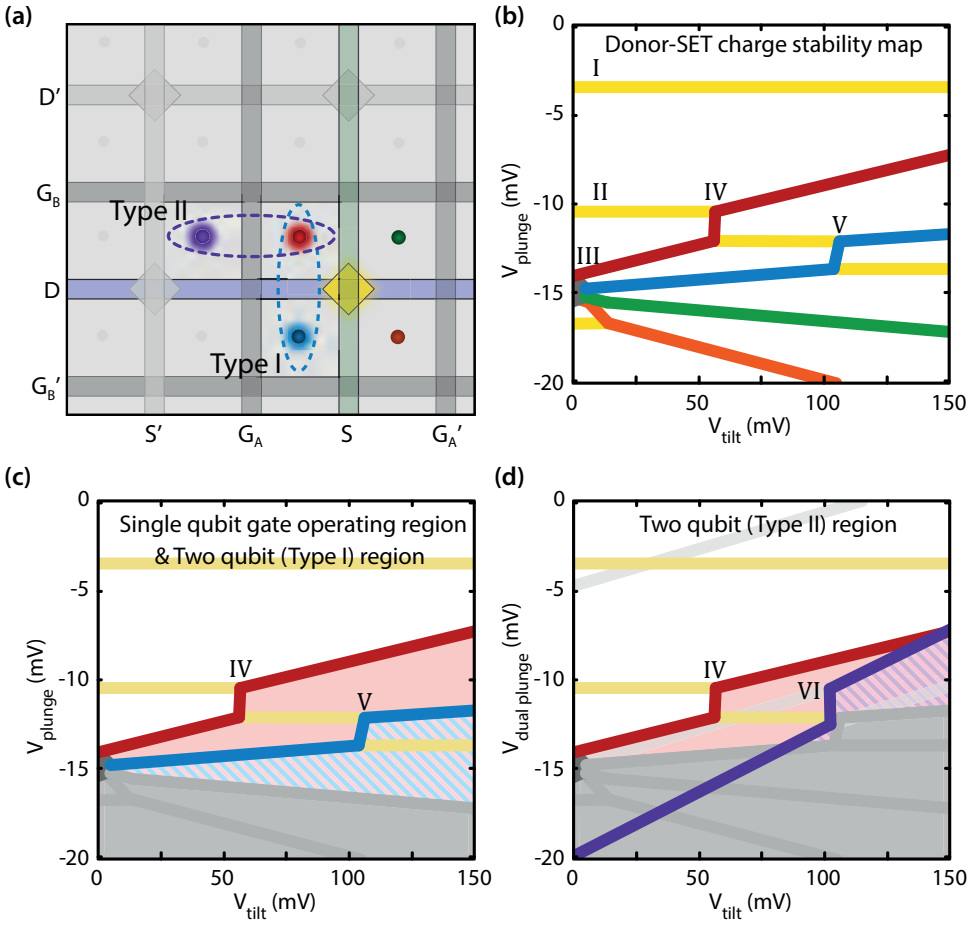

Figure 6.14: Gate voltage conditions for one and two qubit gates. (a) Colour-coded diagram indicating the four donors surrounding a single SET island, and an additional donor (purple) in the neighbouring SET-cell. Two types of 2-qubit gates are marked, 'Type I' where both donors share an SET island, and 'Type II' where each donor gains its electron from distinct SET islands. (b) Simulated charge stability map. Decreasing V_{plunge} adds electrons to the yellow SET (on crossing lines I and II). Increasing V_{tilt} preferentially loads an electron to one of the four donors. In this case the red donor is activated first (on crossing the red line at IV), followed by the blue donor (on crossing the blue line at V). (c) The gate-space region where the red qubit is activated, and all others ionised is shown shaded red. The blue hashed area denotes that both red and blue qubits are activated, and it is in this region that a CNOT gate (of 'Type I') would take place. (d) The purple line shows the loading condition for the purple donor to gain an electron from its local SET island (greyed out on the left of (a)), and thus the hashed purple area is suitable for the 'Type II' CNOT gate.

to select a particular single donor to load an electron to, we increase V_{tilt}, *tiliting* the electric potential so that the charge transition potential for the red donor is lower than the other three. We see that as we move to the right, the loading lines for the four donors separate so that we can preferentially load an electron onto any individual donor using voltages well inside the ±250mV limit discussed above. In this case, an electron loads from the SET to the red donor moving to the right across the red line at IV, and a second electron is loaded onto the blue donor at position V.

Loading, unloading and electron spin readout will always be carried out at the so-called triple-points, where the electrochemical potentials of donor, SET, and source and drain lines are equal. These are the intersection of yellow and red, or yellow and blue lines in Figure 6.14(b). The order of the separated load potentials can be modified to select whichever donor we choose by permuting the polarity and strength of each gate in the definition of V_{tilt}*

Figure 6.14(c) indicates the operating region for a single qubit gate on the red donor. The requirement is simply that the red donor is occupied (in the 'Active' mode) and all other surrounding donors remain ionized (in the 'Memory' mode) – this Coulomb blockaded configuration corresponds to the red shaded area. Beyond the blue line the neighbouring donor marked as blue in (a) will also load, and within the grey regions multiple other unwanted donors become activated.

From an electrostatic perspective there are two classes of two-qubit gate configurations. We label these: 'Type-I', for pairs of donors who share a single SET (blue and red in Figure 6.14(a)); and 'Type-II', for pairs of donors that do not share an SET (purple and red in Figure 6.14(a)).

- In the 'Type-I' case (shown in Figure 6.14(c)), the requirements for the CNOT gate can be met by loading the red donor at its triple point (marked IV), moving into Coulomb blockade in the red shaded area to apply ESR on the CNOT-target electron, loading the blue CNOT-control qubit at its triple point (marked V), and then moving into the blue shaded blockade region, where the dipole-dipole interaction is present, for all remaining ESR and NMR pulses. Importantly our simulation shows that the CNOT-target donor is not ionised at any point during the CNOT operation sequence.

* For example, instead defining $V_{\text{tilt}} = -V_{G_A} = V_{G'_A} = 2V_{G_B} = -2V_{G'_B}$ would load first green, then red, orange, and finally blue.

- To achieve the same stability for the 'Type-II' class of interacting qubit pairs, we must adjust the definition of V_{plunge}. To access the purple qubit loading potential, we additionally plunge the potential of the western neighbour SET with the neighbouring source line (marked S' in (a)), but by a lesser amount than for the first source (S). We plot in Figure 6.14(d) the effect of this dual plunge with $V_{\text{dual plunge}} = V_S - V_{SD} = V_D = 2.2V'_S$, where the factor 2.2 is selected such that the purple donor readout triple point (marked VI) falls between the red and blue qubit loading lines. This facilitates the two-qubit CNOT gate on the red/purple pair, without loading the blue donor or any other. Here the dipole interaction is present within the red/purple hashed shaded region.

We anticipate that further optimisations to this basic biasing scheme are possible; however, the current simulation results indicate that our gate pulsing scheme, with modest voltages and robustness against small variations in donor positioning, is suitable for implementing the surface code on our multi-layer architecture

6.3.6 Preserving phase coherence during ionisation events

Having established the process for activating/deactivating qubits, we now consider these operations from the standpoint of the quantum information encoded on the donor nuclear spin. This is critical, as the addition and removal of an electron subjects our physical qubit to a time-varying Hamiltonian. The activation (and deactivation) process, governed by donor $\leftrightarrow$ SET island electron tunnelling, is key to qubit addressability and therefore the operation of the array to implement the surface code. With donor placement to near single atomic site precision[53], the mean tunnelling time between donor and SET island, τ, can be engineered from nanoseconds at $\sim$ 10nm[1] to tens of milliseconds at $\sim$ 20nm[55]. However, in addition to variations in the characteristic tunnel rate due to donor placement, quantum tunnelling is a naturally stochastic and non-adiabatic process. As soon as the electron is present on the donor (in the 'Active' mode), the qubit nuclear spin begins to acquire phase (at a well defined rate) due to the hyperfine interaction A. If the time at which the electron tunnels to the donor is not known, because of the stochastic nature of the tunnelling process, the abrupt change in A gives

rise to an unknown phase accumulation on the donor qubit state and can be a source of dephasing.

It is possible to engineer tunnelling rates to be faster than the hyperfine interaction; however, this could be problematic for achieving high-fidelity readout, as the same tunnel rate would apply to the readout signal, and state-of-the-art SET measurement bandwidth[220] is at the level of $\sim$ 20MHz, an order of magnitude lower than the hyperfine interaction at $A \sim 117$MHz. Instead, we propose using a more modest ($1/\tau = 1 - 10$MHz) tunnel rate, and we introduce the concept of a phase matched (PM) pulsed loading/unloading sequence.

Timing considerations

Within a time t, a qubit in the 'Memory' mode (an ionised donor nuclei) will acquire (in the laboratory frame) a phase

$$\varphi(t) = 2\pi\nu_0 t \tag{6.38}$$

An 'Active' qubit on the other hand will accumulate

$$\varphi'(t) = 2\pi\nu_1 t \tag{6.39}$$

$$= 2\pi(\nu_0 + \frac{A}{2})t \tag{6.40}$$

$$= \varphi + \pi A t \tag{6.41}$$

Then we define a phase matching condition:

$$\varphi'(t) = \varphi(t) + 2n\pi \tag{6.42}$$

for integers n. Then for values of t when Equation (6.42) is satisfied, the phase of a neutral or ionised nuclear spin differ by a multiple of 2π. If we only allow electrons to tunnel when this condition is satisfied, the issue of phase accumulation is resolved. Solving Equation (6.42) gives $t_A = 2/A \approx 17.1$ns.

Thus we must only permit electrons to tunnel during a small time window around $t = nt_A$, defined by Δt, a duration short compared to t_A. We indicate in Table 6.3 realistic values for the various timescales referred to in this section. Since $\Delta t << \tau$, the electron

Timescale	Description	Nominal Value	Notes
t_A	PM period	17.1ns	fixed at $2/A$
Δt	tunnelling window	$0.1 - 1.0$ns	pulse parameter
τ	electron tunnel time	$0.1 - 1.0\mu$s	set by physical distance
T_{PM}	total PM sequence	$50 - 200\mu$s	pulse parameter
t_{read}	readout time	$2 - 10\mu$s	pulse parameter
t_{unload}	unload time	$2 - 10\mu$s	pulse parameter
M	number of cycles	$50 - 1000$	pulse parameter

Table 6.3: Phase matched loading and unloading timescales. Nominal values are provided, although most variables are parameters that may be modified as required to meet a desired error rate.

must be presented many short opportunities to tunnel, and must be effectively frozen for the intervening time. The PM scheme thereby restricts the stochastic tunnelling events to be synchronous with the natural phase cycle of the qubit. The activation/deactivation process is now semi-deterministic — one does not need to know exactly when the electron tunnelled, only that the PM sequence is long enough for the probability of tunnelling, integrated over many, M, short Δt windows, to be high. This requires a total duration for the PM sequence of $T_{PM} = Mt_a$, where the condition $M\Delta t >> \tau$ ensures that the total time allowed for tunnelling exceeds the characteristic tunnel time τ. A second requirement is that the residual phase error:

$$\epsilon_\varphi = \int_0^{M\Delta t} e^{\frac{t}{\tau}} \Xi(t) dt \tag{6.43}$$

$$\sim \frac{\pi^2}{3} \left(\frac{\Delta t}{t_A} \right)^2 \tag{6.44}$$

should be low with respect to the surface code error threshold. Here the exponentially decaying tunnelling probability is multiplied by the phase error function Ξ which is a sawtooth of period Δt:

$$\Xi(t) = \frac{2\pi\Delta t}{t_A} \left(\frac{t}{\Delta t} - \left\lfloor \frac{t}{\Delta t} \right\rfloor - \frac{1}{2} \right) \tag{6.45}$$

Qubits being activated/deactivated in parallel may individually load/unload at dif-

ferent times within the PM sequence; nevertheless, the phase matching condition is maintained for every qubit, so by timing all pulses with respect to a common clock, qubit phases will remain synchronous across the entire array. This property provides a high degree of robustness to variations in the characteristic tunnelling time for electrons to move to and from each donor. The exact time τ is not important so long as T_{PM} is long enough to allow electrons to move at the donors with slowest τ times.

Phase matched load sequence

In order to maintain control of the phase of our physical qubits (encoded in the nuclear spins) during ionisation events, we define two additional intermediate modes in addition to 'Memory' and 'Active', a 'Load/Read' mode and an 'Unload' mode. We add and remove electrons by carefully switching between these modes following the timing sequences shown in Figure 6.15(a). The gate voltages required for each mode are indicated in Figure 6.15(b), and the electrochemical potential configurations in each mode are represented in Figure 6.15(c-f).

Coloured dots indicate the relevant gate bias conditions on the charge stability map of Figure 6.15(b) around the donor-SET inter-dot transition (a small region of the gate-space around the point IV from Figure 6.14(b)). Charge state labels (in grey) indicate the electron occupancy of the donor and SET in each region. Solid teal and pink lines represent the loading potentials for $|\downarrow\rangle$ and $|\uparrow\rangle$ electrons respectively, and yellow lines the condition for current to flow through the vertical SET at the degeneracy point between N and $N+1$ electron occupancy states of the SET island. Positions of the 4 modes of operation are marked 'Memory','Load/Read','Active', and 'Unload' and colour-coded to Figure 6.15(a). We now describe the procedure:

Memory Between operations, donors are kept idle in the 'Memory' mode (Figure 6.15(c)). Here the SET is occupied by n electrons; the source and drain Fermi levels (grey continuum of states, right of the figure) are offset by a small bias V_{SD} and they lie between the $n-1 \leftrightarrow n$ SET charge transition (lower solid yellow line) and $n \leftrightarrow n+1$ SET charge transition (upper solid yellow line), and also below the donor loading potential, for both Zeeman states (teal and pink). The stable charge configuration in this mode is $(0, N)$.

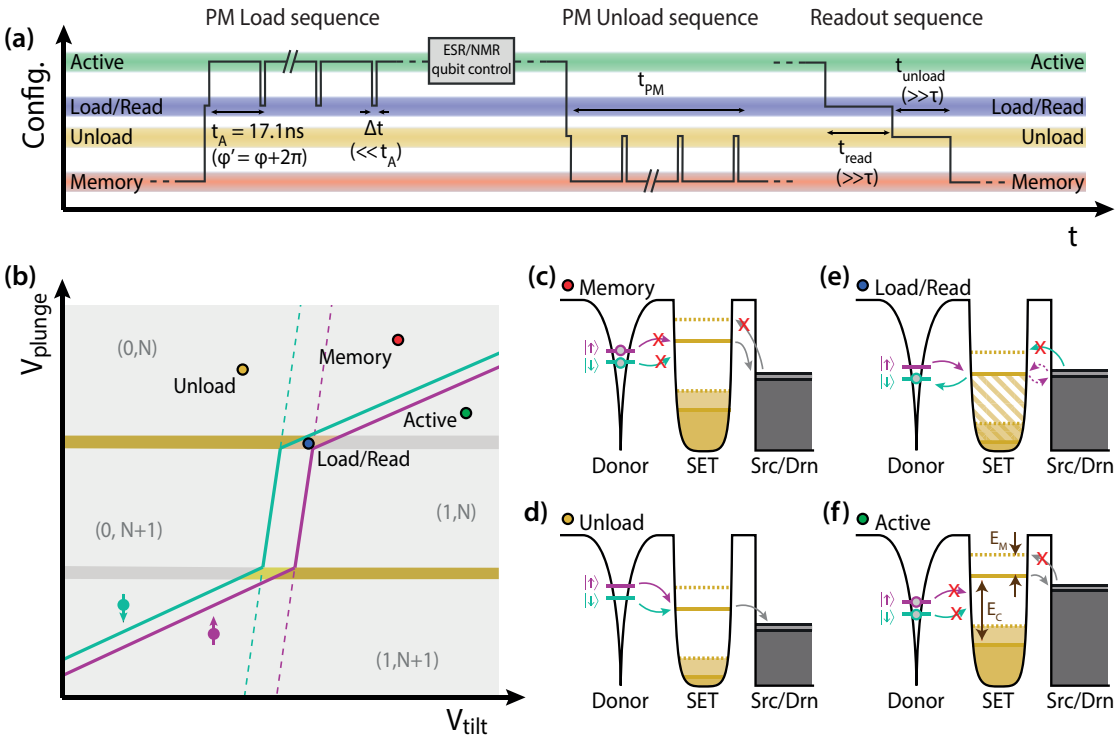

Figure 6.15: **Phase Matched tunnelling scheme, facilitated by the interplay of Coulomb and Zeeman energies.** (a) Sequence of events defining phase matched (PM) load and unload operations, as well as phase agnostic qubit readout. (b) shows schematically the location of the required bias points on a charge stability diagram corresponding to 'Memory', 'Active', 'Load/Read', 'Unload' modes. (c-f) energy level diagrams for the 4 configurations, schematically showing the electrochemical potentials for transitions involving donor Zeeman states, SET island charge states and the Fermi energy of source and drain lines (Src/Drn) for each case. Dotted yellow lines indicate the SET charge transition potentials when an electron is present on the donor, and solid lines indicate transition potentials when the donor is ionized. The hashed region in (e) represents constant switching of the charge state while current flows through the SET. Allowed electron motion is indicated by small arrows, coloured if the tunnelling is spin dependent, grey otherwise. Energetically forbidden electron motion is indicated with red crosses.

Load The PM load sequence begins by moving to the 'Load' configuration (Figure 6.15(e)) for a time Δt. In this arrangement of energy levels an electron may move from source to SET island to drain and so SET current flows (pink dashed arrows), since the $N \leftrightarrow N+1$ potential lies within the source-drain bias window. We assume a strongly coupled vertical SET, where the timescale for this source/island/drain tunnelling is fast compared to Δt, so the $N+1$ SET state is occupied with high probability as indicated by hashed yellow shading up to the resonant transition. The characteristic tunnel time from SET to donor is, however, slow compared to Δt, so although filling of the spin-down donor state is energetically allowed (blue arrow), it is improbable during the first load pulse.

Active The system is next pulsed to the 'Active' configuration (Figure 6.15(f)), and held there for a time $t_a - \Delta t$ until the next phase-matched time window. Assuming the donor has not yet loaded, the additional SET electron will quickly tunnel out to source or drain since it is positioned above the Fermi energy (grey arrow).

Toggle The 'Load' and 'Active' phases repeat M times and at some point during a 'Load' phase (Figure 6.15(e)), an electron will move from SET island to donor (blue arrow). Note that only the spin-down state can load onto the donor due to the Zeeman splitting. The SET size we propose (13×13nm) is in the regime of small orbital energy separation ($\Delta E \sim 250\mu$eV*), providing a quasi-continuum of electron states at the SET's Fermi level. Solid yellow lines in the electrochemical potential diagram of Figure 6.15(e) represent only the electrostatic charging energy $E_C >> \Delta E$. Once the donor is loaded with one electron, the repulsive Coulomb potential adds as additional mutual charging energy E_M, which raises the SET potential to the dotted line, which sits above the level of the source and drain Fermi energy, so that a second electron cannot load onto the SET. Importantly, the 'Active' configuration of Figure 6.15(f) is stable also once the donor is loaded. This bi-stable behaviour, critical to our PM sequence, relies on the large charging energy of the SET E_C, which prevents the donor electron from being able to tunnel back through the SET to the source or drain.

* using a simple particle in a box approximation: $\Delta E \sim \frac{\pi\hbar^2}{gm^*L^2}$ with spin and valley degeneracy $g = 12$, electron effective mass $m^* = 0.28m_e$ and box length $L = 17$nm

Active (ESR/NMR control) At the completion of the PM load operation, the qubit is kept in the 'Active' configuration for all ESR or NMR driven spin manipulations required to execute the desired single- or two-qubit gates.

Phase matched unload sequence

The PM unload proceeds in an analogous way, switching between 'Unload' Figure 6.15(d)) and 'Memory' (Figure 6.15(c)) modes as indicated in the timeline of Figure 6.15(a), in order to preserve the nuclear spin phase. In a similar way to the 'Active' mode, the 'Memory' mode is stable both when the donor is occupied and when it is not, so we are not concerned that probabilistically it takes many cycles before the electron will tunnel out to the SET.

Phase agnostic spin readout

Electron spin readout occurs with the same state configuration as for 'Load' as shown in Figure 6.15(e). For a 'Read' operation however, we do not require phase matching, since the electron readout is part of a projective measurement of the nuclear qubit in the Z-basis, and therefore its phase information is no-longer meaningful. We perform a simple continuous readout step with a duration t_{read} longer than the tunnel rate τ. A $|\uparrow\rangle$ electron will tunnel to the SET (pink arrow in Figure 6.15(e)), lowering the SET potential by the mutual charging energy so that it lies inside the source-drain bias window, and thereby switching on the SET current for some time (pink dashed arrows), before a $|\downarrow\rangle$ electron re-occupies the donor switching the SET back off (blue arrow). This short-lived current response is the signal indicating measurement of a $|\uparrow\rangle$ state, and does not occur if the electron is projected as $|\downarrow\rangle$. The electron spin readout mechanism is identical to the 'spin dependent unload' presented in detail in Section 5.3.2 of Chapter 5. Since the equilibrium groundstate of the 'Load' mode is a donor occupied by a $|\downarrow\rangle$ electron, the electron spin readout step is followed by a single 'Unload' step of duration $t_{\text{unload}} \gg \tau$ to ensure the donor is ionised before returning to the 'Memory' mode. The full timing sequence is shown on the right-side of Figure 6.15(a).

6.3.7 Naturally parallel surface code stabiliser operations

We now move on to a demonstration of the parallel operation of X- and Z-stabiliser operations, the bread and butter of the surface code. These operations must occur with a high degree of parallelism over the array to capture the high threshold of the surface code. Our physical layout and shared control lines mean that our design is naturally suited to such parallel operation. Because the 'Type II' CNOT gates involve two neighbouring SET islands, we cannot act on every Z-plaquette (or X-plaquette) at once – the gate voltages would interfere with one another. Therefore we work with one in every 4 plaquettes simultaneously, as highlighted by red borders in Figure 6.16(a), which shows a schematic of the surface code plaquette operators. To carry out the complete set of all Z-stabilizer measurements across the entire lattice, we therefore need only four stages, independent of the number of qubits. With four more stages the full set of X-stabilisers can also be completed.

A local Z-stabilizer measurement in the syndrome extraction process involves a sequence of four CNOT gates between any given ancilla qubit (CNOT target) and its four neighbouring data qubits (CNOT controls), sequentially cycling north, west, east, and south, followed by measurement of the ancilla. In terms of the basic operations within our architecture: phase-matched electron loading/unloading, global electron/nuclear control, electron dipole-dipole mediated CNOT interactions, and ancilla readout; we show in Figure 6.16(b) the sequence of steps for a Z-stabilizer measurement, with time running left to right. The X-stabilizer case is similar in the essentials, and only differs in that the control and target qubits are switched for the data-ancilla CNOT gates, and the interactions are sandwiched by Hadamard operators on the ancilla, as we showed in Section 6.1.3.

Figure 6.16(c-g) shows how the individual steps within one stage of Z-stabilizer operators proceeds in a parallel fashion:

- Based on the outcome of the previous round of stabiliser measurements, all ancilla qubits are initialised to $|0\rangle$. This can be done in parallel by deterministically loading electrons $|\downarrow\rangle$, swapping the electron and nuclear states, and using a global rotation to leave the ancilla nuclear qubit $|\Uparrow\rangle = |0\rangle$ (not shown in figure).

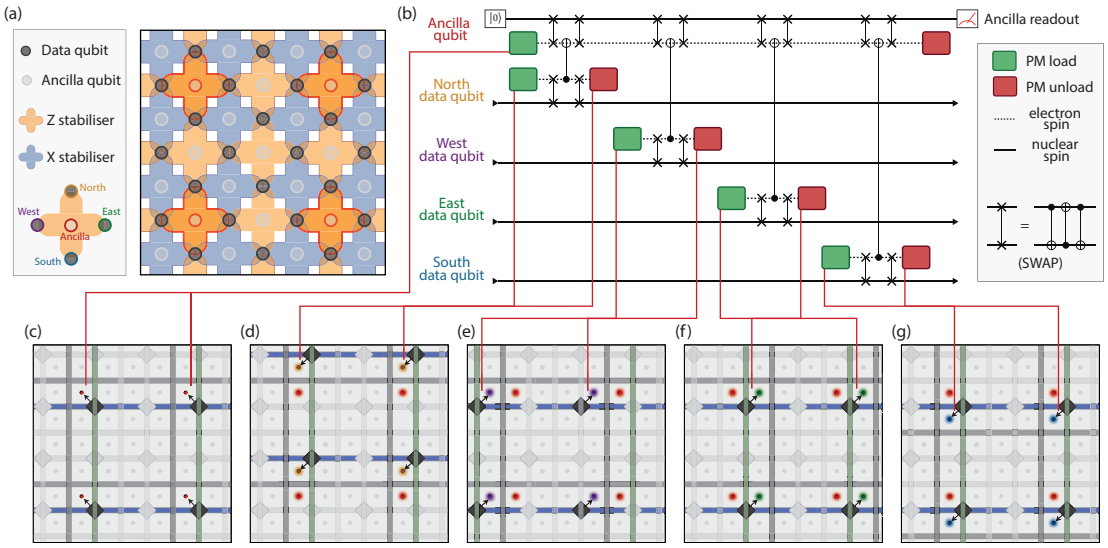

Figure 6.16: Parallel applictaion of stabiliser operations. (a) Schematic of the surface code stabiliser plaquette layout for X and Z error correction. Stabiliser operations on the highlighted plaquettes are performed in parallel in one stage. This density of parallelism covers the entire set of plaquettes in only eight stages. (b) Single stage Z-stabiliser circuit diagram, indicating the steps required to execute the Z-stabiliser operation: interacting an ancilla qubit with its north, west, east and south data qubit neighbours, followed my ancilla measurement in the Z-basis. Solid lines denote nuclear spins, dotted lines electron spins. Green and red boxes represent phase matched loading and unloading sequences. CNOT and SWAP gates are shown by their standard quantum circuit representations. (c) Simultaneous PM activation of multiple X syndrome qubits (d) simultaneous activation of north neighbour data qubits, global electron and nuclear resonance pulses achieve the required CNOT gate, before parallel deactivation of the data qubits (e,f,g) equivalent simultaneous CNOT gates for west, east and south data qubits surrounding the X syndrome ancilla

- The set of ancilla qubits for one stage of plaquette operations (here one quarter of all Z-plaquettes) is first activated (Figure 6.16(c)). This is done using the phase-matched loading pulse sequence to preserve the initialised nuclear qubit state.

- The north neighbouring data qubits are also activated (Figure 6.16(d)), and the CNOT procedure detailed in Section 6.3.4 is performed. To summarise, the CNOT consists of: a nuclear-electron spin SWAP on both donors, the CPHASE interaction (with dynamical decoupling pulses interleaved), transformed into a CNOT operation by Hadamard transforms on the target qubit (the ancilla in this case), a SWAP back between electron and nuclear spins before the north data qubits are de-activated by unloading the electron (with PM pulsing).

- The west neighbouring data qubits are then activated (Figure 6.16(e)). As was the case for north neighbours, this is a 'Type II' configuration. The full CNOT sequence is repeated once more, and the west qubits deactivated.
- The east data qubit set is activated, the CNOT applied, and then east qubits are deactivated. Note that this configuration is an example of many parallel 'Type I' two-qubit gates.
- South neighbouring data qubits are activated, entangled with the CNOT gate, and deactivated once again.
- Finally, the ancilla qubit is deactivated. At this point, its nuclear spin is measured, by repeated electron-nuclear entanglement and electron readout as described in Section 6.3.3. This measurement is also carried out in parallel across the array

The sequence of steps is then repeated 3 more times for the other groups of Z-plaquettes in the four stage system, and an additional 4 times for the X-plaquettes. Ancilla state measurements are collated, and form the syndrome measurement used to detect the location and type of errors occurring within the array.

The analysis so far has focused on the stabilizer measurements required for one round of quantum error correction across the entire lattice and sets the basis for higher-order protocols on the surface code. Logical qubit operations are topologically more complex; however, the physical operations required of the architecture are in essence particular geometric patterns of stabilizer measurements. As we have seen, the geometric layout places some constraint on which donors can be activated in parallel; hence, not every geometric pattern can be created in a single step. For example, it would not be possible to operate on three of the four highlighted plaquettes in Figure 6.16(a) simultaneously, it would need to be done in two or three stages. This is the trade-off for multiplexing every control line across many qubits. However, simple geometric patterns, such as lines and rectangles, can generally be created in a small number of stages. More complex patterns can be created by sequentially combining these simple geometric patterns to load electrons and construct more complex regions and patterns. The required geometric patterns for the implementation of the surface code paradigm can thus be created in parallel using a finite number of steps, independent of the number of qubits. The intrusion into the error threshold, due to the reduction in parallelism for complex patterns is minimal owing to the extremely long qubit memory time of donor nuclei.

6.3.8 Gate errors and threshold analysis

To validate the operation of our architecture below the surface code error threshold, we performed numerical simulations* of each of the quantum gates within the Lindblad super-operator formalism (see Section A.7), including in the model the following potential sources of error:

Nuclear spin dephasing This is expected to be negligible on the operational timescale of our stabiliser operations. Nuclear T_2 times longer than 30s have been measured[37,38] for donors in isotopically purified ^{28}Si.

Electron spin dephasing We use an electron T_2 of 2s in the simulation, based on the extrapolated dephasing time for a single donor in a bulk environment (away from interfaces) measured in donor ensembles[117] in ^{28}Si.

Phase error in PM sequence We expect the dominant source of qubit error to be due to non-perfect phase matching during electron load and unload actions. To load the electron within a finite time, the loading window Δt cannot be infinitely short, the small random phase consequently accumulated by the nuclear spin contributes to the probability of a Z-error appearing.

We initially set aside the phase matched loading process, and analyse the 'bare' CNOT operation consisting of only the electron-nuclear SWAP, and dipole-dipole interaction time. Single-qubit operation times are $T_{\hat{X},N} \sim 21\mu$s for nuclei and $T_{\hat{X},e} \sim 10$ns for electrons. The error in these single spin rotations from electron spin dephasing is $\epsilon_{\hat{X}} \sim 5 \times 10^{-5}$. We estimated above in Section 6.3.4 the required CPHASE interaction duration as 260μs with 30nm donor separation

Combining these times we obtain a (bare – without loading) CNOT operation time $\bar{T}_{CNOT} = 2T_{\hat{X},N} + 4T_{\hat{X},e} + T_{\text{CPHASE}} \sim 300\mu$s and over this longer time, the electron dephasing leads to an increased (bare) error rate $\bar{\epsilon}_{CNOT} \sim 1 \times 10^{-3}$, which is still an order of magnitude lower than P_{th}.

* these simulations were performed by Charles Hill

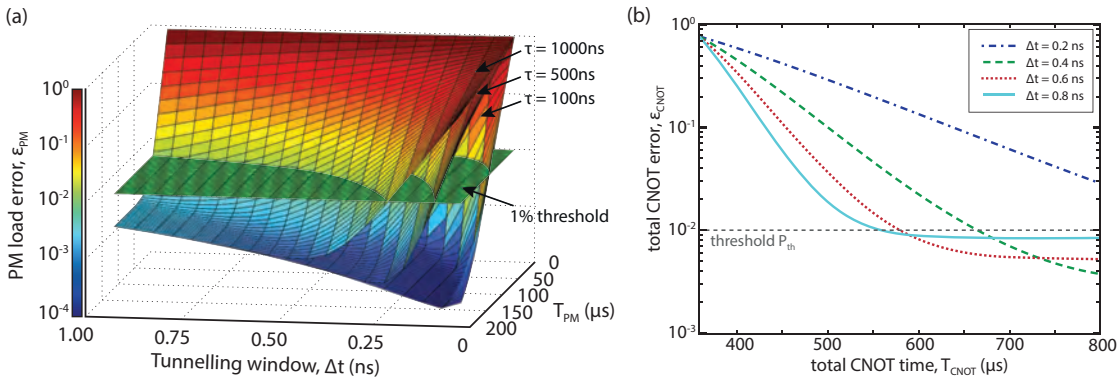

Figure 6.17: Error analysis of the PM load sequence and CNOT gate. (a) Error rate in the Phase Matched (PM) loading sequence ϵ_{LOAD}, as a function of tunnel rate τ, loading window time Δt, and total load sequence duration T_{PM}. There are regions of this parameter space with an error below the surface code error correction threshold at $\epsilon_{\text{LOAD}} = P_{th} = 1\%$ which is marked by a green plane. (b) Overall physical CNOT gate error ϵ_{CNOT} as a function of total time taken for the two-qubit gate T_{CNOT}, and calculated for different values of the tunnelling window duration Δt. Here we take a tunnel rate $\tau = 500$ns. A lower error is achievable with shorter Δt, but at the expense of a slower overall CNOT time. The threshold error rate for topological error correction, $P_{th} = 1\%$, can be reached for $T_{\text{CNOT}} > 600\mu$s.

To show the error due to the phase-matched (PM) load/unload process, we plot in Figure 6.17(a) the simulated error ϵ_{PM} due to imperfect phase matching, as a function of the pulse parameters Δt (the tunnelling window duration in each phase cycle), T_{PM} (the total load sequence time), and τ (the characteristic electron tunnelling time). The same error rate is expected for a PM unload sequence.

The results show that there is a region of parameter space, that is, values of τ, Δt, and T_{PM}, where the loading error is below the surface code's error correction threshold of 1%. Improved performance (lower error) is seen with faster tunnel rate, shorter tunnelling window, and longer total pulse sequence duration. In particular $\epsilon_{PM} < 10^{-3}$ can be achieved with $\tau \sim 500$ns, $\Delta t \sim 0.3$ns, and $T_{PM} \sim 150\mu$s. In comparison to the bare gate operation times, we see that the total single-qubit gate operation time and error rate will be dominated by the qubit activation/deactivation processes and timescales. The results also show that as long as the PM pulse train is sufficiently long, the scheme is robust against variations in the tunnelling time τ resulting from fabrication and voltage control variations.

The complete CNOT gate incorporating the PM sequences was simulated, and the resulting total error ϵ_{CNOT} is shown in Figure 6.17(b). For an SET-donor tunnel time

of $\tau \sim 500$ns, commensurate with achievable readout bandwidth on the order of tens of MHz, we have $\epsilon_{CNOT} < P_{th}$ for a range of parameters in the region $T_{CNOT} = \bar{T}_{CNOT} + 2T_{PM} \sim 600\mu$s and $\Delta t \sim 0.6$ns.

Residual uncertainties and optimisations

The CNOT gate could be made significantly faster through improvements to: charge sensitivity and readout bandwidth, donor placement precision, and any additional miniaturisation that may become possible with optimised fabrication techniques. This could allow closer placement of the donors and hence faster loading sequences and shorter interaction times, both of which will drive down the total error rate.

Potential sources of error not accounted for in our analysis include variations in the hyperfine strength A or g-factor g_e due to non-uniform electric fields from donor to donor. Up to $\sim 20\%$ variation in A has been observed in experiments[146] on single donor qubits. Any non-uniformity here may be alleviated with dynamical decoupling sequences[218,221] to refocus any uncontrolled phase accumulation due to variations in the electron and nuclear spin resonance frequencies.

A final consideration in terms of potential errors is the impact of a fabrication defect. The lack of a qubit where one is expected is a common problem faced in photonic quantum computing, and there has been much effort in developing schemes to cope with so-called loss-errors[222,223]. Importantly, any defect locations can be identified, and the topology of the code's surface modified around defective sites by a strategy termed lattice-surgery[224].

Nevertheless, with the realistic and achievable parameters presented, we have shown in this section that our architecture indeed does allow for error corrected quantum computation in a large 2D array.

6.4 Conclusions and outlook

We have proposed a scalable quantum computing architecture using a dense two-dimensional array of donor nuclear spin qubits in entirely crystalline isotopically pure ^{28}Si. In contrast to other current blueprints for scalable donor-based qubit arrays, we embrace the small size of a donor atom, and build upon recent improvements in STM-based atomic precision fabrication to position neighbouring qubits in close proximity, proposing a dense surface code array of donors placed 30nm away from one another. This permits fast ($\sim 100\mu$s) qubit interactions without the need for any long-distance coupling.

We have described how to utilise the removable electron spin as a resource to facilitate addressable single qubit nuclear spin operations, and to mediate two qubit interactions between neighbouring qubits. Relative to an ionised donor, the addition of the hyperfine coupling energy when an electron is loaded into the donor potential well shifts the qubit resonance frequency in a binary fashion, providing a means to addressably execute a particular nuclear spin operation which will act on a desired subset of all qubits in parallel across the array. When two neighbouring qubits are 'activated', with bound electrons, the dipole-dipole interaction naturally implements a controlled phase gate between the two electron spin states.

We have analysed the gate voltage requirements for one and two qubit gates, and verified that with an efficient gate design consisting of two sets of long parallel nanowires, oriented perpendicular to one-another in vertically separated layers above and below the qubit array, we are able to selectively and simultaneously operate large numbers of qubits in parallel, owing to the uniformity inherent to donor atoms. This is a remarkable result considering our design requires only $\sim 2\sqrt{N}$ control nanowires for N qubits.

In particular we have developed a novel 'phase-matched' electron tunnelling scheme, which overcomes the natural randomness in quantum mechanical tunnelling. By locking to a phase cycle with frequency proportional to the hyperfine interaction strength, the phase acquired by a nuclear spin can be made independent of the exact time at which an electron tunnels onto that donor. We have performed quantum-mechanical simulations indicating that the phase matching is a critical requirement in attaining the error threshold of 1% where the topological protection of the surface code formalism becomes

effective.

The essence of the design presented in this chapter is that the key challenges to implementing a surface code-compatible qubit array have been reduced to two basic requirements: high fidelity global ESR and NMR control pulses, and precise timing control over locally addressable electron loading and unloading processes. Our shared-control donor-based architecture thus presents a well-defined route to large-scale error-corrected quantum computing.

This is not just a great position to be in, this is truly a superposition!

Malcolm Turnbull

7 Conclusions

Atomic precision donor devices provide a promising framework for quantum computation. Building on the successes of recent years in miniaturising delta-doped quantum dots[65] to the limit of a single atom[53], the integration of charge-sensing single electron transistors (SETs)[107] to enable high fidelity spin readout[54,55], and the first steps in scaling up to multiple interacting donors[56,57], in this thesis we have made significant developments along the path toward implementing a donor-based quantum processor.

7.0.1 Summary of results

There are four themes running through the three major results chapters (Chapters 4 to 6), which we summarise below. The key concepts uniting the various results are addressability and scalability.

Radio frequency reflectometry

In Chapter 4 we investigated the benefits of alternate charge sensing methods using radio frequency (RF) signals, in particular utilising an RF-SET, and also a tunnel-coupled reservoir. We presented a hybrid device combining an RF-SET with a tunnel-coupled reservoir, and demonstrated the clear discrimination between elastic and inelastic tunnelling processes. The additional information available from the phase and amplitude of a reflected RF signal, relative to the DC conductance signal historically used to monitor electron tunnelling events, allows us to unambiguously differentiate intentionally placed donors from randomly occurring electronic trap states due to crystal defects. We showed how the effective lever arm of a tunnel coupled reservoir can be significantly greater than that possible with capacitively coupled gates, and discussed why this, combined with the much smaller spatial footprint of a single terminal makes the tunnel-coupled reservoir an attractive charge sensing tool compared to the single electron transistor in increasingly complex devices. In a double quantum dot device, we explored how using a reflected RF signal provides an accurate measure of the tunnel rates for electrons moving between a reservoir and a quantum dot. In particular we measured rates spanning over two orders of magnitude (from 1×10^8 to $1 \times 10^{10}\text{s}^{-1}$) as the number of electrons bound by a 3P donor quantum dot increases from 1 to 4.

RF reflectometry facilitates the use of a single terminal readout device, providing a promising solution to scale up our technology to the many qubit regime because it consumes significantly less physical area than traditional three terminal readout SETs or other alternatives. Furthermore, the strong coupling that we have demonstrated suggests that this can be done while retaining clear addressability over each individual qubit.

Two donor interactions

Having established the RF technique we then applied this to a two donor system to determine if we could more accurately measure the exchange interaction between two donor based quantum dots. At the end of Chapter 4 we demonstrated Pauli spin blockade within a 2P-3P double quantum dot system, where we measured the strength of the tunnel coupling between the two potential wells to be $\sim 47 \pm 5\mu$eV, significantly more accurate that direct transport measurements where the error was found to be $\sim 150\mu$eV.

We also showed that the electron exchange energy could be varied from 20μeV to 120μeV as the potentials of the two quantum dots are detuned. A controllable exchange energy is one way of constructing a two qubit gate, and in Chapter 5 we introduced a different two qubit double quantum dot device, now with an integrated SET charge sensor. After careful analysis of the charging energies, we identified one qubit as a single P donor, and the other as a 2P molecule. Using the SET tunnel coupled to the qubits, we demonstrated initialisation and high fidelity ($> 96\%$) single shot readout of the electron spin states of both qubits. We measured the electron spin relaxation time T_1 independently for the two qubits and verified that the two spin states can be isolated from one another. Importantly we were able to show that by detuning the potentials we were able to controllably switch on a strong exchange interaction between the two electrons, resulting in anti-correlated spin states. The ability to switch on and off the interaction between qubits is a fundamental starting requirement for a scalable quantum processor.

Single electron spin control

Following careful theoretical consideration of the transmission of a microwave frequency signal to the donor atoms within a precision donor qubit device, we fabricated a broad-band microwave antenna on the surface of the 1P-2P two qubit device. We developed an automated alignment scheme to compensate for long term charge noise within the device, permitting reliable spin readout over timescales of days without manual intervention to tune the gate voltages. Utilising an adiabatic passage technique to overcome magnetic field noise due to the bath of fluctuating ^{29}Si nuclear spins within the silicon substrate, we performed spin resonance experiments on both the 1P and 2P qubits. The spin resonance spectra obtained validated the assigned donor number for each qubit. For the single donor we observed two resonance peaks, associated with the nuclear spin-up and -down states, separated by a hyperfine splitting of $97MHz$. For the 2P molecule the three observed peaks correspond with the expected resonances of the four two-donor spin product states with a hyperfine splitting of of 262MHz. The hyperfine interaction strength in the 2P case was more than double the single donor value, reflecting the more tightly confined wavefunction within the donor molecule. Comparison with tight-binding theoretical simulations allowed us to determine the inter-donor separation of the two atoms comprising the 2P molecule and also provided an indication of their exact geometric configuration within the silicon crystal lattice.

In a second two qubit device we achieved coherent rotation of a spin 1/2 electron spin state, observing Rabi oscillations in the measured spin-up probability. In analysing the damping envelope of the observed oscillations, we determined that our spin rotation is hampered by fluctuations of the Overhauser magnetic field caused by interacting ^{29}Si nuclear spins in the substrate. Using spin echo sequences, we partially compensate for the effect of nuclear spins, in order to measure an electron spin decoherence time $T_2 = 298\mu$s, three orders of magnitude larger than the observed pure dephasing time $T_2^* = 284$ns. We also demonstrated full control over the Bloch sphere, by effecting spin rotations about an arbitrary axis, achieved by modifying the phase of the applied microwave frequency field. Thus, we showed in Chapter 5, the full set of operations needed to define a qubit – initialisation, projective state read-out and arbitrary control of the qubit state over the full Hilbert space.

The unique hyperfine coupling of donor molecules provides an effective means of addressing qubits within a small scale system, and the spin control techniques we have demonstrated are the critical development translating our established scalable quantum dot technology into a true scalable qubit.

Scalable surface code architecture

In Chapter 6, we have laid out the concept for a large-scale array of donor qubits capable of correcting errors arising as a result of environmental decoherence and relaxation. In developing an implementation of the surface code error correction protocol, we have embraced the characteristics of donors, in particular their small size, and their uniformity. We outlined a three-layer geometry, with a 2D lattice of single P donors spaced 30nm apart, along with readout SETs in a central layer, with parallel sets of control wires 40nm above and below, all within a solid crystal of isotopically purified ^{28}Si. We described the qubit basis states, taking advantage of the long decoherence time of an ionised phosphorus atom's nuclear spin as a memory qubit, and digitally detuning the resonant frequency by loading an electron in order to addressably activate a chosen set of qubits. We specified the universal set of one and two qubit quantum gates required to implement the surface code protocol. In particular we focussed on the two qubit CNOT gate which is achieved by transferring the quantum information from nuclear spins to electron spins, and then allowing the electrons to evolve under the dipole-dipole interaction between their magnetic moments. The complexities of qubit control in our proposed architecture

are largely distilled into controlled electron tunnelling. Thus we outlined a non-trivial method to load or remove an electron whilst preserving the phase information encoded in the nuclear spin. We carefully analysed both the electrostatic control requirements, concluding that all the required operations can be executed with gate voltages on the order of only 100mV. Furthermore, we determined that the overall error rate achievable in our design, based on current technological limitations is below the 1% threshold required for error corrected quantum computing.

The architecture presented is scalable by design, and even using a remarkably small number of control gates, each qubit is individually addressable.

7.0.2 Future work

The results summarised above suggest a number of directions for continued research, some of which are already in progress. Here we describe briefly our expectations for the future evolution of the research program.

Precision fabrication

Understanding the relationship between the geometry of lithographically defined phosphorus incorporation regions and the resulting electron tunnel rates is critical in designing a qubit device. These tunnel rates ultimately determine the timescale of inter-qubit interactions and also the timescale of initialisation and readout processes. Whilst we have some guidance from theoretical modelling, from the various devices we have measured, it appears that not only the distance is important, but also the size and shape of the two features an electron is tunnelling to and from. For instance, a single donor and a 2P molecule may have different tunnel rates to a large SET even if the separation distance is the same. Investigating the sensitivity to various geometric parameters, including the importance of the various axes of the crystal structure will be important in progressing to more complex multi-qubit devices. Additionally, whilst our current understanding of the phosphorus incorporation pathway allows the prediction of the final donor location to within 1nm accuracy, there is scope for reducing this residual uncertainty.

Improved measurement and control speed

In combating decoherence, a faster operation speed is desirable, since a greater number of operations can be performed before the onset of decoherence. Ongoing work aims to increase the oscillating B_1 field strength by reducing microwave signal loss in our measurement set-up. This is a simple technical enhancement, which we expect will reduce the time required to rotate the electron spin substantially, potentially increasing the Rabi frequency by two orders of magnitude from the current value of $\sim$ 1MHz.

Faster tunnel rates and higher bandwith gates and sensors will permit more rapid single shot readout, also desirable. Recent experiments by Tettamanzi *et al.*[13]* looking into the bandwidth of our phosphorus doped nanowires have shown that signals up to at least 10GHz can be applied to donor defined in-plane gates without significant degradation of the signal due to the impedance of the nanowires. Current results from House *et al.*[220] show that RF reflectometry does allow for high bandwidth charge sensing, with usable bandwidth beyond the 1MHz level for an RF-SET, and above 100kHz for a single terminal sensor. Of course to capture the benefits of these fast gate and sensor speeds, the electron tunnel rates must be increased accordingly by reducing the physical dimensions of the relevant tunnel gaps.

Coherent two qubit coupling

Our success with controlling the strength of the exchange interactions between electrons in donor quantum dots will have to be extended to achieve coherent control in the singlet-triplet basis. Broome *et al.*[3] have recently developed additional analysis and modelling relating to our 1P-2P two qubit device, indicating that the tunnel coupling required to observe coherent swapping of the spin states via the exchange interaction is on the order of several GHz, an order of magnitude stronger than was present in our two qubit device. Thus, ongoing work continues to realise a two qubit device with a stronger tunnel coupling suitable for observing exchange oscillations.

Removal of nuclear spin noise

An active area of development over the next years will be the integration of isotopically purified ^{28}Si into our fabrication scheme. This requires not only purified wafer stock,

* work that I was substantially involved in, but which is not included in this thesis

but also a significant quantity (cubic centimetres) of bulk material as a source for the epitaxial encapsulation layer to be grown over the donor layer. Thus the prospect is technically challenging. Based on results from Muhonen *et al.*[38], who have shown that electron spin coherence can be extended to over half a second in a device fabricated in ^{28}Si, we expect to achieve several orders of magnitude enhancement of the coherence time of our electron qubits, and also long coherence times for nuclear spins in purified ^{28}Si. Isotopic purification has also been shown to dramatically improve quantum gate fidelity, with Muhonen *et al.*[51] measuring an electron spin rotation fidelity above 99.9%, well within the surface code's error correction threshold.

Entanglement between nuclear and electron spins

One of the key advantages of donors is that each atom naturally provides two qubits. Dehollain *et al.*[225] utilised entanglement between the nuclear and electron spins of a donor to perform a Bell test, and observed verifiably non-classical correlations. An exciting near term goal following our electron spin resonance results, it to use nuclear magnetic resonance to coherently control the nuclear spin state of a donor, or potentially multi-donor molecules. This is promising, not only for the addition of a second qubit and expanded Hilbert space, but also because the nuclear spin can be used as a resource to increase the fidelity of electron spin readout, by mapping the electron state to the nucleus and repeatedly and non-destructively measuring the nuclear spin state[50].

Demonstrating surface code fragments

A natural set of goals following from our surface code architecture proposal is the experimental realisation of individual elements of the design. Notably: (i) a demonstration of the phase matched loading process, showing that nuclear phase can be preserved by a pulse train of carefully timed windows for electron tunnelling; (ii) simultaneous and parallel application of nuclear qubit gates addressed by the presence of an electron on the donor; and (iii) the controlled phase gate mediated by dipolar coupling. All of these can be achieved with a simple two donor device, built in a single plane, but of course the continued development of three dimensional devices is also a priority for the near future, with tunnelling through a vertically oriented SET being one clear goal. Moving beyond two qubits, the next challenges will be to demonstrate successful operation of

the error correcting protocol on a group of several qubits – as has been achieved recently with superconducting quantum circuits[226,227].

It is an exciting time for the solid-state quantum computing community, as the technology matures to the point where few-qubit devices become possible. Superconducting[228,229], photonic[230,231] and trapped ion[232,233] based qubits are already producing fascinating demonstrations of the usefulness of even small sets of interacting qubits. There are many 'competing' implementations, and it is fiendishly difficult to predict the trajectory of any one of them towards so-called quantum supremacy – the point at which a large-enough quantum computer outperforms a classical processor. The transistor was invented in 1947[234] with the express purpose of amplifying telephone signals – and no clue of the role it has since played in facilitating the information age. Whilst there are many proposed algorithms and applications for a quantum computer already at this early stage, one has to wonder just what its total impact on the world will be.

A

Supplementary details

A.1 RF reflectometry: hardware setup

The RF reflectometry experiments were performed in a cryogen free dilution refrigerator*.

The RF signal is generated† with a power of 16dBm at room temperature, then split with a 6 dB power splitter‡, one half providing the excitation signal to the device, the other providing the local oscillator signal for mixing with the output. The incoming RF signal is attenuated at each thermal stage of the dilution refrigerator (60 dB at RT; 10 dB at 3 K; 3 dB at 800 mK; and 3 dB at 50 mK) to reduce thermal noise.

A directional coupler§ at the mixing chamber plate then routes the signal into the resonant circuit via the CPL port (with 15dB attenuation) and back out to an amplifier⁂ (18 dB gain) at 3 K. We note that this is not an engineered cryogenic amplifier, but was

* Leiden Cryogenics CF500 † SRS SG386 ‡ Minicircuits ZFRSC-42-S § Minicircuits ZEDC-15-28 ⁂ Minicircuits ZX60-P103LN+

found to work satisfactorily after modification to remove a power supply protection capacitor.

At room temperature, two cascaded amplifiers[*] (40 dB total gain) precede the homodyne detector, which is composed of a 6 dB power splitter[†] to distribute the RF signal, a hybrid phase splitter[‡] to offset the two local oscillator signals by 90°, and two mixers[§] outputting the baseband signals I and Q to digitising multimeters[ℵ].

DC bias voltages are provided by low noise voltage sources[⊕].

A.2 Spin readout experiments: Hardware setup

The dual spin readout and spin correlation experiments were performed in a cryogen free dilution refrigerator[♯], within a superconducting magnet[◇].

Voltage pulses to perform spin readout are produced by an arbitrary waveform generator[♭], and added to DC bias voltages[**] with active summing amplifiers[††].

The time dependent SET current signal is digitised by a real-time sampling oscilloscope[‡‡] after being amplified with a low noise transimpedance amplifier[§§], electrically decoupled[ℵℵ] and filtered[⊕⊕].

A.3 Spin readout experiments: Fidelity

In this appendix we analyse the fidelity of our dual spin readout protocol. The assignment of a spin-up or -down electron from each SET current trace comprises of two

[*] Minicircuits ZFL-1000LN+ [†] Minicircuits ZFRSC-42-S [‡] Minicircuits ZX10Q-2-13-s
[§] Minicircuits ZEM-2B [ℵ] Keithley 2001 [⊕] Yokogawa 7561 [♯] Leiden Cryogenics CF500
[◇] Cryogenic Limited - custom make [♭] Tektronix AFG3052C [**] SRS SIM-928 [††] SRS SIM-980
[‡‡] Keysight MSOX3024A [§§] Femto DLPCA-200 [ℵℵ] SRS SIM-910 [⊕⊕] SRS SIM-965

separate parts, (i) spin-to-charge conversion and (ii) electrical readout. For clarity, we describe the mechanisms as for the 1P spin-dependent unloading readout mode. Equivalent mechanisms apply for the D^- spin-dependent loading readout mode.

(I) Spin-to-charge conversion

We optimise the spin-to-charge conversion fidelity by determining the optimum length of time for each read phase of the readout sequence. During spin-to-charge conversion, errors are introduced from three main sources: T_1 relaxation of spin-up electrons; spin-up electrons failing to tunnel to the SET during the designated read time; and spin-down electrons tunnelling to the SET due to thermal excitation.

We use a rate equation model[54,55] to determine the optimum readout time, Δt, by maximising the probability that an electron will tunnel when expected to, or not tunnel as expected to, given its spin state – α and β respectively. As an input to the model, the tunnelling times of $|\uparrow\rangle \rightarrow |0\rangle$, $\tau_{\uparrow \mathrm{out}}$ and $|0\rangle \rightarrow |\downarrow\rangle$, $\tau_{\downarrow \mathrm{in}}$ are shown in Figure A.1(a,b), obtained by analysis of single-shot readout data - the start and end times of single blips describe $\tau_{\uparrow \mathrm{out}}$ and $\tau_{\downarrow \mathrm{in}}$. In addition, the spin-down tunnelling time from the qubit site to the SET, $\tau_{\downarrow \mathrm{out}}$ was also measured experimentally to be and 0.61±0.06s and 25±5s for qubit-L and -R respectively. We refer the reader to Büch *et al.*[54] for details of the derivation of the following terms using a rate equation model.

$$\beta(t) = \exp\left(\frac{-t}{\tau_{\downarrow,out}}\right) \tag{A.1}$$

$$\alpha(t) = \frac{1}{T'}\left[T' - \frac{\tau_{\uparrow,out}\tau_{\downarrow,out}}{exp(\frac{t}{\tau_{\downarrow,out}})} - \frac{T_1(\tau_{\downarrow,out} - \tau_{\uparrow,out})}{exp(\frac{t}{T_1})exp(\frac{t}{\tau_{\uparrow,out}})}\right] \tag{A.2}$$

$$T' = T_1(\tau_{\downarrow,out} - \tau_{\uparrow,out}) + \tau_{\uparrow,out}\tau_{\downarrow,out} \tag{A.3}$$

The fidelities α and β are shown in Figure A.1(c,d) as a function of readout time, Δt. The visibility of spin-to-charge conversion is calculated as V_{STC}=α+β−1. The optimum readout time is chosen where V_{STC} is maximised.

(II) Electrical readout

The electrical readout involves determining whether a given SET current trace can be assigned as having a 'blip' during the read phase i.e. whether during the readout time

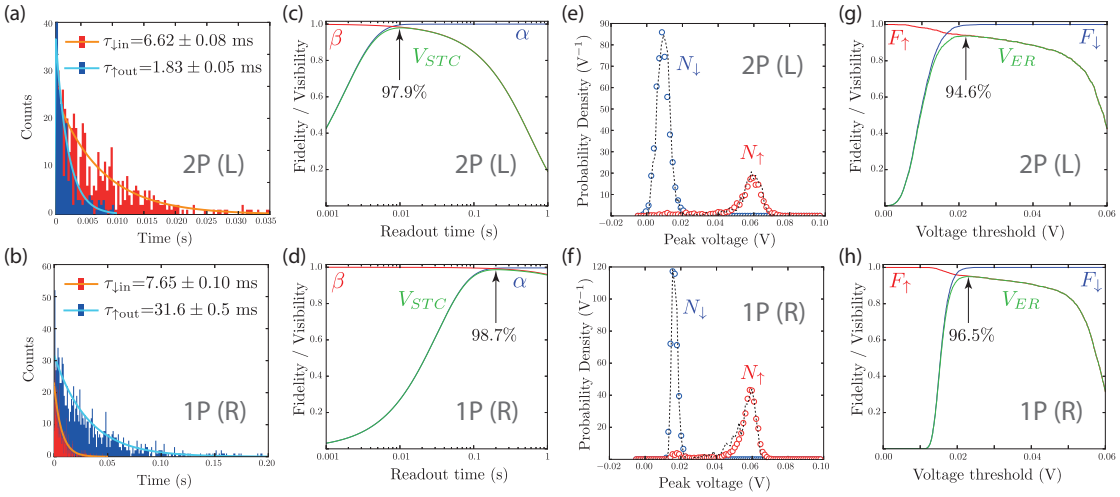

Figure A.1: Spin readout fidelity characterisation. (a,b) L, and R qubit histograms of spin dependent tunnelling times, with characteristic values $\tau_{\downarrow in}$,$\tau_{\uparrow out}$. (c,d) L, and R qubit spin-to-charge conversion visibility $V_{STC} = \alpha + \beta - 1$; probability of a spin-up state tunnelling within the readout time α; probability of a spin down state not tunnelling within the readout time β. Readout time is selected based on the maxima of V_{STC}. (e,f) L, and R qubit experimental datasets (black curve), and simulated histograms (blue/red dots) based on emperically determined noise and filter characteristics, of the distribution of observed peak values in a single readout current trace during the optimised readout time. (g,h) L, and R qubit electrical readout visibility $V_{ER} = F_\uparrow + F_\downarrow - 1$; probability of correctly assigning spin-down measurements using a particular voltage threshold, $F_\downarrow$; probability of correctly assigning spin-up measurements using a particular voltage threshold, $F_\uparrow$. Voltgate threshold for state discrimination is selected based on the maxima of V_{ER}.

(optimised in step i) the current surpasses a threshold value I_t. We optimise the threshold by simulating single-shot traces with statistical properties matching the experimental dataset, and assessing the level of erroneous state assignments.

From a simulation of 10,000 SET traces with characteristic tunnel times based on those determined in (a,b), 50% of which contain a 'blip', with added white Gaussian noise equivalent the signal-to-noise ratio observed in the experiment (an average of SNR=17dB for readout of both qubits), histograms of peak voltages V_p are generated, proportional to the SET current. The histograms are shown in Figure A.1(e,f) for L and R respectively. Note the use of peak voltage not current due to the use of a current amplifier on the drain of the SET charge sensor.

From these histograms the probability of correctly assigning either spin-up or -down

Parameter	Left qubit (2P)	Right qubit (1P)
Δt (ms)	10.5±0.1	209.0±30.0
α (%)	99.6±0.1	99.5±0.1
β (%)	98.2±0.1	99.1±0.1
V_{STC} (%)	97.9±0.1	98.7±0.2
V_t (V)	0.022±0.001	0.016±0.002
$F_\uparrow$ (%)	94.9±0.8	96.8±1.6
$F_\downarrow$ (%)	99.7±0.2	99.8±0.2
V_{ER} (%)	94.6±1.0	96.5±2.0
F_M (%)	96.2±1.1	97.6±2.1

Table A.1: Fidelity analysis of the 2P and 1P qubit spin readout at $B_0 = 2.5$T: optimal values of readout time Δt and voltage threshold V_t maximising the spin-to-charge and electrical-readout visibility parameters, producing an overall readout fidelity F_M

($F_\uparrow$ or $F_\downarrow$) to each current trace is calculated using the following set of equations,

$$F_\uparrow = 1 - \int_{-\infty}^{V_t} N_\uparrow(V_P) dV_p \tag{A.4}$$

$$F_\downarrow = 1 - \int_{V_t}^{\infty} N_\downarrow(V_P) dV_p \tag{A.5}$$

where V_t is the equivalent voltage threshold for I_t after the current amplifier and N_i is the fraction of spin state i. The results are shown in Figure A.1(g,h) with the addition of the calculated electrical readout visibility V_{ER}=$F_\uparrow$+$F_\downarrow$−1. From this we can determine the optimum voltage threshold, V_t, where V_{ER} is maximised.

Table A.1 gives a summary of the fidelity calculations for both qubits, where the final measurement fidelity is given by, $F_M = (\alpha F_\uparrow + \beta F_\downarrow)/2$.

Experiments with the second two qubit device are ongoing at the time of writing and an optimised fidelity assessment has not yet been performed at the time of writing.

A.4 ESR experiments: Hardware setup

The electron spin resonance experiments were performed in a liquid helium bath dilution refrigerator* containing a superconducting magnet.

ESR signals upto 44GHz were produced with a microwave generator† and fed from room temperature through a double DC-block‡ into a UT-85 stainless steel cable within the dilution refrigerator insert. In addition to the significant thermalisation from the cable, we use a 1dB attenuator§ at the 4K stage. The signal is launched⋈ from the cable to a custom PCB with a low loss substrate and impedance matched coplanar waveguide, and finally wire-bonded (1 wire for the signal pin, and 3 for the ground connection on either side) to the on-chip waveguide/antenna described in Section 5.4.1.

Modulation was applied for the adiabatic passage experiments using an external multi-channel arbitrary waveform generator (AWG)⊕, providing both frequency and pulse modulation signals to the FM and pulse-gating functionalities of the microwave generator. In the coherent control experiments the same AWG was used to provide I and Q signals used as inputs to the microwave generator's vector modulation functionality.

Instruments were triggered by a multi-channel digital-to-analog/analog-to-digital device♯ which also provides the pulsed gate voltage signals, and digitises the SET current readout signal after it has been amplified by a low noise transimpedance amplifier◇, electrically decoupled♭ and filtered**.

A.5 ESR experiments: Electric fields

We have estimated the electric field present at each donor site in a simple finite-element field solver. The simulation was performed using *Comsol Multiphysics* software, modelling the P doped conducting structures as perfect conducting sheets within an infinite

* Oxford Instruments Kelvinox400 † Keysight E8267D ‡ Pasternack PE8227 § Huber & Suhner 6601_SMA-50-1 ⋈ Southwest Microwave 1092-04A-5 ⊕ Tektronix 5014C ♯ National Instruments USB-6363 ◇ Femto DLPCA-200 ♭ SRS SIM-910 ** SRS SIM-965

block of silicon. Real gate voltages were applied to each of the conducting regions corresponding to their values in the experiment, and as provided in Table A.2. The results of the simulation are shown in Figure A.2.

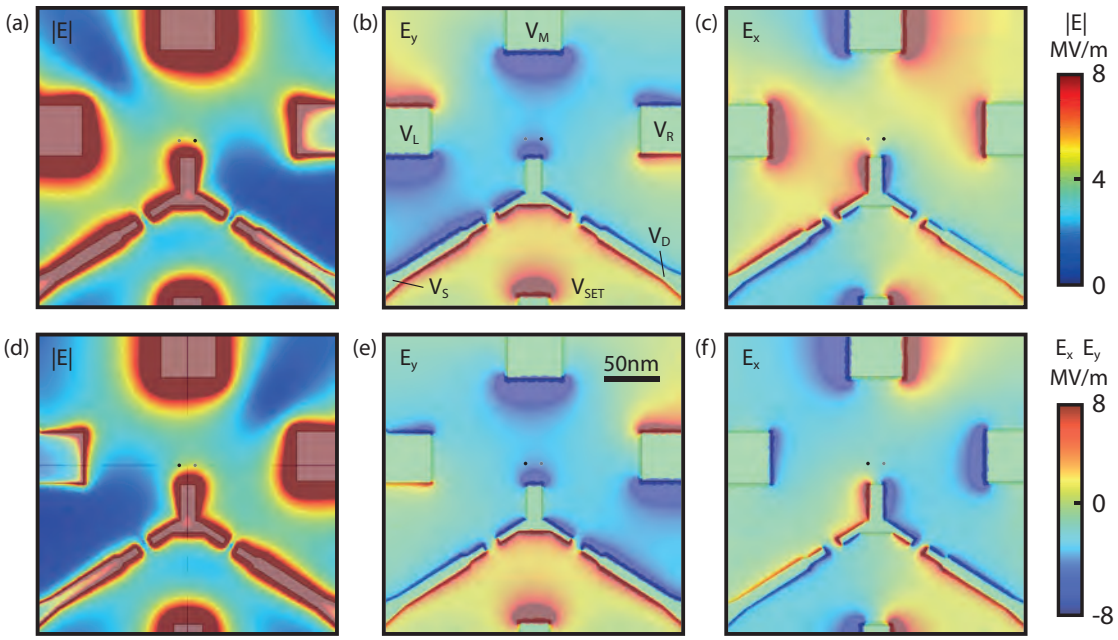

Figure A.2: Electric fields at the 1P and 2P qubit operating points. (a,b,c) Electric field magnitude, y-component, and x-component as simulated for the gate voltage configuration corresponding to the working point for the 1P qubit (d,e,f) Electric field magnitude, y-component, and x-component as simulated for the gate voltage configuration corresponding to the working point for the 2P qubit. Colourbars are provided separately for the field magnitude ($0 - 8\text{MV/m}$) and in-plane field components ($-8 - 8\text{MV/m}$), the qubit positions are marked as black dots, and applied voltage labels are shown in (b).

A.6 Hyperfine energy simulations: NEM0-3D

Simulations to determine the hyperfine interaction energy based on donor configuration and electric field were carried out by collaborators* using a software framework called

* Yu Wang, Chin-Yi Chen, and Rajib Rahman at Purdue University

Parameter	Right qubit (1P)	Left qubit (12P)
V_S (mV)	2	2
V_D (mV)	0	0
V_L (mV)	730	43
V_M (mV)	800	800
V_R (mV)	-50	650
V_{SET} (mV)	600	600
$\|E\|$ (MV/m)	4.5±0.1	4.3±0.1
E_x (MV/m)	0.9±0.2	-0.5±0.2
E_y (MV/m)	-4.4±0.1	-4.3±0.1

Table A.2: Gate settings and resultant E-field estimates at the two qubit working points: the E-field is numerically computed by solving the Poisson equation with boundary conditions derived from the gate settings. The uncertainty in field values are based on a positional uncertainty for the qubits of $\sim$ 1nm.

NEMO-3D (NanoElectronic MOdelling tool - in 3 Dimensions)[151,235]. The sophisticated framework encompasses numerical computation of electronic bandstructure, potential, charge density and other physical properties based on benchmarking by self-consistently solving the Schrödinger and Poisson equations in a domain encompassing several million atoms, where the wavefunction for each atom is described in a $sp^3d^5s^*$ spin-resolved (therefore 20 states) tight-binding orbital basis. NEMO-3D has been successfully applied to reproduce measured values in precision donor defined devices fabricated by STM lithography, including: the binding energies of single donor[53,113] and few donor[56] quantum dots, transport currents though atomic scale nanowires[66] and delta-doped layers[112], T_1 spin relaxation times in single donors and few donor quantum dots[152]; as well as providing predictions of hyperfine energies[54,150] and tunnel coupling strengths between donor quantum dots[154].

The simulation process starts with a Hamiltonian H comprising terms describing:

- the full silicon lattice H_{Si}, describing $\sim$ millions of atoms
- the Coulomb potential wells of any P donors H_{D}, truncated at the donor site to a value U_D benchmarked to produce accurate bound state binding energies.
- electron-electron interactions $H_{\text{e-e}}$, in a Hartree mean-field approximation ob-

tained by iteratively and self-consistently computing the electron density via the Shcrodinger equation, and mean-field potential via the Poisson equation after assuming that electrons fill the lowest available states according to the Pauli exclusion principle

- electric fields H_E, as a simple position dependent potential of the form $\vec{E} \cdot \vec{r}$
- magnetic fields H_B, as a simple spin dependent Zeeman energy of the form $\vec{B} \cdot \vec{\sigma}$ for all unpaired electrons and donor nuclei spins $\vec{\sigma}$
- Hyperfine interaction H_A, comprising contact and dipolar hyperfine components, although the dipolar term is in most cases omitted from calculations after verifying that the dipolar contribution is negligible.

The complete Hamiltonian is input into the time independent Schrödinger equation

$$H\Psi_m = \varepsilon_m \Psi_m \tag{A.6}$$

and the solutions for the eigenfunctions Ψ_m and eigenenergies ε_m are computed in the $sp^3d^5s^*$ basis using a parallel block Lanczoz algorithm, and the few lowest energy eigenstates (i.e. Ψ_m for small m) are taken and used to calculate the relevant properties of the system.

Full set of computed hyperfine energies for 2P molecules

The geometrical layout for the full set of out-of-plane configurations are displayed in Figure A.3, considering up to 2 monolayers of vertical diffusion or segregation of one of the two donors. Figure A.3 plots the full set as coloured markers based on the A value, with out-of-plane geometries indicated by dashed circles. The point shown with a red cross corresponds to nearest neighbour pairs, which are electrically inactive and therefore not relevant in our analysis. The layout of these points in the [001] plane is shown in Figure A.3(b), with fill-colours corresponding to their A values and line-styles denoting the vertical offset from the plane of the reference atom as indicated in the inset.

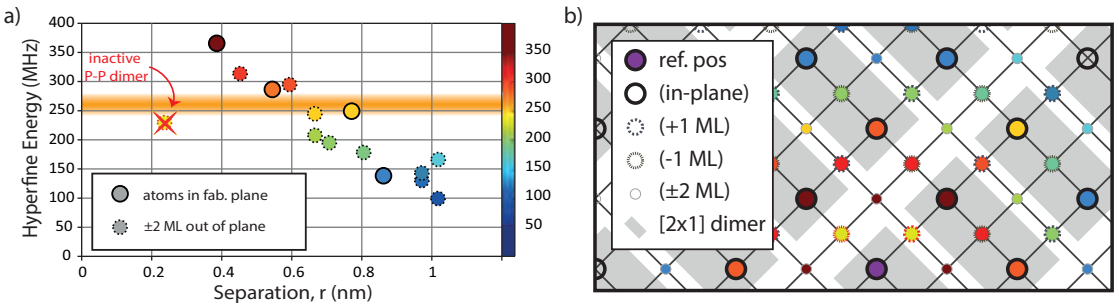

Figure A.3: Intrinsic hyperfine energies for different donor configurations of a 2P molecule. (a) Simulated Hyperfine interaction energy A, for atomic configurations of a 2P quantum dot with donor separation less than 1nm, and with upto a 2 monolayer vertical offset between the two donor atoms. (b) Schematic showing the layout of the [001] crystal plane and several monolayers above and below. Atoms are shown coloured according to their relationship to the central purple reference site, and with a line-style indicating their vertical offset in monolayers (ML). The dimer structure present at the surface during fabrication is indicated by grey rectangles.

A.7 Surface code architecture simulations: Super-operator formalism

Simulations to compute the error rate associated with our proposed Phase-Matched tunnelling sequence, and were carried out by collaborators* using the Lindblad super-operator formalism[236]. The technique is a commonly used to model so-called open quantum systems[237]. It is a master equation approach which encompasses the coherent quantum dynamics as well as classical evolution due to decoherence and loss.

Non-unitary dynamics are captured by the density matrix, an operator describing a probabilistic mixture of quantum states:

$$\rho = \sum_n p_n \left|\psi_n\right\rangle \left\langle\psi_n\right| \tag{A.7}$$

where p_n is the classical probability that the quantum system may be found in a state $|\psi_n\rangle$

By including a description of the system's environment in the von Neumann equation, and making some approximations, the standard time-dependent Lindblad master

* Charles Hill and Lloyd Hollenberg at the University of Melbourne

equation is obtained:

$$\frac{\partial \rho(t)}{\partial t} = \frac{-i}{\hbar}\left[H(t), \rho(t)\right] + \sum_n \frac{1}{2}\left[2\hat{L}_n \rho(t) \hat{L}_n^\dagger - \rho(t)\hat{L}_n\hat{L}_n^\dagger - \hat{L}_n^\dagger \hat{L}_n \rho(t)\right] \tag{A.8}$$

where $H(t)$ is the time dependent Hamiltonian of the internal system dynamics, and $\hat{L}_n = \sqrt{\gamma_n}\hat{\Lambda}_n$ are collapse operators describing interactions $\hat{\Lambda}_n$ between the system and environment, acting with a characteristic timescale $1/\gamma_n$. The sum in Equation (A.8) represents a set of operators that act on the density matrix operator – hence the name super-operator.

The core assumptions in deriving Equation (A.8) are:

- That the system and environment are separable, and there are no correlations between them at $t = 0$.
- That the environment influences the system, but the back action onto the environment due to the system dynamics is negligible.
- The environment has effectively no memory, or that time correlations in the environment decay much faster than the timescale of the system dynamics
- Oscillating terms describing the system-environment interaction with frequencies faster than internal system dynamics are assumed to average to zero, and are neglected.

The master equation Equation (A.8) can be integrated in time to produce the system dynamics – the probabilities p_n of occupation for a chosen set of basis states $|\psi_n\rangle$ as a function of time, according to a time dependent Hamiltonian reflecting the pulse sequence we intend to apply. A part of the full CNOT sequence is displayed in Figure A.4(a), indicating the operators applied to electron and nuclear spins of the target and control qubits.

An example of the computed time evolution is shown in Figure A.4(b), with colour-coded basis state labels describing each curve. This plot shows the state preparation up to the start of the electron dipole-dipole mediated CPHASE operation, for an initial nuclear spin state of $|\Uparrow, \Uparrow\rangle$ – both qubits in their ground state.

The error analysis of Section 6.3.8 involves repeatedly simulating the dynamics for various pulse parameters and initial conditions, and determining the departure from the ideal unitary behaviour in the absence of collapse operators.

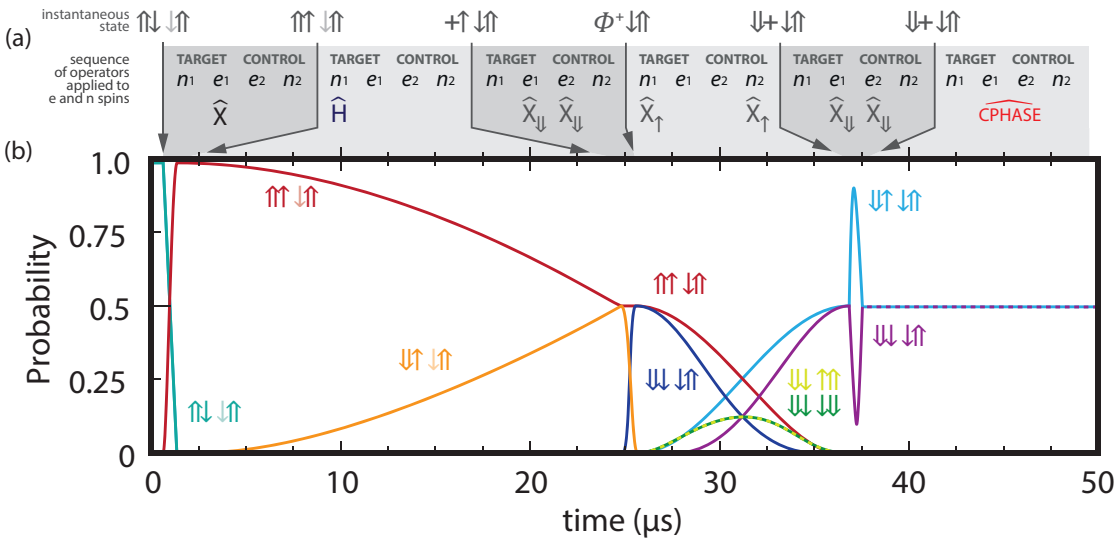

Figure A.4: **Simulated spin dynamics in the super-operator formalism.** (a) Sequence of operators applied in order to effect the first part of a physical qubit CNOT, up to the start of the dipole-dipole interaction period. Including electron initialisation nuclear Hadamard transform, three electron-nuclear CNOT gates in order to SWAP the qubit state from the nuclear subspace to the electron subspace. Above the sequence is shown the progression of intermediate states, starting with both nuclear spin qubits in the ground state. ($+$ denotes a superposition $1/\sqrt{2}(\uparrow + \downarrow)$ or $1/\sqrt{2}(\Uparrow + \Downarrow)$ and $\Phi^+ = 1/\sqrt{2}(\Uparrow\Uparrow + \Downarrow\Downarrow)$ is the positive even Bell state.) (b) The probability of occupation is calculated as a function of time for each of the spin product basis states, as indicated.

References

[1] S. J. Hile, M. G. House, E. Peretz, J. Verduijn, D. Widmann, T. Kobayashi, S. Rogge, and M. Y. Simmons, "Radio frequency reflectometry and charge sensing of a precision placed donor in silicon," Applied Physics Letters **107**, 093504 (2015).

[2] M. G. House, T. Kobayashi, B. Weber, S. J. Hile, T. F. Watson, J. van der Heijden, S. Rogge, and M. Y. Simmons, "Radio frequency measurements of tunnel couplings and singlet-triplet spin states in Si:P quantum dots," Nature Communications **6**, 8848 (2015).

[3] M. A. Broome, S. K. Gorman, M. G. House, S. J. Hile, J. G. Keizer, D. Keith, C. D. Hill, T. F. Watson, W. J. Baker, L. C. L. Hollenberg, and M. Y. Simmons, "Two-electron spin correlations in precision placed donors in silicon," Submitted (2017).

[4] S. J. Hile, L. Fricke, M. G. House, E. Peretz, Y. Wang, C. Y. Chen, M. A. Broome, S. K. Gorman, J. G. Keizer, R. Rahman, and M. Y. Simmons, "Electron spin resonance spectra of precision donor qubits," in Preparation (2017).

[5] S. J. Hile, L. Fricke, M. G. House, P. Pakkaim, S. K. Gorman, J. G. Keizer, and M. Y. Simmons, "Coherent oscillations and electron spin decoherence in precision donor qubits," in Preparation (2017).

[6] C. D. Hill, E. Peretz, S. J. Hile, M. G. House, M. Fuechsle, S. Rogge, M. Y. Simmons, and L. C. Hollenberg, "A surface code quantum computer in silicon," Science Advances **1**, e1500707 (2015).

[7] L. C. L. Hollenberg, C. D. Hill, M. Y. Simmons, E. Peretz, S. Rogge, M. Fuechsle, and S. J. Hile, "Apparatus and method for quantum processing [i]," (2016), US Patent 20,160,125,310.

[8] M. Fuechsle, S. J. Hile, C. D. Hill, L. C. L. Hollenberg, M. G. House, E. Peretz, S. Rogge, and M. Y. Simmons, "Apparatus and method for quantum processing [ii]," (2016), US Patent 20,160,125,311.

[9] M. G. House, E. Peretz, J. G. Keizer, S. J. Hile, and M. Y. Simmons, "Single-charge detection by an atomic precision tunnel junction," Applied Physics Letters **104**, 113111 (2014).

[10] T. Kobayashi, J. van der Heijden, M. G. House, S. J. Hile, P. Asshoff, M. F. Gonzalez-Zalba, M. Vinet, M. Y. Simmons, and S. Rogge, "Resonant tunneling spectroscopy of valley eigenstates on a donor-quantum dot coupled system," Applied Physics Letters **108**, 152102 (2016).

[11] S. K. Gorman, M. A. Broome, J. G. Keizer, T. F. Watson, S. J. Hile, W. J. Baker, and M. Y. Simmons, "Extracting inter-dot tunnel couplings between few donor quantum dots in silicon," New Journal of Physics **18**, 053041 (2016).

[12] M. A. Broome, S. K. Gorman, J. G. Keizer, T. F. Watson, S. J. Hile, W. J. Baker, and M. Y. Simmons, "Mapping the chemical potential landscape of a triple quantum dot," Physical Review B **94**, 054314 (2016).

[13] G. C. Tettamanzi, S. J. Hile, M. G. House, M. Fuechsle, S. Rogge, and M. Y. Simmons, "Probing the quantum states of a single atom transistor at microwave frequencies," ACS Nano **11**, 2444–2451 (2016).

[14] M. A. Broome, T. F. Watson, D. Keith, S. K. Gorman, M. G. House, S. J. Hile, J. G. Keizer, W. J. Baker, and M. Y. Simmons, "High fidelity single-shot singlet-triplet readout of precision placed donors in silicon," Submitted (2017).

[15] R. P. Feynman, "Simulating physics with computers," International journal of theoretical physics **21**, 467–488 (1982).

[16] D. Deutsch, "Quantum theory, the church-turing principle and the universal quantum computer," in *Proceedings of the Royal Society of London A: Mathematical, Physical and Engineering Sciences*, Vol. 400 (The Royal Society, 1985) pp. 97–117.

[17] S. Lloyd, "Universal quantum simulators," Science **273**, 1073 (1996).

[18] P. J. J. O'Malley, R. Babbush, I. D. Kivlichan, J. Romero, J. R. McClean, R. Barends, J. Kelly, P. Roushan, A. Tranter, N. Ding, *et al.*, "Scalable quantum simulation of molecular energies," Physical Review X **6**, 031007 (2016).

[19] P. W. Shor, "Algorithms for quantum computation: Discrete logarithms and factoring," in *Foundations of Computer Science, 1994 Proceedings., 35th Annual Symposium on* (IEEE, 1994) pp. 124–134.

[20] L. K. Grover, "Quantum mechanics helps in searching for a needle in a haystack," Physical Review Letters **79**, 325 (1997).

[21] M. A. Nielsen and I. L. Chuang, *Quantum Computation and Quantum Information* (Cambridge University Press, 2010).

[22] D. P. DiVincenzo, "The physical implementation of quantum computation," Fortschritte der Physik **48**, 771 (2000).

[23] T. D. Ladd, F. Jelezko, R. Laflamme, Y. Nakamura, C. Monroe, and J. L. O'Brien, "Quantum computers," Nature **464**, 45–53 (2010).

[24] E. Knill, "Quantum computing with realistically noisy devices," Nature **434**, 39–44 (2005).

[25] R. Raussendorf and J. Harrington, "Fault-tolerant quantum computation with high threshold in two dimensions," Physical Review Letters **98**, 190504 (2007).

[26] D. Loss and D. P. DiVincenzo, "Quantum computation with quantum dots," Physical Review A **57**, 120 (1998).

[27] L. P. Kouwenhoven, C. M. Marcus, P. L. McEuen, S. Tarucha, R. M. Westervelt, and N. S. Wingreen, "Electron transport in quantum dots," in *Mesoscopic electron transport* (Springer, 1997) pp. 105–214.

[28] R. Hanson, L. P. Kouwenhoven, J. R. Petta, S. Tarucha, and L. M. Vandersypen, "Spins in few-electron quantum dots," Reviews of Modern Physics **79**, 1217 (2007).

[29] J. M. Elzerman, R. Hanson, L. H. W. Van Beveren, B. Witkamp, L. M. K. Vandersypen, and L. P. Kouwenhoven, "Single-shot read-out of an individual electron spin in a quantum dot," Nature **430**, 431–435 (2004).

[30] F. H. L. Koppens, C. Buizert, K.-J. Tielrooij, I. T. Vink, K. C. Nowack, T. Meunier, L. P. Kouwenhoven, and L. M. K. Vandersypen, "Driven coherent oscillations of a single electron spin in a quantum dot," Nature **442**, 766–771 (2006).

[31] K. C. Nowack, M. Shafiei, M. Laforest, G. E. D. Prawiroatmodjo, L. R. Schreiber, C. Reichl, W. Wegscheider, and L. M. K. Vandersypen, "Single-shot correlations and two-qubit gate of solid-state spins," Science **333**, 1269–1272 (2011).

[32] J. R. Petta, A. C. Johnson, J. M. Taylor, E. A. Laird, A. Yacoby, M. D. Lukin, C. M. Marcus, M. P. Hanson, and A. C. Gossard, "Coherent manipulation of

coupled electron spins in semiconductor quantum dots," Science **309**, 2180–2184 (2005).

[33] J. R. Petta, J. M. Taylor, A. C. Johnson, A. Yacoby, M. D. Lukin, C. M. Marcus, M. P. Hanson, and A. C. Gossard, "Dynamic nuclear polarization with single electron spins," Physical Review Letters **100**, 067601 (2008).

[34] F. A. Zwanenburg, A. S. Dzurak, A. Morello, M. Y. Simmons, L. C. Hollenberg, G. Klimeck, S. Rogge, S. N. Coppersmith, and M. A. Eriksson, "Silicon quantum electronics," Reviews of Modern Physics **85**, 961 (2013).

[35] K.-i. Takyu, K. M. Itoh, K. Oka, N. Saito, and V. I. Ozhogin, "Growth and characterization of the isotopically enriched ^{28}Si bulk single crystal," Japanese Journal of Applied Physics **38**, L1493 (1999).

[36] K. M. Itoh and H. Watanabe, "Isotope engineering of silicon and diamond for quantum computing and sensing applications," MRS Communications **4**, 143–157 (2014).

[37] M. Steger, K. Saeedi, M. L. W. Thewalt, J. J. L. Morton, H. Riemann, N. V. Abrosimov, P. Becker, and H.-J. Pohl, "Quantum information storage for over 180 s using donor spins in a ^{28}Si "semiconductor vacuum"," Science **336**, 1280–1283 (2012).

[38] J. T. Muhonen, J. P. Dehollain, A. Laucht, F. E. Hudson, R. Kalra, T. Sekiguchi, K. M. Itoh, D. N. Jamieson, J. C. McCallum, A. S. Dzurak, *et al.*, "Storing quantum information for 30 seconds in a nanoelectronic device," Nature Nanotechnology **9**, 986–991 (2014).

[39] C. B. Simmons, M. Thalakulam, N. Shaji, L. J. Klein, H. Qin, R. H. Blick, D. E. Savage, M. G. Lagally, S. N. Coppersmith, and M. A. Eriksson, "Single-electron quantum dot in Si/SiGe with integrated charge sensing," Applied Physics Letters **91**, 213103 (2007).

[40] W. H. Lim, F. A. Zwanenburg, H. Huebl, M. Möttönen, K. W. Chan, A. Morello, and A. S. Dzurak, "Observation of the single-electron regime in a highly tunable silicon quantum dot," Applied Physics Letters **95**, 242102 (2009).

[41] E. Kawakami, P. Scarlino, D. R. Ward, F. R. Braakman, D. E. Savage, M. G. Lagally, M. Friesen, S. N. Coppersmith, M. A. Eriksson, and L. M. K. Vandersypen,

"Electrical control of a long-lived spin qubit in a si/sige quantum dot," Nature Nanotechnology **9**, 666–670 (2014).

[42] E. Kawakami, T. Jullien, P. Scarlino, D. R. Ward, D. E. Savage, M. G. Lagally, V. V. Dobrovitski, M. Friesen, S. N. Coppersmith, M. A. Eriksson, *et al.*, "Gate fidelity and coherence of an electron spin in an si/sige quantum dot with micromagnet," Proceedings of the National Academy of Sciences **113**, 11738–11743 (2016).

[43] M. Veldhorst, J. C. C. Hwang, C. H. Yang, A. W. Leenstra, B. De Ronde, J. P. Dehollain, J. T. Muhonen, F. E. Hudson, K. M. Itoh, A. Morello, *et al.*, "An addressable quantum dot qubit with fault-tolerant control-fidelity," Nature Nanotechnology **9**, 981–985 (2014).

[44] M. Veldhorst, C. H. Yang, J. C. C. Hwang, W. Huang, J. P. Dehollain, J. T. Muhonen, S. Simmons, A. Laucht, F. E. Hudson, K. M. Itoh, *et al.*, "A two-qubit logic gate in silicon," Nature **526**, 410–414 (2015).

[45] B. E. Kane, "A silicon-based nuclear spin quantum computer," Nature **393**, 133–137 (1998).

[46] G. W. Morley, M. Warner, A. M. Stoneham, P. T. Greenland, J. Van Tol, C. W. Kay, and G. Aeppli, "The initialization and manipulation of quantum information stored in silicon by bismuth dopants," Nature Materials **9**, 725–729 (2010).

[47] C. D. Hill, L. C. L. Hollenberg, A. G. Fowler, C. J. Wellard, A. D. Greentree, and H.-S. Goan, "Global control and fast solid-state donor electron spin quantum computing," Physical Review B **72**, 045350 (2005).

[48] R. de Sousa, J. D. Delgado, and S. D. Sarma, "Silicon quantum computation based on magnetic dipolar coupling," Physical Review A **70**, 052304 (2004).

[49] J. J. Pla, K. Y. Tan, J. P. Dehollain, W. H. Lim, J. J. Morton, D. N. Jamieson, A. S. Dzurak, and A. Morello, "A single-atom electron spin qubit in silicon," Nature **489**, 541–545 (2012).

[50] J. J. Pla, K. Y. Tan, J. P. Dehollain, W. H. Lim, J. J. Morton, F. A. Zwanenburg, D. N. Jamieson, A. S. Dzurak, and A. Morello, "High-fidelity readout and control of a nuclear spin qubit in silicon," Nature **496**, 334–338 (2013).

[51] J. T. Muhonen, A. Laucht, S. Simmons, J. P. Dehollain, R. Kalra, F. E. Hudson, S. Freer, K. M. Itoh, D. N. Jamieson, J. C. McCallum, *et al.*, "Quantifying the quantum gate fidelity of single-atom spin qubits in silicon by randomized benchmarking," Journal of Physics: Condensed Matter **27**, 154205 (2015).

[52] S. R. Schofield, N. J. Curson, M. Y. Simmons, F. J. Rueß, T. Hallam, L. Oberbeck, and R. G. Clark, "Atomically precise placement of single dopants in si," Physical Review Letters **91**, 136104 (2003).

[53] M. Fuechsle, J. A. Miwa, S. Mahapatra, H. Ryu, S. Lee, O. Warschkow, L. C. Hollenberg, G. Klimeck, and M. Y. Simmons, "A single-atom transistor," Nature Nanotechnology **7**, 242–246 (2012).

[54] H. Büch, S. Mahapatra, R. Rahman, A. Morello, and M. Y. Simmons, "Spin readout and addressability of phosphorus-donor clusters in silicon," Nature Communications **4**, 2017 (2013).

[55] T. F. Watson, B. Weber, M. G. House, H. Büch, and M. Y. Simmons, "High-fidelity rapid initialization and read-out of an electron spin via the single donor D^- charge state," Physical Review Letters **115**, 166806 (2015).

[56] B. Weber, Y. H. Tan, S. Mahapatra, T. F. Watson, H. Ryu, R. Rahman, L. C. Hollenberg, G. Klimeck, and M. Y. Simmons, "Spin blockade and exchange in coulomb-confined silicon double quantum dots," Nature Nanotechnology , 430 (2014).

[57] T. F. Watson, B. Weber, Y.-L. Hsueh, L. L. Hollenberg, R. Rahman, and M. Y. Simmons, "Atomically engineered electron spin lifetimes of 30 s in silicon," Science Advances **3**, e1602811 (2017).

[58] C. Kittel, *Introduction to solid state physics* (John Wiley & Sons, 1966).

[59] N. W. Ashcroft and N. D. Mermin, "Solid state physics," Cengage Learning (1976), 10.1063/1.3037370.

[60] J. R. Chelikowsky and M. L. Cohen, "Electronic structure of silicon," Physical Review B **10**, 5095 (1974).

[61] T. F. Rosenbaum, R. F. Milligan, M. A. Paalanen, G. A. Thomas, R. N. Bhatt, and W. Lin, "Metal-insulator transition in a doped semiconductor," Physical Review B **27**, 7509 (1983).

[62] A. F. Da Silva, "Metal-insulator transitions in doped silicon and germanium," Physical Review B **37**, 4799 (1988).

[63] D. J. Carter, O. Warschkow, N. A. Marks, and D. R. McKenzie, "Electronic structure models of phosphorus δ-doped silicon," Physical Review B **79**, 033204 (2009).

[64] S. R. McKibbin, C. M. Polley, G. Scappucci, J. G. Keizer, and M. Y. Simmons, "Low resistivity, super-saturation phosphorus-in-silicon monolayer doping," Applied Physics Letters **104**, 123502 (2014).

[65] M. Fuechsle, S. Mahapatra, F. A. Zwanenburg, M. Friesen, M. A. Eriksson, and M. Y. Simmons, "Spectroscopy of few-electron single-crystal silicon quantum dots," Nature Nanotechnology **5**, 502–505 (2010).

[66] B. Weber, S. Mahapatra, H. Ryu, S. Lee, A. Fuhrer, T. C. G. Reusch, D. L. Thompson, W. C. T. Lee, G. Klimeck, L. C. Hollenberg, *et al.*, "Ohm's law survives to the atomic scale," Science **335**, 64–67 (2012).

[67] W. G. Van der Wiel, S. De Franceschi, J. M. Elzerman, T. Fujisawa, S. Tarucha, and L. P. Kouwenhoven, "Electron transport through double quantum dots," Reviews of Modern Physics **75**, 1 (2002).

[68] W. Kohn and J. M. Luttinger, "Theory of donor states in silicon," Physical Review **98**, 915 (1955).

[69] A. K. Ramdas and S. Rodriguez, "Spectroscopy of the solid-state analogues of the hydrogen atom: donors and acceptors in semiconductors," Reports on Progress in Physics **44**, 1297 (1981).

[70] P. J. Mohr, D. B. Newell, and B. N. Taylor, "Codata recommended values of the fundamental physical constants: 2014," Journal of Physical and Chemical Reference Data **45**, 043102 (2016).

[71] G. Feher, "Electron spin resonance experiments on donors in silicon. i. electronic structure of donors by the electron nuclear double resonance technique," Physical Review **114**, 1219 (1959).

[72] M. Steger, T. Sekiguchi, A. Yang, K. Saeedi, M. E. Hayden, M. L. W. Thewalt, K. M. Itoh, H. Riemann, N. V. Abrosimov, P. Becker, *et al.*, "Optically-detected NMR of optically-hyperpolarized ^{31}P neutral donors in ^{28}Si," Journal of Applied Physics **109**, 102411 (2011).

[73] R. P. Feynman, R. B. Leighton, and M. Sands, *The Feynman lectures on physics, Vol. III: Quantum mechanics*, edited by M. A. Gottlieb and R. Pfeiffer, Vol. 3 (California Institute of Technology, 1965) http://www.feynmanlectures.caltech.edu/III_12.html .

[74] A. Schweiger and G. Jeschke, *Principles of pulse electron paramagnetic resonance* (Oxford University Press, 2001).

[75] M. H. Levitt, *Spin dynamics: basics of nuclear magnetic resonance* (John Wiley & Sons, 2001).

[76] F. J. Ruess, L. Oberbeck, K. E. J. Goh, M. J. Butcher, E. Gauja, A. R. Hamilton, and M. Y. Simmons, "The use of etched registration markers to make four-terminal electrical contacts to STM-patterned nanostructures," Nanotechnology **16**, 2446 (2005).

[77] J. W. Lyding, T.-C. Shen, J. S. Hubacek, J. R. Tucker, and G. C. Abeln, "Nanoscale patterning and oxidation of h-passivated Si (100)-2×1 surfaces with an ultrahigh vacuum scanning tunneling microscope," Applied Physics Letters **64**, 2010–2012 (1994).

[78] H. F. Wilson, O. Warschkow, N. A. Marks, N. J. Curson, S. R. Schofield, T. C. G. Reusch, M. W. Radny, P. V. Smith, D. R. McKenzie, and M. Y. Simmons, "Thermal dissociation and desorption of PH_3 on Si (001): A reinterpretation of spectroscopic data," Physical Review B **74**, 195310 (2006).

[79] I.-W. Lyo and P. Avouris, "Field-induced nanometer-to atomic-scale manipulation of silicon surfaces with the STM," Science **253**, 173–177 (1991).

[80] J. L. O'Brien, S. R. Schofield, M. Y. Simmons, R. G. Clark, A. S. Dzurak, N. J. Curson, B. E. Kane, N. S. McAlpine, M. E. Hawley, and G. W. Brown, "Towards the fabrication of phosphorus qubits for a silicon quantum computer," Physical Review B **64**, 161401 (2001).

[81] M. M. Fuechsle, *Precision few-electron silicon quantum dots*, Ph.D. thesis, Physics, Faculty of Science, U N SW, Sydney (2011), http://handle.unsw.edu.au/1959.4/51332 .

[82] T. C. G. Reusch, N. J. Curson, S. R. Schofield, T. Hallam, and M. Y. Simmons, "Phosphorus and hydrogen atoms on the (001) surface of silicon: A comparative

scanning tunnelling microscopy study of surface species with a single dangling bond," Surface Science **600**, 318–324 (2006).

[83] T. Hallam, F. J. Rueß, N. J. Curson, K. E. J. Goh, L. Oberbeck, M. Y. Simmons, and R. G. Clark, "Effective removal of hydrogen resists used to pattern devices in silicon using scanning tunneling microscopy," Applied Physics Letters **86**, 143116 (2005).

[84] T. Hallam, M. J. Butcher, K. E. J. Goh, F. J. Ruess, and M. Y. Simmons, "Use of a scanning electron microscope to pattern large areas of a hydrogen resist for electrical contacts," Journal of Applied Physics **102**, 034308 (2007).

[85] M. Rudolph, S. M. Carr, G. Subramania, G. Ten Eyck, J. Dominguez, T. Pluym, M. P. Lilly, M. S. Carroll, and E. Bussmann, "Probing the limits of Si:P δ-doped devices patterned by a scanning tunneling microscope in a field-emission mode," Applied Physics Letters **105**, 163110 (2014).

[86] S. R. Schofield, N. J. Curson, O. Warschkow, N. A. Marks, H. F. Wilson, M. Y. Simmons, P. V. Smith, M. W. Radny, D. R. McKenzie, and R. G. Clark, "Phosphine dissociation and diffusion on Si (001) observed at the atomic scale," The Journal of Physical Chemistry B **110**, 3173–3179 (2006).

[87] O. Warschkow, H. F. Wilson, N. A. Marks, S. R. Schofield, N. J. Curson, P. V. Smith, M. W. Radny, D. R. McKenzie, and M. Y. Simmons, "Phosphine adsorption and dissociation on the Si (001) surface: An ab initio survey of structures," Physical Review B **72**, 125328 (2005).

[88] J. M. Bennett, O. Warschkow, N. A. Marks, and D. R. McKenzie, "Pathways for thermal phosphorus desorption from the silicon (001) surface," Physical Review B **82**, 235417 (2010).

[89] K. E. J. Goh and M. Y. Simmons, "Impact of Si growth rate on coherent electron transport in Si:P delta-doped devices," Applied Physics Letters **95**, 142104 (2009).

[90] K. E. J. Goh, L. Oberbeck, M. Y. Simmons, A. R. Hamilton, and R. G. Clark, "Effect of encapsulation temperature on Si:P δ-doped layers," Applied physics letters **85**, 4953–4955 (2004).

[91] S. R. McKibbin, W. R. Clarke, and M. Y. Simmons, "Investigating the surface quality and confinement of Si:P δ-layers at different growth temperatures," Physica E: Low-dimensional Systems and Nanostructures **42**, 1180–1183 (2010).

[92] M. Fuechsle, F. J. Rueß, T. C. Reusch, M. Mitic, and M. Y. Simmons, "Surface gate and contact alignment for buried, atomically precise scanning tunneling microscopy–patterned devices," Journal of Vacuum Science & Technology B: Microelectronics and Nanometer Structures Processing, Measurement, and Phenomena **25**, 2562–2567 (2007).

[93] A. C. Johnson, J. R. Petta, J. M. Taylor, A. Yacoby, M. D. Lukin, C. M. Marcus, M. P. Hanson, and A. C. Gossard, "Triplet–singlet spin relaxation via nuclei in a double quantum dot," Nature **435**, 925–928 (2005).

[94] A. Morello, J. J. Pla, F. A. Zwanenburg, K. W. Chan, K. Y. Tan, H. Huebl, M. Möttönen, C. D. Nugroho, C. Yang, J. A. van Donkelaar, *et al.*, "Single-shot readout of an electron spin in silicon," Nature **467**, 687–691 (2010).

[95] R. J. Schoelkopf, P. Wahlgren, A. A. Kozhevnikov, P. Delsing, and D. E. Prober, "The radio-frequency single-electron transistor (rf-set): A fast and ultrasensitive electrometer," Science **280**, 1238–1242 (1998).

[96] B. J. Villis, A. O. Orlov, X. Jehl, G. L. Snider, P. Fay, and M. Sanquer, "Defect detection in nano-scale transistors based on radio-frequency reflectometry," Applied Physics Letters **99**, 152106 (2011).

[97] A. Aassime, G. Johansson, G. Wendin, R. J. Schoelkopf, and P. Delsing, "Radio-frequency single-electron transistor as readout device for qubits: Charge sensitivity and backaction," Physical Review Letters **86**, 3376 (2001).

[98] T. Fujisawa and Y. Hirayama, "Charge noise analysis of an algaas/gaas quantum dot using transmission-type radio-frequency single-electron transistor technique," Applied Physics Letters **77**, 543–545 (2000).

[99] S. J. Angus, A. J. Ferguson, A. S. Dzurak, and R. G. Clark, "A silicon radio-frequency single electron transistor," Applied Physics Letters **92**, 112103 (2008).

[100] J. I. Colless, A. C. Mahoney, J. M. Hornibrook, A. C. Doherty, H. Lu, A. C. Gossard, and D. J. Reilly, "Dispersive readout of a few-electron double quantum dot with fast rf gate sensors," Physical Review Letters **110**, 046805 (2013).

[101] J. Verduijn, M. Vinet, and S. Rogge, "Radio-frequency dispersive detection of donor atoms in a field-effect transistor," Applied Physics Letters **104**, 102107 (2014).

[102] M. F. Gonzalez-Zalba, S. Barraud, A. J. Ferguson, and A. C. Betz, "Probing the limits of gate-based charge sensing," Nature Communications **6** (2015), 10.1038/ncomms7084.

[103] J. M. Hornibrook, J. I. Colless, A. C. Mahoney, X. G. Croot, S. Blanvillain, H. Lu, A. C. Gossard, and D. J. Reilly, "Frequency multiplexing for readout of spin qubits," Applied Physics Letters **104**, 103108 (2014).

[104] F. Persson, C. M. Wilson, M. Sandberg, G. Johansson, and P. Delsing, "Excess dissipation in a single-electron box: The sisyphus resistance," Nano Letters **10**, 953–957 (2010).

[105] J. Gabelli, G. Fève, J.-M. Berroir, B. Plaçais, A. Cavanna, B. Etienne, Y. Jin, and D. C. Glattli, "Violation of kirchhoff's laws for a coherent rc circuit," Science **313**, 499–502 (2006).

[106] A. Cottet, C. Mora, and T. Kontos, "Mesoscopic admittance of a double quantum dot," Physical Review B **83**, 121311 (2011).

[107] S. Mahapatra, H. Büch, and M. Y. Simmons, "Charge sensing of precisely positioned P donors in Si," Nano Letters **11**, 4376–4381 (2011).

[108] T. F. Watson, B. Weber, J. A. Miwa, S. Mahapatra, R. M. Heijnen, and M. Y. Simmons, "Transport in asymmetrically coupled donor-based silicon triple quantum dots," Nano Letters **14**, 1830–1835 (2014).

[109] K. D. Petersson, C. G. Smith, D. Anderson, P. Atkinson, G. A. C. Jones, and D. A. Ritchie, "Charge and spin state readout of a double quantum dot coupled to a resonator," Nano Letters **10**, 2789–2793 (2010).

[110] M. D. Schroer, M. Jung, K. D. Petersson, and J. R. Petta, "Radio frequency charge parity meter," Physical Review Letters **109**, 166804 (2012).

[111] B. Weber, S. Mahapatra, T. F. Watson, and M. Y. Simmons, "Engineering independent electrostatic control of atomic-scale (4 nm) silicon double quantum dots," Nano Letters **12**, 4001–4006 (2012).

[112] S. Lee, H. Ryu, H. Campbell, L. C. Hollenberg, M. Y. Simmons, and G. Klimeck, "Electronic structure of realistically extended atomistically resolved disordered Si:P δ-doped layers," Physical Review B **84**, 205309 (2011).

[113] H. Ryu, S. Lee, M. Fuechsle, J. A. Miwa, S. Mahapatra, L. C. Hollenberg, M. Y. Simmons, and G. Klimeck, "A tight-binding study of single-atom transistors," Small **11**, 374–381 (2015).

[114] R. Kalra, A. Laucht, C. D. Hill, and A. Morello, "Robust two-qubit gates for donors in silicon controlled by hyperfine interactions," Physical Review X **4**, 021044 (2014).

[115] J. P. Gordon and K. D. Bowers, "Microwave spin echoes from donor electrons in silicon," Physical Review Letters **1**, 368 (1958).

[116] G. Feher and E. A. Gere, "Electron spin resonance experiments on donors in silicon. ii. electron spin relaxation effects," Physical Review **114**, 1245 (1959).

[117] A. M. Tyryshkin, S. Tojo, J. J. Morton, H. Riemann, N. V. Abrosimov, P. Becker, H.-J. Pohl, T. Schenkel, M. L. Thewalt, K. M. Itoh, *et al.*, "Electron spin coherence exceeding seconds in high-purity silicon," Nature Materials **11**, 143–147 (2012).

[118] E. Abe, A. M. Tyryshkin, S. Tojo, J. J. Morton, W. M. Witzel, A. Fujimoto, J. W. Ager, E. E. Haller, J. Isoya, S. A. Lyon, *et al.*, "Electron spin coherence of phosphorus donors in silicon: Effect of environmental nuclei," Physical Review B **82**, 121201 (2010).

[119] A. M. Tyryshkin, J. J. L. Morton, S. C. Benjamin, A. Ardavan, G. A. D. Briggs, J. W. Ager, and S. A. Lyon, "Coherence of spin qubits in silicon," Journal of Physics: Condensed Matter **18**, S783 (2006).

[120] E. L. Hahn, "Spin echoes," Physical Review **80**, 580 (1950).

[121] A. W. Overhauser, "Polarization of nuclei in metals," Physical Review **92**, 411 (1953).

[122] W. M. Witzel, R. de Sousa, and S. D. Sarma, "Quantum theory of spectral-diffusion-induced electron spin decoherence," Physical Review B **72**, 161306 (2005).

[123] R. de Sousa and S. D. Sarma, "Theory of nuclear-induced spectral diffusion: Spin decoherence of phosphorus donors in Si and GaAs quantum dots," Physical Review B **68**, 115322 (2003).

[124] W. M. Witzel and S. D. Sarma, "Quantum theory for electron spin decoherence induced by nuclear spin dynamics in semiconductor quantum computer architec-

tures: Spectral diffusion of localized electron spins in the nuclear solid-state environment," Physical Review B **74**, 035322 (2006).

[125] T. G. Castner, "Orbach spin-lattice relaxation of shallow donors in silicon," Physical Review **155**, 816 (1967).

[126] V. V. Kurshev and T. Ichikawa, "Effect of spin flip-flop on electron-spin-echo decay due to instantaneous diffusion," Journal of Magnetic Resonance (1969) **96**, 563–573 (1992).

[127] J. Lu, F. Hoehne, A. R. Stegner, L. Dreher, M. Stutzmann, M. S. Brandt, and H. Huebl, "High-resolution electrical detection of free induction decay and Hahn echoes in phosphorus-doped silicon," Physical Review B **83**, 235201 (2011).

[128] A. Yang, M. Steger, T. Sekiguchi, M. L. W. Thewalt, T. D. Ladd, K. M. Itoh, H. Riemann, N. V. Abrosimov, P. Becker, and H.-J. Pohl, "Simultaneous subsecond hyperpolarization of the nuclear and electron spins of phosphorus in silicon by optical pumping of exciton transitions," Physical Review Letters **102**, 257401 (2009).

[129] X. Hao, R. Ruskov, M. Xiao, C. Tahan, and H. W. Jiang, "Electron spin resonance and spin–valley physics in a silicon double quantum dot," Nature Communications **5** (2014), 10.1038/ncomms4860.

[130] F. H. L. Koppens, K. C. Nowack, and L. M. K. Vandersypen, "Spin echo of a single electron spin in a quantum dot," Physical Review Letters **100**, 236802 (2008).

[131] H. Bluhm, S. Foletti, D. Mahalu, V. Umansky, and A. Yacoby, "Enhancing the coherence of a spin qubit by operating it as a feedback loop that controls its nuclear spin bath," Physical Review Letters **105**, 216803 (2010).

[132] H. Bluhm, S. Foletti, I. Neder, M. Rudner, D. Mahalu, V. Umansky, and A. Yacoby, "Dephasing time of gaas electron-spin qubits coupled to a nuclear bath exceeding 200 [thinsp][mu] s," Nature Physics **7**, 109–113 (2011).

[133] F. K. Malinowski, F. Martins, P. D. Nissen, E. Barnes, Ł. Cywiński, M. S. Rudner, S. Fallahi, G. C. Gardner, M. J. Manfra, C. M. Marcus, *et al.*, "Notch filtering the nuclear environment of a spin qubit," Nature Nanotechnology **12**, 16–20 (2016).

[134] J. P. Dehollain, J. J. Pla, E. Siew, K. Y. Tan, A. S. Dzurak, and A. Morello, "Nanoscale broadband transmission lines for spin qubit control," Nanotechnology **24**, 015202 (2012).

[135] H. Y. Carr and E. M. Purcell, "Effects of diffusion on free precession in nuclear magnetic resonance experiments," Physical Review **94**, 630 (1954).

[136] S. Meiboom and D. Gill, "Modified spin-echo method for measuring nuclear relaxation times," Review of Scientific Instruments **29**, 688–691 (1958).

[137] D. Suter and G. A. Álvarez, "Colloquium: Protecting quantum information against environmental noise," Reviews of Modern Physics **88**, 041001 (2016).

[138] A. M. Tyryshkin, Z.-H. Wang, W. Zhang, E. E. Haller, J. W. Ager, V. V. Dobrovitski, and S. A. Lyon, "Dynamical decoupling in the presence of realistic pulse errors," arXiv preprint (2010), https://arxiv.org/abs/1011.1903 .

[139] L. Viola, S. Lloyd, and E. Knill, "Universal control of decoupled quantum systems," Physical Review Letters **83**, 4888 (1999).

[140] Y. Tokura, W. G. van der Wiel, T. Obata, and S. Tarucha, "Coherent single electron spin control in a slanting zeeman field," Physical Review Letters **96**, 047202 (2006).

[141] J. Yoneda, T. Otsuka, T. Nakajima, T. Takakura, T. Obata, M. Pioro-Ladrière, H. Lu, C. J. Palmstrøm, A. C. Gossard, and S. Tarucha, "Fast electrical control of single electron spins in quantum dots with vanishing influence from nuclear spins," Physical Review Letters **113**, 267601 (2014).

[142] M. Pioro-Ladriere, T. Obata, Y. Tokura, Y.-S. Shin, T. Kubo, K. Yoshida, T. Taniyama, and S. Tarucha, "Electrically driven single-electron spin resonance in a slanting zeeman field," Nature Physics **4**, 776–779 (2008).

[143] P. Scarlino, E. Kawakami, D. R. Ward, D. E. Savage, M. G. Lagally, M. Friesen, S. N. Coppersmith, M. A. Eriksson, and L. M. K. Vandersypen, "Second-harmonic coherent driving of a spin qubit in a si/sige quantum dot," Physical Review Letters **115**, 106802 (2015).

[144] A. Noiri, J. Yoneda, T. Nakajima, T. Otsuka, M. R. Delbecq, K. Takeda, S. Amaha, G. Allison, A. Ludwig, A. D. Wieck, *et al.*, "Coherent electron-spin-resonance manipulation of three individual spins in a triple quantum dot," Applied Physics Letters **108**, 153101 (2016).

[145] T. Otsuka, T. Nakajima, M. R. Delbecq, S. Amaha, J. Yoneda, K. Takeda, G. Allison, T. Ito, R. Sugawara, A. Noiri, *et al.*, "Single-electron spin resonance in a quadruple quantum dot," Scientific Reports **6** (2016), 10.1038/srep31820.

[146] A. Laucht, J. T. Muhonen, F. A. Mohiyaddin, R. Kalra, J. P. Dehollain, S. Freer, F. E. Hudson, M. Veldhorst, R. Rahman, G. Klimeck, *et al.*, "Electrically controlling single-spin qubits in a continuous microwave field," Science Advances **1**, e1500022 (2015).

[147] F. R. Bradbury, A. M. Tyryshkin, G. Sabouret, J. Bokor, T. Schenkel, and S. A. Lyon, "Stark tuning of donor electron spins in silicon," Physical Review Letters **97**, 176404 (2006).

[148] M. Friesen, "Theory of the stark effect for P donors in Si," Physical Review Letters **94**, 186403 (2005).

[149] R. Rahman, C. J. Wellard, F. R. Bradbury, M. Prada, J. H. Cole, G. Klimeck, and L. C. Hollenberg, "High precision quantum control of single donor spins in silicon," Physical Review Letters **99**, 036403 (2007).

[150] Y. Wang, C.-Y. Chen, G. Klimeck, M. Y. Simmons, and R. Rahman, "Characterizing Si:P quantum dot qubits with spin resonance techniques," Scientific Reports **6** (2016), 10.1038/srep31830.

[151] G. Klimeck, F. Oyafuso, T. B. Boykin, R. C. Bowen, and P. von Allmen, "Development of a nanoelectronic 3-D (NEMO 3-D) simulator for multimillion atom simulations and its application to alloyed quantum dots," Comput. Model. Eng. Sci **3**, 601 (2002).

[152] Y.-L. Hsueh, H. Büch, Y. Tan, Y. Wang, L. C. Hollenberg, G. Klimeck, M. Y. Simmons, and R. Rahman, "Spin-lattice relaxation times of single donors and donor clusters in silicon," Physical Review Letters **113**, 246406 (2014).

[153] T. Watson, *Multi-qubit architectures for donor-based silicon quantum computing*, Ph.D. thesis, Physics, Faculty of Science, U N SW, Sydney (2015), http://handle.unsw.edu.au/1959.4/55032 .

[154] Y. Wang, A. Tankasala, L. C. Hollenberg, G. Klimeck, M. Y. Simmons, and R. Rahman, "Highly tunable exchange in donor qubits in silicon," npj Quantum Information **2**, 16008 (2016).

[155] C. D. Hill and H.-S. Goan, "Fast nonadiabatic two-qubit gates for the kane quantum computer," Physical Review A **68**, 012321 (2003).

[156] M. F. Gonzalez-Zalba, A. Saraiva, M. J. Calderón, D. Heiss, B. Koiller, and A. J. Ferguson, "An exchange-coupled donor molecule in silicon," Nano Letters **14**, 5672–5676 (2014).

[157] H. Büch, M. Fuechsle, W. Baker, M. G. House, and M. Y. Simmons, "Quantum dot spectroscopy using a single phosphorus donor," Physical Review B **92**, 235309 (2015).

[158] J. M. Taylor, J. R. Petta, A. C. Johnson, A. Yacoby, C. M. Marcus, and M. D. Lukin, "Relaxation, dephasing, and quantum control of electron spins in double quantum dots," Physical Review B **76**, 035315 (2007).

[159] L. M. Roth, "g factor and donor spin-lattice relaxation for electrons in germanium and silicon," Physical Review **118**, 1534 (1960).

[160] H. Hasegawa, "Spin-lattice relaxation of shallow donor states in ge and Si through a direct phonon process," Physical Review **118**, 1523 (1960).

[161] D. K. Wilson and G. Feher, "Electron spin resonance experiments on donors in silicon. iii. investigation of excited states by the application of uniaxial stress and their importance in relaxation processes," Physical Review **124**, 1068 (1961).

[162] B. Weber, , T. F. Watson, Y. Wang, C.-Y. Chen, R. Rahman, L. C. Hollenberg, and M. Y. Simmons, "Anisotropy in the spin relaxation time of donor bound electrons," Submitted (2017).

[163] B. M. Maune, M. G. Borselli, B. Huang, T. D. Ladd, P. W. Deelman, K. S. Holabird, A. A. Kiselev, I. Alvarado-Rodriguez, R. S. Ross, A. E. Schmitz, *et al.*, "Coherent singlet-triplet oscillations in a silicon-based double quantum dot," Nature **481**, 344–347 (2012).

[164] R. N. Simons, *Coplanar waveguide circuits, components, and systems*, Vol. 165 (John Wiley & Sons, 2004).

[165] S.-G. Mao, C.-T. Hwang, R.-B. Wu, and C. H. Chen, "Analysis of coplanar waveguide-to-coplanar stripline transitions," IEEE Transactions on Microwave Theory and Techniques **48**, 23–29 (2000).

[166] S. J. Hile, *Toward spin control of phosphorus donor qubits in silicon*, Master's thesis, School of Physics, UNSW, Sydney (2011).

[167] E. Kawakami, P. Scarlino, L. R. Schreiber, J. R. Prance, D. E. Savage, M. G. Lagally, M. A. Eriksson, and L. M. K. Vandersypen, "Excitation of a si/sige quantum dot using an on-chip microwave antenna," Applied Physics Letters **103**, 132410 (2013).

[168] M. Braun and G. Burkard, "Nonadiabatic two-parameter charge and spin pumping in a quantum dot," Physical Review Letters **101**, 036802 (2008).

[169] S. Shamim, S. Mahapatra, C. Polley, M. Y. Simmons, and A. Ghosh, "Suppression of low-frequency noise in two-dimensional electron gas at degenerately doped Si:P δ-layers," Physical Review B **83**, 233304 (2011).

[170] S. Shamim, B. Weber, D. W. Thompson, M. Y. Simmons, and A. Ghosh, "Ultralow-noise atomic-scale structures for quantum circuitry in silicon," Nano Letters **16**, 5779–5784 (2016).

[171] P. Du, W. A. Kibbe, and S. M. Lin, "Improved peak detection in mass spectrum by incorporating continuous wavelet transform-based pattern matching," Bioinformatics **22**, 2059–2065 (2006).

[172] M. Garwood and L. DelaBarre, "The return of the frequency sweep: designing adiabatic pulses for contemporary NMR," Journal of magnetic resonance **153**, 155–177 (2001).

[173] E. Kupce and R. Freeman, "Adiabatic pulses for wideband inversion and broadband decoupling," Journal of Magnetic Resonance, Series A **115**, 273–276 (1995).

[174] A. Laucht, R. Kalra, J. T. Muhonen, J. P. Dehollain, F. A. Mohiyaddin, F. Hudson, J. C. McCallum, D. N. Jamieson, A. S. Dzurak, and A. Morello, "High-fidelity adiabatic inversion of a ^{31}P electron spin qubit in natural silicon," Applied Physics Letters **104**, 092115 (2014).

[175] R. A. De Graaf and K. Nicolay, "Adiabatic rf pulses: Applications to in vivo NMR," Concepts in Magnetic Resonance **9**, 247–268 (1997).

[176] D. Pines, J. Bardeen, and C. P. Slichter, "Nuclear polarization and impurity-state spin relaxation processes in silicon," Physical Review **106**, 489 (1957).

[177] D. R. McCamey, J. Van Tol, G. W. Morley, and C. Boehme, "Fast nuclear spin hyperpolarization of phosphorus in silicon," Physical Review Letters **102**, 027601 (2009).

[178] J. J. Morton, A. M. Tyryshkin, R. M. Brown, S. Shankar, B. W. Lovett, A. Ardavan, T. Schenkel, E. E. Haller, J. W. Ager, and S. A. Lyon, "Solid-state quantum memory using the ^{31}P nuclear spin," Nature **455**, 1085–1088 (2008).

[179] D. R. McCamey, J. Van Tol, G. W. Morley, and C. Boehme, "Electronic spin storage in an electrically readable nuclear spin memory with a lifetime> 100 seconds," Science **330**, 1652–1656 (2010).

[180] A. R. Stegner, C. Boehme, H. Huebl, M. Stutzmann, K. Lips, and M. S. Brandt, "Electrical detection of coherent ^{31}P spin quantum states," Nature Physics **2**, 835–838 (2006).

[181] G. Pica, G. Wolfowicz, M. Urdampilleta, M. L. Thewalt, H. Riemann, N. V. Abrosimov, P. Becker, H.-J. Pohl, J. J. Morton, R. N. Bhatt, *et al.*, "Hyperfine stark effect of shallow donors in silicon," Physical Review B **90**, 195204 (2014).

[182] Ł. Cywiński, W. M. Witzel, and S. D. Sarma, "Electron spin dephasing due to hyperfine interactions with a nuclear spin bath," Physical Review Letters **102**, 057601 (2009).

[183] R. de Sousa, "Electron spin as a spectrometer of nuclear-spin noise and other fluctuations," in *Electron Spin Resonance and Related Phenomena in Low-Dimensional Structures* (Springer, 2009) pp. 183–220.

[184] F. H. L. Koppens, D. Klauser, W. A. Coish, K. C. Nowack, L. P. Kouwenhoven, D. Loss, and L. M. K. Vandersypen, "Universal phase shift and nonexponential decay of driven single-spin oscillations," Physical Review Letters **99**, 106803 (2007).

[185] E. I. Rashba, "Theory of electric dipole spin resonance in quantum dots: Mean field theory with gaussian fluctuations and beyond," Physical Review B **78**, 195302 (2008).

[186] V. V. Dobrovitski, A. E. Feiguin, R. Hanson, and D. D. Awschalom, "Decay of rabi oscillations by dipolar-coupled dynamical spin environments," Physical Review Letters **102**, 237601 (2009).

[187] Y.-C. Tang and G.-X. Miao, "Robust surface code topology against sparse fabrication defects in a superconducting-qubit array," Physical Review A **93**, 032322 (2016).

[188] J. P. Home, D. Hanneke, J. D. Jost, J. M. Amini, D. Leibfried, and D. J. Wineland, "Complete methods set for scalable ion trap quantum information processing," Science **325**, 1227–1230 (2009).

[189] J. Q. You, J. S. Tsai, and F. Nori, "Scalable quantum computing with Josephson charge qubits," Physical Review Letters **89**, 197902 (2002).

[190] M. Gimeno-Segovia, P. Shadbolt, D. E. Browne, and T. Rudolph, "From three-photon Greenberger-Horne-Zeilinger states to ballistic universal quantum computation," Physical Review Letters **115**, 020502 (2015).

[191] K. Nemoto, M. Trupke, S. J. Devitt, A. M. Stephens, B. Scharfenberger, K. Buczak, T. Nöbauer, M. S. Everitt, J. Schmiedmayer, and W. J. Munro, "Photonic architecture for scalable quantum information processing in diamond," Physical Review X **4**, 031022 (2014).

[192] C. Monroe, R. Raussendorf, A. Ruthven, K. R. Brown, P. Maunz, L.-M. Duan, and J. Kim, "Large-scale modular quantum-computer architecture with atomic memory and photonic interconnects," Physical Review A **89**, 022317 (2014).

[193] J. Preskill, "Reliable quantum computers," in *Proceedings of the Royal Society of London A: Mathematical, Physical and Engineering Sciences*, Vol. 454 (The Royal Society, 1998) pp. 385–410.

[194] A. G. Fowler, M. Mariantoni, J. M. Martinis, and A. N. Cleland, "Surface codes: Towards practical large-scale quantum computation," Physical Review A **86**, 032324 (2012).

[195] R. W. Hamming, "Error detecting and error correcting codes," Bell Labs Technical Journal **29**, 147–160 (1950).

[196] P. W. Shor, "Scheme for reducing decoherence in quantum computer memory," Physical review A **52**, R2493 (1995).

[197] A. R. Calderbank and P. W. Shor, "Good quantum error-correcting codes exist," Physical Review A **54**, 1098 (1996).

[198] A. M. Steane, "Error correcting codes in quantum theory," Physical Review Letters **77**, 793 (1996).

[199] A. M. Steane, "Overhead and noise threshold of fault-tolerant quantum error correction," Physical Review A **68**, 042322 (2003).

[200] S. B. Bravyi and A. Y. Kitaev, "Quantum codes on a lattice with boundary," arXiv preprint (1998), https://arxiv.org/abs/quant-ph/9811052 .

[201] E. Dennis, A. Kitaev, A. Landahl, and J. Preskill, "Topological quantum memory," Journal of Mathematical Physics **43**, 4452–4505 (2002).

[202] J. Edmonds, "Paths, trees, and flowers," Canadian Journal of Mathematics **17**, 449–467 (1965).

[203] D. S. Wang, A. G. Fowler, A. M. Stephens, and L. C. L. Hollenberg, "Threshold error rates for the toric and planar codes," Quantum Information & Computation **10**, 456–469 (2010).

[204] D. S. Wang, A. G. Fowler, and L. C. Hollenberg, "Surface code quantum computing with error rates over 1%," Physical Review A **83**, 020302 (2011).

[205] S. Bravyi and A. Kitaev, "Universal quantum computation with ideal clifford gates and noisy ancillas," Physical Review A **71**, 022316 (2005).

[206] J. O'Gorman, N. H. Nickerson, P. Ross, J. J. Morton, and S. C. Benjamin, "A silicon-based surface code quantum computer," NPJ Quantum Information **2**, 15019 (2016).

[207] G. Pica, B. W. Lovett, R. N. Bhatt, T. Schenkel, and S. A. Lyon, "Surface code architecture for donors and dots in silicon with imprecise and nonuniform qubit couplings," Physical Review B **93**, 035306 (2016).

[208] G. Tosi, F. A. Mohiyaddin, H. Huebl, and A. Morello, "Circuit-quantum electrodynamics with direct magnetic coupling to single-atom spin qubits in isotopically enriched ^{28}Si," AIP Advances **4**, 087122 (2014).

[209] G. Tosi, F. A. Mohiyaddin, S. B. Tenberg, R. Rahman, G. Klimeck, and A. Morello, "Silicon quantum processor with robust long-distance qubit couplings," arXiv preprint (2015), https://arxiv.org/abs/1509.08538 .

[210] S. R. McKibbin, G. Scappucci, W. Pok, and M. Y. Simmons, "Epitaxial top-gated atomic-scale silicon wire in a three-dimensional architecture," Nanotechnology **24**, 045303 (2013).

[211] J. G. Keizer, S. Koelling, P. M. Koenraad, and M. Y. Simmons, "Suppressing segregation in highly phosphorus doped silicon monolayers," ACS Nano **9**, 12537–12541 (2015).

[212] W. M. Haynes, *CRC Handbook of Chemistry and Physics* (CRC Press, 2016).

[213] A. Soare, H. Ball, D. Hayes, J. Sastrawan, M. C. Jarratt, J. J. McLoughlin, X. Zhen, T. J. Green, and M. J. Biercuk, "Experimental noise filtering by quantum control," Nature Physics **10**, 825–829 (2014).

[214] J. S. Waugh, L. M. Huber, and U. Haeberlen, "Approach to high-resolution NMR in solids," Physical Review Letters **20**, 180 (1968).

[215] K. R. Mote, V. Agarwal, and P. K. Madhu, "Five decades of homonuclear dipolar decoupling in solid-state NMR: Status and outlook," Progress in Nuclear Magnetic Resonance Spectroscopy **97**, 1–39 (2016).

[216] S. Wimperis, "Broadband, narrowband, and passband composite pulses for use in advanced NMR experiments," Journal of Magnetic Resonance, Series A **109**, 221–231 (1994).

[217] M. J. Testolin, C. D. Hill, C. J. Wellard, and L. C. L. Hollenberg, "Robust controlled-not gate in the presence of large fabrication-induced variations of the exchange interaction strength," Physical Review A **76**, 012302 (2007).

[218] C. D. Hill, "Robust controlled-not gates from almost any interaction," Physical Review Letters **98**, 180501 (2007).

[219] K. Nabors and J. White, "Multipole-accelerated 3-D capacitance extraction algorithms for structures with conformal dielectrics," in *Design Automation Conference, 1992. Proceedings., 29th ACM/IEEE* (IEEE, 1992) pp. 710–715.

[220] M. G. House, I. Bartlett, P. Pakkiam, M. Koch, E. Peretz, J. van der Heijden, T. Kobayashi, S. Rogge, and M. Y. Simmons, "High-sensitivity charge detection with a single-lead quantum dot for scalable quantum computation," Physical Review Applied **6**, 044016 (2016).

[221] M. J. Biercuk, A. C. Doherty, and H. Uys, "Dynamical decoupling sequence construction as a filter-design problem," Journal of Physics B: Atomic, Molecular and Optical Physics **44**, 154002 (2011).

[222] S. D. Barrett and T. M. Stace, "Fault tolerant quantum computation with very high threshold for loss errors," Physical Review Letters **105**, 200502 (2010).

[223] A. C. Whiteside and A. G. Fowler, "Upper bound for loss in practical topological-cluster-state quantum computing," Physical Review A **90**, 052316 (2014).

[224] C. Horsman, A. G. Fowler, S. Devitt, and R. Van Meter, "Surface code quantum computing by lattice surgery," New Journal of Physics **14**, 123011 (2012).

[225] J. P. Dehollain, S. Simmons, J. T. Muhonen, R. Kalra, A. Laucht, F. Hudson, K. M. Itoh, D. N. Jamieson, J. C. McCallum, A. S. Dzurak, *et al.*, "Bell's inequality violation with spins in silicon," Nature Nanotechnology **11**, 242–246 (2015).

[226] J. Kelly, R. Barends, A. G. Fowler, A. Megrant, E. Jeffrey, T. C. White, D. Sank, J. Y. Mutus, B. Campbell, Y. Chen, *et al.*, "State preservation by repetitive error detection in a superconducting quantum circuit," Nature **519**, 66–69 (2015).

[227] A. D. Córcoles, E. Magesan, S. J. Srinivasan, A. W. Cross, M. Steffen, J. M. Gambetta, and J. M. Chow, "Demonstration of a quantum error detection code using a square lattice of four superconducting qubits," Nature Communications **6** (2015), 10.1038/ncomms7979.

[228] P. Roushan, C. Neill, A. Megrant, Y. Chen, R. Babbush, R. Barends, B. Campbell, Z. Chen, B. Chiaro, A. Dunsworth, *et al.*, "Chiral ground-state currents of interacting photons in a synthetic magnetic field," Nature Physics **13**, 146–151 (2016).

[229] C. Neill, P. Roushan, M. Fang, Y. Chen, M. Kolodrubetz, Z. Chen, A. Megrant, R. Barends, B. Campbell, B. Chiaro, *et al.*, "Ergodic dynamics and thermalization in an isolated quantum system," Nature Physics **12**, 1037–1041 (2016).

[230] E. Martín-López, A. Laing, T. Lawson, R. Alvarez, X.-Q. Zhou, and J. L. O'brien, "Experimental realization of shor's quantum factoring algorithm using qubit recycling," Nature Photonics **6**, 773–776 (2012).

[231] X.-D. Cai, C. Weedbrook, Z.-E. Su, M.-C. Chen, M. Gu, M.-J. Zhu, L. Li, N.-L. Liu, C.-Y. Lu, and J.-W. Pan, "Experimental quantum computing to solve systems of linear equations," Physical Review Letters **110**, 230501 (2013).

[232] S. Debnath, N. M. Linke, C. Figgatt, K. A. Landsman, K. Wright, and C. Monroe, "Demonstration of a small programmable quantum computer with atomic qubits," Nature **536**, 63–66 (2016).

[233] T. Monz, D. Nigg, E. A. Martinez, M. F. Brandl, P. Schindler, R. Rines, S. X. Wang, I. L. Chuang, and R. Blatt, "Realization of a scalable shor algorithm," Science **351**, 1068–1070 (2016).

[234] M. Riordan, L. Hoddeson, and C. Herring, "The invention of the transistor," Reviews of Modern Physics **71**, S336 (1999).

[235] S. Steiger, M. Povolotskyi, H.-H. Park, T. Kubis, and G. Klimeck, "Nemo5: A parallel multiscale nanoelectronics modeling tool," IEEE Transactions on Nanotechnology **10**, 1464–1474 (2011).

[236] G. Lindblad, "On the generators of quantum dynamical semigroups," Communications in Mathematical Physics **48**, 119–130 (1976).

[237] C. M. Caves, "Quantum error correction and reversible operations," Journal of Superconductivity **12**, 707–718 (1999)

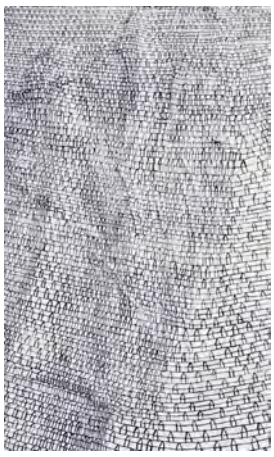

This thesis was typeset using XeLaTeX, developed by Jonathan Kew based on Leslie Lamport's LaTeX and Donald Knuth's TeX, with reference management using Oren Patashnik's BibTeX. A template that may be used to produce a document with this look & feel is available thanks to Jordan Suchow (dissertate.io). The artworks above, entitled *'Effect of Butterflies on Boat Building Blocks II'*, *'Phase Transition: Boat to Bird'*, and *'Evolution in a Q-Bit'*, as well as the cover art, were created by Steven Durbach (sidsledge.com) during a collaborative artistic residency with the research group during the course of this research. Thanks for reading :-)